BIOLOGICAL EFFECTS OF GOLD NANOPARTICLES IN THE LUNG

NG CHENG TENG

(B.Sc.(Hons), NUS)

A THESIS SUBMITTED FOR

THE DEGREE OF DOCTOR OF PHILOSOPHY

DEPARTMENT OF ANATOMY

YONG LOO LING SCHOOL OF MEDICINE NATIONAL UNIVERSITY OF SINGAPORE

2014

DECLARATION

I hereby declare that this thesis is my original work and it has been written by me in its entirety. I have duly acknowledged all the sources of information which have been used in the thesis.

This thesis has also not been submitted for any degree in any university previously.

_____

Ng Cheng Teng

(22nd December 2014)

ACKNOWLEDGEMENTS

All the research studies performed in the past 4 years and this thesis would not have been possible without the guidance, support and help from many people. Hence, with heartfelt gratitude, I would like to acknowledge and thank:

Professor Bay Boon Huat, the HOD of Department of Anatomy, my doctoral supervisor, for giving me tremendous support, mentorship, enlightenment, patience, constructive critique & suggestion, guidance and encouragement. It has been my great honour to carry out my doctoral studies under his supervision, to learn not only research-related matters, but many other things under the sun. Given his wealth of knowledge, I thank him for sharing his knowledge and ideas, for being critical yet supportive, for inspiring me in my studies despite his busy schedule. I thank him from the bottom of my heart, for all the valuable lessons which he has taught me throughout the years; for being supportive especially during my pregnancy. I am indeed greatly indebted to him, for his time spending for discussion and reading my thesis. His tutelage to his students will not be forgotten and will continue to be my inspiration. Thanks for giving me an enriching and fulfilling journey in pursuing my PhD.

A/P Lanry Yung, my co-supervisor, for his mentorship and valuable suggestions. I have learnt a great deal from him, as he is always insightful and he has trained me to exercise critical thinking during my PhD candidature. I also thank him for being supportive, and his relentless efforts in helping me in my research works, and completing this degree. I learnt so much from him, although he is of different disciplinary backgrounds. He has showed me how he, as an engineer, can pick up biological knowledge so well.

Thesis Advisory Committee: Dr Karthik and A/P George Yip WC. Also thanks A/P George Yip for assisting the statistical analysis for the microarray work.

A/P Dheen ST for providing suggestions for epigenetic works.

Dr Jayantha G for our collaborative work. Thanks for opening up new methodology for proteomic studies. Also thank his lab members, Dr Claire Swa and Ms Rachel for the proteomic work and statistical analysis.

A/P Manoor Prakash Hande, for allowing me to perform comet assay in his lab. Also thank his current and former lab members Dr Grace Lim, Dr Shriram and Ms Dimphy for helping me in my experiments.

Dr Chen Ee Sin from Dept. of Biochemistry, for teaching and providing me technical support in my coIP experiment.

A/P Liya Yu, for allowing me to use her instrument for microwave digestion. Also thank her former student, Dr Balasubraniam SK for teaching me the experimental techniques, pioneering and assisting the animal work.

A/P Ong Wei Yi, for allowing me to use his lab to perform microwave digestion, and also thank his lab members.

Acknowledgements

Co-workers at A/P Lanry's lab: Dr Deny Hartono and Ms You Fang for synthesizing the NPs used in my studies; Ms Huang Shu-Ying for teaching me how to use ICPMS.

Prof. Ong Choon Nam for his continual support to the Nanotoxicology programme.

Dr Jasmine Li, the pioneer in AuNP study, Prof Bay's former PhD student, for being such a wonderful senior in teaching and guiding me, especially in the beginning of my studies. She has given me unwavering support whenever I am in doubt or being confused. Thanks for being helpful, understanding my worries and concern, and guiding me, as a newbie, to the field of nanotoxicology. Thanks for the wonderful companionship especially during the 5th Nanotox Congress in UK.

Dr Wu Yajun and Ms Chan Yee Gek for helping me in all things related to microscopy works. Thanks for guiding me, teaching me patiently to the world of microscopy. Not to forget all the staff in EMU too.

Ms Rebecca Poh, for collaboration with Zeiss, and open up a new horizon in NP viewing. Thanks for all the wonderful nice, high resolution images.

All the staff from Dept of Anatomy, Mrs Yong Eng Siang, Mr Poon Zhung Wei, Mrs Ng Geok Lan, Ms Pan Feng, Ms Bay Song Lin and everyone under the family of Anatomy.

Former and current Prof Bay's lab members. Thanks for all the help, friendship and joy we had spent in lab. Dr Guo Chunhua, Dr Lai Yiyang, Dr Alice Zin, Dr Yu Yingnan, Dr Chua Pei Jou, Dr Lo Soo Ling, Dr Sukanya, Mr Ding Jian, Ms Guo Tiantian, Ms Olivia and my "in the same boat" junior, Ms Cynthia Ong.

Research grant involved throughout my studies: Singapore Ministry of Education Academic Research Fund Tier 2 via grant MOE2008-T2-1-046; Singapore National Research Foundation and the publication is supported under the Campus for Research Excellence And Technological Enterprise (CREATE) programme.

National University of Singapore for providing me Graduate Research Scholarship /President Graduate Fellowship to pursue my PhD studies.

Lastly, my parents, brother, Yoke Chye, and my newborn for accompanying me throughout this journey and being supportive in many ways. Thanks for all the love and concern, and for being understanding.

TABLE OF CONTENTS

Table of Contents

Table of Contents

SUMMARY

Advances in nanotechnology have given rise to the rapid development of many novel applications in the biomedical field. Therefore, there is a need to elucidate the safety and health risks of these nanomaterials.

The hypothesis in this study is that gold nanoparticles (AuNPs) exert both cytotoxic and genotoxic effects in lung cells *in vitro* and *in vivo*. This thesis aims to evaluate the biological effects of AuNPs in human lung cell lines (small airway epithelial cells and MRC5 lung fibroblasts) and rat lung tissues. The methodologies covered in this study include characterization of the AuNPs, cellular uptake of AuNPs, cytotoxic and genotoxic studies, transcriptomic, epigenetic and advanced proteomic approaches.

Verification of internalization of AuNPs in human lung cells were performed by light microscopy, transmission electron microscopy, focused ion beam-scanning electron microscopy and inductively coupled plasma mass spectrometry. Clathrin-mediated endocytosis was observed to be the pathway responsible for their uptake into the cells. Lipid hydroperoxide (LPO) assays revealed that AuNPs were able to induce oxidative stress in lung cells concomitant with an increased in anti-oxidant gene expression. Following oxidative stress, AuNP treatment caused increased lactate dehydrogenase (LDH) leakage and non-viability of the cells. Comet assay revealed DNA fragmentation after 72 h AuNP exposure in SAECs, concomitant with up-regulation of DNA repair *Xeroderma pigmentosum* gene.

A genome wide microarray study was conducted and a total of 42 and 19 genes were found to be differentially expressed in SAECs and MRC5 fibroblasts respectively. These altered genes included up-regulation of serum amyloid A-1 (*SAA1*) and toll-like receptor 2 (*TLR2*) in SAECs as well as up-regulation of miR-155 with down-regulation of protein S alpha 1 (*PROS1*) in MRC5 lung fibroblasts. The four differentially expressed genes were selected for down-stream analysis as they were postulated to be associated with AuNP-induced biological effects.

As SAA1 is known to interact with TLR-2 to trigger nuclear factor kB (NFkB) activation, a co-immunoprecipitation assay was performed with TLR2-SAA1 in SAECs, with positive results. TLR2-SAA1 protein-protein interaction was also verified by *in silico* modeling. There was also concomitant activation of NFkB activity, suggesting that SAA1-TLR2 interaction could activate NFkB.

The epigenetic studies suggest that miR-155 and histone deacetylases (HDAC) activity could regulate expression of PROS1, but not DNA methylation in AuNP-treated MRC5 lung fibroblasts. Silencing of miR-155 established the *PROS1* gene as a putative target gene, together with the observation of nuclear chromatin condensation and re-organization at the ultrastructural level.

To mimic the physiological condition in the lung, a co-culture of lung epithelial cells and lung fibroblasts was performed. Proteome analysis using the stable isotope labeling by amino acids in cell culture (SILAC) -mass spectrometry (MS) based approach, revealed a significant perturbation of cell motility and extracellular network in the underlying lung fibroblasts which were co-cultured with lung epithelial cells pre-exposed to AuNPs. There was associated up-regulation of Paxillin (PXN), breast cancer anti-estrogen resistance 1 (BCAR1) and Caveolin-1 (Cav-1) protein expression, which led to disruption in focal adhesion (FA) formation and an increase in vinculin binding sites. In addition, there was a significant increase in cell adhesion towards fibronectin as well as Collagen I. These results demonstrate that AuNP treatment could induce by-stander effects in neighboring unexposed fibroblasts, possibly via cell-cell crosstalk.

Finally, a proof of concept study was performed in rats injected with AuNPs intravenously. Biodistribution analysis confirmed the accumulation of AuNPs in the rat lungs. Systemic inflammation was observed as evidenced by the increase in serum Transforming growth factor beta (TGF-β), interleukin 6 (IL-6) and IL-1α. Prolonged blood coagulation time was observed in the AuNP-treated rats, implying that AuNP exposure could potentially lead to bleeding diathesis. Moreover, there was also inflammation of lung tissues in AuNP-treated rats, as evidenced by the presence of lymphocytic

infiltration, influx of macrophages and increased IL-1α expression in the tissues. A miRNA expression profiling study using real-time PCR showed that expression of miR-327 was significantly decreased in single dose of AuNP exposure.

In sum, the presence of AuNPs is likely to induce biological effects in the lung through the generation of oxidative stress, leading to cellular damage and inflammation. The results from this nanotoxicological study has provided data that will help to address the health concerns associated with AuNPs, and the safer use of AuNPs for biomedical applications and the industry.

LIST OF TABLES

LIST OF FIGURES

LIST OF ABBREVIATION

3D	Three Dimensional
5-Aza	5-Azacytidine
11-MUA	11-mercaptoundecanoic acid
AgNPs	Silver Nanoparticles
AMG	Automegallography
AO/EtBr	Acridine orange and ethidium bromide
AP2	Adaptor Protein 2
Au	Gold
AuNPs	Gold Nanoparticles
BBB	Blood Brain Barrier
BCAR1	Breast cancer anti-estrogen resistance 1
BSE	Backscattered electron
BSP	Bisulfite Sequencing PCR
Cav-1	Caveolin-1
CdTeQDs	Cadmium Telluride Quantum Dots
C. elegans	*Caenorhabditis elegans*
cLSM	Confocal laser scanning microscope
CME	Clathrin-Mediated Endocytosis
Co-IP	Co-immunoprecipitation
ConA	Concanavalin A
Cox-2	Cyclooxygenase
CTAB	Cetyl trimethylammonium
CvME	Caveolae-Mediated Endocytosis
DAB	3,3-diaminobenzidene
DAVID	Database for Annotation, Visualization and Integrated Discovery
DLS	Dynamic Light Scattering
ECM	Extracellular matrix
EDX	Energy Dispersive X-ray
ENMs	Engineered Nanomaterials
EsB	Energy selective Backscattered
ESI	Energy Spectroscopic Imaging
FA	Focal Adhesion
FBS	Fetal Bovine Serum
FDA	Food and Drug Administration
FIB-SEM	Focused ion beam-scanning electron microscopy
FCM	Flow Cytometry
GA	Glutaraldehyde
GO	Gene Ontology
H&E	Hematoxylin and Eosin
$HAuCI_4$	Tetrachloroauric acid
HCl	Hydrochloric Acid
HDAC 8	Histone Deacetylase 8
HNO_3	Nitric Acid
H_2O_2	Hydrogen peroxide
IACUC	Institutional Animal Care and Use Committee
ICC	Immunocytochemistry
ICPMS	Inductively coupled plasma mass spectrometry
IF	Immunofluorescence

IHC	Immunohistochemistry
IL	Interleukin
IP	Intraperitoneally
IPI	International Protein Index
IV	Intravenous
KEGG	Kyoto Encyclopedia of Genes and Genomes
KFeCN	Potassium Ferrocyanide
LB	Luria-Bertani
LDH	Lactate Dehydrogenase
LM	Light Microscope
LPO	Lipid hydroperoxide
LRR	Leucine repeats
MDA	Malonaldehyde
MTs	*Metallothioneins*
miRNA	microRNA
MSP	Methylation-Specific PCR
MWCNT	Multi-walled Carbon Nanotubes
NER	Nucleotide excision repair
NFkB	Nuclear factor kB
NiO	Nickel oxide
NO	Nitric Oxide
NMs	Nanomaterials
NPs	Nanoparticles
OsO_4	Osmium Tetroxide
PF	Paraformaldehyde
PARP-1	Poly-ADP-ribose polymerase-1
PBS	Phosphate Buffer Saline
PI	Propidium Iodide
PT	Prothrombin time
PXN	Paxillin
QI	Quartz inserts
qRT-PCR	quantitative real-time RT-PCR
RIN	RNA integrity Number
RLU	Relative light unit
RME	Receptor-Mediated Endocytosis
ROS	Reactive Oxygen Species
RPMI	Roswell Park Memorial Institute
SAA1	Serum amyloid A-1
SAECs	Small Airway Epithelial Cells
SDS-PAGE	Sodium dodecyl sulfate–polyacrylamide gel
SEM	Standard error of the mean
SERPINE1	Serpin peptidase inhibitor, clade E
SILAC	Stable isotope labeling by amino acids in cell culture
SiO_2	Silicon Dioxide
SOD	Superoxide Dismutase
SWCNT	Single-wall carbon nanotubes
TEM	Transmission Electron Microscope
TGF-β	Transforming growth factor beta
TiO_2	Titanium dioxide

TIR	Toll/IL-1 receptor
TLR2	Toll-like receptor 2
TMAT	N,N,N-trimethylammoniumethanethiol
TNF-α	Tumour Necrosis Factor-α
TSA	Trichostatin A
UP	Ultrapure
USEPA	U.S Environmental Protection Agency
XPA	*Xeroderma pigmentosum*

LIST OF PUBLICATIONS

Journals

1) **Ng CT**, Yung LYL, Swa LFH, Poh WYR, Jayantha G, Bay BH. Altered protein expression profile associated with phenotypic changes in lung fibroblasts co-cultured with gold nanoparticle-treated small airway epithelial cells. Biomaterials, 2015 Jan;39:31-8.

2) **Ng CT**, Tang FM, Li J J, Ong C, Yung LYL, Bay BH. Clathrin-mediated Endocytosis of Gold Nanoparticles In Vitro. Anat Rec 2015 Feb;298(2):418-27.

3) **Ng CT**, Li JJ, Gurung RL, Hande MP, Ong CN, Bay BH and Yung LYL. Toxicological profile of small airway epithelial cells exposed to gold nanoparticles. Exp Biol Med (Maywood), 2013 Dec 1;238(12):1355-61.

4) **Ng CT**, Dheen ST, Yip WC, Ong CN, Bay BH, Yung LYL. The induction of epigenetic regulation of PROS1 gene in lung fibroblasts by gold nanoparticles and implications for potential lung injury. Biomaterials 2011;32(30):7609-7615.

5) Lim ZZ, Li JE, **Ng CT**, Yung LYL, Bay BH. Gold nanoparticles in cancer therapy. Acta Pharmacol Sin 2011;32(8):983-990.

6) Li JJ, Lo SL, **Ng CT**, Gurung RL, Hartono D, Hande MP, et al. Genomic instability of gold nanoparticle treated human lung fibroblast cells. Biomaterials 2011;32(23):5515-5523.

7) **Ng CT**, Li JJ, Bay BH, Yung LYL. Current studies into the genotoxic effects of nanomaterials. J Nucleic Acids 2010;2010.

8) Li JJ, Muralikrishnan S, **Ng CT**, Yung LYL, Bay BH. Nanoparticle-induced pulmonary toxicity. Exp Biol Med (Maywood) 2010;235(9):1025-1033.

Book Chapter

1) **Ng CT**, Li JJ, Perumalsamy R, Watt F, Yung LYL, Bay BH. Localizing cellular uptake of nanomaterials in vitro by transmission electron microscopy. Microscopy: Science, Technology, Applications and Education A. Méndez-Vilas and J. Díaz (Eds.), pg 316-320, 2010.

2) **Ng CT**, Ong C, Lim ZZJ, Li JJ, Bay BH, Yung LYL. Application of nanotechnology in breast cancer diagnosis and therapy. G. Yip and B.H.Bay (Eds), 2013.

List of Publications

Oral presentations

1) **Ng CT**, Poh WYR, Yung LYL, Bay BH. Application of Focused Ion Beam-Scanning Electron Microscopy (FIB-SEM) and nanotomography for examination and microanalysis of Gold Nanoparticles (AuNPs) in biological samples in vitro. In Proceedings of the 2014 Annual General and Scientific Meeting of the Microscopy Society (Singapore), Singapore.

2) **Ng CT**, Bay BH, Yung LYL. The induction of epigenetic regulation of PROS1 gene in lung fibroblasts by gold nanoparticles and implications for lung injury. Oral Presentation Annual Student Congress (AGSC) 2013, National University of Singapore

Poster presentations

1) **Ng CT**, Bay BH, Yung LYL. Three-dimensional visualization of gold nanoparticles in lung cells using focused ion beam-scanning electron microscopy. Microscience Microscopy Congress, Manchester, UK, 30 June-3rd July 2014.

2) **Ng CT**, Bay BH, Yung LYL. Gold nanoparticle exposure not linked to cytotoxicity in Chang liver cells. NANOTOX 2014, 7th International Nanotoxicology Congress, Turkey, 23-26th April 2014.

3) Tang MF, **Ng CT**, Bay BH, Yung LYL. Expression of antioxidant and DNA repair genes in small airway epithelial cells exposed to gold nanoparticles. NANOTOX 2014, 7th International Nanotoxicology Congress, Turkey, 23-26th April 2014.

4) **Ng CT**, Bay BH, Yung LYL. The induction of epigenetic regulation of PROS1 gene in lung fibroblasts by gold nanoparticles and implications for lung injury. 6th HOPE Meeting, Tokyo, Japan, 10-15th March 2014.

5) **Ng CT**, Ong C, Li JJ, Lim ZZJ, Bay BH, Yung LYL. Metallothioneins (MT) protect gold nanoparticle-induced oxidative stress and modulate DNA damage repair activity in MT-2A over-expressing MCF-7 breast cancer epithelial cells. ACMM22/ICONN2012/APMC10 Conference, Perth Convention and Exhibition Centre, Australia, 05 - 09 February 2012.

6) Ong C, Lim ZZJ, Li JJ, Lai Y, Bay BH, **Ng CT**, Yung LYL. Gold nanoparticles induced cytotoxic effects in vitro is abrogated by Metallothionein-2A overexpression. In Proceedings of 10th Asia-Pacific Microscopy Conference, 22nd Australian Microscopy and Microanalysis Conference and 2012 International Conference on Nanotechnology and Nanoscience, Perth, Western Australia, 5-9 February 2012.

7) **Ng CT**, Bay BH, Yung LYL. Global gene analysis of gold nanoparticle-treated lung fibroblast. In Proceedings of 3rd Nanotoxicology Conference, Edinburgh Napier University, UK, 2 – 4 June 2010.

Chapter 1

Introduction

1 INTRODUCTION

1.1 Nanotechnology and Nanomaterials (NMs)

The rapid development of nanotechnology worldwide has enabled nano-sized materials to be used across various fields such as for biomedicine, industrial and commercial applications. An example of the use of nanoparticles (NPs) in breast cancer diagnosis and therapy is shown in Figure 1.1.

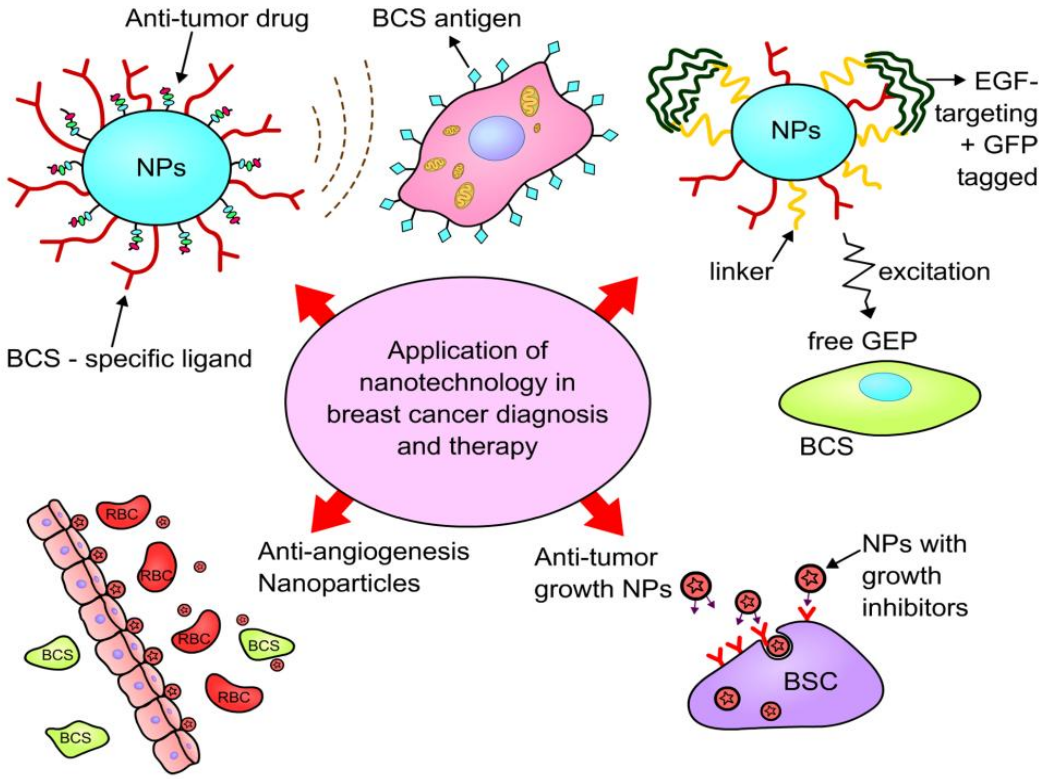

Figure 1.1: Schematic diagram showing nanoparticles and their applications in both diagnosis and therapy for breast cancer.

Engineered nanomaterials (NMs), including NPs, are defined as the creation and production of materials with the size range within 100 nm in at least one of its dimension (in length or diameter) (Warheit et al., 2008). As such, these nanoscale (10^{-7}-10^{-9} nm) innovations possess properties which differ distinctively from their bulk form of the same materials (USEPA, 2007). Owing to their small size and hence large

surface area to volume ratio, NMs exhibit high reactivity and attractive physicochemical properties. Depending on their size, charge, surface properties and shape, engineered NMs possess unique optical, magnetic and electronic properties which hold the key to unlock a wealth of opportunities in the global market (Wolfgang, 2004). Nanotechnology has emerged as an important sector in the global economy, and estimated to contribute to USD 3.3 trillion worth of investment by 2018 (Global-Industry-Analysts, 2012).

The U.S Environmental Protection Agency (USEPA) has classified engineered NMs based on chemical constituent and physical structure into 4 main classes as below:

1) carbon-based NMs, for example, fullerenes and carbon nanotubes

2) metal-/metal oxide based NMs, for example, gold (Au) and silver nanoparticles (AgNPs)

3) dendrimers

4) composites (USEPA, 2007)

1.2 Au and AuNPs

Gold nanoparticles (AuNPs) have been selected out of a vast variety of available NMs as a model of engineered NMs for further study in this thesis. Au, being a noble and inert d-block element in its bulk form, has been used for medicinal purpose as early as 2500 B.C. Colloidal Au was regarded as the magic potion for longevity in ancient Chinese society (Higby, 1982). Moreover, in the country of India, colloidal Au has served as a medicine or elixir of youth, which helps in rejuvenation (Richards et al., 2002). Nowadays, Auronofin and Aurasol, a gold complex have been recognized as modalities of treatment for rheumatoid arthritis (Tsai et al., 2007; Dykman and Khlebtsov, 2011) and tuberculosis (Kean et al., 1985); while CYT-6091, 27-nm citrate-coated GNPs conjugated with PEG-thiol and tumour necrosis factor-α (TNF-α) (Aurimmune) have entered a phase I clinical trial (Libutti et al., 2010). Other than exposure to Au mediated through medications, dermal contact to Au (in the form of jewellery and dental restoration) is common in humans (Sung et al., 2011a).

AuNPs possess unique surface plasmon resonance and optical properties which lead to their applications as a drug carrier, bio-imager and bio-sensor (Jain et al., 2006; Tsyusko et al., 2012). Furthermore, being a d-block element, AuNPs are able to excite the electrons in the conduction band, resulting in the loss of energy in the form of heat, making them a suitable candidate as a photothermal agent in cancer therapy (Jain et al., 2008). Other than their medicinal values, AuNP innovations have infiltrated commercial products and the industrial settings, including solar cells, automobiles, cosmetics (as anti-aging agent) and conductive ink (Keel T; Sung et al., 2011a). The top 6 nanotechnology-based products are nano-Au-based, and hence make AuNP a relevant candidate for toxicological evaluation.

1.3 Cellular uptake of NPs

Understanding the mechanism of NP internalization into cells is important for determining the intracellular delivery and fate of NPs. In addition, optimization of parameters affecting the NP uptake into cells will aid in the design of smart NP carriers for better applications in the biomedical setting.

(A) Cellular uptake mechanism of NPs

Endocytosis has been recognized as one of the major pathways that account for intracellular uptake of NPs. Endocytosis comprises several pathways including macropinocytosis, caveolae dependent and independent, and clathrin dependent and independent pathway (Hao et al., 2012; Munoz and Costa, 2012). In particular, receptor-mediated endocytosis (RME) which is mediated through interaction between the adsorption of serum proteins onto NPs and receptors present on the cell membrane, has been identified as a major uptake pathway for AuNPs (Chithrani, 2010). RME is an ATP-dependent process which involves membrane invagination around the NPs through clathrin, caveolae and other lesser-known pathways. To confirm if uptake of NPs occur via endocytosis, a lower temperature (4 ^{o}C) or sodium azide (an ATPase inhibitor) has been used to compare with uptake at 37 ^{o}C. As there is energy depletion at 4 ^{o}C or in the presence of the inhibitor, RME is therefore not possible (Xiang et al., 2012). Upon internalization of NPs via RME, NPs are found to be enclosed within double membrane vesicles, which will integrate with late

endsosomes, followed by delivery of the NPs to lysosomes subsequently for degradation (also known as the classical endocytic pathway) (Rejman et al., 2004; Johnston et al., 2010a).

Clathrin-mediated endocytosis (CME) occurs via five key assembly and maturation steps which are: nucleation, cargo selection, coat assembly, followed by scission and lastly uncoating (Munoz and Costa, 2012). The clathrin-coated pit, which originates from plasma membrane, has varying sizes in a species dependent manner, but do not exceed 200 nm in general. The invagination of clathrin pits continue till vesicle fission is formed (Xiang et al., 2012). Adaptor protein 2 (AP 2) is one of the adaptors which assists in pit formation. As CME is lipid raft-mediated, depletion of cholesterol is known to disrupt the vesicle formation by preventing pit detachment from the plasma membrane.

Caveolae-mediated endocytosis (CvME) is also a receptor mediated and ATP-dependent process. GTPase dynamin mediates the fission of caveolae at its neck; while receptors located in caveolae (including epidermal growth factor and insulin receptor) are known to mediate CvME too (Xiang et al., 2012). Similar to CME, Cvme is also cholesterol-dependent; and what differs between these two pathways is that CvME is a non-digestive route, bypassing lysosomal degradation and the classical endocytic pathway (Bengali et al., 2007). However, this notion still remains debatable.

(B) Pharmalogical inhibitors as tools for mechanistic studies of uptake

Inhibitors are widely used to block a specific endocytic pathway. Pharmacological inhibitors exert homogenous effects on cells and require little time to achieve an inhibitory effect, making them useful for this purpose. However, the lack of specificity and possible side effects associated with their use are frequently encountered (Ivanov, 2008). Moreover, these inhibitors may results in cell type variations, thus warranting an unbiased view of these disadvantages.

To study CME, chlorpromazine is employed to disrupt the formation of clathrin pits. Chlorpromazine is a cationic amphipathic inhibitor, which reversibly inhibit AP2 adaptor complex and clathrin from translocation at the cell surface (Ivanov, 2008). In addition, chlorpromazine alters the plasma membrane fluidity due to its amphipathic nature, thereby blocking the membrane invagination and

formation of clathrin coated pits (Ogiso et al., 1981). Other than chlorpromazine, Concanavalin A (ConA) is also an inhibitor for CME which blocks the internalization of receptors on the cell surface through agglutination of receptors (Markelc et al., 2014).

CvME, being cholesterol-dependent for caveolae synthesis, can be inhibited by blocking cholesterol biosynthesis. One such inhibitor is nystatin, which creates large aggregates in the cholesterol-rich membrane, causing cholesterol to be sequestered from the cell membrane, and inducing distortion in caveolar shape and lipid raft ligand internalization (Ros-Baro et al., 2001).

(C) Physicochemical properties affect cellular uptake of NPs

The size, shape and surface functionalization of NPs influence the amount and type of pathways for their internalization. Energetic and kinetic models have elucidated a size-dependent uptake of NPs, in which 50 nm NPs possessed the highest uptake while NPs smaller than 50 nm showed lesser uptake due to prohibitive thermodynamic barriers as they are too small to be recognised, hence restricting their uptake (Chithrani and Chan, 2007; Jin et al., 2009). Other than size, Chithrani *et al* (2007) also investigated the effect of shape on uptake of NPs. Uptake of rod-shaped NPs (with a higher surface area as compared with spherical shape) is found to be lesser than spherical NPs of the same surface coating; and it is speculated that nanorod requires a longer wrapping time by the membrane, resulting in lower uptake.

The presence of surface modification affects the uptake of NPs as well as protein adsorption onto the NPs. While clathrin-mediated endocytosis is responsible for the uptake of transferrin-coated AuNPs (Chithrani and Chan, 2007), both clathrin- and caveolae-mediated endocytosis are involved in the uptake of PEG-modified AuNPs (Nativo et al., 2008). External factors such as the extent of protein adsorption onto the NP affect its uptake. Unbound or naked NPs are able to compete with protein-adsorbed NPs at the receptor binding sites (Johnston et al., 2010a). On the other hand, Cetyl trimethylammonium (CTAB)-coated NPs can inhibit the amount of adsorbed proteins onto the surface of NPs, resulting in lesser binding and interaction of NPs with receptors, thereby influencing uptake (Chithrani, 2010). These findings highlight the combinatorial effect of surface modification and surface adsorption in determining

the uptake of NPs. As such, uptake efficacy of NPs can be manipulated through this ligand-receptor conjugation relationship.

Studies have shown that the surface charge carried by NPs affects the uptake of NPs. In general, cationic NPs exhibit greater uptake into cells due to interaction with the negatively charged plasma membrane; while anionic NPs would be repelled during such an interaction (Chithrani, 2010). Furthermore, the different surface charge possessed by NPs will affect the degree of protein denaturation, affecting protein structure and function (Aubin-Tam and Hamad-Schifferli, 2008). The findings from these *in vitro* studies have highlighted the need to consider these physicochemical effects during the design of NP-based carriers for *in vivo* experiments.

1.4 Nanotoxicology

Human exposure to engineered NMs can occur intentionally or unintentionally. Intentional exposure includes medical application where NMs are introduced into body via for example, an intravenous injection (IV) route, for diagnostic or the therapeutic purpose or both. Unintentional (or accidental) exposure includes occupational exposure to NMs by workers (such as by inhalation and dermal contact routes) at the workplace or manufacturing plant (Oberdorster et al., 2005). Regardless of how NMs enter the body, they will be systemically distributed throughout the body and accumulate in various organs, if they are not removed by the first pass effect or by phagocytic processes.

Emergence of engineered NM-related products has generated a great concern for health issues, due to the increasing risks of exposure. As NMs has high surface reactivity (i.e., redox ability), they are bio-reactive and can interact with intracellular organelles and biomolecules of a similar size scale, thereby altering their structures and triggering undesired effects such as oxidative stress, autophagy, inflammation and cellular injury (Krpetic et al., 2014). Therefore, understanding the uptake mechanism, biodistribution and potential adverse effects of these NMs upon entering into human body is of the upmost importance. Besides, target specific study such as effects of NMs at secondary organs is fundamental in the assessment of NM toxicity and NM interaction mechanism(s) with cells *in vitro*.

It has been demonstrated that the toxicity of metal NPs is greater than the toxicity of microparticles of the same parent chemical. Owing to their small sizes, the NPs are shown to be more reactive and possess higher penetrative efficiency and cellular uptake than microparticles (Desai et al., 1996)). NPs were also reported to be more toxic than microparticles both in vitro and in vivo (Jiang et al., 2009; Lin et al., 2009; Moos et al., 2010; Nair et al., 2009; Gaiser et al., 2011).

With the increased production and utilization of engineered NMs and their related products worldwide, the likelihood of releasing and exposure to NMs in human also increased. Thus, there is a need to institute appropriate guidelines on handling engineered NMs and evaluate their potential effects on human and environment. Information gleaned from the toxicity studies will aid in risk assessment and help to set safe exposure limits. Hence, knowledge of proper characterization of each engineered NM becomes crucial in determining their properties and understanding their behaviour under different environmental conditions (such as exposure route, duration and dosage). Although the literature on nanotoxicology of AuNPs is widely available, there are still questions that remain to be addressed with regard to AuNP-associated health risks.

1.4.1 The lung as a model for nanotoxicology

The lung is a respiratory organ which is in first line and high contact with atmospheric exposure to pollutants. Being an organ with large surface area, comprising approximately 2300 km long of airways and 300 million alveoli, the lung could be exposed to variety of airborne particles (Li et al., 2010a). Although the presence of nasal cilia could help in getting rid of these particles, NPs are likely to evade the mechanism responsible for their clearance due to their small size, leading to biopersistence. As such, the lung is vulnerable for NP invasion and accumulation in the deep regions, making the lung particularly susceptible to their toxic effects (as shown in Fig 1.2).

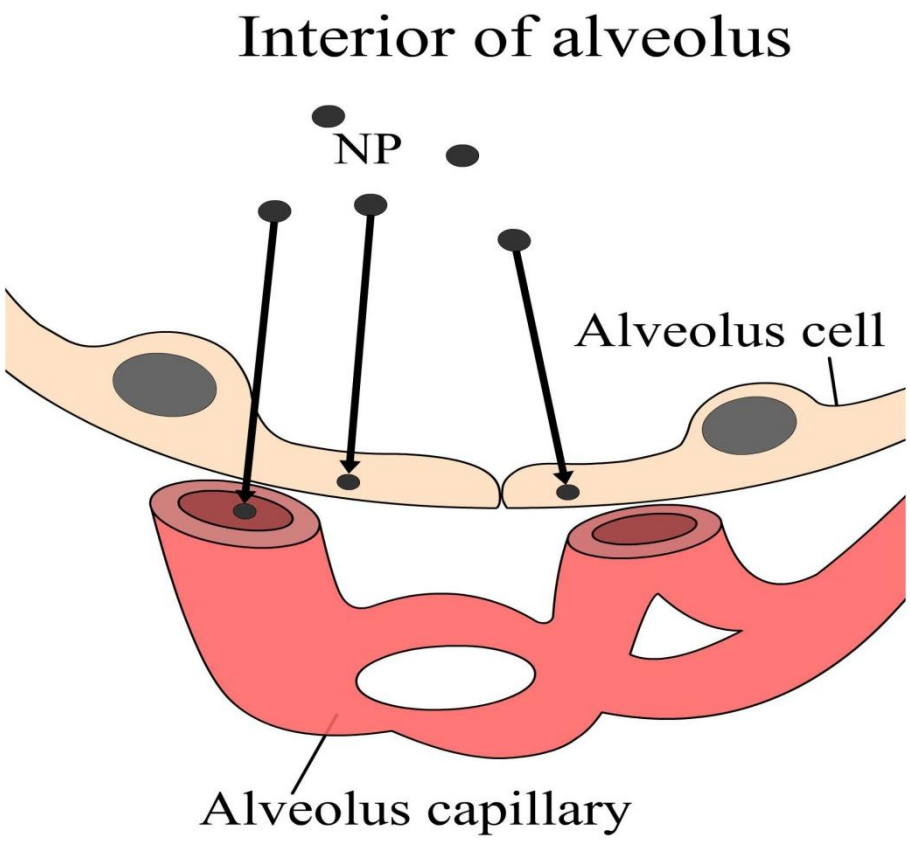

Figure 1.2. NP invasion and penetration into the deep regions of the lung, and enter the alveolus capillary into pulmonary circulation.

Occupational exposure to NMs mediated via inhalation allows accumulation of NMs in lungs. Assessing pulmonary toxicity using epithelial cells lining the alveoli; or lung fibroblasts which constitute the major stromal component, is appropriate as these two cell types have the highest risk from exposure to NMs. Hence, the lung has been used as a model of study *in vitro* and *in vivo* to understand the potential impacts of NMs through the inhalation and injection routes. Lung cell lines which have been used for pulmonary toxicity of metal NPs include normal human lung fibroblast cells (IMR-90), human alveolar macrophage cell line (THB-1) and human epithelial cell line (A549) (Johnston et al., 2010a). From these studies, it would appear that different cell types possess varying degree of sensitivity towards the same type of NPs, implying the need to use two different cell types for better comparison and evaluation of toxicity.

Based on the literature search (as summarized above), human exposure to AuNPs is likely to occur by several routes, including inhalation, intratracheal instillation and IV injection. Despite

differences in the routes of exposure, Au has been found to enter the body, translocate to other secondary target sites or to developing embryos/fetus (Myllynen, 2009) and accumulate at varying amount at different organs. Among these organs, the lung is found to be one of the target sites for Au accumulation.

Several possible clearance pathways including mucociliary clearance and pulmonary surfactant protein D modulated clearance (Yu et al., 2007; Semmler-Behnke et al., 2008; Schleh et al., 2013), and alveolar elimination by macrophages in the alveolar region (which does not apply to large agglomerates) (Takenaka et al., 2012) are available, but this process is often size dependent. Moreover, the lung is only protected by a poor barrier of 500 nm thickness made up by a single-cell layer from the blood capillaries (Hoet et al., 2004; Li et al., 2010a). Chen *et al* (2009) reported that AuNPs accumulated in mouse lung following IP injection, resulting in loss of structural integrity in lungs. Likewise, subchronic exposure to AuNPs via inhalation caused pathological signs including inflammatory infiltrate of mixed cell type (lymphocyte/neutrophil/macrophage) in male and female AuNP-exposed rats (Sung et al., 2011a).

Previous studies by Balasubramaniam and colleagues have shown accumulation of 20 nm AuNPs in rat lung following both inhalation and IV injection studies (Yu et al., 2007; Balasubramanian et al., 2010a). However, as the major reservoirs for Au accumulation have been reported to be in the liver and spleen, the effects of AuNPs on the lung after IV injection have received little attention.

1.4.2 Nanotoxicity of AuNPs

Biodistribution studies have demonstrated translocation of AuNPs to the lung via the blood circulation. Studying the effects of AuNPs in lung may provide additional insights into the pulmonary toxicity of AuNPs. However, previous *in vitro* and *in vivo* studies showed contradictory results for AuNP-related toxicity due to inconsistency in the parameters (Khlebtsov and Dykman, 2011). Furthermore, extrapolation of *in vitro* results to *in vivo* settings is not possible, due to the complexity of the biology of the whole organism (Tsyusko et al., 2012). Various factors have been identified to influence the toxicity of AuNPs. Physicochemical properties such as size, shape, surface modification and surface charge contribute to varying degrees of toxicity as observed in *in vitro* and *in vivo* studies.

The animal model is a preferred system for toxicity evaluation. Other than animal models, three-dimensional (3D) system and co-culture system are emerging platforms that simulate physiological conditions which are lacking in 2D cell culture system (Lee et al., 2009; Herzog et al., 2014). A tissue is made up of a collection of different cell types, and each cell type responds differently to NM exposure, as evidenced by cell-type specific effects. Moreover, as NM-induced toxic effects may be enhanced through cellular crosstalk, these aspects would deserve consideration when designing a model for NM toxicology (Johnston et al., 2010a).

1.4.2.1 *In vitro* toxicity of AuNPs

(A) Cytotoxicity

Toxicity profiles of AuNPs have become widely available. AuNP-toxicity studies have been conducted with different surface properties, sizes and functionalization, implying that the toxic effects may not be caused by AuNPs alone, but due to combinatorial effects. Many studies have attributed the exposure of AuNPs to induce toxicity through disturbance to cell cytoskeleton, breakdown of the cellular permeability barrier, reduction of cell survival, apoptosis and activation of signaling pathways which are highlighted below.

Uptake of AuNPs cause decreased cell proliferation and autophagy in MRC5 lung fibroblasts as reported previously (Li et al., 2008; Li et al., 2010a). Upon entry into human dermal fibroblasts, AuNPs were found to disrupt cytoskeleton filaments, causing decreased cell motility (Mironava et al., 2010). In addition to size, surface charge has been reported to be associated with toxicity. Cationic AuNPs are reported to be more toxic and has the ability to disrupt the integrity of plasma membrane, compared to neutral or anionic AuNPs (Goodman et al., 2004). A detailed study has revealed that cationic AuNPs caused more disruption to the negatively charged lipid-bilayered plasma membrane; while anionic AuNPs impeded such an effect (Tatur et al., 2013).

Particle size influences the cytotoxicity, with smaller size of AuNPs observed to exhibit a greater toxicity due to higher surface reactivity. 1.2 nm AuNPs is found to cause significant cell death by

apoptosis (Pan et al., 2007) while Pan *et al* showed that 1.4 nm AuNPs are much more cytotoxic than 15 nm AuNPs of the same chemical constituents (Pan et al., 2009), causing necrosis through oxidative damage. Moreover, it appears that different sizes of AuNPs (1.2 nm vs 1.4 nm) induced cell death via different mechanism (apoptosis vs necrosis).

Other than particle size, studies using different surface-modified AuNPs have been performed. 20 nm AuNPs have been observed to inhibit cell proliferation, concomitant with down-regulation of cell cycle related genes (Li et al., 2008). Imidazole-stabilized AuNPs have been reported to induce neuronal death by apoptosis both *in vitro* and *in vivo* (Imperatore et al., 2014). Sodium-citrate capped AuNPs were observed to reduce cell viability, proliferation and induce leakage of lactate dehydrogenase (LDH) through the plasma membrane in human alveolar type-II cells *in vitro* (Uboldi et al., 2009).

Moreover, opsonization of proteins which form the protein corona, has been shown to facilitate the uptake of NPs into cells by promoting the interaction with cellular receptors (Nativo et al., 2008). Upon entering the human body, NPs will be opsonized with biomolecules (e.g., serum proteins) and this may modify the behavior of the NPs. Also, formation of protein corona on NPs could potentially alter the protein conformation and function, adding confounding factors to toxicity studies (Johnston et al., 2010a). Binding of FBS as protein corona to the surfaces of AuNPs, has been shown to possess lesser non-specific affinity to cell surface and reduced toxicity, as compared with naked AuNPs (Tenzer et al., 2013). Likewise, coating of AuNPs with bovine serum albumin has been observed to be non-toxic in MRC5 fibroblasts (Das et al., 2012). Hence, such effects have to be considered when interpreting toxicity data.

(B) Oxidative stress

Other than cytotoxicity, oxidative stress is an important molecular mechanism in toxicity studies as heightened or uncontrolled oxidative stress may lead to unwanted effects such as fibrosis (Cheresh et al., 2013) and DNA damage (Pizarro et al., 2009). The small size and bioreactivity of NPs aid in free radical generation and hence, oxidative stress induction (Yao et al., 2013). Oxidative stress has been demonstrated to contribute significantly to cytotoxicity and genotoxicity. AuNPs, 13 nm and 20 nm

diameter, were found to trigger oxidative stress (Jia et al., 2009; Li et al., 2010a), by releasing nitric oxide (NO) and up-regulating stress-responsive genes such as cyclooxygenase (Cox-2). Jia *et al* (2009) monitored AuNP-induced production of NO in a dose-dependent manner using a NO microsensor, which was possibly due to the catalytic effect of AuNPs on NO generation from endogenous S-nitroso adducts with the thiol (-SH) group.

Mitochondrial stress test conducted in the human keratinocyte cell line suggest that both cationic and anionic AuNPs triggered oxidative stress through generation of reactive oxygen species (ROS), which then elevates superoxide dismutase (SOD) production (Schaeublin et al., 2011). Another study demonstrated a cell-line dependent dysregulation of SOD activity following increased ROS production in human leukemia and HepG2 cell lines, and concluded that cytotoxicity of AuNPs could be attributed to oxidative stress (Mateo et al., 2014). It is also acknowledged that AuNPs have strong binding affinity to the -SH group, which is a common functional group present in SOD. Therefore, the interaction between AuNPs and -SH group may also account for the accumulation of ROS (Johnston et al., 2010a).

PEGylated AuNPs was observed to disturb the membrane integrity of erythrocytes, and induce oxidative stress accompanied by increased malonaldehyde (MDA) levels in the cells (He et al., 2014). Surface functionalization of AuNPs with CTAB is found to be more toxic than naked AuNPs (Connor et al., 2005); while AuNPs conjugated to -SH peptides do not enhance ROS formation. It has been previously reported that ~15 nm size citrate-capped AuNPs without surface functionalization, can trigger an increase in ROS, due to Au-S bonding interactions with intracellular proteins, such as, glutathione and –SH group containing proteins (Tedesco et al., 2010a). On the other hand, AuNPs conjugated to thiol peptides do not enhance ROS formation, as such interactions are deterred by the chain length and steric effect of the conjugated-peptide system through Au-S bonds (Morales-Avila et al., 2012).

(C) Genotoxicity

Genotoxicity refers to DNA damage, which may or may not result in mutation (Yao et al., 2013). Genotoxicity is harder to detect, as alteration in the genome and transcription may not be phenotypically

expressed. Proposed mechanisms which may lead to NP-induced genotoxicity include direct binding of NPs to DNA; direct binding of NPs to DNA associated proteins and indirect cellular response such as oxidative stress (Yao et al., 2013). Genotoxic studies using the *Salmonella typhimurium* bacteria, demonstrated that AuNPs induced photomutagenicity, which was postulated to be caused by both citrate and Au^{3+} (or auric compounds) due to the formation of free radicals (Wang et al., 2011). In previous studies, AuNPs were found to induce genomic instability without causing massive cell death in MRC5 fibroblasts. Comet and FISH assays revealed DNA damage and chromosomal breaks, coupled with dysregulation of DNA repair genes, thereby, leading to persistent DNA damage (Li et al., 2008; Li et al., 2011a). While DNA damage could be rescued through DNA-repair mechanism, such repair is rendered impossible as NPs have altered the function of DNA repair genes. Citrate-capped 20 nm AuNPs have been reported to cause genotoxicity in human liver HepG2 cells using the comet assay. This phenomenon was not observed when AuNPs were functionalized with 11-mercaptoundecanoic acid (11-MUA), highlighting the effects of surface properties on the genotoxic effects observed (Fraga et al., 2013).

1.4.2.2 *In vivo* toxicity of AuNPs

Biodistribution and toxicity studies of AuNPs have been performed in several animal models including *Caenorhabditis elegans* (*C. elegans*), zebrafish, Drosophila fly and rodents. The parameters that were examined include size of AuNPs, surface modification, route of exposure and dose on the biodistribution and toxicity of AuNPs.

Genome-wide analysis of AuNP-exposed *C. elegans* revealed accumulation of AuNPs and activation of biological pathways associated with protective mechanism against AuNPs (Tsyusko et al., 2012). A study of AuNPs functionalized with N,N,N-trimethylammoniumethanethiol (TMAT-AuNPs), a cationic ligand, revealed a smaller malpigmented eyes coupled with cell death in eye using embryonic zebrafish model (Kim et al., 2013). This effect has also been extended to other toxicity-related health issues such as behavioral and neuronal damage in zebra fish at the developmental stage. Using the same model, Truong *et al* (2012) showed that 1.5 nm AuNPs with different surface charges exhibited acute

toxicity which caused abnormalities to the larval and adult behavior. Citrate-capped 15 nm AuNPs, formulated into the diet of Drosophila flies, are known to cause genotoxic and mutagenic effects in the fruit flies, accompanied by impaired fecundity, fertility and morphological defects on the wings and eyes (Vecchio et al., 2012).

Smaller size AuNPs were reported to have a better biodistribution, leading to a greater amount of accumulation in various organs (Zhang et al., 2010; Glazer et al., 2011). For example, a size distribution study in mice after IV injection, revealed a wide-spread organ distribution for 15 nm AuNPs as compared to 200 nm AuNPs. Furthermore, 15 nm and 20 nm AuNPs were found to translocate to the brain, indicating the ability of these AuNPs to pass through blood brain barrier (BBB). Besides, the highest accumulation of Au after IV injection was observed to be predominantly in the liver and spleen (Sonavane et al., 2008; Wojnicki et al., 2013), accompanied by gene expression changes (Balasubramanian et al., 2010a). Other than distribution in various organs, a study has investigated size-dependent passage of AuNPs across different types of barriers from the respiratory tract to the blood. Intratracheal instillation of 1.4 nm radiolabelled AuNPs in rats demonstrated increased translocation of AuNPs to secondary targets, in comparison with 18 nm AuNPs where a majority of AuNPs (99.8%) were retained within the lung. This finding indicates that smaller size of AuNPs are not only able to pass through BBB effectively, but also able to penetrate the air-blood barrier of the lungs (Semmler-Behnke et al., 2008). Overall, AuNPs are able to translocate from the primary site and smaller sizes result in wider organ distribution, with liver and spleen as preferential sites.

Surface modification of AuNPs study using 13 nm PEG-coated AuNPs have a longer half life, resulting in greater retention in blood after single IV injection in mice, concomitant with the induction of acute inflammation and apoptosis in liver (Cho et al., 2009), which is similar to that reported by Hwang *et al* (2012). In addition, inflammation in the liver, influx of neutrophils and increased expression of cytokines and cell adhesion molecules were also observed Another study showed that 10 nm naked AuNPs induced oxidative damage such as lipid peroxidation in rat liver tissues (Khan et al., 2012). Inflammatory responses to acute and sub-chronic exposure to AuNPs in rats, revealed a transient

induction of pro-inflammatory cytokines in liver and kidney (Khan et al., 2013). However, conjugation of immunogenic peptides onto the surface of the AuNPs reduced their toxicity (Chen et al., 2009). The propensity of AuNPs to trigger inflammation is worthy of consideration for further investigations.

Other than physicochemical properties of AuNPs, different routes of exposure have been reported to possess varying degrees of toxicity to the animal studied. In a study tracing administration routes of AuNPs in mice, Zhang *et al* found that tail vein injection was less toxic than the oral and intraperitoneal injection (Zhang et al., 2010). While exposure routes has been shown to pose effects when interpreting toxicity results, the experimental model used and the consequent bioavailability of AuNPs are dependent on the exposure route too. For example, pulmonary toxicity study using IV injection as the route of exposure, resulted in accumulation of <0.7% of Au in the lung. On the other hand, instillation of AuNPs resulted in accumulation of >91% of Au in the lung (Semmler-Behnke et al., 2008). These findings suggest that tissue distribution of Au is dependent on exposure routes, highlighting the importance of choosing an appropriate route of exposure for toxicity studies in a specific target organ.

Besides physicochemical properties and exposure routes of AuNPs, the treatment dose remains one of the major factors which has lead to vast ambiguity in toxicity findings related to AuNPs. For example, 8 mg/kg of Au injected intraperitoneally (IP) into mice caused toxicity in one study (Chen et al., 2009) while 400 µg/kg of Au did not cause toxicity in another study (Lasagna-Reeves et al., 2010). Administration of a physiologically relevant dose for both *in vitro* and *in vivo* studies has been challenging. There has been a lack of consensus on the dose metrics especially for *in vitro* studies (Joris et al., 2013). Relatively high doses applied in *in vitro* studies have raised questions on the relevance of the findings in the *in vivo* environment (Oberdorster et al., 2005). It has been advocated that the dose administered should be comparable in the different settings (Johnston et al., 2010a), especially for preclinical studies assessing the toxicity of NPs using animal models (Madl and Pinkerton, 2009).

1.5 Epigenetics and nanotoxicology

The prefix "Epi" means "above" (in Greek) and hence epigenetic refer to the changes in gene expression pattern and phenotypes, which is often reversible and heritable, without a change in the primary gene sequence (Goldberg et al., 2007; Lopez-Otin et al., 2013). There are three main mechanisms involved in regulating such changes, namely microRNA (miRNA), DNA methylation and posttranslational modification of histone tails. Epigenetic studies on NP-related toxicity have been under-explored; but some NPs have already been reported to impose epigenetic effects associated with health risks (Table 1.1). As such, epigenetic factors should be included as they may in part, hold the key in the understanding the toxicity of engineered NMs.

Table 1.1: Epigenetic studies of NPs.

Study model	Type of NPs used	Findings	Reference
miRNA expression			
Mouse	AuNPs	miR-183 and Let-7a alteration and AuNP-induced transplacental clastogenic effects	(Balansky et al., 2013)
Rat	AuNPs	miRNA expression dysregulation in blood serum; potential use of miRNA as biomarker	(Chew et al., 2012)
Jurkat cells	AgNPs and Ag ions	Epigenetic-regulated differential cell sensitivity towards AgNPs and Ag ions	(Eom et al., 2014)
Mouse	TiO_2NPs	Regulation of inflammation and acute phase response genes by miRNAs	(Halappanavar et al., 2011)
NIH/3T3	Fe_2O_3 NPs, CdTe QDs and MW-CNTs	Sequencing-based total miRNA profiling pattern revealed alteration of miRNAs induced by these ENMs	(Li et al., 2011b; Li et al., 2011c)
DNA methylation			
MCF-7 cells	QD	Decrease in DNA methylation	(Choi et al., 2008)
HaCaT cells	SiO_2	Global genomic DNA hypomethylation	(Gong et al., 2010)
HaCaT	SiO_2	Hypermethylation of PARP-1	(Gong et al., 2012)
Histone modification			
Ex vivo	AuNPs	AuNPs bind strongly to histone deacetylase 8, exhibit inhibitory effects	(Sule et al., 2008)
HeLa cells	AuNPs	NPs act as epigenetic agents	(Mazumder and Shivashankar, 2007)
MCF-7 cells	QD	Global hypoacetylation of histone 3	(Choi et al., 2008)

(A) miRNAs

miRNAs, which belong to the family of small, non-coding RNA, mediate gene silencing at either transcription or translational level (Bhattacharyya et al., 2011), based on the degree of seed region (6-8 mers) complementarity between the miRNA and its putative targets. mRNA of the target gene will be degraded, resulting in gene transcription suppression if there is high complementarity. On the other hand, translational repression or inhibition on protein translation will occur in the case of partial complementarity (Eulalio et al., 2008; Bartel, 2009). miRNAs are ubiquitously expressed and each miRNA may have multiple mRNA targets and vice versa (Miranda et al., 2006).

There are a few reports on the involvement of miRNAs in relation to AuNP-induced effects. Maternal exposure to AuNPs is reported to induce alteration of miRNA expressions (miR-183 and Let-7a) in the lung and liver of the fetus that was not directly exposed to AuNPs (Balansky et al., 2013). This is also the first report thus far, reporting on the transplacental clastogenic effects of AuNPs in mouse fetus, together with miRNA regulation. Furthermore, miRNA expression changes in rat blood has been investigated and it was observed that there were 23 dysregulated miRNAs and 45 dysregulated miRNAs in rat exposed to AuNPs following IV injection after 1 week and 2 months respectively (Chew et al., 2012). Although the targets and functions of the dysregulated miRNAs in both studies remain unknown, understanding the interplay between miRNA and NPs will definitely aid in bridging gaps that exist in NP-related toxicity studies.

Other than AuNPs, a recent study compared the difference in miRNA expression in Jurkat cells after treatment with AgNPs and Ag ions. A correlation analysis between mRNA and miRNA expression revealed involvement of epigenetic mechanism in regulating the cell sensitivity towards AgNPs and Ag ions (Eom et al., 2014). A mouse model study to examine the epigenetic effects was performed by Halappanavar *et al* (2011) using titanium dioxide NPs (TiO_2NPs). 53 genes associated with inflammation and acute phase response were found to be dysregulated in mouse lung exposed to TiO_2NPs. As there was no correlation between the transcriptomic and protein expression level, the investigators ruled out the involvement of miRNAs in regulating the post-transcriptional mechanism.

Sequencing-based miRNAs expression profiling was performed in NIH/3T3 cells using three different types of ENMs including iron oxide NPs, cadmium telluride quantum dots (CdTeQDs) and multi-walled carbon nanotubes (MWCNTs). A high-throughput deep sequencing method (SOLiD sequencing) was employed to detect low coverage miRNAs and revealed dsyregulation of miRNAs post ENM exposure. Among the dysregulated miRNAs, those which are co-regulated have been identified to exert similar cytotoxic effects common among ENMs (Li et al., 2011b). A previous study by the same group of researchers analyzed the global miRNA expression pattern using the same sequencing method using CdTeQD treated cells and observed an association between apoptosis-like death and miRNA expression pattern (Li et al., 2011b).

(B) DNA methylation

CpG islands are located at the promoter region of a gene and are normally unmethylated (Deaton and Bird, 2011). The cytosine residue on CpG islands is subjected to modification such as the addition of methyl group catalyzed by DNA methyltransferase to its fifth position, forming 5'methylated cytosine. Excessive methylation of cytosines and their interactions with methyl-CpG binding proteins will impede the access of the transcription initiator, resulting in alteration of gene expression (Edwards and Ferguson-Smith, 2007). Hypermethylation at the promoter region of a gene will lead to gene silencing and vice versa, but with few exceptions (Yao et al., 2013). DNA methylation occurs not only at the promoter regions, as intragenic regions are also subjected to methylation (Ball et al., 2009).

The first report on the DNA methylation study after NP treatment was initiated by Choi *et al* (2008) using QDs in MCF7 breast cancer cells. There was a decreased in DNA methylation post NP treatment, which is in concordance with the gene expression changes observed. Moreover, global genomic DNA hypomethylation in silicon dioxide (SiO_2) NP-treated human HaCaT cells was observed, implying epigenomic response induced by NPs occurred through DNA methyltransferase (Gong et al., 2010). Following this observation, the same group observed a decrease expression of DNA repair protein

poly-ADP-ribose polymerase-1 (PARP-1), concomitant with promoter hypermethylation of PARP-1 in the same cell line. This inhibitory effect was abrogated after DNMT1 silencing (Gong et al., 2012).

Although there have been no studies performed on AuNP-induced hypo- or hypermethylation, epigenetic changes may impose a long term effect on future gene expression profiles and in the case of persistent changes through cell division, the effect would be heritable (Yao et al., 2013).

(C) Histone modification

Chromatin packs the DNA which is wrapped around histone proteins, enabling tight packaging of the whole human genome content into the nucleus of the cell. Histone proteins are subjected to post-translational modification through enzymatic reaction which in turn, results in gene expression regulation (Kouzarides, 2007). Depending on the types of modification, chromatin may present in compact structure (heterochromatin) or in non-condensed structure (euchromatin).

There are only a few reports with regard to NPs and histone modification. As AuNP binds strongly to the thiol group present on histone deacetylase 8 (HDAC 8), a study has shown that the catalytic function of this enzyme is impaired. This enzymatic inhibitory effect is almost as potent as the use of Trichostatin A (TSA), an inhibitor for HDAC (Sule et al., 2008). A similar finding has shown the possibility of NPs as epigenetic agents due to their ability to modulate heterochromatin assembly (Mazumder and Shivashankar, 2007). In a similar study by Choi *et al* (2008), QD treatment was found to result in dose-dependent global hypoacetylation of histone 3 in MCF-7 cells, and this effect was reversible by the use of an inhibitor. This finding suggests the involvement of histone modifying enzymes in QD-induced histone modification and regulating cell death. Although these studies have explored the effects of NP exposure on histone acetylation and deacetylation status, other types of histone post-translational modifications such as methylation, sumoylation and phosphorylation are yet to be investigated.

Figure 1.3 summarizes the possible epigenetic pathways of NP-induced toxicity based on information available in the literature.

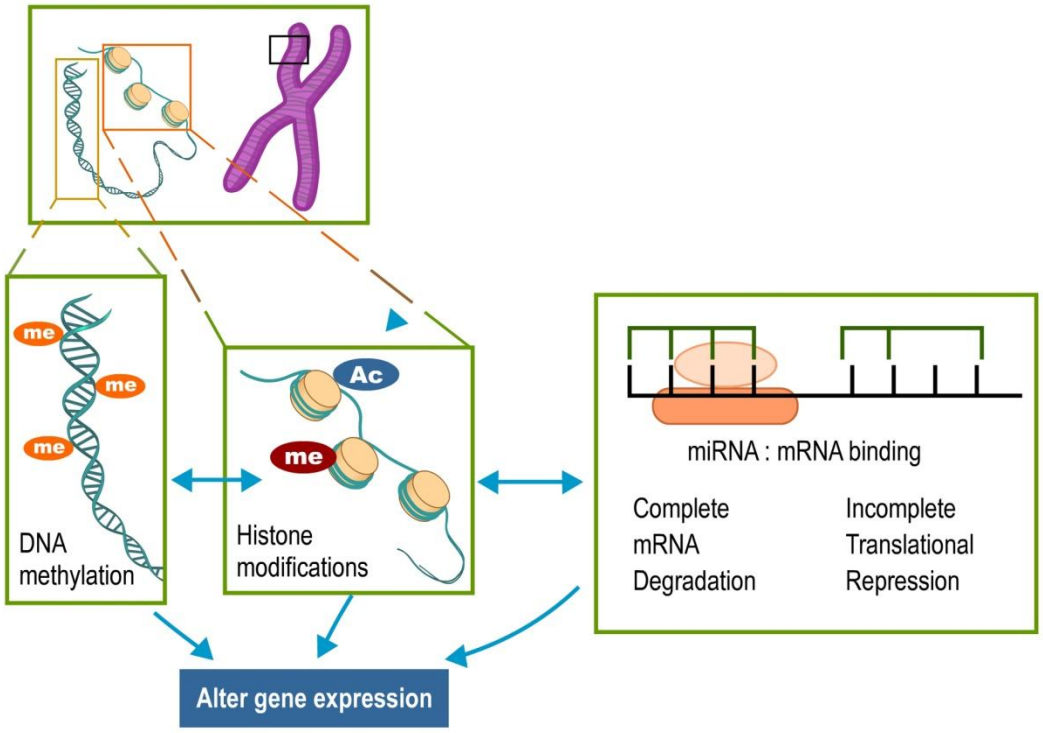

Figure 1.3: Possible mechanistic epigenetic pathways associated with NP-induced deregulation.

1.6 Scope of study

Advances in nanotechnology have given rise to a rapid development of many novel applications in the biomedical field. Hence, studies into the risks and health safety of these nanomaterials are essential. The findings gleaned from this study will provide a better insight into molecular mechanisms underlying gold nanotoxicity induced by AuNPs. Biodistribution studies have identified the lung as one of the target sites of accumulation for AuNPs, necessitating further studies into nanotoxicological effects in the lung.

The hypothesis of this study is that AuNPs exert cytotoxic, genotoxic and epigenetic effects in lung cells *in vitro* and *in vivo*.

The objectives of this study are:

1) Investigating the intracellular localization of AuNPs in lung cells and morphological effects using various microscopic methods so as to determine the route of uptake.

2) Determining the *in vitro* effects of AuNPs on the cytotoxicity and genotoxicity of lung cells.

3) Performing genomic, proteomic and epigenetic analysis in AuNP-treated lung cells.

4) Analyzing study cell-cell interaction post AuNP exposure using a co-culture system.

5) Evaluating toxicity associated with AuNP exposure in male *Wistar-Kyoto* rats via IV injection *in vivo*.

A flow chart of the experiments performed as related to the specific objectives in this study is illustrated in Figure 1.4.

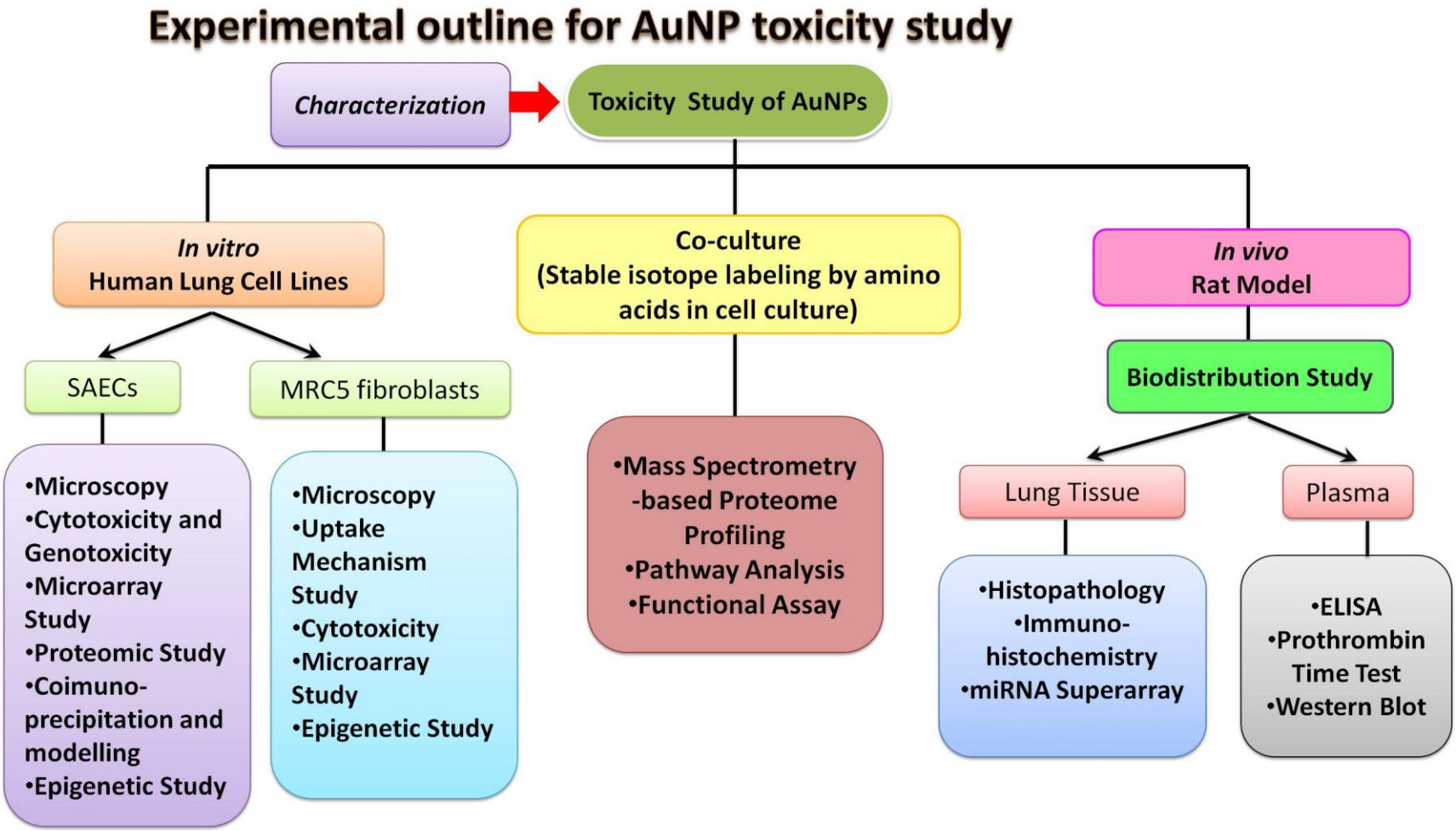

Figure 1.4: Flow chart of experimental outline for the study of AuNP toxicity in the lung *in vitro* and *in vivo*.

Chapter 2

Materials and Methods

2 MATERIALS AND METHODS

2.1 AuNP synthesis

AuNPs (20 nm, 2 nM in concentration) used in this study were synthesized in colloidal form by citrate reduction of gold salts from Au^{+3} ($HAuCl_4$) to Au^0 following the Turkevich method as previously described (Li et al., 2010a). Briefly, 95 ml of tetrachloroauric acid ($HAuCl_4$) solution consisting of 5 mg of Au was boiled and stirred vigorously, with addition of 5 ml of 1% sodium citrate solution for reduction of Au ions to take place. Stirring was continued till a wine red colored solution was formed. The AuNP solution was then concentrated via centrifugation following the published protocol of Balasubramanian *et al* (2010b), before functionalization with fetal bovine serum (FBS) in a water bath at 37°C. After FBS adsorption for 5 h, AuNPs were washed with phosphate buffer saline (PBS) and finally reconstituted to 10 nM NP solution. The AuNP colloidal solution was then filtered with a 0.2 µm filter before using for experimentation.

2.2 Characterization of AuNPs

Transmission electron microscopy (TEM) was performed using the CM120 BioTWIN transmission electron microscope. The NanoDrop ND-1000 UV-Vis Spectrophotometer (NanoDrop Technologies Inc., USA) was used to analyze the absorption spectrum of AuNPs. In addition, dynamic light scattering (DLS) and zeta potential (Zetasizer Nano ZS, UK) were performed to assess the hydrodynamic size and surface charge of AuNPs in solution.

2.3 *In vitro* AuNP experimentation

2.3.1 Cell culture

SAEC cells, a human small airway epithelial cell line (CC-2547S), purchased from Lonza were grown in SAGM supplemented with BulletKit (CC-3119). Human MRC5 fetal lung fibroblasts (ATCC® CCL-171™), were cultured in Roswell Park Memorial Institute (RPMI 1640). The medium was supplemented with 10% heat-inactivated FBS together with 100 µg/ml streptomycin and 100 units/ml penicillin. The cells were maintained in a cell culture incubator (THERMO Electron Corporation, MA) with humidified atmosphere of 37^{o}C and 5% CO_2:95% $O_{2,}$ before passaging. The morphology of cells was examined with a Nikon Eclipse TS100 microscope (Nikon Corporation, Japan) attached with a Digital Sight DS-U1 camera. The setup is also equipped with the ACT-2U imaging software version 1.60.

2.3.2 AuNP treatment *in vitro*

As-synthesized AuNPs were used to prepare a range of concentrations (0, 0.1, 0.25, 0.5, 1 and 2 nM) from 10 nM of AuNP stock solution, for treating the cells for 24 h, 48 h and 72 h.

2.3.3 Automegallography (AMG)

50 µl GoldEnhance™ from the silver enhancement kit (Cytodiagnostics, Canada) sufficient to cover the specimens, were applied at 24 h post exposure to AuNPs in SAECs and MRC5 fibroblasts, and allowed to develop for 10 min. The reaction was then stopped by rinsing with deionized water. After which, micrographs of cells showing deposition of silver ions on Au under light microscopy were taken.

2.3.4 TEM and Energy Dispersive X-ray (EDX) microanalysis

SAECs and MRC5 fibroblasts were treated with 1 nM AuNPs for 72 h and cultured in LabTeck culture chambers. AuNPs exposed cells were fixed in 2.5% glutaraldehyde (GA) for 1 h before rinsing 3 times with PBS at the time interval of 5 min each. Samples were osmified with 1 % osmium tetroxide (OsO_4) and bits of potassium ferrocyanide (KFeCN) (Agar Scientific Ltd, UK) at room temperature for 1 h. Following which, samples were dehydrated by immersing in a graded series of ethanol for 10 min each and embedded in epoxy resin (polymerization at 60 °C overnight) (Ted Pella Inc, USA). This was followed by slicing of ultrathin sections, which were subsequently mounted on formvar-coated copper (Cu) grids. Sections were then doubly stained with uranyl acetate (BDH, UK) and lead citrate (BDH, UK). Digital micrographs were obtained using a Gatan 792 Bioscan 1k×1k Wide Angle Multiscan CCD camera attached to the Philips EM280S transmission electron microscope. Determination of the elemental composition in the sample was achieved by elemental analysis using the CM120 BioTWIN electron microscope coupled with a Philips EDAX Microanalysis system.

2.3.5 Inductively coupled plasma mass spectrometry (ICPMS)

Nitric acid (HNO_3) and hydrochloric acid (HCl) purchased (Merck, Germany) for ICPMS were of analytical grade. Cells pre-treated with AuNPs were harvested by using trypsin. Aqua regia solution was prepared by mixing one part of HNO_3 to three parts of HCI for dissolving Au. Aqua regia was added into each specimen and acid digestion of cells was performed overnight.

Specimens were diluted at a concentration of 1 aqua regia: 9 ultrapure (UP) water. The calibration standard solution of Au and Platinum (Pt) (as internal standard) were prepared from single element stock solutions and diluted to the desired range of concentrations. UP water was used as the diluent. The quantification and calculation was

performed by using external calibration with internal standard correction. All measurements were carried out with the ICPMS Agilent 7500 instrument (Perkin Elmer, USA).

2.3.6 Focused ion beam-scanning electron microscopy (FIB-SEM), nanotomography, elemental analysis and mapping

Polymerized resin blocks were trimmed and polished with a glass knife to expose the SAECs on the block surface. The block was then mounted on aluminum SEM specimen stub with silver adhesive paint, leaving the block face exposed to enhance electrical conductivity during the milling and imaging process. A Zeiss Auriga 60, CrossBeam instrument (Carl Zeiss Microscopy, Germany) equipped with a Cobra-focused gallium ion beam column and Gemini electron column with a Schottky field emission gun was employed for all the milling and imaging work in this study. For milling and imaging, the sample was tilted to 54^{o} angle and positioned at 5 mm working distance such that the sample surface was aligned perpendicular to the intersection point (defined as the meeting point of the electron beam and ion beam).

To acquire the 3D stacks in an automated process alternating between milling and imaging, the ion beam was set at 30 kV and 600 pA current to remove a slice thickness (z-axis) of 8 nm each time. The milling volume was set at x = 30 µm, y = 30 µm and z = 5 µm. Backscattered electron (BSE) imaging was performed using electron beam at an acceleration voltage of 2 kV with a 1.2 nA probe current. The backscattered electrons signal was collected by an in-column Energy-selective Backscattered detector. The imaging frame was set at a field-of-view of x = 25 µm by y = 10 µm and store resolution of 3840 resulted in image pixel size of 8 nm. All post-processing of the data set was done using the ImageJ software (National Institutes of Health, NIH). First, alignment of the image stack was performed using the StackReg Plugin. Milling

consistency was then assessed via continuous playback of the images. The 3D stack was reconstructed with the 3D Viewer Plugin.

For elemental analysis, the ultrathin sections were further analyzed in a Zeiss Libra 120, Energy Filter TEM system. Elemental distributed mapping was calculated using Energy Spectroscopic Imaging (ESI) with three window power law method. The recorded images were taken with a slow scan CCD camera and processed with iTEM software (OSIS, Germany).

2.3.7 Lipid hydroperoxide (LPO) assay

AuNP-treated and untreated SAECs and MRC5 fibroblasts were trypsinized and centrifuged at 1,000 rpm for 5 min. A positive control sample was prepared by treating the cells with 50 µM H_2O_2 for 1 h. 600 µl of UP water was added to the pellet and sonicated on ice at 50 amplitude for 40 s, with manual pulsing every 10 s using VibracellTM ultrasonic processor (Sonics & Material, USA). Lipid hydroperoxides were extracted in chloroform and quantified using the Lipid Hydroperoxide Assay Kit (Cayman Chemical Company, USA) following the manufacturer's instructions. After addition of the chromogen for color development, the samples were aliquoted into 96 well glass plates and absorbance readings were taken at 500 nm with spectrophotometer.

2.3.8 Lactate dehydrogenase (LDH) assay

The Roche Cytotoxicity Detection Kit was used to quantify AuNP-mediated cytotoxicity by measuring the amount of LDH released from the cytosol of damaged cells. Briefly, cells were seeded into a 96 well plate for 24 h. Subsequently, the medium was aspirated and replaced with 200 µl of medium containing 0, 0.1, 0.25, 0.5, 1 and 2 nM of AuNPs into each well. After 24 h, 48 h and 72 h incubation, 100 µl of supernatant was decanted, spun down to remove AuNPs and transferred to a new plate. 100 µl of reaction mixture

(consisting of a catalyst and dye solution) was then added. Following 30 min of incubation at room temperature, the LDH activity in the supernatant was quantified using a SpectraMax M5 MicroPlate reader at 490 nm wavelength. Controls which test for AuNP interference were included.

2.3.9 Trypan blue dye exclusion assay for cell viability

SAECs and MRC5 fibroblasts were cultured in 6 well plate and subjected to AuNP treatment for 24 h, 48 h and 72 h at different concentrations. After each time point, cells were harvested and spun down before resuspending with fresh medium. 50 µl of trypsinized cell suspension was added into 50 µl of 0.4% Trypan blue stain (1:1 dilution) (Sigma, USA) and mixed well. 10 µl of stained cell suspension was filled to a hemocytometer for cell counting either manually or by using an automated cell counter. For the manual method, the number of non-viable cells that were stained blue and viable cells that excluded the dye, was scored separately under a light microscope.

2.3.10 Acridine orange and ethidium bromide (AO/EtBr) staining

1 mg/ml acridine orange and ethidium bromide were constituted from the powder form with PBS. For discrimination of live from dead cells, acridine orange fluoresces as green color, indicating live viable cells; ethidium bromide fluoresces as orange color when intercalated with DNA, representing dead cells. The medium was first removed from AuNP-treated cells. Stock solution was further diluted 100x with PBS to working concentration before adding into cells. Diluted dyes were added for 1 min at room temperature, removed and washed with PBS before micrographs were taken.

2.3.11 Flow Cytometry (FCM) for cell cycle analysis

Cells were plated onto 6 well culture plates and AuNP treatment was performed for 48 h and 72 h. After each time point, both adherent and floating cells were pooled into a 15 ml centrifuge tube and then pelleted by centrifugation at 1800 rpm for 5 min. Cell pellets were washed twice with PBS and then fixed in 70% ethanol (and chilled to -20°C) overnight. A hypotonic cocktail consisting of 8 ml PBS + 2 ml RNase A + 10 µl TX + 200 µl Propidium Iodide (PI) was prepared. After washing twice with PBS, 1 ml of the cocktail was added to the samples. DNA content of cells was counterstained with 1 mg/ml PI (Sigma-Aldrich, USA). 1x 10^4 events for each sample were analyzed and scored by Dako Cyan flow cytometer (DakoCytomation) supplemented with the Summit^{TM} software.

2.3.12 Alkaline single-cell gel electrophoresis (Comet assay)

The SAECs were first embedded in 0.8% low melting point agarose (IBI Scientific, USA) on specially prepared comet slides (Trevigen, USA) and lysed in cold lysis solution (comprising 2.5 M NaCl, 0.1 M EDTA, 10 mM Tris base, at pH 10) containing 1% Triton X (Trevigen) for 1 h at 4°C. SAECs were denatured in alkaline electrophoresis buffer (0.3 M NaCl, 1 mM EDTA) in the absence of light, at room temperature for 40 min. Subsequently, electrophoresis was performed at 25 V and 300 mA for 20 min. Alkaline condition was removed by using neutralization buffer (0.5 M Tris-HCl, pH 7.5) for 15 min. Dehydration was achieved using 70% ethanol. Subsequently, the slides were dehydrated before stained with SYBR green dye. The tail moments of the SAECs nuclei were scored as an indication of DNA damage. 100 comets were analyzed per concentration and this was done by using comet imager v1.2 software (Metasystems GmbH).

2.3.13 RNA extraction, reverse transcription (RT) and quantitative real-time RT-PCR (qRT-PCR)

The RNeasy Mini Kit (QIAGEN, Germany) was used to isolate total RNA. The RNA quality was anlayzed using the NanoDrop® ND-1000 Spectrophotometer at absorbance reading of 260 nm and 280 nm wavelengths. Cultured monolayer of SAECs and MRC5 fibroblasts were lysed, followed by addition of an equal volume of 70% ethanol. Samples were then transferred into an RNeasy MinElute Spin Column and centrifuged for 15 s at 13200 rpm. Samples were subjected to washing steps using RWI and RPE salt buffer, spun dry to remove excessive ethanol, followed by elution with RNase-free water.

For cDNA conversion, Super ScriptTM III First-Strand Synthesis System for RT-PCR kit (Invitrogen, USA) was used for RT according to manufacturer's instructions. The volume needed to reverse-transcribe RNA is shown below:

n µl of total RNA

1 µl of 50 ng / µl random hexamer

1 µl of 10 mM dNTP mix

n µl of DEPC-treated water (make up to total volume of 10 µl)

Firstly, samples were incubated in the PCR machine at 65ºC, 5 min, and then chilled on ice for ≥1 min. For 1 reaction, cDNA Synthesis Mix were prepared by addition of the following reagents in the following order as per instruction:

2 µl 10x RT buffer

4 µl 25 mM $MgCI_2$

2 µl 0.1 M DTT

1 µl RNAseOUT

1 µl SuperScript III

Samples were further incubated in the thermocycler following the thermal profile as indicated: 25°C for 10 min, 50°C for 50 min and 85°C for 5 min. Storage was at -20°C for later use.

The primer sequences for MT isoforms, cell cycle related genes, DNA repair, antioxidant genes used in this study are listed in Table 2.1. Mixture consisting of diluted cDNA, SYBR Green PCR Master Mix (Applied Biosystems, Foster City, California, United States) and primer for each gene were run by a 7900HT Fast Real-Time PCR machine (Applied Biosystems, USA) following the thermal profile settings: 95°C, 20 s; 95°C, 1 s followed by 60°C, 20 s for 40 cycles. The Ct values were normalized to an endogenous housekeeping gene (GAPDH) where $\Delta Ct = Ct_{target} - Ct_{GAPDH}$. The average values of the Δ Ct of the samples were then used to calculate the ΔΔCt value ($\Delta\Delta Ct = \Delta Ct_{treated} - \Delta Ct_{control}$). The fold change in expression for each gene of the samples was calculated by $2^{-\Delta\Delta Ct}$.

Table 2.1: List of primers' sequences used for qRT-PCR.

Gene Symbol	*Forward*	*Reverse*
SLC38A5	GTTGGGTGGCAAGGAGTTTA	GCTTGGATTACACGGCATTT
ZC3HAV1	GGCAGCACTTACCTTGCTTC	TCTGGTGGTCACAGCTTCAG
VEGFC	TACAGACGGCCATGTACGAA	TTTGTTAGCATGGACCCACA
ITGA2	CAAGTGGGATTCAGTGCAGA	GAGCACCAGCAACAAAGTGA
RELN	ATGTGGTAAAGGCGTTCCTG	AACCCAGGGGCTGTAGAAGT
ATP10A	AAGCTGGAGAGGCAGATGAA	GCTGTGACTGGGGATAAGGA
ADAR	GTCAACTGGTGTCTGGCTGA	TAGTCACGGGCAGCTTTCTT
SC4MOL	AGGCCTGAAGTTCACATTGG	GCAGTGAGCTGAGACTGTGC
TAF9B|LOC728	TCTCCTCCCCCAAGAGATTT	TCCCTTGGTTAGGTCCCTTT
PROS1	CCTAGTGCTTCCCGTCTCAG	TTTCCGGGTCATTTTCAAAG
C5orf21	CGCTCACATTAAGGCTGACA	GATTAAGGAGGGGGAAGCAG
FAP	CTTGTCCTGGCTTCAGCTTC	AGGTGGCAACTCCAAATACG
IDI1	CAGTCAGCCACTGCTTTTGA	GGGTTTTATCCAGCCCAAAT
ZMAT3	GGCAGAGAATTCCACGTGAT	CCTGTACCGCTGTTCAGACA
TRPA1	TTCTGAGCCACAATGCTGAC	CTTCATGCATTCAGGGAGGT
STYX|LOC73043	TCATAGGGAGCTGCCATACC	GCTAGCAGCATCTTGCACTG
RFTN2	CGGGGCTATTCATCCTGTTA	TTCTTTTGCTGCGTCATTTG
FYB	TTCCCTAAGGCCCCTTCTAA	TAAGACGTCTGGCCTTTGCT
AKR1C2	GGTCACTTCATGCCTGTCCT	ACTCTGGTCGATGGGAATTG
KYNU	CAAGAGAGGGGGAAGAAACC	TAACAACCCTTCGCTTGTCC
SAA1	TGGTTTTCTGCTCCTTGGTC	CCCGAGCATGGAAGTATTTG
NQO1	TTACTATGGGATGGGGTCCA	CCACAAGAGGGCAGTGTTTT
TXNRD1	AATTTGCCCCTGTGTGCTAC	TCAGCTTGCTTAGACCAGCA
AKR1C3	GATTTGGCACCTATGCACCT	CACACTGCCATCTGCAATCT
FTH1	GCTAAGCCTCGGGCTAATTT	CGGCACTTAAGGAATCTGGA
PTGR1	CCTGCTTGAAGCTTTGTTCC	AGAAATGGAGTGCGTTGTCC
CYP24A1	CCCTGCCTACCACATTCACT	TTCATGGGAGGCCTGATAAC
UIMC1	TGATGGAGAGGAACCAAAGG	GGTAGCGGAAGCATCAGAAG
PNLIPRP3	GGGAGTTTGCCATTGTCAGT	AGCATGGTTTCAGGTTCTGG
DSC2	CGTCCTGTAGATCGTGAGCA	TCGTGTCAGGCTCATCTTTG
NTN4	GGCCTGGAAGATGATGTTGT	TTGAGGCTCTTCGTTCAGGT
NRIP1	GCACTGTGGTCAGACTGCAT	GTGTTCACAAGGGCTTGGTT
SH3KBP1	CGGAAGAGGCTGTCTGATTC	AGGGCATATCCTTGCTCCTT
TLR2	GGGTTGAAGCACTGGACAAT	TCCTGTTGTTGGACAGGTCA
TLK1	CTGTGATCTCAGACGGCAAA	TGAAGCGCCATGTCTAACTG
CDK1|CDC2	CCATGGGGATTCAGAAATTG	CCATTTTGCCAGAAATTCGT
SERPINE1	CAACTTGCTTGGGAAAGGAG	GGGCGTGGTGAACTCAGTAT
CAT	GCCTGGGACCCAATTATCTT	GAATCTCCGCACTTCTCCAG
GPX1	GGACTACACCCAGATGAACGA A	GCACTTCTCGAAGAGCATGAA
GPX2	CAAGCGCCTCCTTAAAGTTG	GAGGGTTGGGAGAGGAAAAG
PRX1	CAGCCTGTCTGACTACAAAGGA	CCAGTCCTCCTTGTTTCTTAGG
PRX3	TTAAACATGGTTAGTTGCTAGTACA	TTGAGACATGATCTAAGAATAGCCT
SOD1	GAAGGTGTGGGGAAGCATTA	ACATTGCCCAAGTCTCCAAC

SOD2	TCCACTGCAAGGAACAACAG	TCTTGCTGGGATCATTAGGG
SOD3	TCTCTTGGAGCTGGAAAG	CGTACATGTCTCGGATCCACT
APEX2	AATCAGGAACCCAGCAACTG	CACTGGGGTAGCATTGTCCT
ATM	GGACAGTGGAGGCACAAAAT	GTGTCGAAGACAGCTGGTGA
ATRX	ATACTCCCATGCTGCCAAAG	GCTTCATACTCAGCCCAAGC
BTG2	CCTGGGCAGAGAGTGAAAAG	CCTTCCATCCTAACCCCAAT
ERCC2	GCTGGACATCTACCCCAAGA	CCGGATCACAGCAATATCCT
LIG1	ACAAATATGACGGGCAGAGG	ACTTGGAATGGCTGGATCTG
RPA1	CCGACTCAGGACTGCAATAAG	CAGCAGACTCCTGGAAACAAG
XPA	GCGAAGAATGTGGGAAAGAA	CCCATTGTGAATGATGTGGA
XPC	GACAAGCAGGAGAAGGCAAC	GGTTCGGAATCCTCATCAGA
XRCC1	GATTCTGGGGACACAGAGGA	AGGGAACTCCCCGTAAAGAA
MT-1A	CTCGAAATGGACCCCAACT	ATATCTTCGAGCAGGGCTGTC
MT-1B	GCTTGTCTTGGCTCCACA	AGCAAACCGGTCAGGTAGTTA
MT-1E	GCTTGTTCGTCTCACTGGTG	CAGGTTGTGCAGGTTGTTCTA
MT-1F	AGTCTCTCCTCGGCTTGC	ACATCTGGGAGAAAGGTTGTC-
MT-1G	CTT CTC GCTTGGGAACTCTA	AGGGGTCAAGATTGTAGCAAA
MT-1H	CCT CTTCTCTTCTCGCTTGG	GCAAATGAGTCGGAGTTGTAG
MT-1X	TCTCCTTGCCTCGAAATGGA	GGGCACACTTGGCACAGC
MT-2A	GGATCCGATCCCAACTGCTCCTGCG CC	CTCGAGTCAGGCGCAGCAGCTGCAC TT
MT-3	CCGTTCACCGCCTCCAG	CACCAGCCACACTTCACCACA
MT-4	CATGGACCCCAGGGAATGTGT	GGGGTGGGAACGATGGA

2.3.14 Global gene array and data analysis

Transcriptomic analysis using the Affymetrix Human Gene 1.0 ST Array comprising 764,885 gene probes, was carried out to compare global gene expression patterns of the MRC5 lung fibroblasts and SAECs treated with or without AuNPs. RNA was extracted following the method mentioned above. RNA samples were sent to Origen Laboratories Pte Ltd (Singapore) for further analysis (comprising labeling, hybridization, scanning and data analysis.

Data was analyzed with GeneSpring software GX v11.5. The fold change of each gene that was ≥ 1.5 fold and with p value < 0.05 was selected. These genes were hierarchically clustered based on either up-regulation or down-regulation.

2.3.15 Validation of microarray results and Database for Annotation, Visualization and Integrated Discovery (DAVID)

The differentially expressed genes were clustered according to their functional groups using data clustering, annotation and functional characterization of genes available from DAVID version 6.7, Functional Annotation Bioinformatics Microarray Analysis.

2.3.16 Total RNA isolation and qRT-PCR (for miRNAs)

Total RNA was isolated from SAECs and MRC5 fibroblasts using the mirVana™ miRNA Isolation Kit (Ambion, Austin, TX). Quantity and purity of extracted RNA were determined using the NanoDrop ND-1000 Spectrophotometer (NanoDrop Technologies Inc., USA).

Mature hsa-miR-155, hsa-miR-125b, hsa-miR-146a and endogenous controls, U6 snRNA and SNORD68 were quantified using TaqMan® (Applied Biosystems) or miScript (Qiagen) microRNA assay kits specific for each miRNA. RT was performed using the settings of: 16°C, 30 min; 42°C, 30 min; 85°C, 5 min, before holding at 4°C.

The expression of mature miR-155 relative to internal control, U6 snRNA was determined using SYBR green qRT-PCR assay. For qPCR, the setting was 95°C, 1 min; 95°C, 15 sec followed by 60°C, 30 sec and cycled 40 times using 7900HT Fast Real Time PCR System equipped with sequence detection system software (Sequence Detection System, version 2.1; Applied Biosystems).

For miScript system, miScript II RT kit was used for RT. The volume needed to reverse transcribe miRNAs is shown below:

4 µl miScript HiSpec buffer

2 µl 10x miScript Nucleics Mix

n µ l RNase-free water

2 µl miScript RT mix

n µl template RNA

Total volume: 20 µl

Samples were incubated at 37^{o}C for 60 min followed by 95^{o}C for 5 min. For quantitative PCR, the setting was 95^{o}C, 15 min; 94^{o}C 15 sec followed by 55^{o}C, 30 sec and 70 ^{o}C, 30 sec and cycled 40 times.

miRNA expression was expressed as fold change and was calculated the same method as mentioned in section 2.3.13.

2.3.17 Proteome profiling by multiplex peptide stable isotope dimethyl labeling and mass spectrometry

This experiment was performed based on a protocol described earlier (Boersema et al., 2009). Briefly, AuNP-treated and untreated SAEC protein lysates were subjected to trypsin digestion, let dry, followed by isotopomeric dimethyl labeling. Labeling reaction was halted by adding 1% ammonia solution followed by formic acid. Differentially

labeled samples were loaded and analyzed by nanoLC Orbitrap-MS (Thermo Scientific). MS data were analyzed using MaxQuant software.

2.3.18 Western Blot

Protein from cells was extracted using MPER lysis buffer. Protein lysate was collected and denatured with loading dye at 95°C. The protein sample was separated by electrophoresis (SDS-PAGE) using 10% sodium dodecyl sulfate–polyacrylamide gel. Subsequently, proteins were transferred onto a PVDF membrane (Bio-Rad). Blocking was carried out with 5% milk for an hour.

Primary antibodies used were: PROS1 (Abcam, USA); SAA1, TLR2 and beta-actin (Bio-Rad, USA) (as internal loading control). Following overnight incubation of the primary at 4°C, the secondary antibody-HRP conjugate (Amersham Biosciences, NJ) was then added. The bands of the proteins of interest were visualized at their respective protein sizes using the SuperSignal West Pico Chemiluminescent Substrate (Thermo Scientific). Band intensity was quantified by densitometer GS-710 (Bio-Rad, USA).

2.3.19 Co-immunoprecipitation (co-IP) and western blot

The agarose beads (Roche Applied Science) were washed three times prior use. The protein lysate was prepared in Co-IP buffer (150 mM NaCI, 20 mM TrisCI pH 8.0, 1% Triton-X100, 2 mM PMSF, 1 mM sodium orthovanadate, 5 mM sodium fluoride). Next, the protein was incubated with anti-SAA1, TLR2 and IgG (Santa Cruz) antibodies in rotating motion for 2 h at 4°C. Following that, the agarose beads were incubated together for 1 h and washed with Co-IP buffer to remove unbound proteins. The bound proteins were analyzed on western blot.

Next, the protein complexes pulled down from co-IP were separated using 10% and 15% SDS-PAGE. The protein bands of interest were visualized at 12 kDa (SAA1)

and 90 kDa (TLR2) using SuperSignal West Pico Chemiluminescent Substrate (Thermo Scientific).

2.3.20 Transient transfection and luciferase assay using Cignal finder reporter array

50 µl of Opti-MEM was added into each well of a Stress and toxicity Cignal Finder Array plate (Qiagen) and resuspended thoroughly. Mixture was left 5 min at room temperature before addition of 50 µl diluted Attractene transfect reagent (1:1 ratio). The diluted nucleic acid construct-Attractene was mixed before incubating for 20 min to allow complexes formation. SAECs post exposed to 1 nM AuNPs were trypsinised and final cell density of 1×10^4 cells/well resuspended using Opti-MEM (Gibco) complemented with 10% FBS was seeded. The complexes and cells were mixed gently and incubated for 24 h at 37°C. After 24 h transfection, medium was replaced and Dual-Glo Luciferase Assay (Promega) was performed according to manufacturer's instruction. Briefly, for measurement of firefly luciferase activity, equal volume of Dual-Glo® Luciferase Reagent was added into culture medium (1:1 ratio) and firefly luminescence was measure after 20 min. For Renilla luciferase activity, equal volume of Dual-Glo® Stop & Glo® Reagent (Promega) was added before measurement was taken after 20 min. Luciferase activity was measured and results are expressed as fold change of activation. T-test was performed by comparing the normalized luciferase activities for the Nrf2/Nrf1 and NFkB reporter treated with AuNPs versus the normalized luciferase activity for the untreated reporter. Experiments were done in quadruplicates, and the standard error means are indicated.

2.3.21 Trichostatin A (TSA) and 5-Azacytidine (5-Aza) treatment

$8x10^4$ of MRC5 cells were plated onto a 6 well plate. 400 nM of TSA (Sigma Aldrich, USA) was used to treat MRC5 cells for 48 h followed by 72 h AuNP treatment.

For 5-Aza (Sigma Aldrich, USA) and TSA in SAECs, $5x10^4$ cells were plated. After 24 h, 4 µM of 5-Aza was used to treat the cells for 6 days followed by 72 h of AuNP treatment.

RNA was extracted from cells following TSA or 5-Aza treatment.

2.3.22 Cell Proliferation assay (MTS)

The cytotoxicity of cellular uptake inhibitors against MRC5 fibroblasts was determined using the MTS assay. Briefly, MRC5 fibroblasts (seeded at 1×10^4 cells/well) were incubated for 24 h in 96 well plates. 0.5 µg/mL concanavalin A, 10 µg/mL chlorpromazine and 25 µg/mL nystatin were separately added and incubated for 4 h. After 4 h, the Promega CellTiter 96® AQueous Non-Radioactive Cell Proliferation Assay Kit (Promega, USA) was used to quantify cell viability by measuring the amount of formazan formed. After removal of existing medium, 100 µl of fresh medium followed by 20 µl of MTS tetrazolium reagent, was added to each well. Incubation was carried out for 3-4 h before the reading was measured using SpectraMax M5 MicroPlate reader at 490 nm wavelength. A control and a blank set (wells with only culture medium and no cells) were also prepared. The % of cell viability was calculated as shown below.

% cell viability = (AbsTest – AbsBlank) / (AbsControl - AbsBlank) x 100%

2.3.23 Hoechst 33342 staining for confocal microscopy

After AuNP cellular uptake inhibitor treatment, cells were fixed in 4% paraformaldehyde (PF) at room temperature for 20 min. Cells were then washed with PBS for 3 times with the interval of 5 min each, stained with Hoechst 33342 stain, before being mounting onto

a glass slide using Dako mounting medium (Dako Corporation, USA). Specimen was kept moist in the dark. The specimens were observed using the Olympus Fluoview™ FV1000 confocal laser scanning microscope (cLSM) equipped with Fluoview v5.0 software to capture images of the cellular architecture. A negative control was included and processed similarly.

2.3.24 Endocytosis inhibition and ICPMS

Endocytosis inhibitors, concanavalin A, chlorpromazine and nystatin (Sigma Aldrich, USA) for endocytosis were applied to MRC5 lung fibroblasts. Inhibition of clathrin-mediated endocytosis was performed with 0.5 μg/ml concanavalin A and 10 μg/ml chlorpromazine; and caveolae-dependent endocytosis inhibition with 25 μg/ml nystatin. All the inhibitors used were following reported concentrations reported in the literature (Singh et al., 2003; Morisco et al., 2008; Vercauteren et al., 2010) with treatments carried out for 4 h at 37°C. After which, the medium was replaced with 1 nM AuNPs and incubated for 24 h at 37°C. Subsequently, cells were rinsed with PBS, trypinized then pelleted by undergoing centrifugation for 5 min at 1,000 rpm. Acid digestion was performed using aqua regia on the cells collected overnight. Samples were analyzed as described in section 2.3.5 with the ICPMS instrument.

2.3.25 Immunocytochemistry (ICC)

AuNP-treated and untreated cells cultured on the Lab-Tek® 4-Chambered Coverglass were washed with PBS thrice for 5 min each. Fixation of cells was performed using 4% PF. The cells were again washed with PBS, followed by 0.2% Triton-X 100 in 1x PBS (PBS-TX) (pH 7.4) to permeabilize the cells. 0.5% hydrogen peroxide was added and incubated for 30 min to prevent endogenous peroxidase. This was followed by blocking with 5% horse serum (Vectastain® ABC Kit, Vector Laboratories, CA) for 1 h, room

temperature and lastly primary mouse antibody for MT (Abcam, UK), (Dako Corporation, USA) and incubated at 4 ºC, overnight. For the negative control, the primary antibody was omitted.

Following overnight incubation, the cells were rinsed with 0.2% PBS-TX, followed by addition of 200 µl of biotinylated, affinity-purified secondary anti-mouse antibody (1:200) and incubation at room temperature for 1 h. This was followed by incubation for 1 h at room temperature in ABC solution (comprising Avidin DH and Biotinylated Horseradish Peroxidase H diluted in PBS-TX) (Vector Laboratories, CA) before addition of 3,3-diaminobenzidene (DAB) mixture (comprising 1 ml of 10x DAB, 9 ml of TBS and 3.3 µl of hydrogen peroxide, H_2O_2) for 10 min. The cells were washed 3 times with TBS and the coverslip at the base of the chambered coverglass was detached using a blade. The brown color stained cells were counterstained with Shandon's Haematoxylin, and mounted onto a glass slide with Permount® (Fisher Scientific, USA). The air dried slides were examined under a microscope.

2.3.26 FCM for protein quantification

$5x10^5$ MRC5 cells were seeded separately into a 6 well plate before exposure to 1 nM AuNP for 72 h. After 72 h, the used medium was aspirated out and rinsed thrice with PBS. Cells were permeabilized with 0.1% PBS-TX before incubation with diluted primary antibodies for MT (1:200) at 4 ºC, overnight. Next, Cy-3 conjugated secondary anti-mouse antibody (1:200) was added for 1 h at room temperature. The cells were washed, and finally resuspended in fresh medium. Samples were stored in the dark before acquisition by Mo-Flo cell sorter (BeckmanCoulter). Negative control was included for acquisition compensation.

2.3.27 Luciferase reporter assay

DH5α competent *Escherichia coli* transformation with plasmid for pMiR-Luc reporter gene for miR-155 (Signosis, CA) was performed to propagate the plasmid prior to the start of this assay. Heat shock transformation was done and the transformed DH5α cells were plated by streaking on Luria-Bertani (LB) plates containing 100 µg/ml Ampicillin and cultured overnight at 37°C. A single bacterial colony was picked and transferred to 1 ml LB medium containing 100 µg/ml Ampicillin and shook at 37^{o}C overnight. Plasmids was purified and checked on gel for specificity.

Triplicate samples of $1.5x10^{4}$ cells resuspended in RPMI supplemented with serum without antibiotics were seeded into 24 well plate. Cells were transfected with 0.2 µg of the reporter vector using 0.6 µl of FuGENE®6 Transfection Reagent (Roche Molecular Biochemicals, Germany). Reporter vector/ FuGENE®6 complexes formed after 30 min incubation was added into the cell culture medium (up to final volume of 500 µl). Following this, the cells were incubated overnight, before exposure to AuNPs for another 48 h. Transfected cells were then lysed and the luciferase expression level was quantified using the Luciferase Assay System (Promega, USA). The relative renilla luciferase light output was normalized to parallel firefly luciferase output (relative light unit, RLU).

2.3.28 Target genes prediction

Given that miRNAs perform their biological function as regulator for their target protein-coding genes, the predicted targets of miRNAs were analyzed in this study. The prediction was performed using the top 5 most used miRBase algorithms, including PicTar (http://pictar.mdc-berlin.de), miRanda (http://microrna.sanger.ac.uk), TarBase,, mirBase (http://www.mirbase.org/), TargetScan Release 6.2 (http://www.targetscan.org), and MicroCosm Targets Version 5.

2.3.29 Silencing of mir155 in MRC5 cells

2.3.29.1 Sequence of miRNA inhibitor

Anti-miR™ miRNA 155 inhibitor (Ambion, Inc.) was used to suppress the endogenous mir-155 expression. The sequence of the miR-155 inhibitor can be found online from Anti-miR™ miRNA Inhibitors and Libraries (Ambion, Inc.) The mature (capitalized 'miR') miR-155 sequence was UUAAUGCUAAUCGUGAUAGGGGU which can be retrieved from either the miRNA Registry or the Sanger miRBase database.

2.3.29.2 miR-155 knockdown

Knockdown of miR-155 in MRC5 fibroblasts was performed using HiPerFect Transfection Reagent (Qiagen). Experiments (including the negative control set) were performed in triplicates. Transfection efficiency was pre-optimized in MRC5 cells prior to the start of experiment. Parameters such as density of cells, duration of exposure, amount of transfect reagent used (Cy-3 conjugated scrambled siRNA and anti-miR-155 oligonucleotide) were adjusted during optimization. Transfection complexes were prepared as per manufacturer's guideline. A final concentration of 20 nM anti-mir-155 was used. After removal of existing culture medium, fresh medium together with transfection complexes were added to the cells before further incubation for another 24 h. RNA or proteins were subsequently extracted for downstream analysis.

2.3.30 Methylation analysis

2.3.30.1 Bisulfite conversion of genomic DNA

Total genomic DNA for MRC5 fibroblasts (post-treated with 1 nM of AuNPs) was extracted using DNeasy Blood and Tissue Kit (Qiagen) following the instructions of the manufacturer. The proteinase K digestion step was included to get rid of the proteins before subjected to bisulfite conversion.

Next, bisulfite conversion of total genomic DNA of MRC5 cells was performed using EpiTect Bisulfite Kit (Qiagen). This step allows the conversion of unmethylated cytosines residues to discriminate from methylated cytosines (U (T) –residues). Briefly, 1 µg of DNA was treated with sodium bisulfite, denatured at high heat of 95°C for 5 min, followed by bisulfate conversion at 60°C. DNA samples were cleaned and eluted after desulphonation.

2.3.30.2 DNA methylation-specific PCR analysis and qRT-PCR

Methyl Primer Express® Software (Applied Biosystems) was used for primer design. Two types of bisulfite PCR primers were designed and MSP primer selection criteria were as outlined by Li and Dahiya (2002). Methylation-Specific PCR (MSP) was used to study the methylation status of CpG sites in the PROS1 using qRT-PCR. Bisulfite Sequencing PCR (BSP) was designed for DNA methylation analysisn by sequencing method by Axil Scientific/ 1st BASE, Singapore.

Amplification of *PROS1* CpG islands was performed using GoTaq® Colorless Master Mix (Promega). Subsequently, the amplified DNA was *PROS1* gene-specific, with RT–PCR amplicons of 280 bp when run on a 2% agarose gel. DNA bands were visualized under UV transilluminator (CHEMI GENIUS2 CG2/D2, USA) and the electrophoretic image was photographed using the GeneSnap image acquisition software version 6.03.01 (SynGene, UK). The product size was then determined using 100 bp DNA ladder (Promega) by comparison. For qRT-PCR, MSP primers were used and qRT-PCR was preformed as described in section 2.3.13.

2.3.30.3 Bisulfite sequencing of methylated *PROS1* and gene cloning

The *PROS1* gene in AuNP treated and untreated samples were selected for BSP-based sequencing. Subcloning of *PROS1* CPG island into pDrive Cloning Vector (Qiagen) was

performed to confirm the degree of methylation. The plasmid was transfected into competent cells and plated on LB agar plate. Blue-white screening and ampicillin selection were employed to select colony (white) before further clone expansion. Purified amplicon insert size was verified via PCR and agarose gel before sent for sequencing by Axil Scientific/ 1st BASE Pte Ltd. Sequences were aligned using BiQ Analyzer (Max-Planck Institut fur informatik, Germany) to generate lolli-pop grid to study the degree of methylation.

2.4 Co-culture Experiments with AuNPs

2.4.1 SAEC-MRC5 Co-culture

For the co-culture system, SAECs were cultured in Transwell chambers with or without AuNPs. After 72 h, the SAECs were then co-cultured with MRC5 lung fibroblasts and incubated for a further 72 h (Fig 2.1).

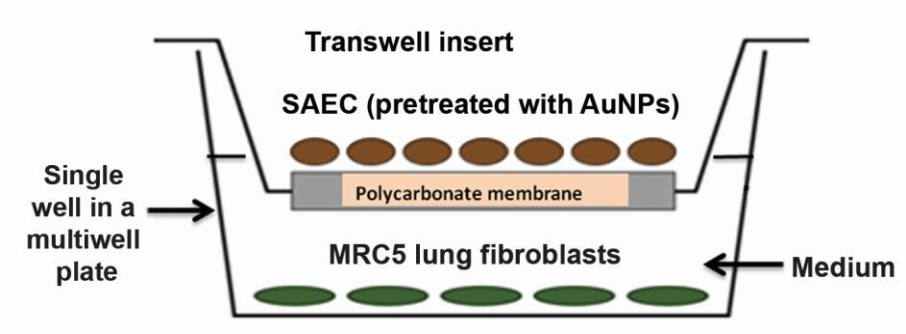

Figure 2.1: Schematic drawing of the SAEC-MRC5 lung fibroblast co-culture system. SAECs (treated with and without AuNPs) were seeded in the upper chamber of a Transwell polycarbonate membrane with the SILAC-labeled MRC5 lung fibroblasts plated in the lower chamber.

2.4.2 Stable isotope labeling by amino acids in cell culture (SILAC)

Incorporation of "heavy" amino acids consisting of substituted stable isotopic nuclei (deuterium, 13C, 15N) into the proteome of MRC5 lung fibroblasts was performed. MRC5 lung fibroblasts were grown in DMEM without Lysine and Arginine amino acids, supplemented with either "light" or with "heavy" forms of the two amino acids isotopes (with13C615N2-L-lysine and 13C615N4-L-arginine). Media were then supplemented with 10% dialyzed FBS and 1% penicillin/streptomycin. "Light" and "heavy" MRC5 lung fibroblasts were grown consecutively for four passages before an incorporation check was performed.

The forward experimental set is defined as lung fibroblasts that were incubated with light isotopes of arginine and lysine (also labelled as "light" or "L" cells) and conversely, the reverse set was incubated with heavy isotopes of arginine and lysine (regarded as "heavy" or "H" cells).

2.4.3 Mass spectrometry analysis

Whole proteomes of the MRC5 lung fibroblasts were extracted after 72 h, and the "light" and "heavy" protein lysates were mixed in a 1:1 ratio according to the weight of the proteins. After 10% SDS-PAGE separation, protein bands were digested with the trypsin enzyme overnight at 37°C. Extraction of tryptic peptides were carried out before LC-MS/MS analysis using the LTQ-Orbitrap mass spectrometer. Protein identification and quantitation were performed using the Mascot (version 2.2; Matrix Science, UK) software against the International Protein Index (IPI) human protein database (V3.68). Fold change was obtained from the normalized ratio of peptides which were quantified in the experimental MRC5 cells labeled with heavy (K8R10) isotopes compared to control MRC5 cells that had been labeled with light (K0R0) and statistical significance was calculated by the MaxQuant version 1.0.13.13 software.

2.4.4 Gene Ontology and IPA analysis

Gene Ontology (GO) annotations enrichment analysis was performed by importing the gene ID into the program and IPA pathway analysis (www.ingenuity.com) was performed by importing the IPI number into the program, with automatic mapping of the pathways performed.

2.4.5 Cell adhesion assay

Co-cultured MRC5 cell suspension was prepared by resuspending the cells in medium at a concentration of 5×10^5 cells/ml. 100 µl of cell suspension ($5x10^4$ cells) was seeded into microwell plates (pre-coated with Collagen I or Fibronectin) for adhesion assay. The plated MRC5 cells were allowed to incubate for 30 min. Removal of non-adherent cells was carried out before washing the well with PBS. The unwashed wells served as loading controls. MTS assay was carried out to quantify number of adhered MRC5 cells.

2.4.6 Immunofluorescence (IF)

Cells were plated onto glass coverslip in a 6 well plate. Cells were fixed with cold 4% PF for 20 min, rinsed with 0.05% Tween-20-PBS, followed by permeabilization with 0.2% Triton-X (pH 7.4). After rinsing with 0.05% PBST, 1% BSA (diluted in 1x PBS) was added for 30 min for blocking non-specific proteins.

Cells were incubated using primary mouse anti-vinculin antibody (Milipore) at 4 ºC, overnight. For the negative control, the primary antibody was omitted. Following overnight incubation, the cells were washed thrice with 0.05% PBST for 5 minutes each, followed by 1 h incubation in the dark with anti-mouse IgG Cy3 conjugate F(ab')2 secondary antibody (Sigma Aldrich, USA) (1:200). Cells were then washed and stained with Phalloidin for F-actin (Sigma Aldrich and Milipore) at a dilution factor of 1:50 for 30 min. Nuclei were counterstained with DAPI (1:1000) for 5 min before the last wash

with 0.05% PBST. The coverslip was removed from the 6-well plate using a forcep and mounted onto a glass slide with Fluorescent Mounting Medium (Dako, Denmark) and kept in the dark at 4°C. Fluorescence images were taken with an Olympus Fluoview™ FV1000 cLSM.

2.5 *In vivo* experimentation with AuNPs

2.5.1 Animals

Male *Wistar-Kyoto* rats aged, 6–8 week old (approximately 250 g body weight) purchased from the Centre for Animal Resources in Lim Chu Kang, were housed at the Comparative Medicine (CARE) facility, National University of Singapore (NUS), Singapore. 1-week acclimatization period was held for newly purchased rats before commencement of study. The rats were housed two per disposable cage provided with free access to water and rodent diet under controlled temperature, humidity and lighting (12-12 h light-dark cycle). All procedures were pre-approved by NUS Institutional Animal Care and Use Committee (IACUC) (protocol number 118/11).

2.5.2 AuNP treatment *in vivo*

For the animal study, washed AuNPs were further diluted with ultrapure (UP) water, resulting in a final mass concentration of 256 µg/ml based on measurement obtained from ICPMS. The concentrated and purified AuNPs were then used for subsequent administration into rats.

Rats were anesthetized by inhalation of 5% isoflurane during AuNP administration. Single doses AuNP suspension was injected intravenously into the rat tail vein of *Wistar* rats and observed for 1 week/ 1 month/ 2 months. Rats were assigned randomly into 7 groups (n = 6 per group for different single doses and time points), in which there were 4 tested concentrations (single injection at 0.025 mg/kg; 0.05 mg/kg;

0.1 mg/kg; 0.2 mg/kg) and animals were sacrificed after 1 week; single injection of 0.1 mg/kg and animals were sacrificed at 2 time points (1 month & 2 months post injection) and UP water (as vehicle-only control). The control group was injected with 0.2 ml UP water. This group served as the internal control to determine the safety of water-only injection. Colloidal Au and UP water were sterile prior to injection. Individual body weight was monitored and recorded 3 times a week. The tested AuNPs were dissolved directly in sterile ultra pure water as mentioned earlier, and IV injection was given once and rats will be euthanized at the stated time points mentioned above.

Tissues were removed for histopathological analysis and blood for serum testing. The dose used in this study was derived from a clinical trial study (Libutti et al., 2010) and based on human equivalent dose (HED) and US Food and Drug Administration (FDA) guidelines.

2.5.3 Rat tissue collection

Tissues from all 7 groups were harvested from the rats at 1 week, 1 month and 2 months post-injection. At each time-point the rats were euthanized using carbon dioxide in excess. Blood was collected from the animals via cardiac puncture with 3.8% trisodium citrate (in ratio of 1:10) used as an anti-coagulant. The blood was centrifuged (3000 rpm for 5 min) and plasma was collected and stored at -80°C for further analysis. The lungs were collected and fixed in 10% formalin followed by paraffin embedding. Tissues were either snap frozen using liquid nitrogen before transferring into -80°C for storage or fixed and preserved for light and electron microscopic analysis.

2.5.4 Quantification of Au in lung tissues

The biodistribution of AuNPs was investigated quantitatively by ICPMS at different time points after different doses of single injection. To perform microwave digestion, all the

quartz inserts, QI, glasswares and Teflon vessel were cleaned with 1% HNO_3 followed by rinsing the glasswares with ultrapure water (3-4 times). Tissues of weight between 100-120 mg were put into each vial. 200 µl Cd standard solution with a concentration of 10 ppm in the final solutions was used as an internal standard and added to the sample inside the QI before putting on the glass cap. 1.5 ml of ultrapure water was added into the Teflon vessel followed by 1 ml water into QI. 2 ml concentrated nitric acid HNO_3 (69%) and 2 ml of HCI (30%) were added to QI using glass pipette before adding 1 ml H_2O_2 solution. 0.5 ml H_2O_2 solution into was also added into the Teflon vessel. QI was put into the Teflon vessel using plastic tweezers and was then placed inside the microwave vessel for digestion. After digestion, the vessel was taken out and cooled. The clear sample solution inside the QI was diluted to 20 ml with ultra pure water and transferred to the cleaned plastic vial and was kept at ~ 4 °C before quantifying with ICPMS.

2.5.5 Enzyme-linked immunosorbent (ELISA) assay

Plasma Transforming growth factor beta (TGF-β) and Interleukin 6 (IL-6) were used as indicators of inflammation. Plasma TGF-β and IL-6 concentration were analyzed in the Control and AuNP groups (6 groups) using rat TGF-β and IL-6 Platinum ELISA commercial kits (eBioscience) following the instructions included in the kit. Each well was washed once with wash buffer before adding in the sample (10 µl of HCI and NaOH pre-treated sample), standard and blank (assay buffer) in duplicate. Samples were incubated for 2 h, on a slow shaker at room temperature. After that, wells were washed five times with washing buffer before the addition of Biotin-Conjugate. Samples were incubated for another hour, washed again, and finally incubated with the Streptavidin-HRP for another hour. Samples were washed, added with TMB substrate solution and incubated for 30 min. The optical density was read at 620 nm to determine the absorbance of the samples tested.

2.5.6 Prothrombin time (PT) test

Rat blood collected from cardiac puncture procedure was emptied into a tube containing 3.8% sodium citrate (at the ratio of 1:10) and centrifuged at 3000 rpm for 10 min at 4^{o}C. Plasma was extracted and immediately stored at -80°C while the pelleted red blood cells were stored in a plastic test tube with a cap at 4°C for subsequent analysis. Separated plasma was used for PT test. Prior to performing prothrombin time test (PT), plasma was thawed at 37°C quickly and was then transferred to siliconized glass. The time required for a fibrin clot to form after the addition of bovine brain thromboplastin (Sigma Aldrich, USA) and calcium (to decalcify rat plasma) was studied. Plasma was mixed with constituted thromboplastin at 37°C and an excess of calcium chloride (25 mM) was added to initiate coagulation. Using tilt-tube technique, a stopwatch was started when the calcium is added and stopped when the clot formed. The time taken for blood clot formation was recorded.

2.5.7 Western Blot

Citrate-treated rat blood was centrifuged at 3000 rpm for 15 min) to obtain plasma. The pellet was discarded and protein quantification was done using Bio-Rad Protein Assay (Bio-Rad, USA). Primary rabbit anti-rat IL-1α antibody (Santa Cruz) and primary rabbit anti-rat albumin (Aviva, USA) (as internal loading control) were used. Rest of procedure is as described in section 2.3.18.

2.5.8 Histopathologic analysis using Hematoxylin and Eosin (H&E) staining

Lung tissues harvested for microscopic examinations were fixed in 10% formalin. Tissues were trimmed, immersed in fresh formalin, dehydrated in alcohol, cleared in clearene and lastly embedded in wax using ATP 700 Tissue Processor. Tissues were paraffinized, sectioned into thickness of 5 µm before H&E staining. Briefly, paraffin

sections were dewaxed with clearene and rehydrated in descending percentage of ethanol. Sections were stained with hematoxalin followed by eosin. Samples were dehydrated, air-dried and mounted using Permount solution before being examined microscopically.

Only four groups of animal tissues based on ELISA analysis of inflammatory cytokines were selected for H&E staining.

2.5.9 Immunohistochemistry (IHC)

Rat lung tissue section were deparaffinized and rehydrated as mentioned in section 2.5.8. Before performing immune-staining in rat lung tissues, enzymatic antigen retrieval was performed. Proteinase K treatment was carried out for 30 min at 37^{o}C. Sections were then allowed to cool at room temperature before rinsing with PBST. Endogenous peroxidation was prevented by incubating the section with 0.5% H_2O_2 prior to blocking with horse serum. Incubation of primary rabbit anti-rat IL-1α antibody (1:200) was performed, followed by secondary antibody and DAB staining as described in section 2.3.25.

2.5.10 Immunofluorescence (IF)

Antigen retrieval and endogenous peroxidation blocking were performed as described in section 2.5.9. Next, lung section was incubated with primary rabbit anti-CD68 (Acris, Germany) (1:200) for 2 h before incubating with secondary goat anti-rabbit Cy-3 conjugated antibody (1:200). Subsequent steps are the same as described in section 2.4.6.

2.5.11 miRNA isolation from lung tissue for miRNA PCR array

Total miRNA was isolated from the rat lung tissues by using the TRIZOL reagent (Invitrogen) and Qiagen miRNA extraction kit according to the manufacturer's instructions. Lung tissues were first homogenized before mixing with chloroform. Centrifugation was performed to extract the aqueous phase separated followed by

addition of 100% ethanol. Samples were washed and total mRNA together with small RNA were eluted with RNAse free water.

Inflammatory Response and Autoimmunity miRNA PCR Array (SA Bioscience), which comprises of 84 miRNAs that regulate the expression of pro-inflammatory or anti-inflammatory genes (prediction) was used. A set of controls present on this array were used as calibrator and data analysis was done using the $_{\Delta\Delta}$CT method of relative quantification. The expression of a focused panel of miRNAs predicted to regulate inflammatory and autoimmune response genes were analyzed with this array. The control group served as the calibrator, and the average value of calibrator was used against treated groups and the results were expressed as a fold difference. The water-only group (control) was used as the normalizer.

2.5.12 qRT-PCR

Rat lung tissues were weighted, approximately 30 mg, before mixing with 350 µl of TRIZOL lysis reagent. The tissues were homogenized on ice and spun at high speed before removing the pellet. The supernatant, which contains RNA, was added with equal volume of ethanol before processing the same way as described in section 2.3.13 for RNA extraction and qRT-PCR. Table 2.2 is a list of all the primers used for qRT-PCR of the genes of interest in the lung tissues.

Table 2.2: List of primers and their sequences used for qRT-PCR for *in vivo* specimen.

Gene	*Forward sequence*	*Reverse sequence*
Rat *PROS1*	CCTTTCCTTGGACCTTGACA	TCACGAAGTGCAATCAGGAG
Rat *Tissue Factor*	GCTCAATGCCTTCTCTCAGG	CACCACTTGTAGCTCGGTGA
Rat *SERPINE1*	GACAATATGTGCCCTGTGATTGTC	AGGCTGCTCTACTGGTCCTTGC

2.6 HumanTissueScan™ qPCR Array

TissueScan Human Normal (48 Tissues) qPCR array (OriGene, MD) consisting of pre-normalized cDNA from 48 human normal tissues was selected. In brief, the array plate was thawed to room temperature. A pre-mix of SYBR® Green dye and *PROS1* primer was prepared and added into each well as instructed by manufacturer's protocol. The plate was sealed tightly and let stand on ice for 15 min. The sequence for *PROS1* primers used were forward 5'- CCTAGTGCTTCCCGTCTCAG-3'; reverse 5'-TTTCCGGGTCATTTTCAAAG-3'. Real-time detection of *PROS1* gene expression using Applied Biosystems 7500 Real-Time PCR System (Applied Biosystems) was performed. The thermocycling conditions used were: 95^{o}C for 15 min for one cycle, followed by 40 cycles of 94^{o}C for 15 sec, 60^{o}C for 30 sec and 72^{o}C for 60 sec.

2.7 Statistical analysis

Statistical calculations were performed using the Graph Pad Prism Version 5.0 (GraphPad Software, USA). Data was presented as mean values ± standard error of the mean (SEM) from triplicates (n=3). Student's t-test was used to analyze differences between two groups; while One Way ANOVA with post hoc test (Tukey's Multiple Comparison Test) was used if there were three or more groups of data involved for comparison. *$p<0.05$; **$p<0.01$ and ***$p<0.001$ were considered as statistically significant.

Chapter 3

Results

3 RESULTS

3.1 Characterization of AuNPs

TEM was used to examine the morphology and size of as-synthesized AuNPs. TEM images of AuNPs showed that AuNPs were well dispersed, well defined and spherical in shape (Fig 3.1A) with an average size distribution of about 20 nm. AuNPs size distribution was analyzed using DLS, which provided size information in aqueous medium (Fig 3.1A inset; Fig 3.1C), and the data was plotted and displayed as % of intensity (Fig 3.1C). The mean hydrodynamic radius measured for spherical AuNPs was 20.15 nm in solution, which is in agreement with the TEM observation. The size of AuNPs increased from 20.15 nm to 44.69 nm (Fig 3.1C cf D), and the zeta potential changed from -28.5± 0.21 mV to -24.6±0.3 mV (Fig 3.1E cf F) (due to citrate-ion capping), after coating with FBS. UV–vis spectroscopy was used to examine the optical absorbance spectra of AuNPs. UV-Vis absorption spectra of AuNPs showed absorption peak at 525 nm (Fig 3.1B).

NPs were provided as a 2 nM colloidal suspension and concentrated and reconstituted to obtain a final concentration 10 nM (486.5 µg/ml). Actual concentrations of AuNPs were determined ICPMS after acid digestion of sample aliquots. Suspensions of FBS-coated AuNPs constituted in biological media were freshly prepared prior use. After optimization, 1 nM of AuNPs was selected as the main concentration used in treating the cells for further experimentation since this dose had been used in previous studies by members of the same laboratory (Li et al., 2008; Li et al., 2010a; Li et al., 2011a). The 1 nM AuNP concentration used in this study is equivalent to 48.65 µg/ml and falls within the range of AuNP concentrations that are utilized for nanotoxicity studies (as summarized in the review by (Khlebtsov and Dykman, 2011).

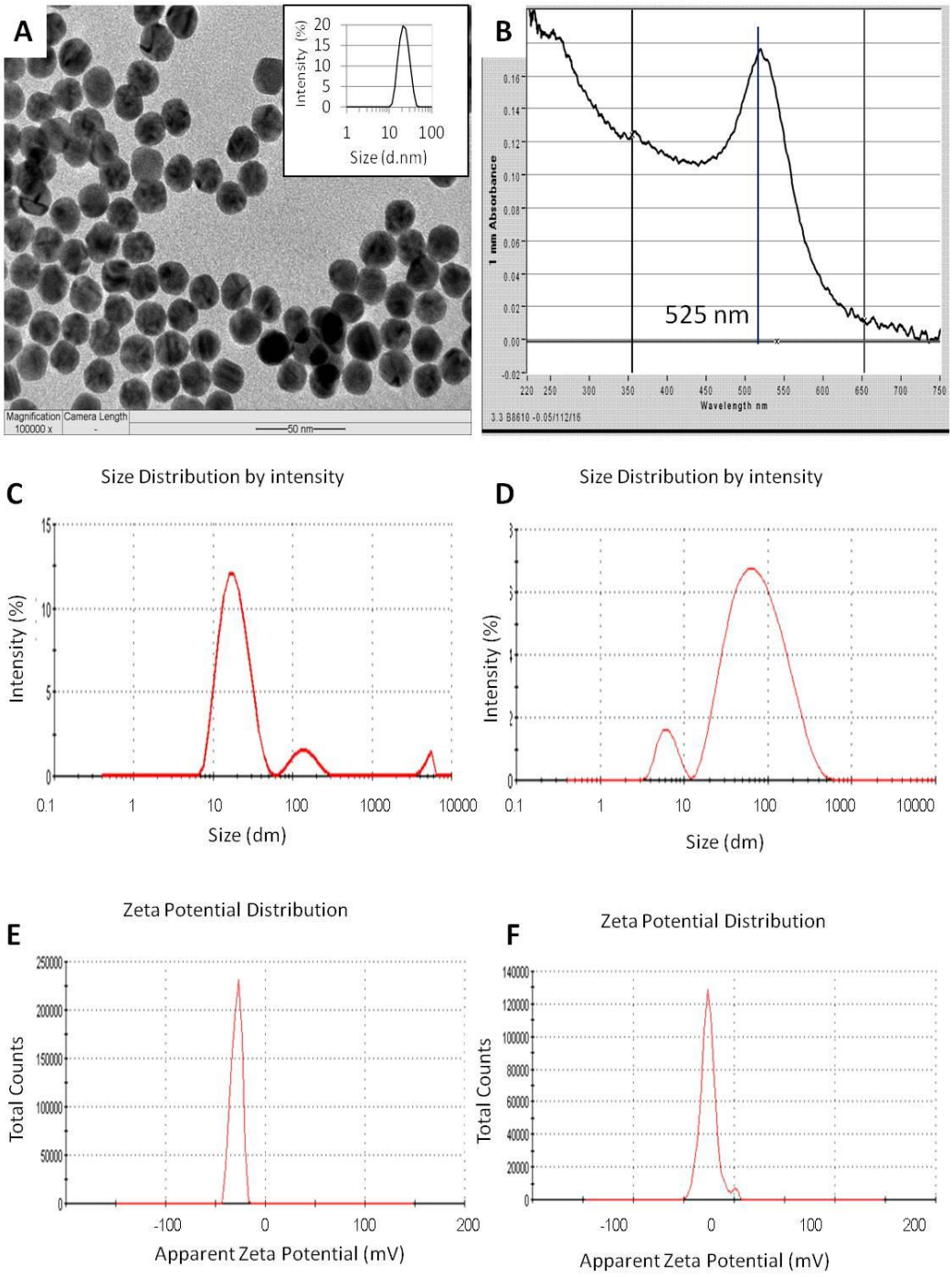

Figure 3.1: Characterization of AuNPs. (A) Representative TEM micrograph of as-synthesized AuNPs (with inset showing size distribution of AuNPs from DLS). AuNPs were synthesized by Turkevich method but modified to obtain a 20 nm size. (B) UV-vis of the as-prepared AuNPs revealed an absorption peak at 525 nm. (C) DLS Z-average measurements showed the AuNPs were approximately 20.15 nm and (D) 44.69 nm (after coated with FBS) in diameter in solution. (E) Zeta potential of AuNPs and (F) FBS-coated AuNPs were -28.9 mV and -25.2 mV respectively.

3.2 Biological effects of AuNPs in SAECs

3.2.1 Uptake of AuNPs into SAECs

(A) LM and AMG study

Internalization of AuNPs did not cause significant morphological changes in SAECs. Aggregates of AuNPs were visualized as bright blue spots under LM (Fig 3.2B cf A). AuNPs were clearly seen after AMG enhancement due to silver ion deposition on AuNPs. Deposition of AMG grains in AuNP-exposed SAECs was clearly visible under LM (Fig 3.2D), in contrast to unexposed SAECs which showed clear cytoplasm (Fig 3.2C).

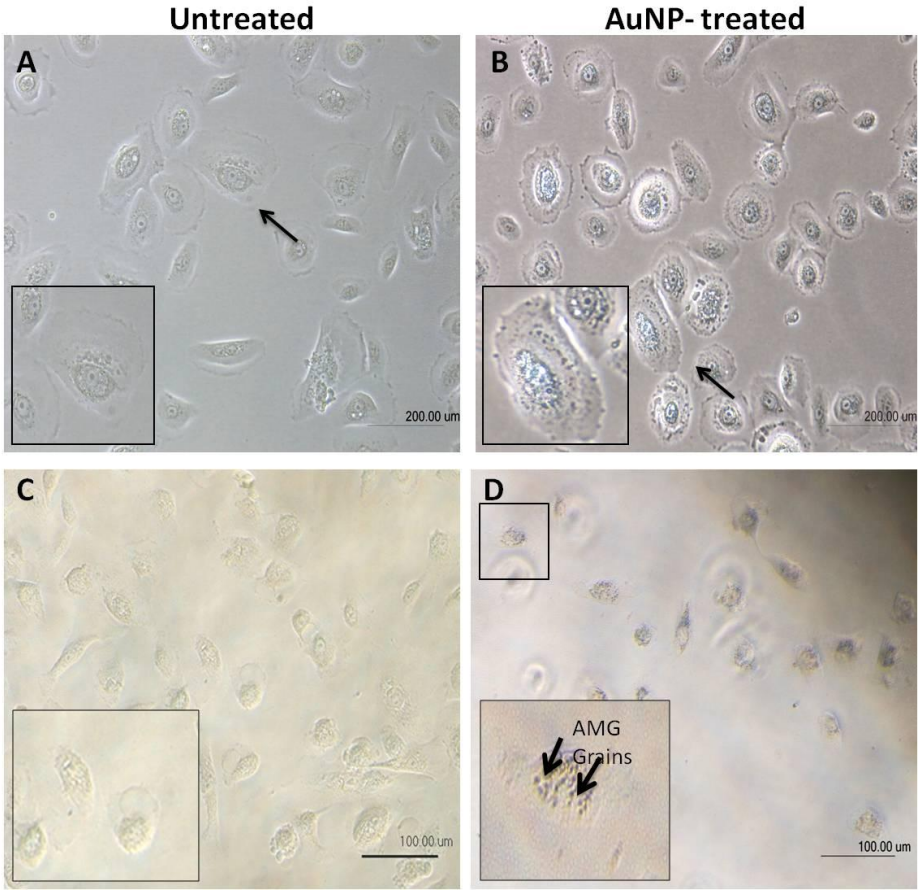

Figure 3.2: AuNP-untreated and AuNP-treated SAECs as observed using LM and AMG. (A) AuNP-untreated SAECs. Scale bar: 200 µm. (B) Micrograph of AuNP-treated SAECs showing appearance of AuNPs as bright blue spots (aggregates of particles). Scale bar: 200 µm. (C) AuNP-untreated SAECs after AMG showed clear cytoplasm. Scale bar: 100 µm. (D) Formation of AMG grains (arrows) as detected using silver enhancement kit. AMG grains were spotted at cytoplasm. Scale bar: 100 µm. Inset shows cells at higher magnification.

(B) TEM-EDX Analysis

Internalization of AuNPs into SAECs was verified using both conventional TEM and FIB-SEM. Under conventional TEM, AuNPs were observed to be taken up by SAECs and localized mainly as clusters inside vesicles in the cytoplasm, but not in the nucleus (Fig 3.3B cf A). Electron dense AuNPs, appearing as black clusters, were found to be enclosed within vesicle-liked structures (arrow). There were no free AuNPs present in the cytosol or the nucleus. Using EDX analysis, presence of AuNPs was confirmed as readings from the M and L shells of Au with a P/B ratio of 6.57 and 59.8 respectively (Fig 3.3C) were detected. Besides, Cu was detected as the specimen was mounted on a Cu grid; while presence of Os was due to the osmification process that was introduced during specimen preparation.

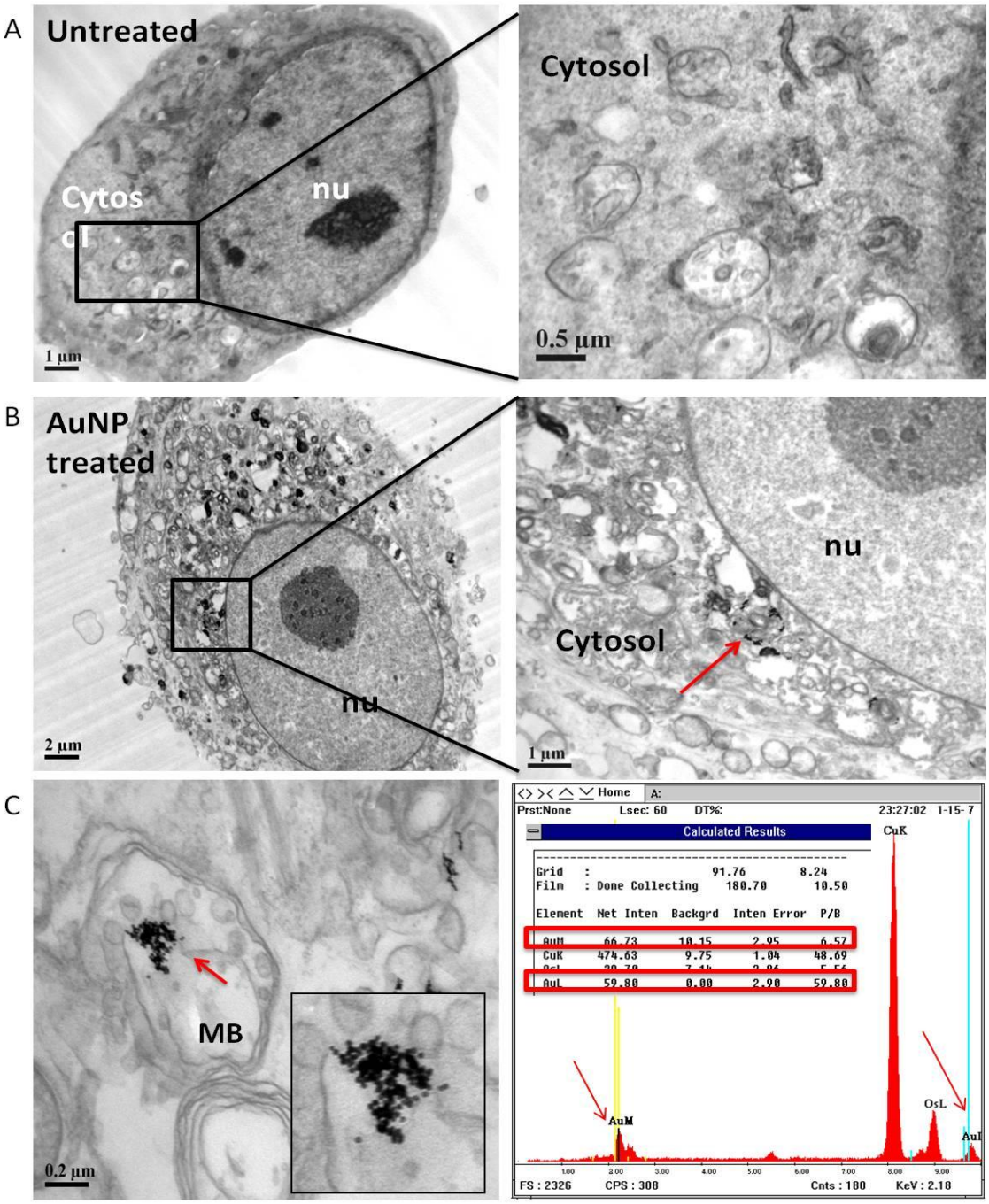

MB: Multivesicular bodies

Figure 3.3: Subcellular morphology and AuNP localization in SAECs observed after 1 nM AuNP treatment for 72 h. (A) Micrograph shows the negative control of SAECs without any AuNPs. Scale bar: 1 µm; inset: 0.5 µm. (B) AuNPs were taken up by SAECs (red arrow) and localized predominantly at cytoplasm, with some enclosed within the endosomes. Scale bar: 2 µm; inset: 1 µm. (C) Micrograph shows AuNPs localized in the endosomes of SAECs as electron dense black clusters. These clusters were verified to be Au using EDX analysis which showed the presence of Au M shell (2.2 KeV) and L shell (9.7 KeV). Scale bar: 0.2 µm.

(C) FIB-SEM, elemental mapping, STEM-EDS and nanotomography

The FIB-SEM was also used to verfy the uptake of AuNPs in SAECs. To identify the initial location of internalized AuNPs in SAECs, SEM was first used to locate a suitable region on the block for FIB-SEM. The milling window size or imaging face (square) was set at width of 20 µm and height of 10 µm and subsequently cut with a gallium ion beam. Figure 3.4A illustrates the set up and pre-selection of a region to be focused later at magnification of 3.98k. Subsequently, the milling process was continued till a smooth imaging face was obtained. Figure 3.4B shows an overview image of a part of SAEC at magnification of 10k with visible structural details obtained using an Energy selective Backscattered (EsB) detector operated at low voltage (1.5 keV) for backscattered imaging. Micrographs were taken from the milled sections of the same area and same specimen of araldite embedded SAECs which had been incubated with AuNPs.

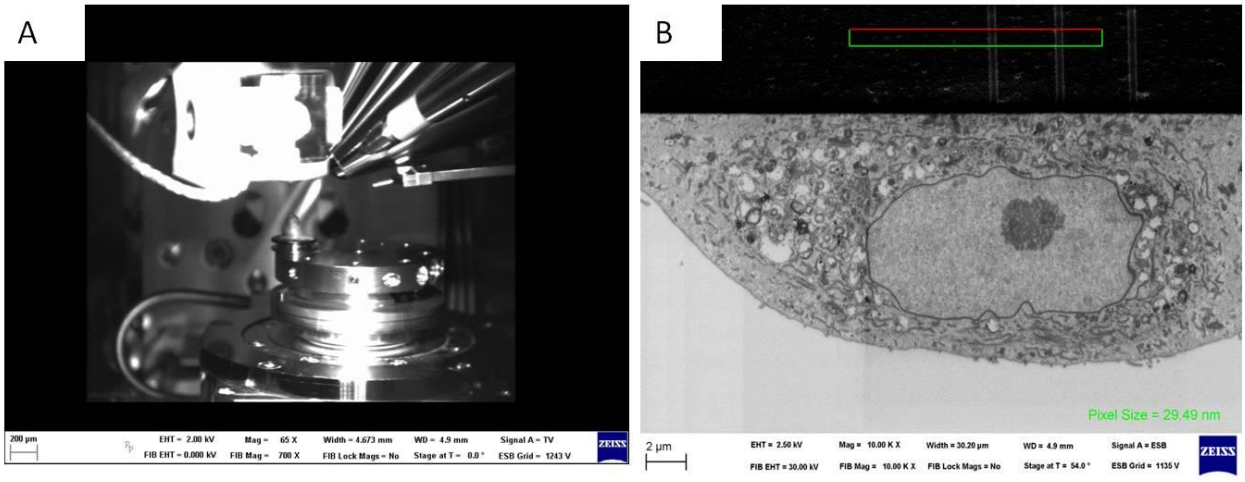

Figure 3.4: Micrographs on FIB-SEM set up and area selection. (A) Milling chamber which consists of sample holder, gallium ion beam and electron beam were used for milling and imaging purpose. Scale bar: 200 µm. (B) SEM was used to survey the area of interest for milling and imaging at higher magnification and resolution subsequently. Scale bar: 2 µm.

A BSE image of SAECs shows ultrastructural details such as a double membrane nucleus and nucleolus, and cytoplasmic organelles that include endoplasmic reticulum, lysosomes and endosomes (Fig 3.5A). Heavy elements such as AuNPs and osmium-incorporated plasma membrane appear bright under BSE detector. The milled and raw image as shown in Fig 3.5B was then subjected to contrast reversal. Fig 3.5C shows the AuNP clusters observed as dark deposits in the in contrast-inverted FIB-SEM image of back-scattered electrons, rendering them easily recognizable.

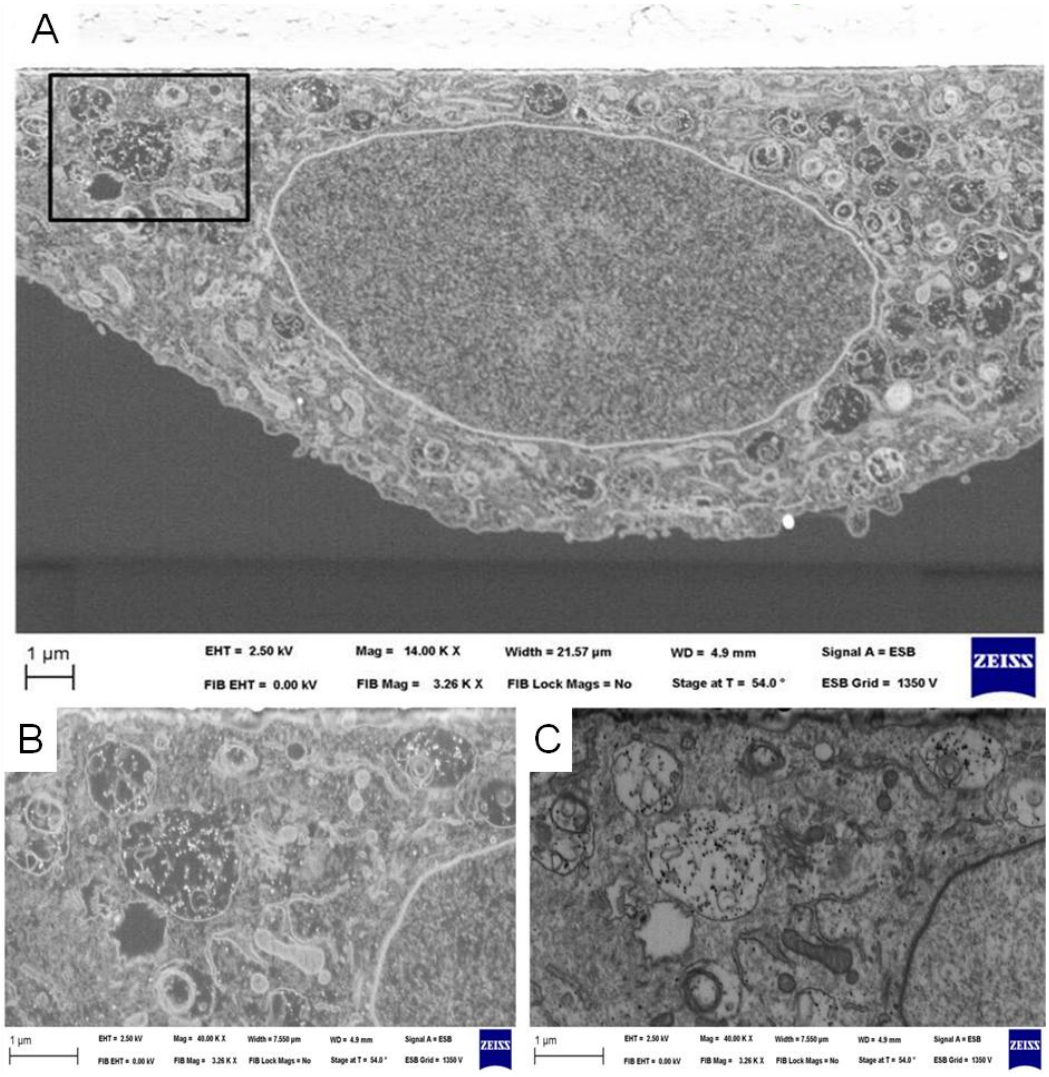

Fig 3.5: FIB-SEM images of AuNP-treated SAECs. (A) Micrograph shows AuNP aggregates localized in the endosomes of SAECs. Scale bar: 1 µm. (B) Micrograph shows the enlarged image of the boxed area in (A) as recorded by the EsB detector, with AuNPs appearing as bright spots. Scale bar: 1 µm. (C) Inverted contrast of image (B) with the same resolution as conventional bright field TEM image. Scale bar: 1 µm.

Element distribution mapping of the electron dense deposits was performed using EDX and the elemental distribution within endosomes was generated based on digital information from an electron detector. AuNPs were represented on the EDX map as red dots (Fig 3.6A). These were performed with a Zeiss Libra 120 Plus Energy Filter TEM. Elemental distribution mapping was calculated using Energy Spectroscopic Imaging (ESI) with 3-window power law method. Figure 3.6B shows the selected area in SAECs with large cluster of AuNPs found within vesicles. Using elemental analysis STEM-EDS coupled with EDAX Octane Plus software, presence of Au in SAECs was confirmed as depicted by the presence of Au M shell (Fig 3.6C, D). Besides, presence of carbon throughout the section suggested the organic nature of the cells (Fig 3.6D).

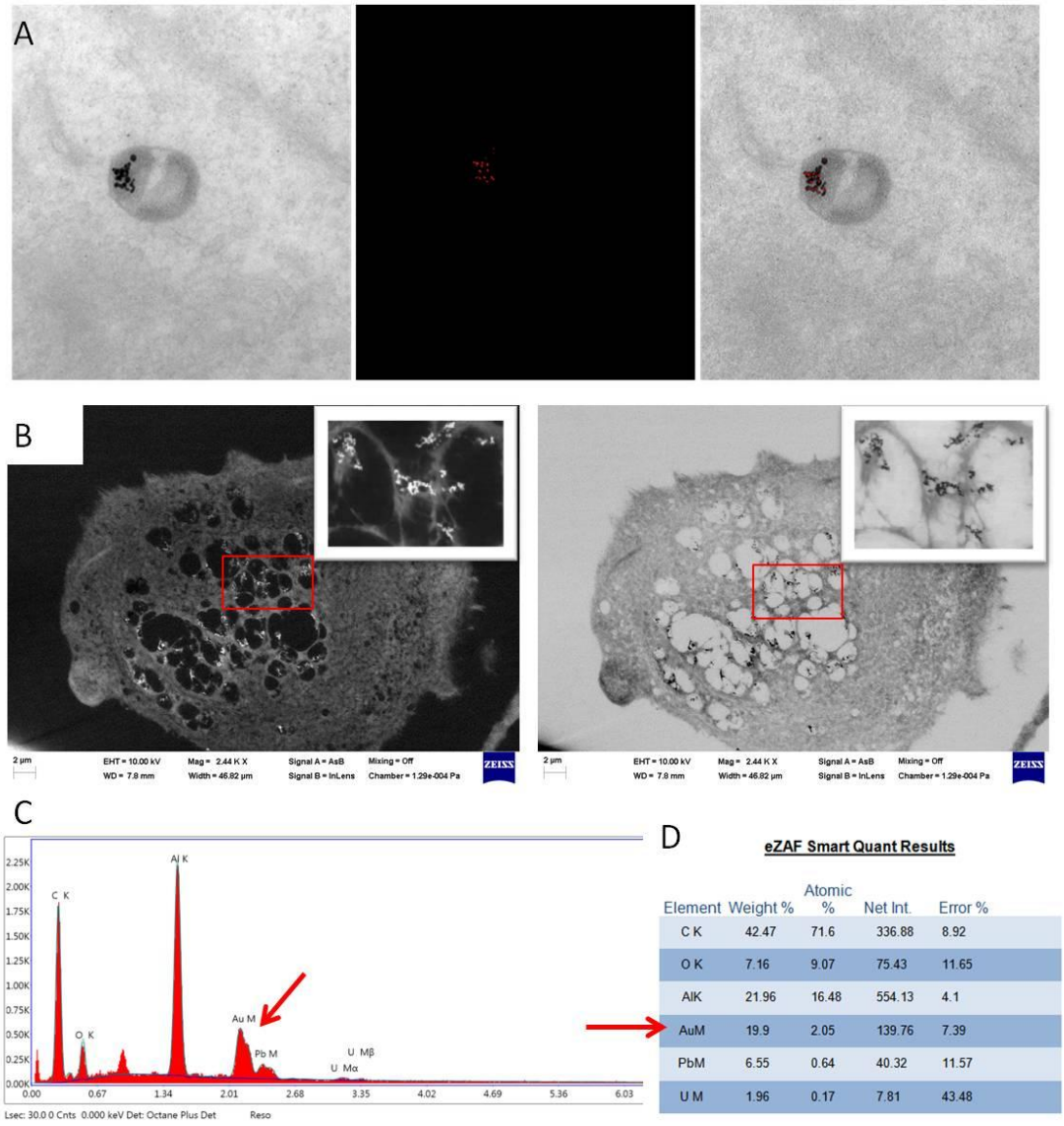

Figure 3.6: Elemental identification of Au and STEM-EDS analysis. (A) Elemental distribution after background substraction is shown for Au (left image), elemental net distribution is presented in red (middle image) and overlay (right image). (B) The contours of the embedded cells are visible and presence of AuNPs was rendered as bright spots (boxed area) as captured by BSE (left). Contrast reversal was performed from raw FIB-SEM image (right). Scale bar: 2 µm. (C) EDX spectrum shows the presence of Au in SAECs using Zeiss Libra 120 Plus Energy Filter TEM. (D) EDS shows the presence of Au in SAECs as a sharp peak at 2.121 keV (red arrows).

3D imaging of AuNPs inside the cells followed by 3D reconstruction for nanotomography was performed (Fig 3.7). A video of the 3D reconstruction is included in the Appendix.

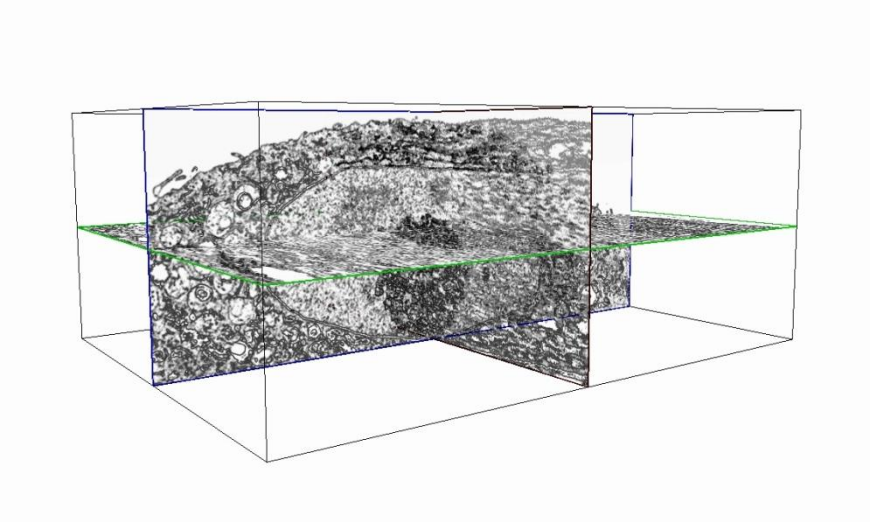

Figure 3.7: 3D Nanotomography using FIB-SEM for visualizing the 3D architecture of AuNPs in SAECs with sequential milling and imaging.

3.2.2 AuNPs induced oxidative stress in SAECs

(A) LPO assay

LPO is an established marker of oxidative stress. There was an increase of the LPO content after 72 h treatment as observed in 1 nM AuNP treated SAECs compared with control (Fig 3.8A). This provides evidence that AuNPs were able to induce oxidative stress in SAECs. Besides, transient transfection of luciferase reporter plasmid containing the transcriptor factor Nrf2/Nrf1, a well-known transcription factor for oxidative stress, showed a significant increase in their activity triggered by AuNPs in SAECs (Fig 3.8B).

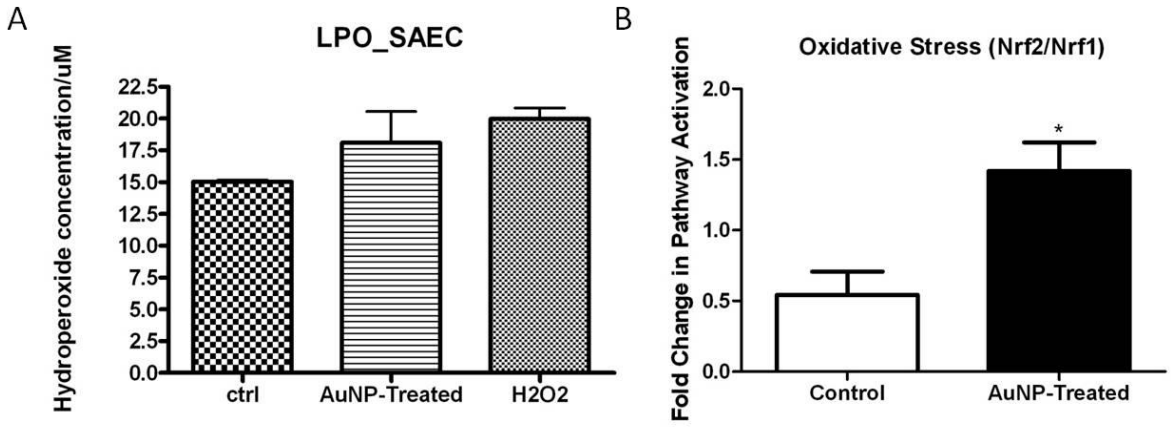

Figure 3.8: Studies on oxidative stress induced by AuNPs in SAECs. (A) Lipid peroxidative stress in SAECs following exposure to AuNPs. A higher level of LPOs was observed in AuNP-treated SAECs when compared with control cells. H_2O_2 treatment served as positive control. (B) Transient transfection studies utilizing Nrf2/Nrf1-regulated luciferase reporter demonstrated an increase their activity following AuNP treatment of the SAECs. All the experiments were conducted in triplicates. Error bars=SEM; *p< 0.05.

(B) MT anti-oxidant gene screening

As oxidative stress was induced after AuNP treatment in SAECs, gene expression of *Metallothioneins* (*MTs*), which are known antioxidants and free radical scavengers (Inoue et al., 2009) was investigated. The expression of functional *MT-1* and *MT-2* gene isoforms was assessed in SAECs (Fig 3.9A). In agreement with previous publication, *MT-1A, MT-1E, MT-1X* and *MT-2A* were found to be the most abundantly expressed isoforms in SAECs. There was a significant decrease in *MT-1A* expression in AuNP-treated SAECs in comparison with untreated cells (Fig 3.9B). *MT-1E, MT-1X* and *MT-2A* gene expression showed no significant changes, although a general down-regulated trend was observed (Fig 3.9 C-E).

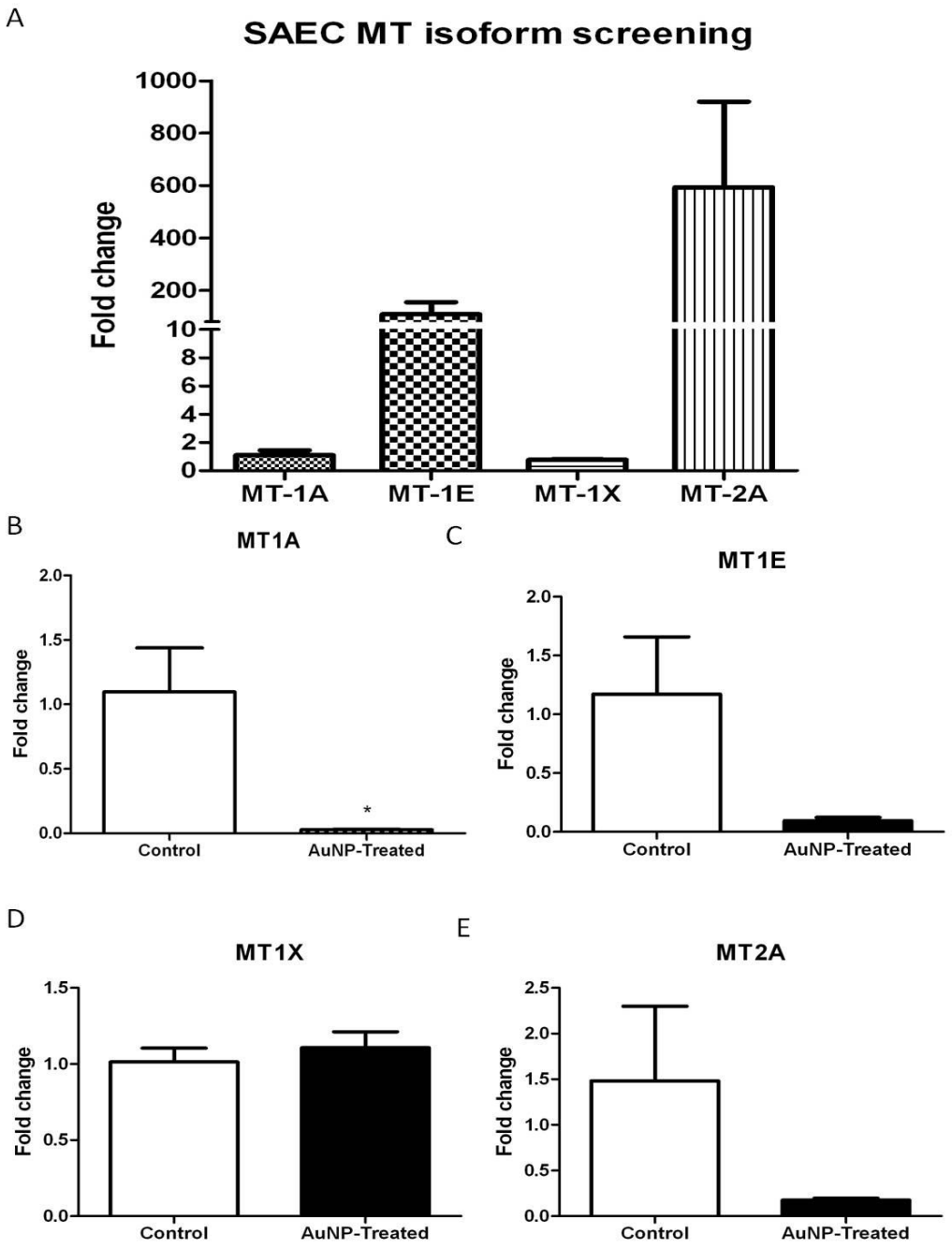

Figure 3.9: MT expression in untreated and AuNP-treated SAECs. (A) Bar chart of MT isoforms that were present endogenously in SAECs. (B) Significant difference in fold change of the MT-1A gene in SAECs was observed after treatment with 1 nM AuNPs. No significant gene expression changes observed in (C) MT-1E, (D) MT-1X and (E) MT-2A after treated with AuNPs in SAECs. Error bars=SEM; *p <0.05.

(C) Screening of other anti-oxidant genes

Next, the transcripts of 8 genes (*CAT, GPX1, GPX2, SOD1, SOD2, SOD3, Prx1, Prx3*) which are involved in anti-oxidative response were examined in SAECs after exposure to 1 nM of AuNPs for 72 h. There was a general upward trend in the expression of anti-oxidant genes (Fig 3.10), although it was not significantly different from control SAECs.

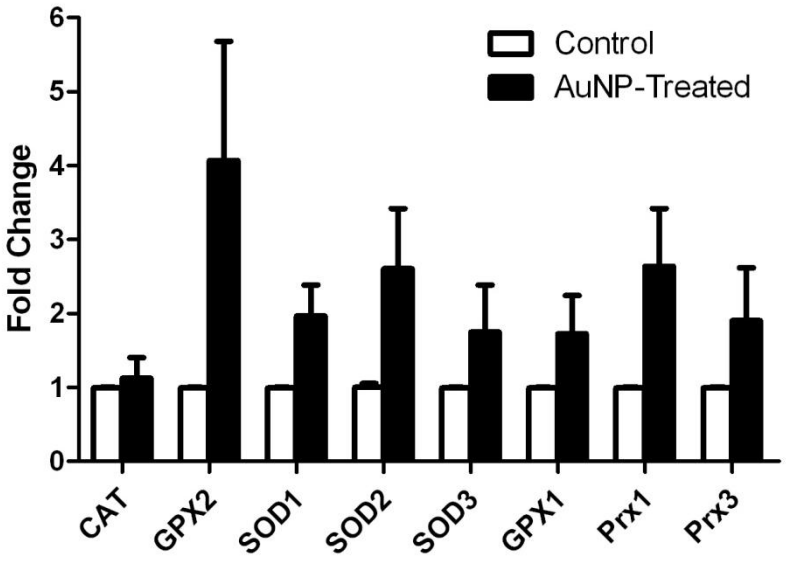

Figure 3.10: Fold change of 8 selected anti-oxidant genes on AuNP exposed SAECs compared with AuNP-unexposed SAECs. Error bars=SEM.

3.2.3 Cytotoxicity of AuNPs

3.2.3.1 Cell viability assessment of AuNP-treated SAECs

(A) LDH assay

As compared with MRC5 fibroblasts, SAECs were more vulnerable towards AuNP treatment. At all tested time points of 24, 48 and 72 h, 1 nM AuNPs caused a significant release of LDH at all concentration tested in SAECs (Fig 3.11A-C).

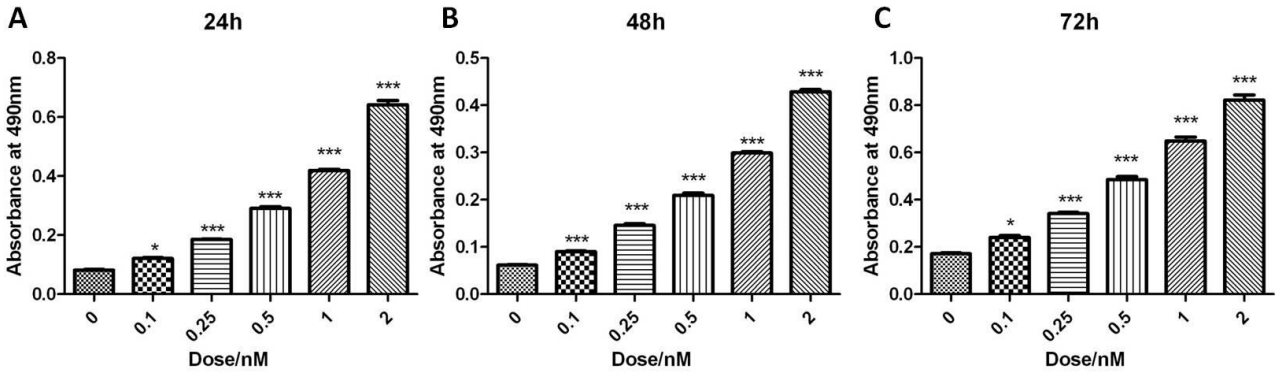

Figure 3.11: LDH assay was used to determine cytotoxicity of SAECs treated with a range of dose with AuNPs. (A) At 24 h, (B) 48 h and (C) 72 h, SAECs showed significant release of LDH into the culture media, as an indicator of cellular membrane disruption at all ranges of tested AuNP concentration. All the experiments were conducted in triplicates. Error bars= SEM; *p<0.05; **p<0.01; ***p<0.001.

(B) Trypan blue assay

Cell viability was significantly decreased as early as 24 h after treatment with 2 nM AuNPs (Fig 3.12D), and persisted after 48 h and 72 h (Fig 3.12E, F) AuNP treatment at the same concentration. There was a decrease of 24.25%, 18.25% and 20.5% in cell viability between the untreated control SAECs and 2 nM AuNP treated SAECs at 24 h, 48 h and 72 h respectively. In conjunction with these observations, total cell count showed a general downward trend as the cell proliferation rate was affected due to the increase in cell death (Fig 3.12A-C). Significant decrease of total cell count was observed when SAECs treated with 2 nM AuNPs, which is in agreement with cell viability data.

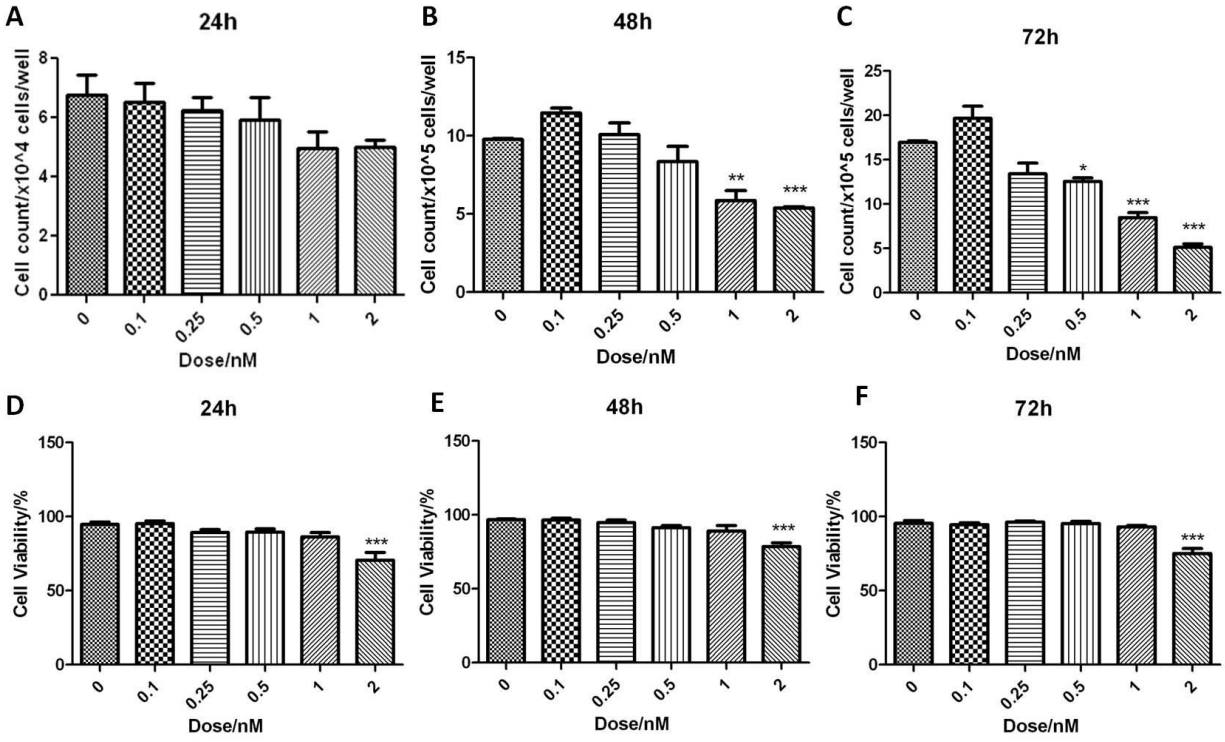

Figure 3.12: Viability of SAECs was determined by 0.4% Trypan blue dye exclusion assay following 24 h, 48 h and 72 h AuNP exposure. (A) Total cell count was decreased when treated with AuNPs at 24 h and was significantly decreased at (B) 48h of 1 nM and 2 nM AuNPs. (C) Total cell count was decreased as low as at 0.5 nM AuNPs. (D-F) Graphical representations of % of cell viability at 24 h, 48 h and 72 h of AuNPs. SAECs showed significant decrease in cell viability when treated with 2 nM of AuNPs. All the experiments were conducted in triplicates. Error bars=SEM; *p < 0.05; **p<0.01; ***p<0.001.

(C) AO/ EtBr staining

Microscopic examination of SAECs was performed to examine the nuclear changes and formation of apoptotic bodies during AuNP-induced cytotoxicity. SAECs were examined after staining using AO/ EtBr, which showed membrane blebbing (indicated by arrows) under a fluorescence microscope. In agreement with the LDH results, AuNP treated SAECs which have lost their membrane integrity were readily stained with EtBr. Live SAECs appeared uniformly green, while dead SAECs (in red) showed formation of blebs, cell shrinkage and condensed nuclei, indicating late apoptosis (Fig 3.13).

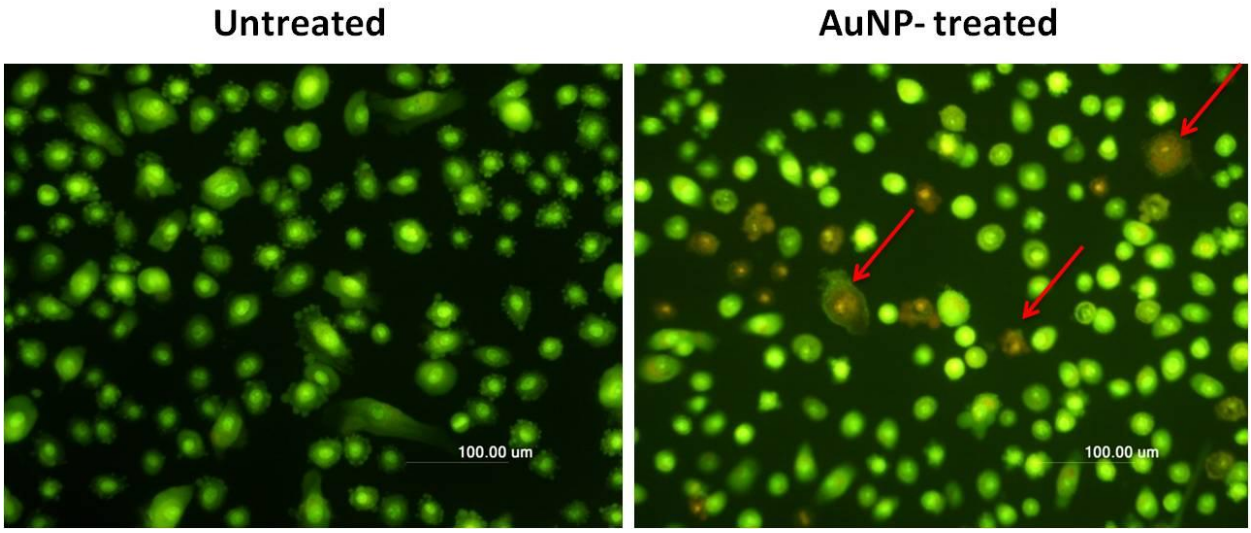

Figure 3.13: Morphologic observation with acridine orange/ethidium bromide (AO/EB) staining. (A) SAECs were treated without AuNPs showed uniform green staining which indicates viable cells. Scale bar: 100 µm. (B) Bright red color staining (arrows) indicates apoptosis after treatment with AuNPs in SAECs. Scale bar: 100 µm.

(D) Cell cycle analysis

Cell cycle analysis showed a significant decrease in the S+G2/M phase in 48 h 1 nM AuNPs treated SAECs (Fig 3.14A). Ten cell cycle related genes were chosen and cell cycle gene transcription analysis revealed a significant down-regulation in the expression of *CDKN2a*, an important gene regulating cell cycle checkpoint and cell cycle arrest (Fig 3.14B).

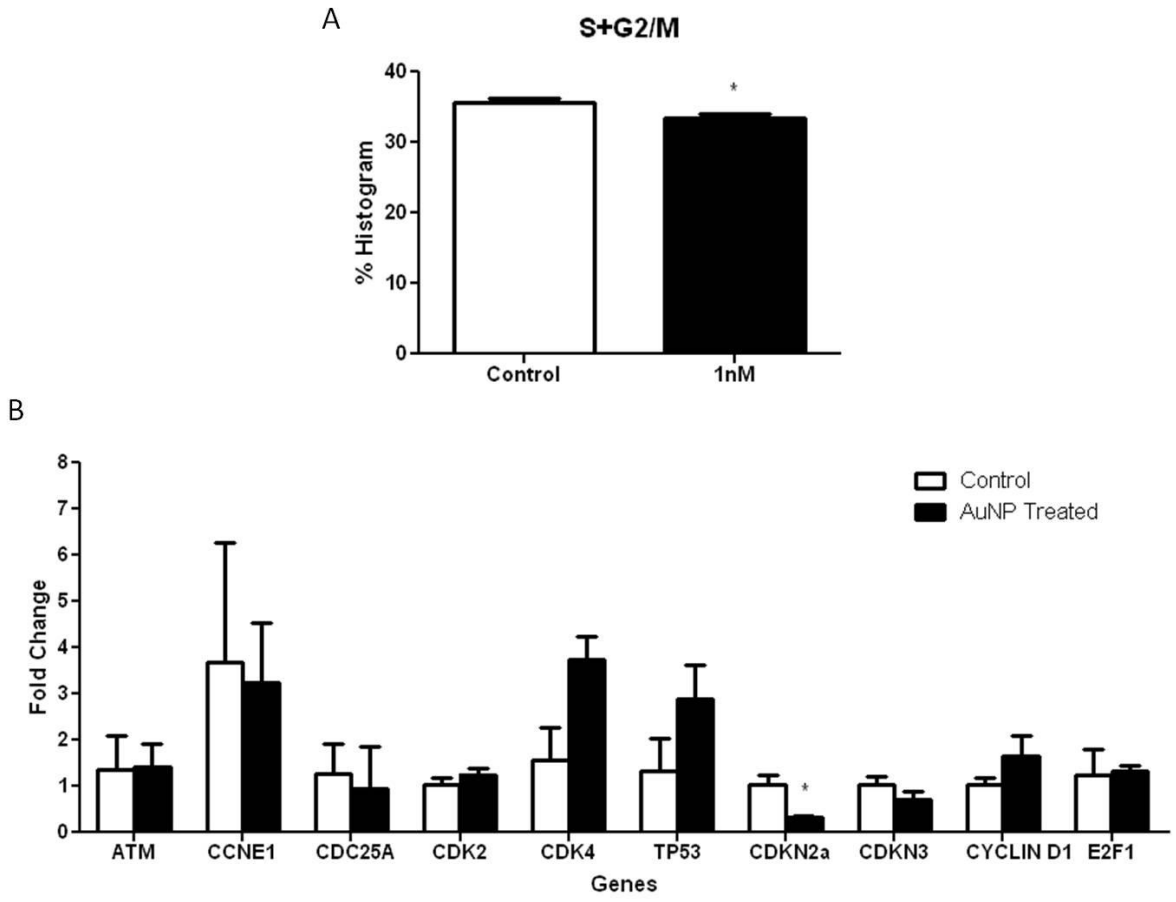

Figure 3.14: Cell proliferation and related genes studies after AuNP treatment in SAECs. (A) Cell cycle analysis shows a significant decrease in total S and G2/M phase of cell cycle, indicates a decrease in cell proliferation rate after treated with 1 nM of AuNPs for 48 h. (B) Decreased in cell proliferation was accompanied by a decrease in *CDKN2a* gene expression level, an important regulator of cell cycle checkpoint and cell cycle arrest. All the experiments were conducted in triplicates. Error bars=SEM; *$p < 0.05$

.

3.2.4 Genotoxicity induced by AuNPs in SAECs

The Comet assay revealed heightened oxidative stress-induced DNA fragmentation after 72 h AuNP exposure. Tail moment, which refers to the percentage of DNA present in the tail multiplied by the length between the center part of head and tail, was significantly greater in 1 nM AuNP-treated SAECs, indicating that a larger extent of DNA fragmentation incurred in AuNP-treated cells (Fig 3.15A). Next, the transcripts of 10 genes (*APEX2, ATM, ATRX, BTG2, ERCC2, LIG1, RPA1, XPC, XPA and XRCC1*) which are involved in DNA repair were examined in SAECs after exposure to 1 nM of AuNPs for 72 h. *Xeroderma pigmentosum (XPA)* gene was found to be significantly up-regulated with AuNP treatment (Fig 3.15B).

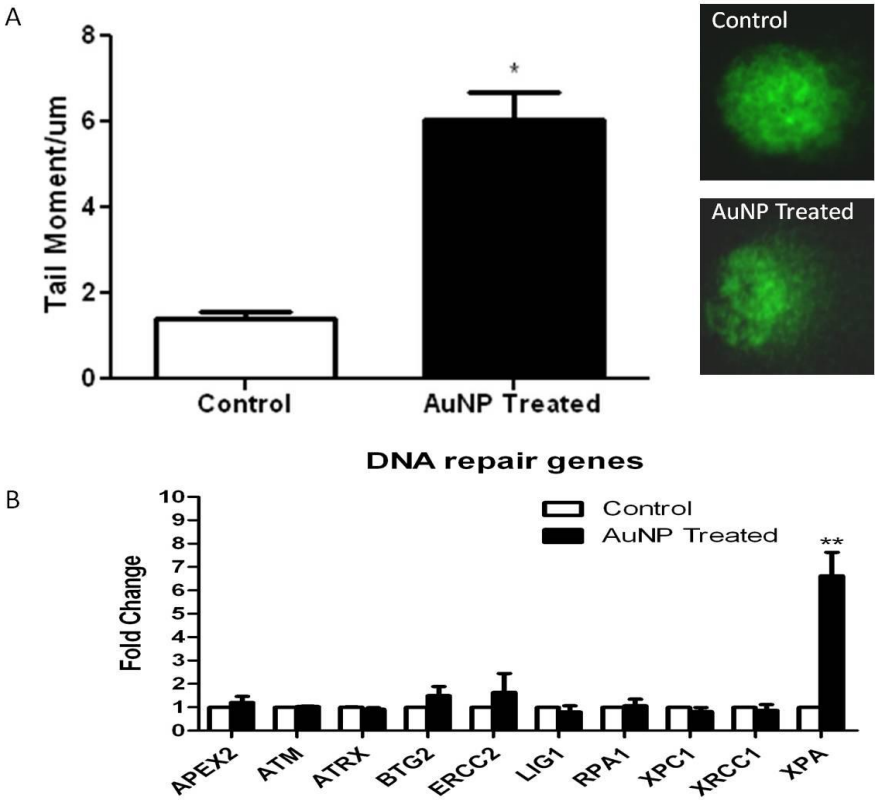

Figure 3.15: Genotoxic effects in AuNP-treated SAECs. (A) Comet assay of SAECs treated with 1nM AuNPs at 72 h and subsequently run on alkaline electrophoresis and stained in SYBR green which visualizes the comet "tail", the length of which is an indicator of DNA damage. Analysis of 100 cells per treatment was performed. Control cells (upper right insert) showed little to no tail. AuNP-treated cells (bottom right insert) displayed a comparatively longer tail, indicative of the presence of higher DNA damage. (B) qRT-PCR revealed an increase in the fold change of *XPA* gene expression level after treated with AuNPs in SAECs. Experiments were done in triplicates. Error bars = SEM; *p <0.05; **p < 0.01.

3.2.5 Microarray analysis of AuNP-treated SAECs

The quality of RNA samples was determined before sending for micro array analysis. The A260/A280 ratio of RNA samples that were sent for analysis were measured by spectrophotometry. The OD260/OD280 ratios of the 6 samples were found to be between 1.9 – 2.21, and concentrations ranged from ~130 ng/µl to ~323 ng/µl (Fig 3.16A). The good quality of the total RNA isolated were also verified by gel electrophoresis (Fig 3.16B). The RNA integrity values or RNA integrity Number (RIN) ranged from 9.1 to 10. 100 ng total RNA from each sample was used for transcriptomic analysis (Fig 3.16C).

A

Samples	OD 260nm	OD 280nm	Ratio 260/280	Concentration ng/ul	RIN
Control1	0.0804	0.0394	2.034	322.75	9.7
Control2	0.0304	0.0144	1.956	130.86	9.1
Control3	0.0754	0.0367	2.039	303.71	9.8
AuNP-Treated 1	0.0725	0.0352	2.044	292.48	10
AuNP-Treated 2	0.0675	0.0336	2	271.48	10
AuNP-Treated 3	0.0431	0.0197	2.027	185.06	10

B

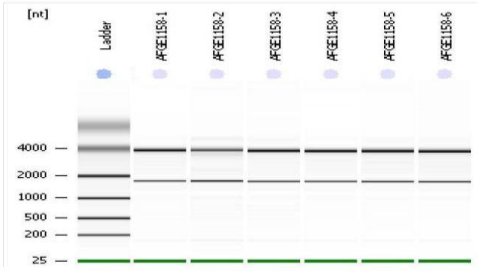

C

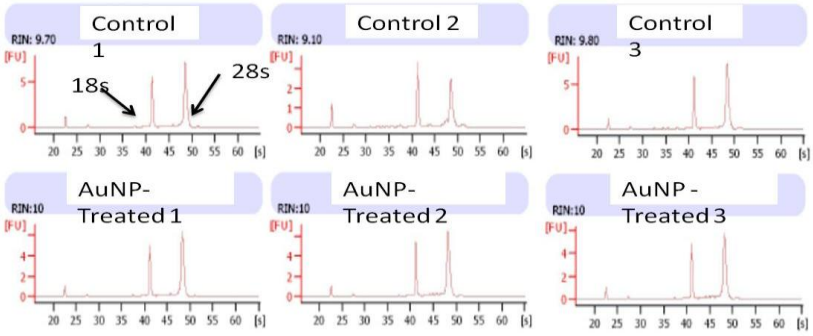

Figure 3.16: Characterization of RNA quality of SAECs for microarray study. (A)The quality of RNA samples was determined. Absorption 260/280 ratio ⩾ 1.8 were used as indicators of acceptable purity. (B) Gel image of RNA samples which showed a band intensity ratio of 28S rRNA (at 4.5kb) to 18S rRNA (at 1.9kb) of 2. (C) Electropherograms of 28S and 18S rRNA with flat baseline and no additional peaks in between indicated an acceptable integrity for mRNA profiling analysis.

The heat map generated using GeneSpring software reflected two distinct clusters. One cluster corresponds to up-regulated genes (red panels), and the other cluster (represented by green panels) depicts those genes which were down-regulated (Fig 3.17A). A volcano plot was generated to compare the transcriptomes of SAECs treated with AuNP versus the cells that were not exposed to the AuNPs (Fig 3.17B). Genes that fulfilled these criteria are represented by the red triangles, while the grey squares represent genes that failed to satisfy these conditions.

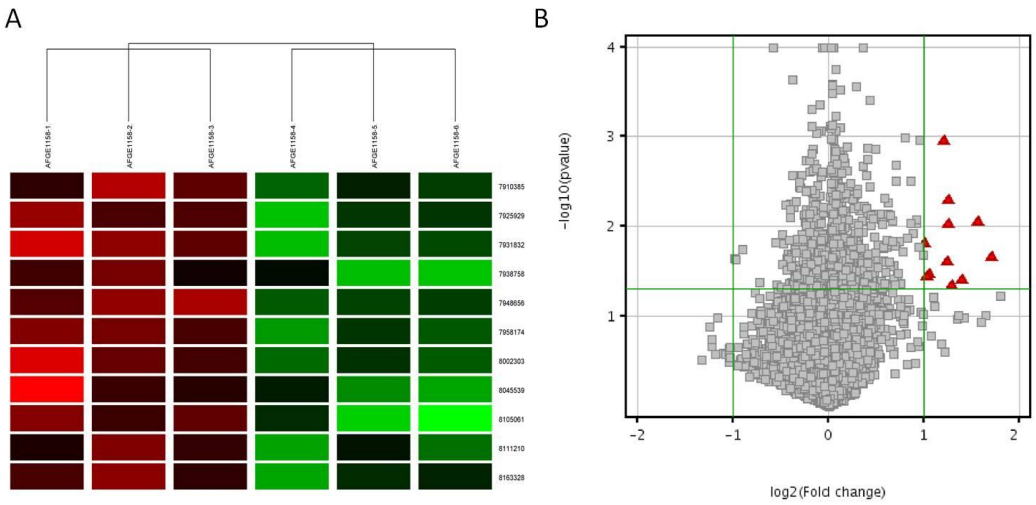

Figure 3.17: (A) Hierarchical clustering for differentially expressed mRNAs in SAECs unexposed vs SAECs exposed to AuNPs and (B) volcano plot (fold-change $\geqslant$1.5).

Differential expression of 42 genes (fold change $\geqslant 1.5$, $p < 0.05$) was observed as compared with AuNP unexposed SAECs. Microarray analyses identified gene expression signature consisting of 40 genes that were up-regulated and 2 genes that were down-regulated (Table 3.1). qRT-PCR was performed and showed a good concordance with microarray data (Fig 3.18). Next, gene ontology analysis was conducted to map genes that were differentially expressed to functional categories using DAVID (Table 3.2). Aberrant genes expressed are related to processes involving the immune system, lipid metabolism, cell homeostasis, stress response, and biological regulation.

Notably, AuNP exposure resulted in increased levels of mRNA for acute phase markers serum amyloid A-1 (*SAA1*) and immune response gene Toll-like receptor 2 (*TLR2*) and interferon gamma receptor 1. Besides, microarray analysis revealed aberrant expression of genes which encode proteins involved in blood coagulation such as serpin peptidase inhibitor, clade E (*SERPINE1*) and also *FYN* binding protein, which is involved in platelet activation. Expression of genes associated with acute phase, inflammation, immune response and impaired regulation of blood coagulation were enriched after 48 h post exposure to AuNPs. The Kyoto Encyclopedia of Genes and Genomes (KEGG) pathways database which was used to identify specific biological pathways associated with the differentially expressed genes, predicted inflammation, complement cascade perturbation and possibly in association with prothrombotic changes. Other affected pathways include biosynthesis of steroids, stress-responsive genes, homeostasis and immune system.

Table 3.1: Differential expression of genes identified from the Affymetrix Human Gene 1.0 ST Array.

Gene symbol	*p-value*	*FC Absolute*	*regulation*
FYB	0.022860235	3.2837753	up
AKR1C2	0.009191448	2.9732397	up
KYNU	0.04031548	2.6664615	up
SAA1	0.04730334	2.4743495	up
NQO1	0.009716617	2.408126	up
TXNRD1	0.005305763	2.3999944	up
AKR1C3	0.025623498	2.390597	up
FTH1	0.001159682	2.3368406	up
PTGR1	0.03761124	2.051098	up
CYP24A1	0.020748194	1.9938025	up
UIMC1	0.022960871	1.9693946	down
PNLIPRP3	0.001092176	1.9500183	up
Serpine1	0.01707216	1.9259968	up
DSC2	0.009166447	1.8937527	up
NTN4	0.011789325	1.8485426	up
NRIP1	0.003064263	1.8251534	up
SH3KBP1	0.009215917	1.8186193	up
TLR2	0.013492571	1.7701886	up
POPDC3	0.001029478	1.7483084	up
TFPI2	0.018800564	1.7164173	up
TLK1	0.042959712	1.6870462	up
AKR1B10	0.014765623	1.6808671	up
ADAM28	0.032992497	1.6552218	up
CDK1|CDC2	0.04141343	1.6473414	down
TM4SF1	0.035336994	1.6408422	up
ERO1L	0.016450878	1.6303246	up
C13orf31	0.002072332	1.6300972	up
UBE2H	0.01624855	1.6162099	up
HTATIP2	0.026787775	1.6044718	up
EPGN	0.038746186	1.60123	up
TACSTD2	0.008609537	1.5931822	up
MTSS1	0.014715695	1.5912739	up
RBP1	0.016130637	1.5851606	up
BVES	0.007454179	1.5648742	up
SEL1L3	0.047575198	1.5641564	up
GPR109A|NIACR1	0.027815467	1.5623207	up
MAP1B	0.024445523	1.5576143	up
DAB2	0.005454687	1.5454847	up
IFNGR1|LOC100131120	0.007339169	1.5366831	up
NRCAM	0.014389291	1.5358087	up
RAI14	0.025009122	1.5215092	up
DSG2	0.032455098	1.5195131	up
IFNGR1	0.004809097	1.5074106	up

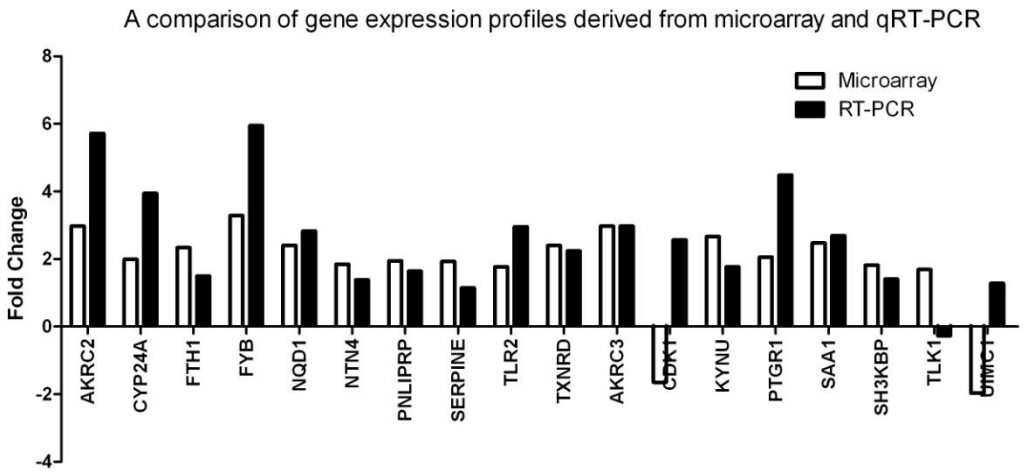

Figure 3.18: Selected gene expression profiles derived from micro-array were verified by q(RT)-PCR which showed a general concordance with microarray data.

Table 3.2: Classification of differentially expressed genes into functional groups using the Database for Annotation, Visualization, and Integrated Discovery (DAVID) software.

Processes	Genes involved
Immune system process	*FYB*
	KYNU
	TLR2
	SAA1
	FTH1
Organic acid, lipid, fatty acid, steroid metabolic process	*AKR1C2*
	AKR1C3
	PTGR1
Response to stress	*SAA1*
	NQO1
Metal ion homeostasis	*FTH1*
	SAA1
Homeostatic process	*TXNRD1*
	FTH1
	SAA1
Response to stimulus	*TLK1*
	UIMC1
	PTGR1
	SAA1
	SERPINE1
	TLR2
	FTH1
	KYNU
	CYP24A1
	FYB
	NQO1
Biological regulation	*NQO1*
	FYB
	CYP24A1
	FTH1
	NRIP1
	SAA1
	SERPINE1
	TXNRD1
	TLK1
	TLR2
	UIMC1
Metabolic process, cellular process	*FYB*
	SH3KBP1
	AKR1C2
	CYP24A1
	FTH1
	KYNU
	NRIP1
	PTGR1
	TXNRD1
	TLK1
	UIMC1

3.2.6 Protein profiling using dimethyl labeling and mass spectrometry analyses

To assess the effects of AuNPs on proteome expression, dimethyl labeling and mass spectrometry on AuNP-treated SAECs were performed. Profiling of proteins between AuNP-treated and untreated SAECs identified 157 differentially expressed proteins, comprising of 82 up-regulated (Table 3.3) and 75 down-regulated proteins (Table 3.4). Among these proteins, 7 proteins were the same as those identified from microarray data with good correlation between the technical replicates (Fig 3.19). Notably, TLR2 protein expression was up-regulated with high ratio of 12. Presence of SAA1 was undetectable using MS.

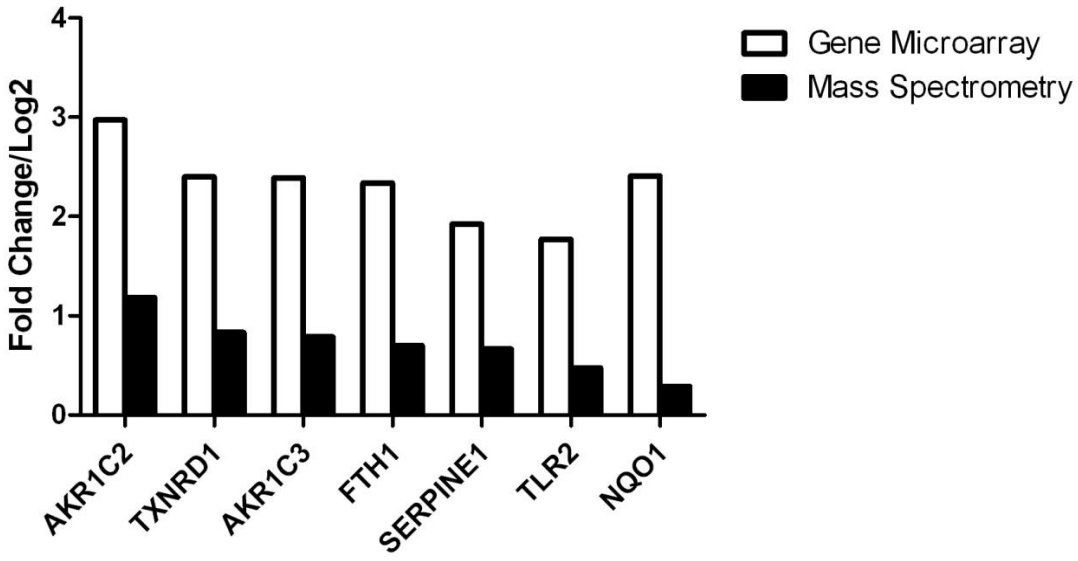

Figure 3.19: Graphical representation shows a good concordance of the 7 overlapping genes/proteins from the gene microarray and mass spectrometry results.

Table 3.3: Up-regulated proteins as quantified by mass spectrometry.

Gene Name	Normalized H/L		Counts
	Forward	Reverse	
AKR1C2	2.2743	0.43243	3
MX1	1.9933	0.47952	11
VDAC3	1.9592	0.5218	9
PODXL	1.9581	0.45725	2
AKR1C1	1.8314	0.56086	26
TXNRD1	1.7807	0.6103	24
AKR1C3;AKR1C4	1.7236	0.70263	8
ACTN1	1.7058	0.59428	80
LCP1	1.679	0.54943	5
HK1	1.678	0.59785	43
HLA-C	1.6706	0.7603	2
IL1A	1.6645	0.77256	5
ACTN4	1.6509	0.58093	34
FTH1	1.6257	0.72765	4
IFIT1	1.6237	0.5283	4
LIPA	1.6232	0.51041	2
AKR1D1	1.5975	0.61471	3
ATP6V0D1	1.59	0.5928	4
SERPINE1	1.5872	0.65773	7
VDAC2	1.5866	0.63935	19
LTBP2	1.5775	0.66815	2
SAMHD1	1.5726	0.70344	4
STAT1	1.5546	0.66881	26
CTSA	1.5522	0.52373	4
FADS2	1.5386	0.50655	2
HEATR7A	1.5123	0.77185	2
NT5E	1.5033	0.61791	9
OAS2	1.4779	0.60354	3
DDX58	1.4753	0.57631	6
HCLS1	1.467	0.68602	8
VDAC1	1.4646	0.654	20
CTSL1;CTSL2;CTSK;CTSL3	1.4556	0.72535	2
C3	1.4534	0.77324	4
HLA-A	1.4528	0.6943	9
GLB1	1.4484	0.59064	2
CCDC56	1.4481	0.81239	3
ICAM1	1.4434	0.62865	16
OAS3	1.4363	0.65464	6
MMP9	1.4293	0.72073	11
ATP6AP2	1.4284	0.68892	2
HIST1H4A	1.4164	0.63119	10
PML	1.416	0.79076	17

IL1B	1.4103	0.70253	5
ANPEP	1.4012	0.75199	33
CORO1C	1.3965	0.70967	14
TLR2	1.391	0.70046	12
HIST1H3A	1.3793	0.77193	2
GCLM	1.3725	0.79589	9
RAB1B;RAB1C	1.3698	0.79192	3
ATP6V0A1	1.3687	0.66258	5
H2AFX	1.3422	0.81385	10
F3	1.3411	0.54824	7
OCIAD2	1.3403	0.8096	12
CYGB	1.3323	0.73613	14
DHRS7	1.3276	0.81053	9
ERAP1	1.3238	0.72575	11
KIAA1279	1.317	0.64104	2
MGST3	1.308	0.69423	5
PSAT1	1.307	0.76046	11
SEC61B	1.3026	0.66886	5
ARMCX3	1.3008	0.7308	6
TP53I3	1.2883	0.81357	16
TRIM25	1.2837	0.78302	15
TAPBP	1.2769	0.81465	7
ACADVL	1.276	0.73839	14
KRT18	1.2735	0.77276	24
GHITM	1.2661	0.7255	3
CLN5	1.2651	0.60156	3
GCLC	1.2598	0.79398	14
MTCH2	1.2541	0.75574	9
NDUFA4	1.2509	0.62878	2
CD47	1.2471	0.73924	3
GLG1	1.2452	0.78204	15
ANXA6	1.2409	0.79771	51
GBP1	1.2402	0.73278	4
STOM	1.2378	0.79191	12
PGD	1.2337	0.76832	30
CLTA	1.2314	0.73569	5
IGF2R	1.2295	0.81054	7
NQO1	1.2225	0.73055	15
HIST2H2BF	1.2177	0.64264	11
VIM	1.2169	0.78233	54

Table 3.4: Down-regulated proteins as quantified by mass spectrometry.

Gene Name	Normalized H/L		Counts
	Forward	Reverse	
ITGA3	0.84053	1.4741	13
WDR77	0.83947	1.2858	3
HBXIP	0.83823	1.5911	2
C19orf10	0.83629	1.3384	4
THOC3	0.83526	1.2611	2
HIST1H1B	0.83041	1.2002	8
SORD	0.82921	1.1917	5
TF	0.82742	1.2016	11
RPS9	0.82583	1.1929	16
TXN	0.82572	1.3374	13
HNRNPH1	0.81697	1.3507	10
LSM3	0.8166	1.4384	5
IVNS1ABP	0.80995	1.3479	2
UBE2M	0.80964	1.3093	7
PYCARD	0.80919	1.5353	2
CSTB	0.80758	1.5329	6
SNAP29	0.80715	1.2787	2
LAD1	0.80177	1.1949	11
PDLIM1	0.80128	1.1993	16
DSP	0.79658	1.247	134
S100A16	0.79482	1.3092	7
MANF	0.79466	1.1986	10
EIF4H	0.78782	1.2364	3
TOMM34	0.78699	1.3286	3
LAMTOR2	0.78656	1.4582	2
EHD2	0.78564	1.4655	8
RTN3	0.78448	1.2264	4
ITGA6	0.78316	1.6618	6
ITGB4	0.78172	1.2673	22
PPIA	0.77424	1.2515	24
TBCA	0.76362	1.7206	4
NSFL1C	0.75873	1.4327	2
NDUFA5;DKFZp781K1356	0.74809	1.262	3
MYO6	0.74285	1.3016	8
HSPB1	0.73718	1.4247	14
PEBP1	0.73011	1.2794	13
YAP1	0.72622	1.2002	3
S100A10	0.72043	1.2144	6
TAGLN2	0.72025	1.2359	36
SRSF7	0.71743	1.5481	4
DAZAP1	0.70677	1.485	3

CD9	0.70643	1.2762	2
HSP90AB4P	0.70611	1.2632	4
TPM1	0.70592	1.2921	2
TNS4	0.69924	1.4825	9
DTYMK	0.69894	1.2604	2
CCDC58	0.69654	1.41	3
ABI1;ABI2	0.6962	1.228	6
IVL	0.6948	1.1984	2
FUBP1	0.69281	1.2335	12
SH3BGRL3	0.68818	1.8901	2
NDRG1	0.68721	1.4779	28
MIF	0.68616	1.3837	3
F11R	0.685	1.3353	4
STMN2	0.67678	1.3355	2
DYNLRB1;DYNLRB2	0.65854	1.2752	3
DDT;DDTL	0.6562	1.257	3
CYCS	0.64469	1.4331	11
UBE2L3	0.64194	1.2726	6
FKBP1A	0.62827	1.3717	6
LGALS3	0.61825	1.3443	7
SNX3	0.59245	1.4392	6
ACP1	0.57683	1.4534	3
S100A14	0.57446	1.6576	10
NOTCH1	0.57153	1.2829	2
MOB4	0.56097	1.2695	6
SCP2	0.55508	1.4574	3
TACSTD2	0.52731	1.797	5
HSPE1	0.49777	1.19	6
S100A8	0.43532	1.9754	8
S100A9	0.37158	2.4236	8
HTRA1	0.37149	2.6637	2
CARHSP1	0.31468	1.2272	2
CYR61	0.23697	4.2387	8
TXNL1	0.18638	6.1531	2

3.2.7 Co-immunoprecipitation (coIP) assay and protein structural alignment analysis

As TLR2 has been identified as a functional receptor of SAA1, coIP assay was performed with TLR2-SAA1 in SAECs to address the question as to whether TLR2 and SAA1 are indeed interlinked. The two proteins tested were found to be immunoprecipitated with each other in SAECs (Fig 3.20A). It was clearly indicated that SAA1 specifically interacts with TLR2 and vice versa, although the majority of the TLR2 protein pool remained as uninteracted form. TLR2 has been demonstrated to bind SAA and this was confirmed through the coIP analysis and structural modeling (Fig 3.20B). These results confirmed the association of SAA1 and TLR2.

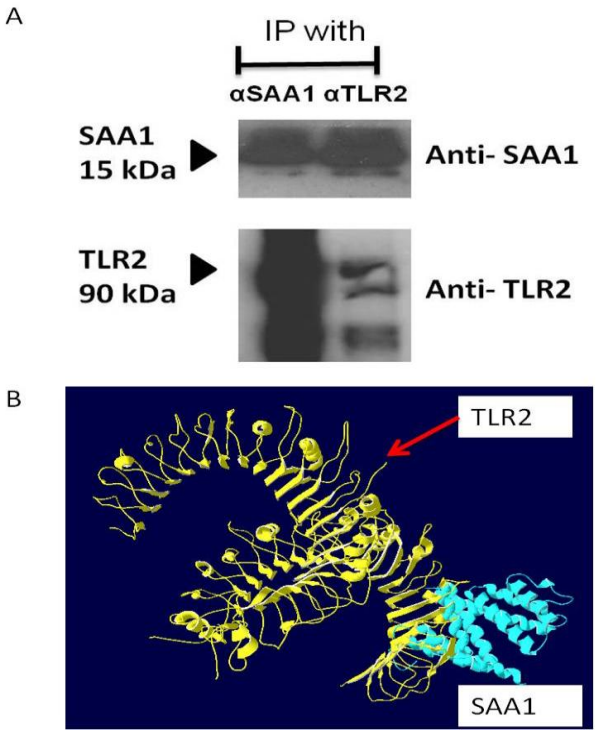

Figure 3.20: Co-immunoprecipitation (coIP) experiments showing TLR2 interacts with SAA1 in SAECs. (A) CoIP was performed using anti-SAA1 and anti-TLR2 from the lysates of SAECs. The precipitates were analysed by immunoblot with anti-SAA1 and anti-TLR2 antibodies, as indicated. Western blots for SAA1 and TLR2 proteins indicate that coIP was seen when using SAA1 antibody as well as with TLR2 antibody. (B) Structural modeling and interaction prediction using Swiss PDB showed asymmetric unit of SAA1 (in blue) interacting with TLR2 (LRR domain) (in yellow).

3.2.8 AuNPs induced NFkB activation in SAECs

To further investigate which signaling pathways involved in transmitting extracellular signal into SAECs after AuNP exposure, transient transfection and luciferase reporter assay were performed. Using NFkB luciferase reporter plasmid, the effect of AuNPs on NFkB activity in SAECs, which were treated with 1 nM of AuNPs for 48 h, was evaluated. There was a significant induction of NFkB activation as revealed by an increase in luciferase enzyme activity (Fig 3.21).

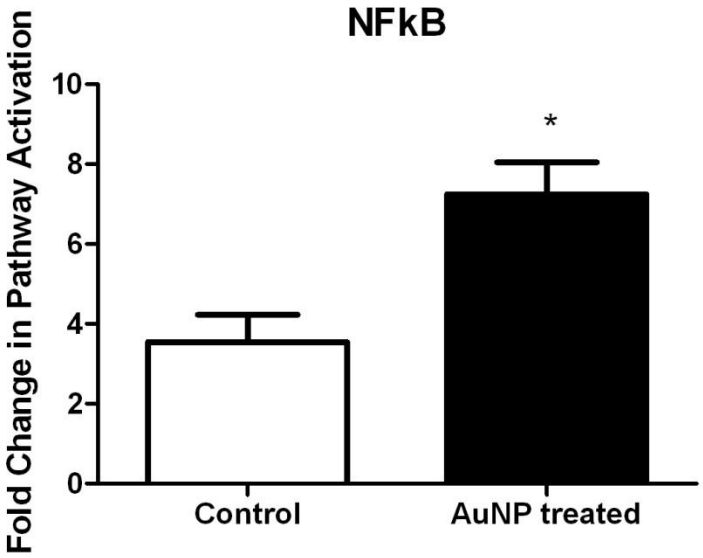

Figure 3.21: NFkB activation. SAECs were transiently transfected with NFkB luciferase reporter plasmid after treated with 1 nm AuNPs for 48 h. Luciferase enzyme activity was measured in relative light units (RLU) and represented on the y-axis as NFkB activity (mean ± SEM) relative to the control. *$p < 0.05$.

3.2.9 Epigenetic mechanisms induced by AuNPs in SAECs

(A) Assessment of miRNAs induced by AuNP exposure

To examine the role of miRNAs in regulating cellular response post AuNP exposure, three miRNAs which were reported to be NFkB downstream targets, *viz*., miR-155, miR-146a and miR-125b were chosen for qRT-PCR analysis. However, miRNA expression levels for AuNP exposed SAECs were not significantly different from control SAECs, (Fig 3.22A-C). Gene expression of *PROS1*, which is known to be regulated by miR-155 in MRC5 lung fibroblasts after exposure AuNPs as reported previously (Ng et al., 2011), was also not unaffected in AuNP-treated SAECs (Fig 3.22D cf C).

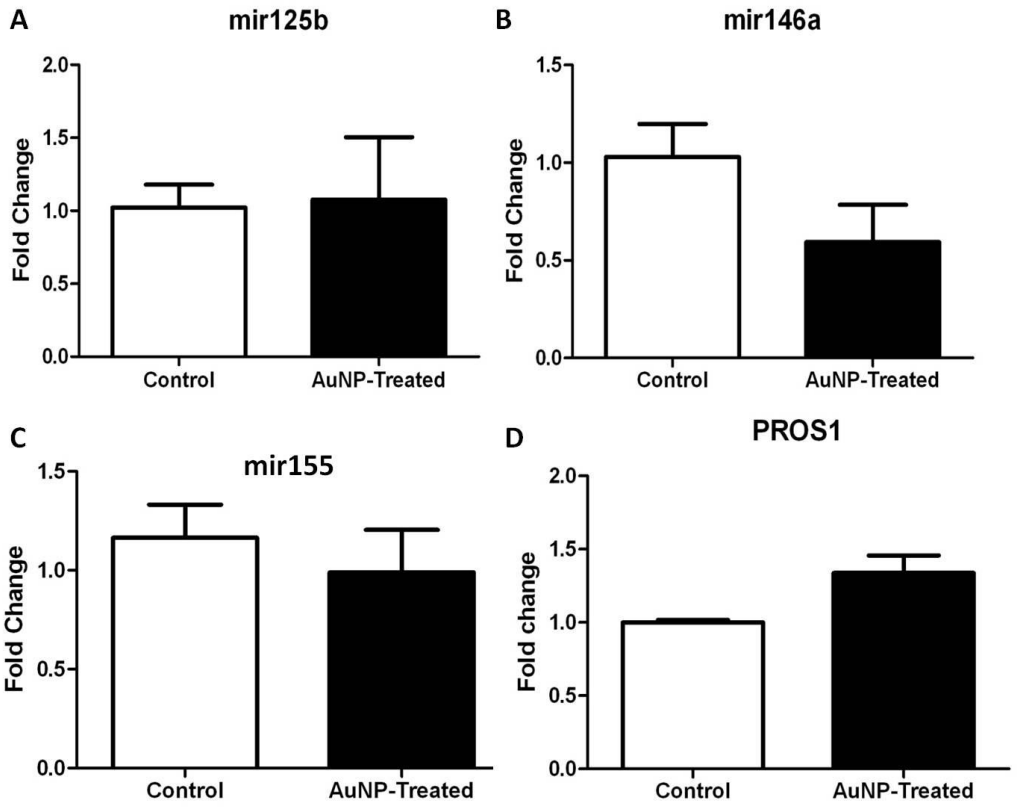

Figure 3.22: miRNA expression in AuNP-treated SAECs. (A) There was no significant change in miR-125b expression level as well as (B) miR-146a and (C) miR-155. (D) PROS1 gene expression in AuNP-treated SAECs. There were no significant changes to PROS1 gene expression observed. Error bar=SEM.

(B) DNA methylation

The *UIMC1* and *CDK1* genes, which are the only two down-regulated genes from the microarray study, were examined to study if DNA methylation could play a role in inhibiting their expression. 5-Aza, an inhibitor of DNA methylation was used to treat SAECs for 6 days before exposure with AuNPs for 72 h. There was no altered expression with 5-Aza treatment, indicating that *CDK1* and *UIMC1* gene expression in AuNP-treated cells was not modulated by this mechanism (Fig 3.23A, B).

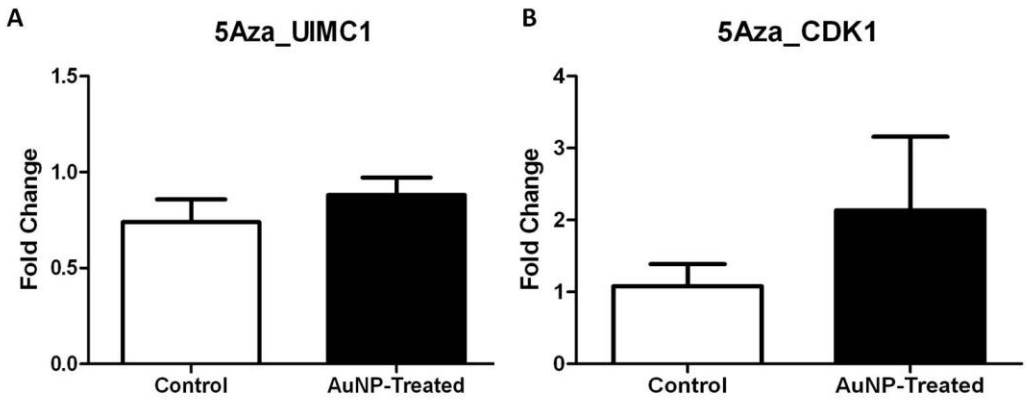

Figure 3.23: Effects of DNA methylation on AuNP-treated SAEC gene expression. (A-B) Down-regulated genes from microarray data analyses, which include UIMC1 and CDK1 expression levels were not affected before and after treatment with 5-azacytidine. Error bars = SEM.

(C) Histone deacetylation

Next, the expression of *UIMC1* and *CDK1* genes were examined to study if histone modification could play a role in inhibiting their expression. Trichostatin A, an inhibitor for class I and II mammalian histone deacetylase (HDAC) were used to treat SAECs for 48 h before exposure with AuNPs for 72 h. *CDK1* expression was significantly up-regulated after treatment with TSA (Fig 3.24B) but there was no altered expression with *UIMC1* gene (Fig 3.24A).

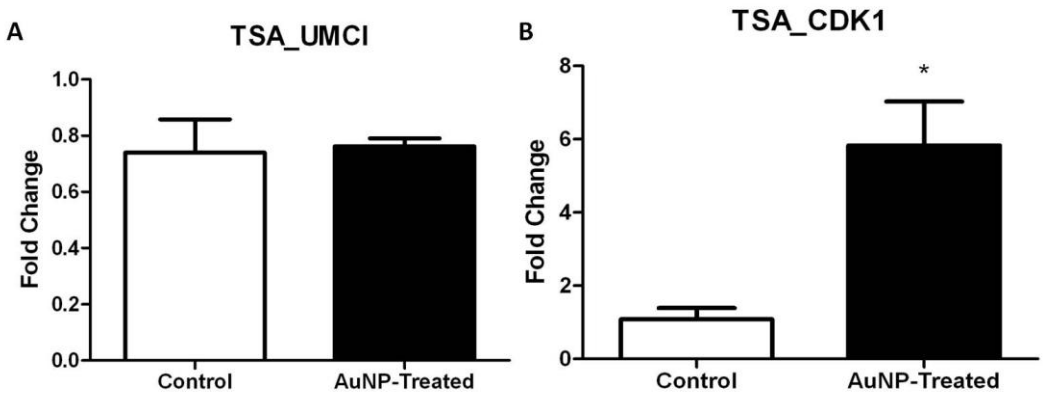

Figure 3.24: Effects of histone modification on AuNP-treated SAEC gene expression. (A) Gene expression of *UIMC1* was not affected by TSA treatment. (B) *CDK1* gene expression increased significantly after treated with TSA. Error bars = SEM; *$p < 0.05$ relative to non-treated control by unpaired t-test.

3.3 Biological effects of AuNPs in MRC5 lung fibroblasts

3.3.1 Uptake of AuNPs into MRC5 lung fibroblasts

(A) LM, AMG and CLSM

In addition to SAECs, biological effects of AuNPs were also examined in MRC5 lung fibroblasts. MRC5 fibroblasts showed no apparent morphological alteration after exposure to AuNPs for 72 h as compared with unexposed fibroblasts (Fig 3.25B cf 3.25A). Under LM, AuNPs which were originally wine-red color, appeared blue-black in color (arrow) inside MRC5 fibroblasts, after aggregation (Fig 3.25B).

Exposure of MRC5 lung fibroblasts to 1 nM AuNPs resulted in internalization of the AuNPs as observed under LM but was more obviously seen after AMG enhancement (Fig 3.25D cf Fig 3.25C). AuNPs were mainly observed as small aggregates appearing as black spots of AMG grains (Fig 3.25D). Enhancement with AMG caused the internalized AuNP aggregates clearly observed due to silver deposition on the AuNPs, inside the fibroblasts (Fig 3.25D, inset).

Under cLSM, nuclei of MRC5 fibroblasts were stained blue. There was no uptake of AuNPs (seen as black spots) into the nuclei (Fig 3.25F cf E).

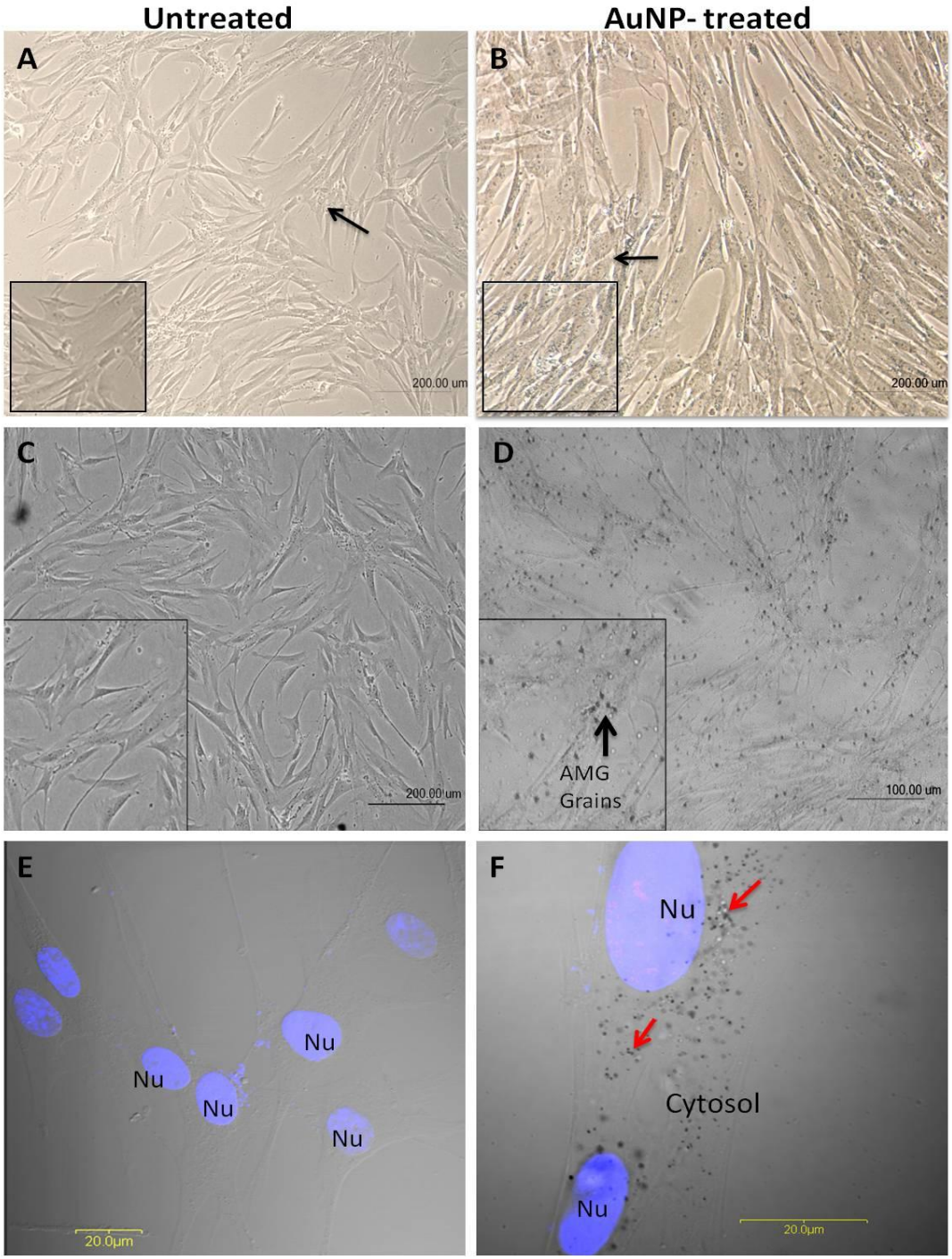

Figure 3.25 Morphological examination of MRC5 fibroblasts. (A) LM micrograph shows control MRC5 lung fibroblast without AuNP treatment. Scale bar: 200 µm. (B) Internalized AuNPs appearing as blue particles under LM. Scale bar: 200 µm. (C) LM micrograph shows control MRC5 lung fibroblasts without AuNP treatment after enhancement with AMG. Scale bar: 200 µm. (D) AMG grains formed after silver enhancement in AuNP-treated MRC5 fibroblasts. Scale bar: 100 µm. (E) CLSM micrograph shows clear cytoplasm without AuNPs. Scale bar: 20 µm. (F) CLSM micrograph shows dark deposits of AuNPs (indicated by arrows) in the cytoplasm of MRC5 fibroblasts. Scale bar: 20 µm.

(B) TEM-EDX Analysis

TEM was performed to validate that AuNPs were indeed internalized by the MRC5 fibroblasts. Intracellular distribution AuNPs in the fibroblasts were visualized in ultrathin sections by TEM. At the ultrastructural level, the well-defined spherical shape and electron dense property of AuNPs enabled their unambiguous identification in ultrathin sections. AuNPs were visualized as black agglomerates 72 h post AuNP exposure (Fig 3.26B cf Fig 3.26A) that were trapped in endosomes and lysosomes (Fig 3.26C), but were not able to enter the nucleus. Some free AuNPs were also found in the cytoplasm of the fibroblasts (Fig 3.26B) (arrows). To confirm the identity of the black deposits as Au, EDX analysis was conducted and verified that the electron dense aggregates were Au as depicted by the presence of two peaks that represent the gold M and L shells (arrows) with a peak over background (P/B) ratio of 4.53 and 34.47 respectively (Fig 3.26D).

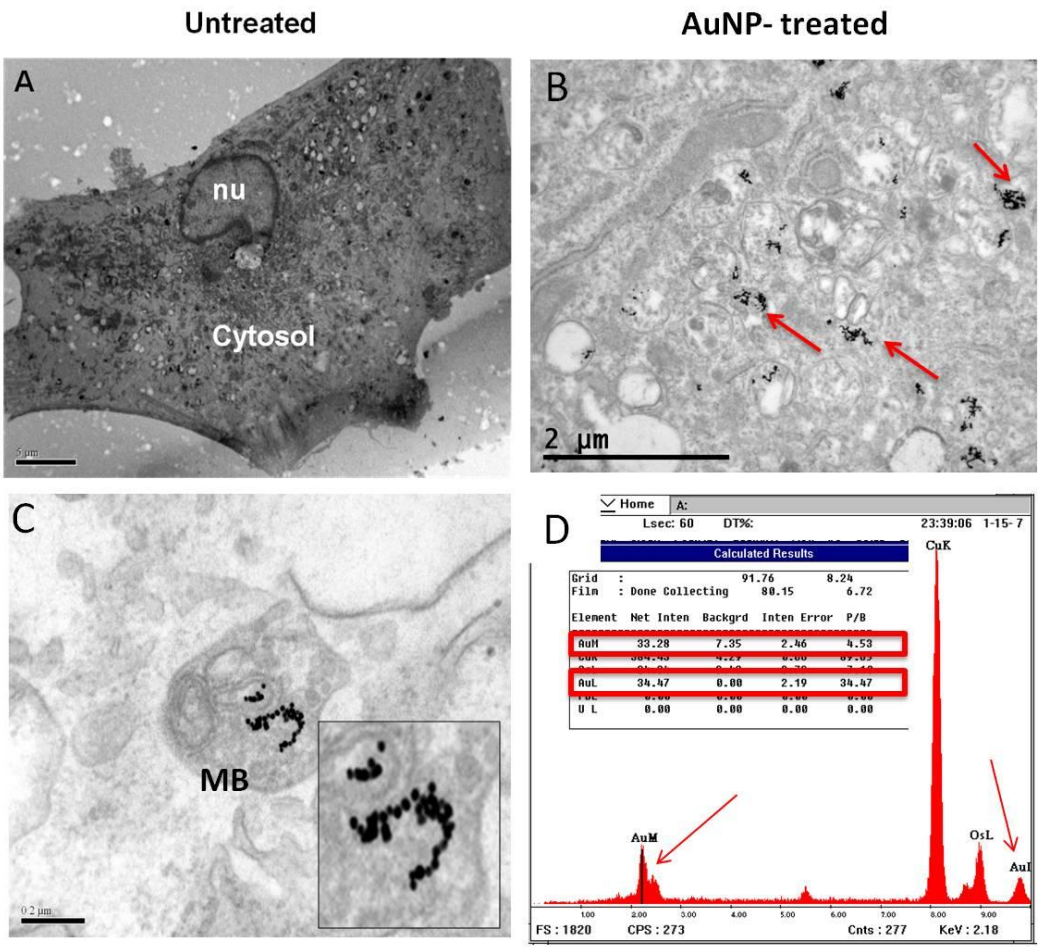

MB: Multivesicular bodies

Figure 3.26: Subcellular morphology of MRC5 cells and AuNP localization after 72 hours AuNP treatment. (A) Micrograph shows the negative control on MRC5 cells without any AuNP uptake. Scale bar: 5 µm. (B) AuNP was taken up my MRC5 cells (red arrows) and localizes predominantly at cytoplasm, with some enclosed within the endosomes. Scale bar: 2 µm. (C) Electron dense AuNPs were clearly seen under EM and localized in the endosomes as black clusters. Inset shows enlarged micrograph on AuNPs localized in vesicles. Scale bar: 0.2 µm. (D) EDX spectrum shows the presence of Au in MRC5 cells as two sharp peaks at 2.121 and 9.712 keV.

(C) ICPMS and mechanistic study on AuNP cellular uptake

To accurately measure the number of AuNPs in MRC5 fibroblasts, ICPMS, a quantitative analysis technique, was employed to analyze the content of Au. The results showed that AuNPs taken up by MRC5 fibroblasts increased linearly with time, peaking at 72 h, before decreasing (Fig 3.27).

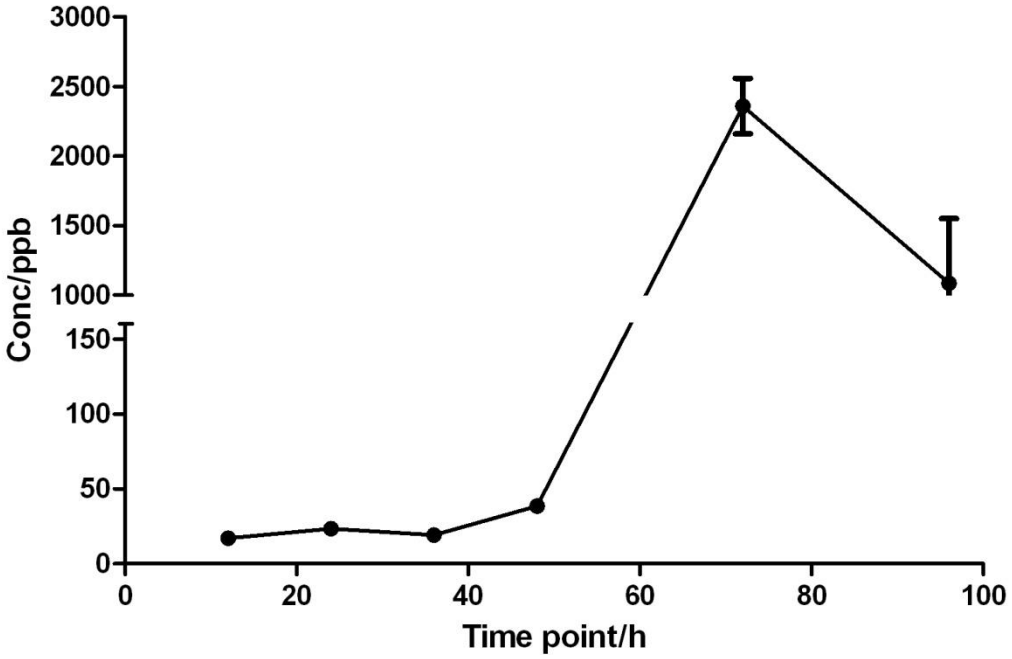

Figure 3.27: ICPMS analysis on the amount of AuNPs (measured in ppb) internalized by MRC5 cells. Uptake of AuNPs increased over the time and peak at 72 h, saturated after 72 h as indicated by the downward trend at 96 h. Error bar=SEM.

AuNPs were enclosed within double membrane cellular vesicles as seen in the TEM shown in Figure 3.29. Hence, it was postulated that AuNP uptake might occur via Receptor Mediated Endocytosis (RME). RME inhibitors were used to study which endocytic pathway was involved in internalization of AuNPs into MRC5 cells. Inhibition of the clathrin-mediated pathway using concanavalin A significantly inhibited the uptake of AuNPs into MRC5 lung fibroblasts by 18.2% as compared with control cells (Fig 3.28). This result suggested that uptake of AuNP into MRC5 fibroblasts occurred via clathrin-mediated endocytosis.

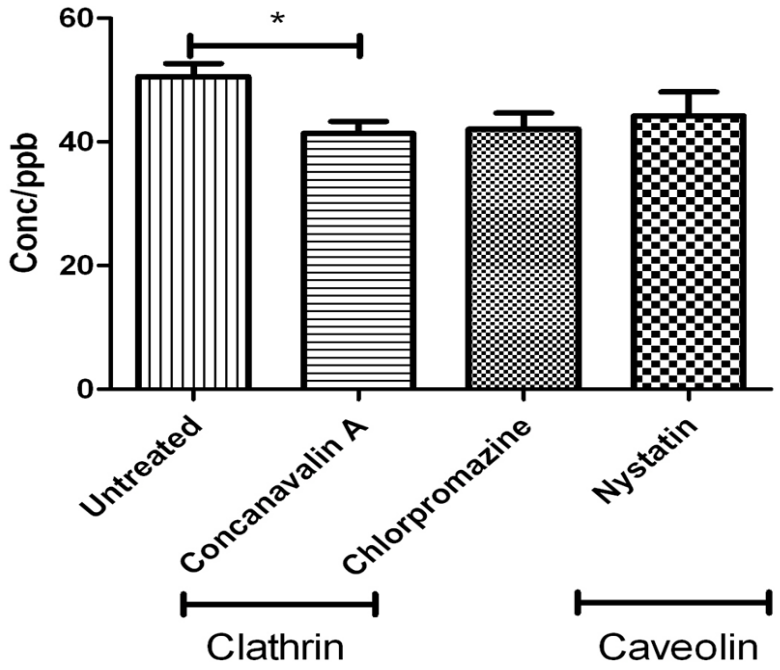

Figure 3.28: Effect of endocytosis inhibitors on the AuNP uptake into MRC5 cells. ICPMS analysis revealed a significant decrease in AuNP uptake after MRC5 cells were treated with Concanavalin A in comparison with control. Experiments were performed in triplicates. Error bar=SEM; *p <0.05.

To ensure that the endocytosis inhibitors did not have an effect on cellular toxicity, thereby influencing uptake of the AuNPs, the viability of the MRC5 cells after treatment with the inhibitors was evaluated using the MTS assay. MRC5 fibroblasts were relatively insensitive to concanavalin A and chlorpromazine treatment since there were no significant differences in cell viability, although nystatin exhibited slight cytotoxicity at 25 μg/ml, but still maintaining an average of 82% cell viability (Fig 3.29A). The F-actin structure which can affect uptake of AuNPs, was also not affected in cells treated with these endocytosis inhibitors (Fig 3.29B). This result indicated no cellular stress was induced by the use of inhibitors which could potentially alter the cytoskeleton network and affect endocytosis.

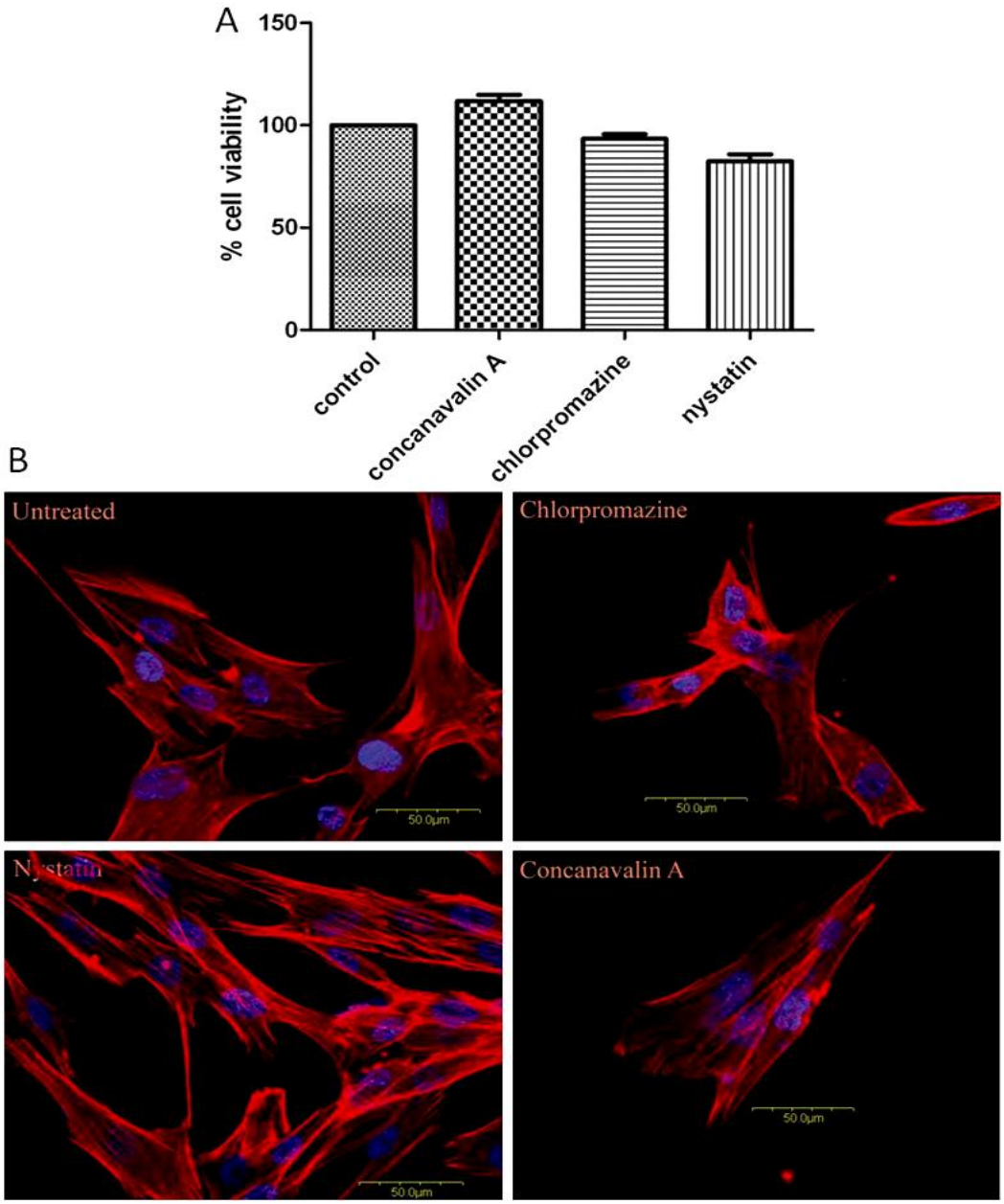

Figure 3.29: Cell viability and F-actin distribution in MRC5 lung fibroblasts treated with endocytosis inhibitors only. (A) There was no significant cytotoxicity observed in MRC5 lung fibroblasts, following exposure to the different endocytosis inhibitors for 4 h. Percentage of cell viability was expressed as mean ± SEM. (B) Confocal microscopy images of MRC5 lung fibroblasts showed the F-actin morphology in control cells and following incubation with concanavalin A, chlorpromazine, and nystatin for 4 h. There was no increase in stress actin bundles in treated cells, indicating no changes in cytoskeletal structure organization. (Blue DAPI stained nuclei, Texas red-phalloidin stained actin filaments, Magnification 200X). Scale bar: 50 µm.

3.3.2 Oxidative stress generated in MRC5 fibroblasts after AuNP exposure

(A) LPO Assay

There was an increase of the LPO content as observed in MRC5 fibroblasts after 72 h of 1 nM AuNP exposure compared with the control cells (Fig 3.30).

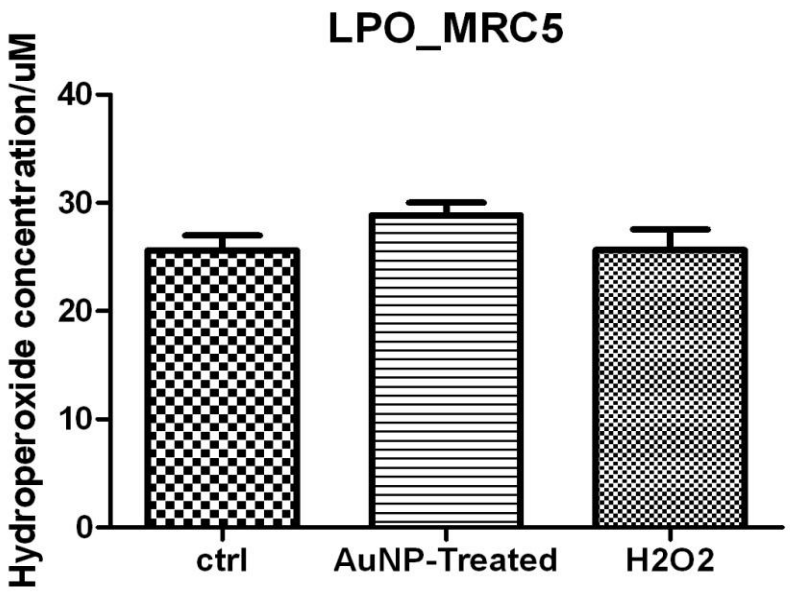

Figure 3.30: Lipid peroxidative stress in MRC5 cells following exposure to 1 nM AuNPs. A higher level of LPOs was observed in AuNP-treated MRC5 cells when compared with control cells. Error bars = SEM.

(B) MT anti-oxidant gene screening

The expression of functional *MT-1* and *MT-2* gene isoforms was assessed initially in MRC5 fibroblasts (Fig 3.31A). The *MT-1E, MT-1X* and *MT-2A* genes were the most abundant isoforms expressed by MRC5 fibroblasts (denoted by a lower delta CT value). There was a significant increase expression of *MT-1X* and *MT-2A* mRNA transcripts in comparison with untreated fibroblasts after exposure to 1 nM AuNPs (Fig 3.31B, C). At the protein level, MT protein expression was higher as validated using ICC (denoted by higher color intensity) (Fig 3.31E cf D). Moreover, there was a right shift in fluorescence signal intensity of Cy-3 conjugated MT antibodies using flow cytometry (Fig 3.31F, G).

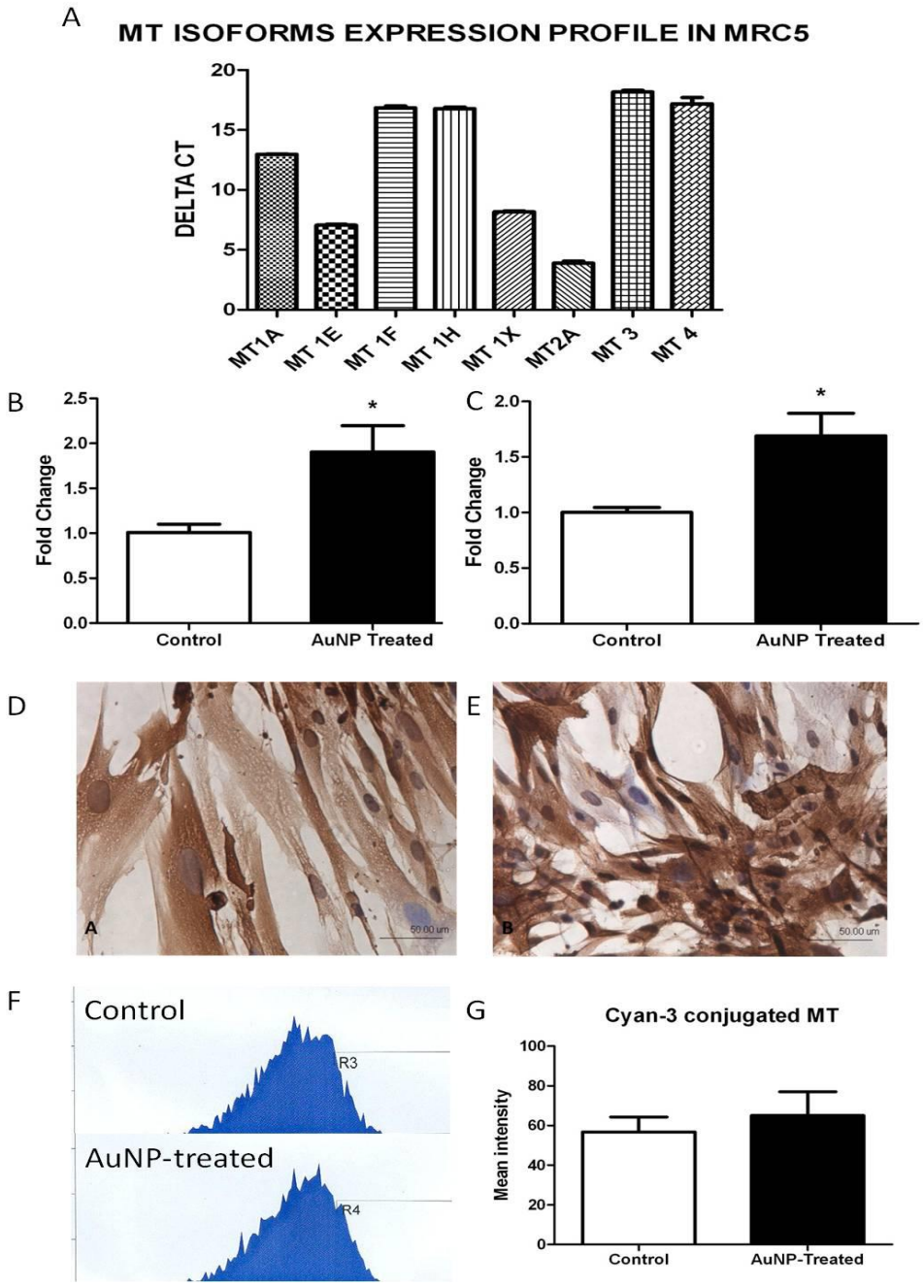

Figure 3.31: MT isoform expression in MRC5 lung fibroblasts exposed to AuNPs. (A) Bar chart of MT isoforms endogenously expressed in MRC5 cells, with *MT-2A* showing the highest expression. (B) Significant up-regulation of *MT-2A* after exposure to AuNPs. (C) *MT-1X* was observed to be increased after treatment with 1 nM AuNPs. (D) LM micrograph of MRC5 cells stained with anti-MT E9 antibody (DAB with haematoxylin counterstain) for AuNP untreated MRC5 cells. (E) AuNP-treated MRC5 cells exhibited higher MT staining (more brown intensity). Scale bar: 50 μm. (F) Detection of MT using flow cytometryr showed a right shift of MT protein, indicating a higher protein expression in AuNP-treated MRC5 cells. (G) The mean intensity obtained from (F) was quantified and the results indicated a higher MT protein expression in AuNP-treated MRC5 cells. All the experiments were conducted in triplicates. Error bars = SEM; *$p < 0.05$.

(C) Screening of other anti-oxidant genes

Next, the transcripts of 8 genes (*CAT, GPX1, GPX2, SOD1, SOD2, SOD3, Prx1, Prx3*) which are involved in anti-oxidative response were examined in MRC5 cells after exposure to 1 nM of AuNPs for 72 h. There was no significant difference in the expression of anti-oxidant genes (Fig 3.32), in comparison with control MRC5 cells.

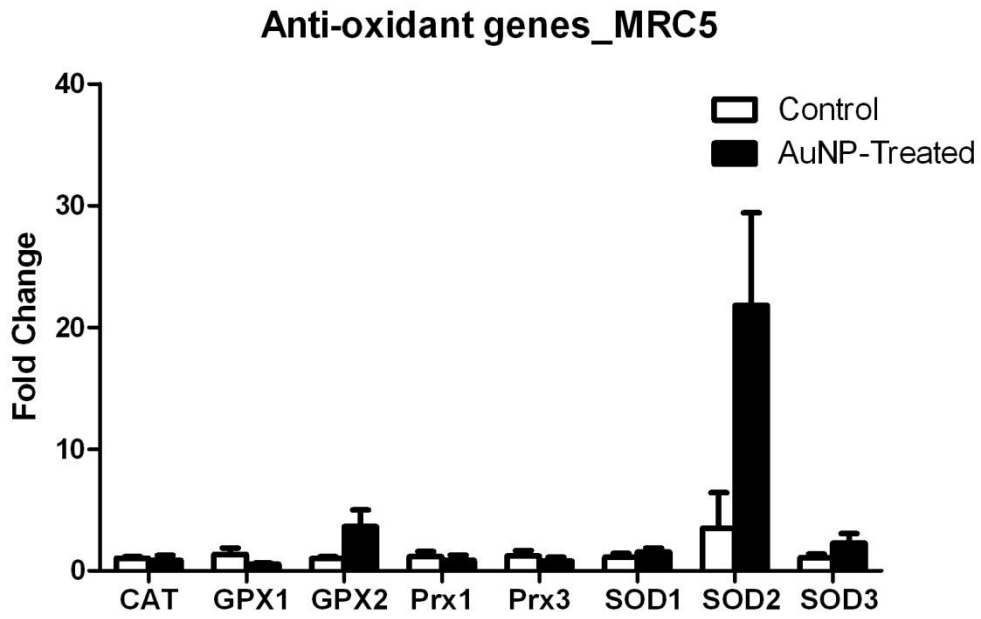

Figure 3.32: Fold change of 8 selected anti-oxidant genes on AuNP exposed MRC5 cells compared with AuNP-unexposed MRC5 cells. Error bars=SEM.

3.3.3 Cytotoxicity of AuNPs

(A) LDH assay

It was observed that AuNPs induced significant cellular release of LDH at 0.5, 1 and 2 nM concentrations at 24 h, indicating cell damage and toxicity (Fig 3.33A). However, only cells treated at 1 and 2 nM AuNPs showed significant LDH release post 48 h and 72 h treatment (Fig 3.33B, C).

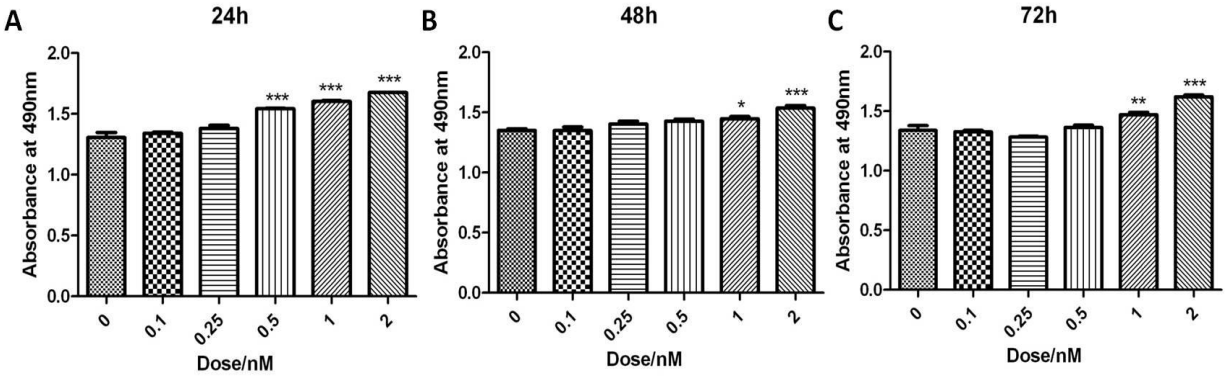

Figure 3.33: LDH assay was used to determine cytotoxicity of MRC5 cells treated with a range of dose with AuNPs. (A) At 24 h, (B) 48 h and (C) 72 h, MRC5 showed significant release of LDH into the culture media, as an indicator of cellular membrane disruption at 0.5 nM, 1 nM and 2 nM. All the experiments were conducted in triplicates. Error bars= SEM; *p<0.05; **p<0.01; ***p<0.001.

(B) Trypan Blue assay

Using trypan blue assay, there was a significant decrease in cell viability of MRC5 fibroblasts treated with 2 nM AuNPs at 24, 48 and 72 h. Although there was a slight decrease in total cell count, the difference was not significant across all time points (Fig 3.34D-F). There was no significant loss of cell viability at 48 and 72 h for all tested concentration except for 1 nM at 24 h (Fig 3.34A), 2 nM at 48 h (Fig 3.34B) and at 72 h (Fig 3.34C).

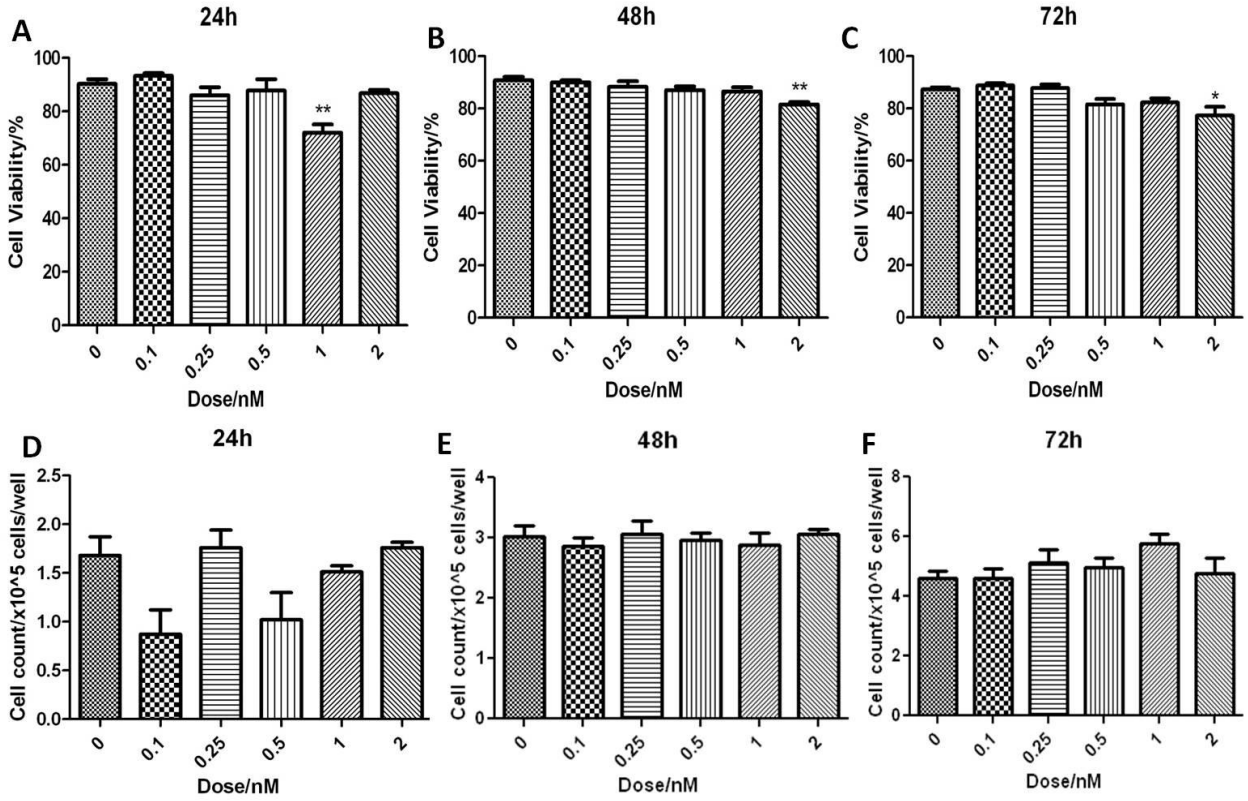

Figure 3.34: Viability of MRC5 cells was determined by 0.4% Trypan blue dye exclusion assay following 24 h, 48 h and 72 h AuNP exposure. (A) Graphical representations of % of cell viability at 24 h, showed significant decrease in cell viability when treated with 1 nM of AuNPs; and 2 nM at (B) 48 h and (C) 72 h. Total cell count was decreased when treated with AuNPs at (D) 24 h (E) 48 h and (F) 72 h, although these were not significant. All the experiments were conducted in triplicates. Error bars = SEM; *p< 0.05; **p<0.01.

(C) Hoechst 33342, AO/ EtBr staining and cell cycle analysis

Hoechst 33342 nucleus staining for living cells was observed in fixed MRC5 fibroblasts, indicates no loss of cell viability after AuNP treatment (Fig 3.35B cf A). On the other hand, AO/EtBr staining showed that the some cells treated with 1 nM of AuNPs appeared orange-red in color (dead cells), while control cells appeared yellowish-green (live cells) under a phase contract microscopy (Fig 3.35D cf C).

Figure 3.35E shows a representative flow cytometry DNA histogram for control and AuNP-exposed MRC5 lung fibroblasts. The percentage of at subG1 and S+G2/M phase of the cell cycle was determined using PI staining. The results show that there was no significant increase in apoptotic cells (denoted by subG1 phase) and no significant decrease in cell proliferation rate (denoted by S+G2/M phase) (Fig 3.35F), which is in agreement with the results from trypan blue assay.

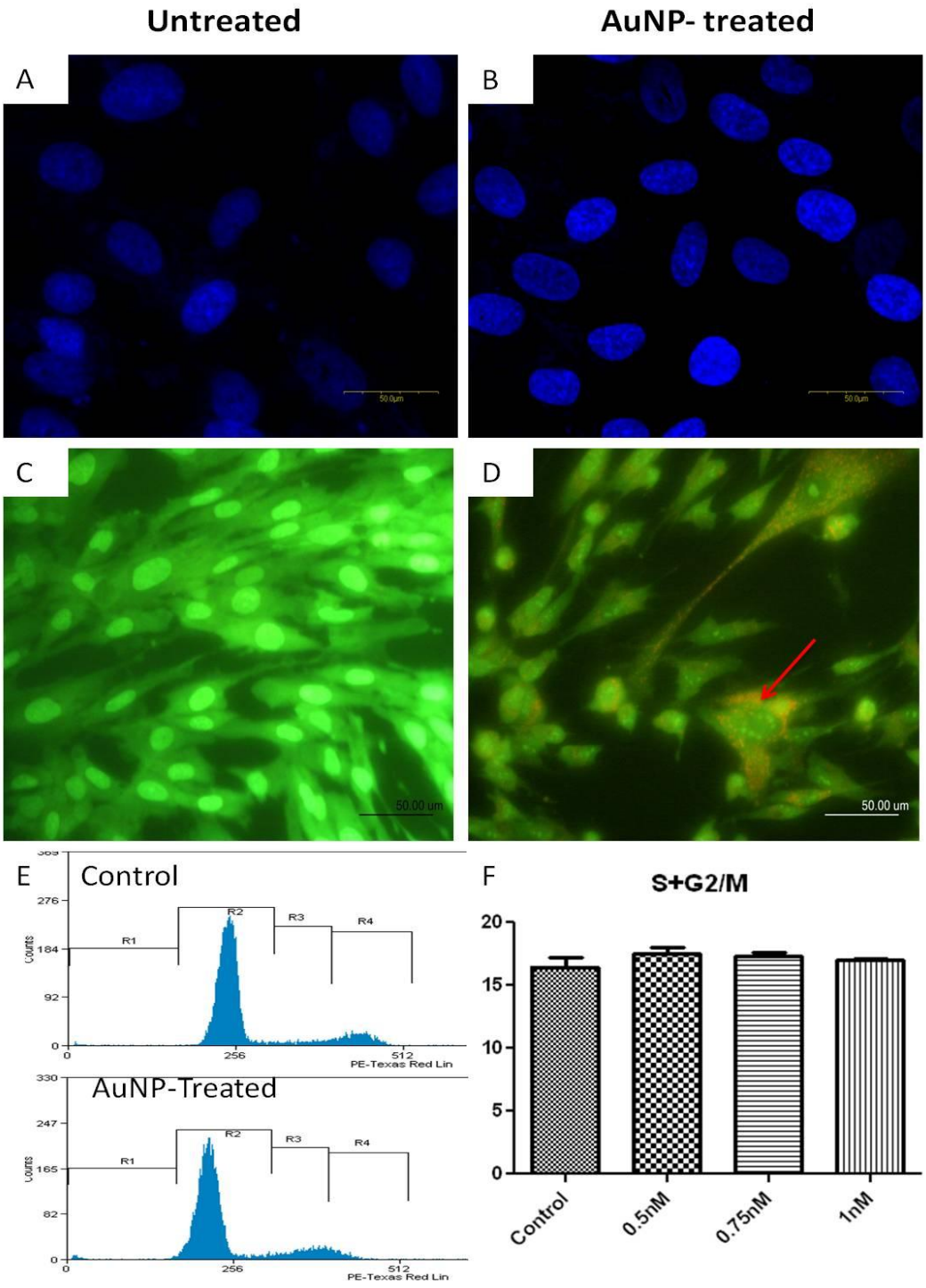

Figure 3.35: Cytotoxic effects of AuNPs on MRC5 cells. (A) Hoechst 33342 nucleus staining (in blue) in (A) control and (B) AuNP-treated MRC5 cells. There was no apparent nuclear change in MRC5 cells after treatment with AuNPs. Scale bar: 50 µm. (C) AO/EtBr staining in control MRC5 cells shows green staining, indicating live viable cells. Scale bar: 50 µm. (D) Some red staining (arrow) was spotted in AuNP-treated MRC5 cells, indicating occurrence of cell death. Scale bar: 50 µm. (E) DNA histogram revealed no changes in cell proliferation rate after treated with AuNPs in MRC5 cells. (F) Bar chart shows no changes in the percentage of S+G2/M. Error bars=SEM.

3.3.4 Microarray analysis of AuNP-treated MRC5 lung fibroblasts

The quality of RNA samples was determined the same way as SAECs. All the samples displayed OD260/OD280 ratios of between 2.01 – 2.21, and concentrations ranged from ~209 ng/µl to ~530 ng/µl (Fig 3.36A). The quality of the RNA was confirmed by performing gel electrophoresis (Fig 3.36B). The RIN obtained ranged from 8.3 to 9.2. For transcriptomic analysis, 300 ng total RNA from each sample was used (Fig 3.36C).

A

Samples	OD 260nm	OD 280nm	Ratio 260/280	Concentration ng/ul
Control1	0.074	0.0361	2.047	295.9
Control2	0.1312	0.063	2.059	530.76
Control3	0.0072	0.0331	2.188	289.55
AuNP-Treated 1	0.0527	0.0264	2.014	209.47
AuNP-Treated 2	0.0791	0.0354	2.218	318.36
AuNP-Treated 3	0.1102	0.0529	2.08	441.89

B

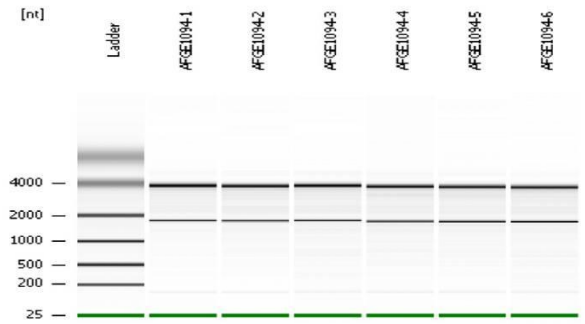

C

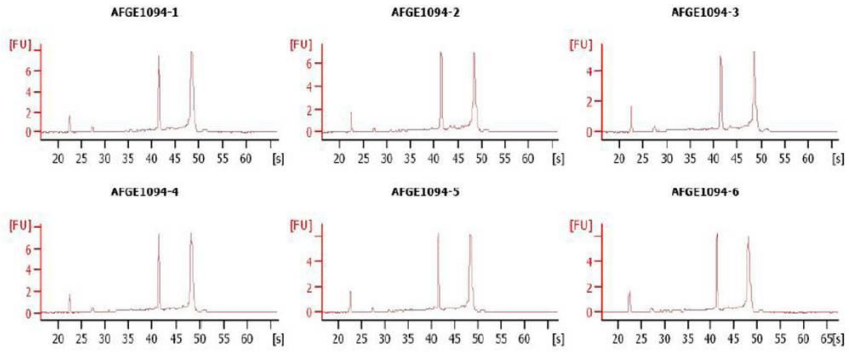

Figure 3.36: Characterization of RNA quality of MRC5 for microarray study. (A) The good quality of RNA samples with 260/280 ratio ⩾ 1.8. (B) Gel image of RNA samples. (C) Electropherograms of 28S and 18S rRNA.

A cut-off at 1.5-fold absolute change was applied for analysis between untreated and treated samples. Heat map (Fig 3.37A) and volcano plot (Fig 3.37B).for the microarray data from MRC5 fibroblasts was generated.

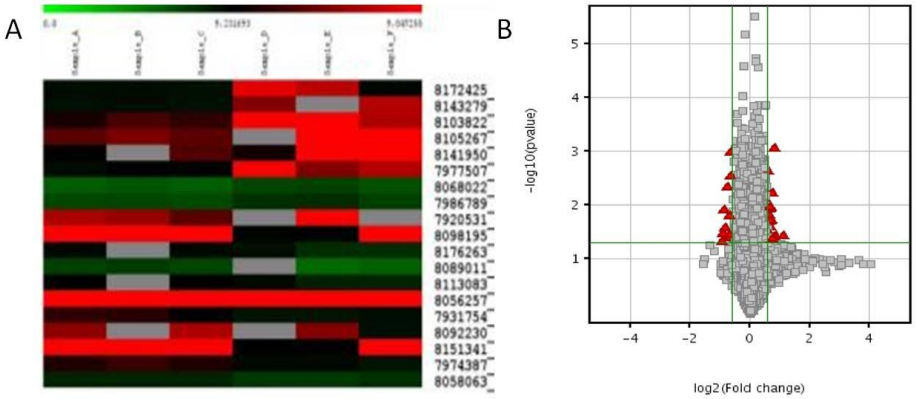

Figure 3.37: Microarray data analysis. (A) A heat-map representation showing the clustering of the control and AuNP-treated MRC5 cells into two separated subclusters. Differentially expressed genes which were represented by their respective Affymetrix probe set Ids are shown in the rows. Columns represent MRC5 RNA samples (Sample A-C: control MRC5 lung fibroblasts; Sample D-F: AuNP-exposed MRC5 lung fibroblasts). (B) Volcano plot for comparison of the transcriptomes of MRC5 cells treated with AuNP versus cells not exposed to the nanoparticles.

19 genes were identified and were regulated over the 1.5-fold change cut off (Table 3.5). Among them, 9 genes were over-expressed, and 10 genes were down-regulated in AuNP-treated cells compared with the untreated MRC5 cells. 11 genes selected for verification by real time RT-PCR had expression levels that were consistent with the data derived from microarray analysis (Fig 3.38).

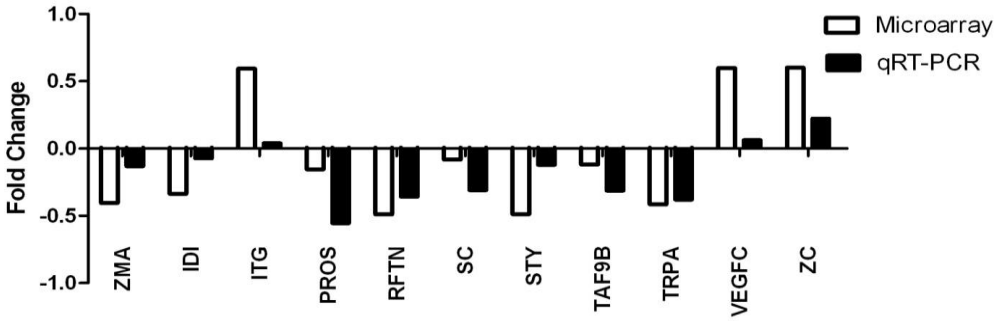

Figure 3.39: A comparison of gene expression profiles derived from microarray and q(RT)-PCR; the bars show the fold changes which were determined for the samples from AuNP treated and untreated MRC5 cells. Expression of the 11 genes by both methods were found to be consistent.

Table 3.5: Differential expression of genes detected by Affymetrix Gene Analysis in AuNP-treated MRC5 lung fibroblasts.

Gene name (description)	Gene Accession	Fold change
Up-regulated genes		
FLJ10246	AK001108	1.70
SLC38A5	NM_033518	1.69
ZC3HAV1	NM_080660	1.60
VEGFC	NM_005429	1.60
ITGA2	NM_002203	1.59
RELN	NM_005045	1.58
MIRNA155	NR_001458	1.56
ATP10A	NM_024490	1.53
ADAR	NM_001033049	1.52
Down-regulated genes		
SC4MOL	NM_006745	1.91
TAF9B|LOC728198	NM_015975	1.88
PROS1	M15036	1.85
C5orf21	NM_018356	1.82
FAP	NM_004460	1.75
IDI1	NM_004508	1.66
ZMAT3	NM_022470	1.60
TRPA1	NM_007332	1.59
STYX|LOC730432	NM_145251	1.51
RFTN2	NM_144629	1.51

*Genes that have at least a 1.5 fold change in AuNP-treated MRC5 lung fibroblasts as compared with control cells, with $p<0.05$.

Using DAVID analysis, the differentially expressed genes could be classified into stress-responsive genes and genes that are known to regulate cellular morphogenesis, blood coagulation, hemostasis, hydrolase activity, metal ion binding and sterol metabolism, as shown in Table 3.6. Genes that are related to sterol biosynthetic process, such as isopentenyl-diphosphate delta isomerase 1 (*IDI1*) and sterol-C4-methyl oxidase-like (*SC4MOL*) have been associated with synthesis of cholesterol while the other identified genes that participate in various cellular pathways may cause pathogenesis of diseases if dysregulated.

Table 3.6: Functional classification of genes using using DAVID analysis.

Processes	**Genes involved**
Response to stress	*RELN* *ZMAT3* *TRPA1* *PROS1* *ITGA2*
Cellular structure morphogenesis	*RELN* *ZMAT3* *ATP10A* *ITGA2* *VEGFC*
Metal ion binding	*ZC3HAV1* *IDI1* *ZMAT3* *ATP10A* *SC4MOL* *TRPA1* *PROS1* *ITGA2* *ADAR*
Sterol biosynthetic process	*IDI1* *SC4MOL*
Hemostasis	*PROS1* *ITGA2*
Hydrolase activity	*RELN* *IDI1* *FAP* *STYX|LOC730432* *ATP10A* *ADAR*

3.3.5 Epigenetic mechanisms induced by AuNPs in MRC 5 lung fibroblasts

(A) Modulation of miR-155 which altered *PROS1* gene expression following AuNP exposure

A gene of interest identified from the microarray analysisis up-regulation of the non-protein coding RNA, microRNA 155 (miR-155) which was concomitant with down-regulation of 10 other genes (including the *PROS1* gene) in AuNP treated fibroblasts. Up-regulation of miR-155 after AuNP exposure was verified using a reporter assay containing a firely luciferase construct with a target site that is complementary to miR-155. AuNPs was found to repress firefly luciferase activity by 63% in MRC5 fibroblasts transfected with the pmiR-155-Luc reporter, demostrating an increased turnover of mRNAs in AuNP-treated cells (Fig 3.39).

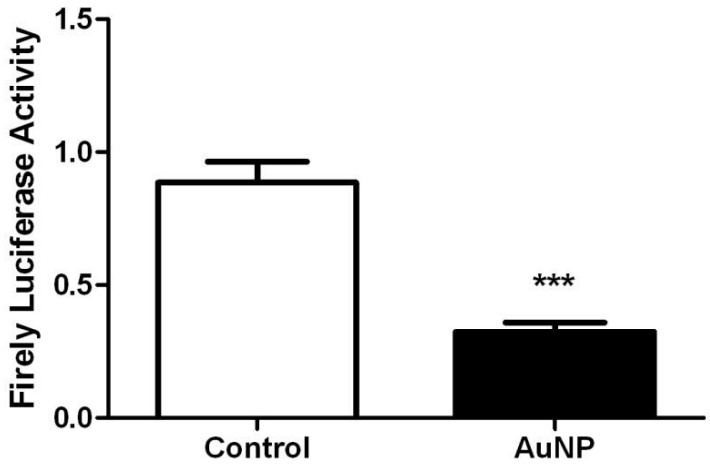

Figure 3.39: MRC5 cells were transfected with the pMiR-Luc Reporter Vector for miR-155 followed by 48 h post AuNP exposure. Firely luciferase activities of AuNP-treated fibroblasts and controls were measured for luminometry using the Dual-Glo™ Assay System. The luciferase activities were measured and showed a significant reduction in firely luciferase activity. The result indicated a higher miR-155 expression following AuNP treatment, resulting in more suppression on firely luciferase activity. Error bar=SEM. *** $p<0.001$ compared with untreated cells.

Given that miR-155 performs its biological function by regulating the target protein-coding genes, the predicted targets of miR-155 were anlayzed using six miRBase algorithms, PicTar (http://pictar.mdc-berlin.de), TarBase, miRanda (http://microrna.sanger.ac.uk) and TargetScan Release 5.1 (http://www.targetscan.org), mirBase (http://www.mirbase.org/) and MicroCosm Targets Version 5. However, none of the differentially expressed genes identified from the microarray data matched the potential predicted miR-155 targets.

In order to better understand the biological role of miR-155 in this experimental setting, anti-miR-155 mediated silencing was performed in lung fibroblasts so as to detect any altered expression of the other 10 down-regulated genes from the microarray data. With this purpose in mind, the MRC5 lung fibroblasts were transfected with anti-miR-155. Prior to this, optimization of the transfection condition using Cy-3 conjugated scrambled siRNA was performed and good transfection efficiency was achieved post 48 h transfection using HIPERFECT (Fig 3.40A). qRT-PCR showed that anti-miR-155 effectively reduced miR-155 expression with a knock down efficiency of 81.8% (Fig 3.40C) coupled with increased in threshold cycle (Fig 3.40B). Silencing of miR-155 was achieved without compromising the cell viability as revealed by MTS assay (Fig 3.40D).

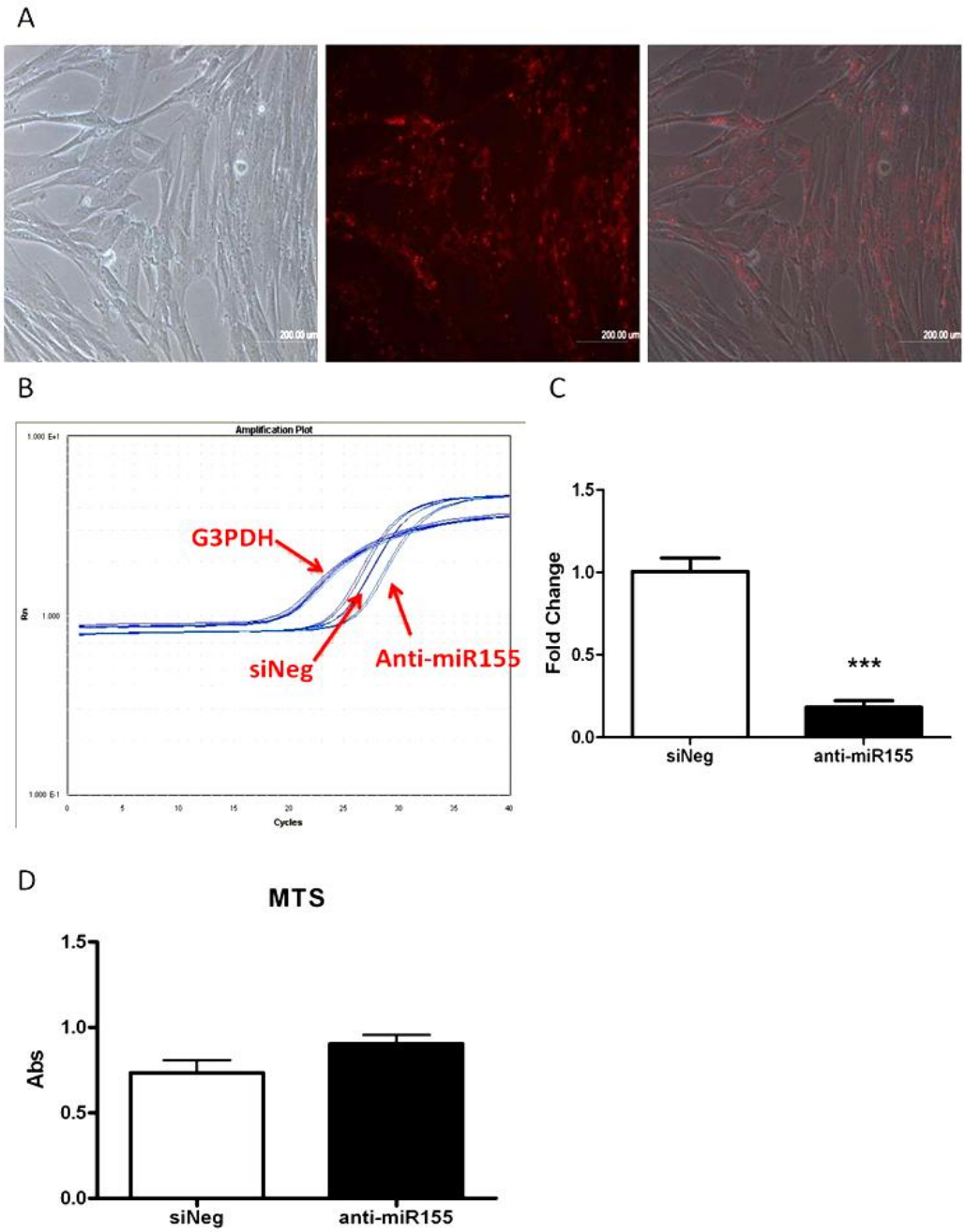

Figure 3.40: Knockdown efficiency of miR-155. (A) A good transfection efficiency was achieved using Cy-3 conjugated scrambled siRNA after 48 h of transfection. (B) Graphical representation of silencing efficiency (denoted by a higher CT value) of miR-155 after inhibited with anti-miR-155. (C) Significant down-regulation of miR-155 expression at 48h post transfection in MRC5 cells with 81.8% of knockdown efficiency. (D) MTS assay revealed non-cytotoxic effect after MRC5 was transfected with anti-miR-155. Error bar=SEM. ***p <0.001.

Silencing of miR-155 caused an increased expression of PROS1 at both mRNA and protein levels (Fig 3.41A-D). Taken together, these results appear to suggest that although endogenous miR-155 was expressed at relatively low levels in the lung fibroblasts, inhibiting its expression induced enhanced levels of PROS1 expression, thereby, indicating that miR-155 could regulate expression of PROS1. Both RNA and protein expression results imply that PROS1 is a target of miR-155.

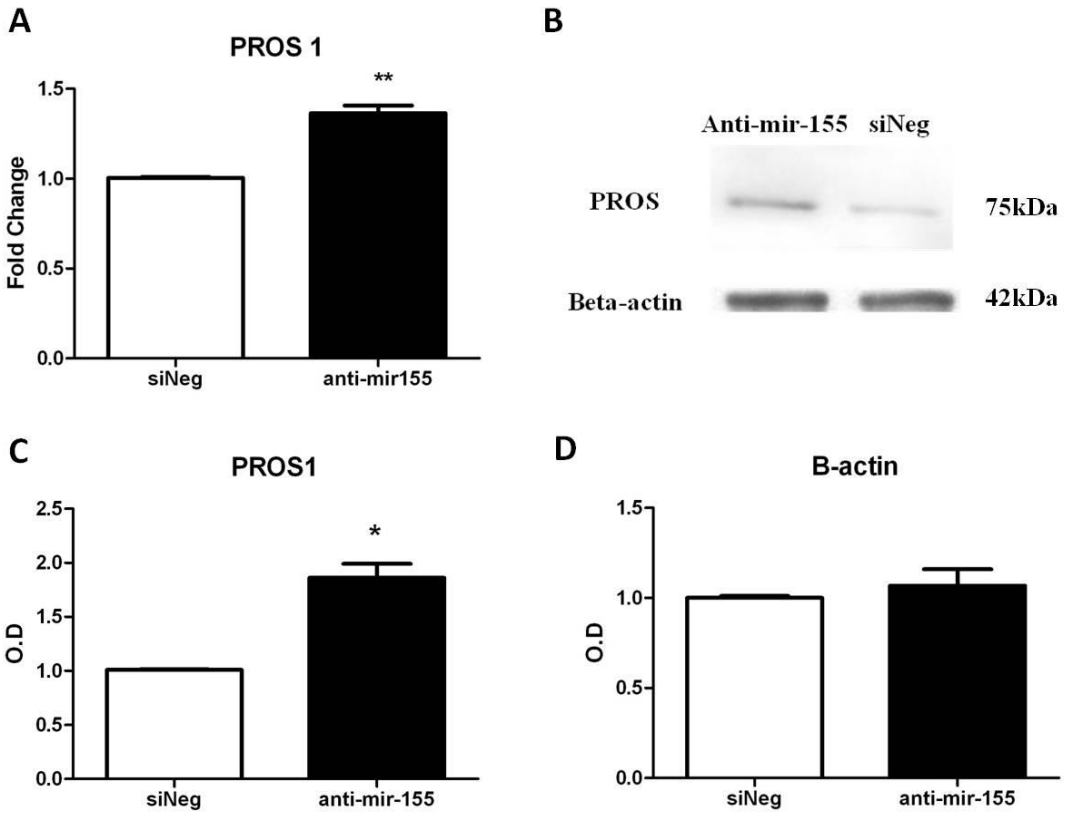

Figure 3.41: Effects of miR-155 inhibition on PROS1 expression. (A) Graphical representation of qRT-PCR analysis of *PROS1* gene expression in MRC5 cells using G3PDH as a normalizer. *PROS1* gene expression was up-regulated in anti-miR-155 treated MRC5 cells. ** $p<0.01$; Error bar = SEM. P value obtained with respect to anti-miR™ miRNA inhibitors negative control. (B) Silencing of the miR-155 gene caused an up-regulation of PROS1 protein expression as revealed by western blot. (C) Western blot analysis performed with antibodies against PROS1 and (D) the housekeeping protein beta-actin (as housekeeping loading control, data not shown). Graphical representation showed the densitometric quantitation of the western blot band intensities. Results are reported as means ± SEM of triplicate experiments. *$p <0.05$.

To show the relevance of the study, the level of *PROS1* mRNA was quantitated in a commercially available normal human tissue array which comprised 48 different human tissues. *PROS1* mRNA was detected in 45/48 normal tissues, and found to be absent in lymphocytes, mammary gland and muscle (Fig 3.42). The highest expression of the *PROS1* gene was detected in lung tissue, which was followed by small intestine, adrenal gland, uterus, pituitary gland, heart, stomach, gonads (penis and ovary) and liver.

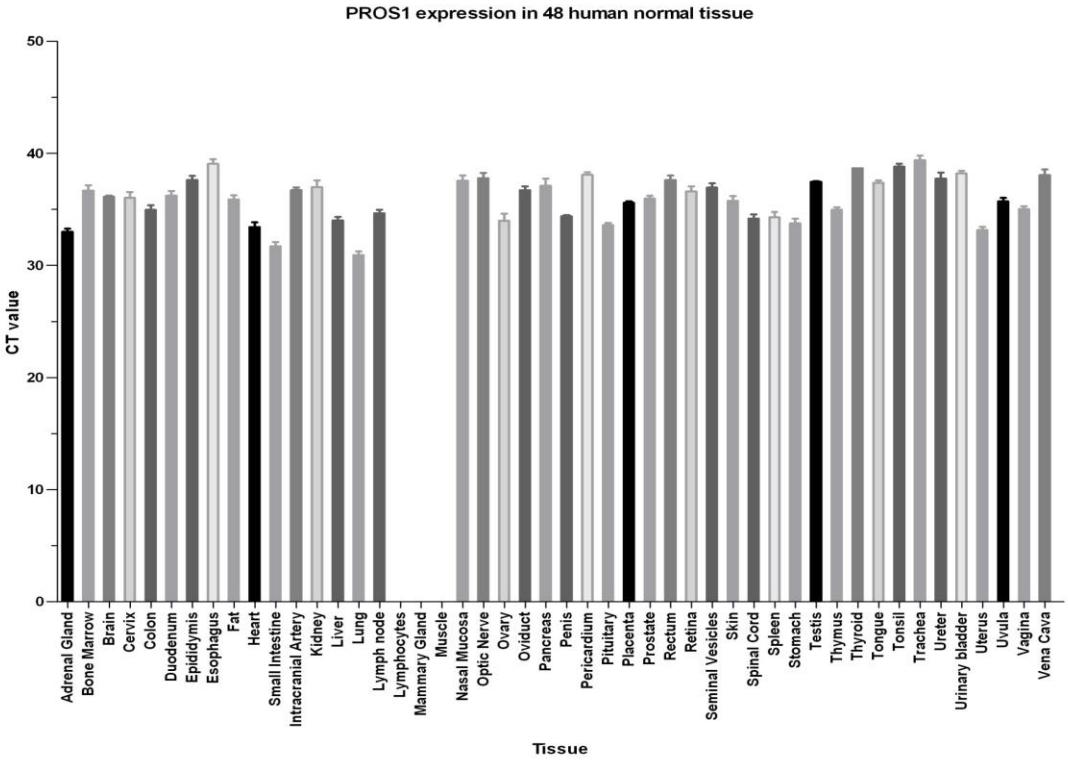

Figure 3.42: TissueScan Human Normal Tissue used in a real-time PCR protocol in a AB 7500 thermal cycler using *PROS1* primers. The *PROS1* amplification products were detected using the SYBR Green I, as fluorescence readings. Result showed that PROS1 was highly expressed in human lung tissues (as denoted by a lower CT value). Error bar=SEM.

(B) DNA Methylation Profiling Analysis of *PROS1* gene

In view of the above finding that miR155 modulate the *PROS1* gene, the CpG island at *PROS1* promoter region was subjected to PCR using BSP primer before cloning into the vector. The PCR product was specific with a product size of approximately 280 bp (Fig 3.43A). There was no change in DNA methylation profile of the *PROS1* gene in AuNP-treated cells as analyzed by bisulfite sequencing (Fig 3.43B), indicating that the absence of AuNP-induced epigenetic modifications with regard to the DNA methylation status of *PROS1* gene. Moreover, MSP analysis was done using primers specific for un-methylated or methylated DNA respectively. MSP result indicated that AuNP-exposed MRC5 cells do not display a high frequency of *PROS1* methylation (Fig 3.43C).

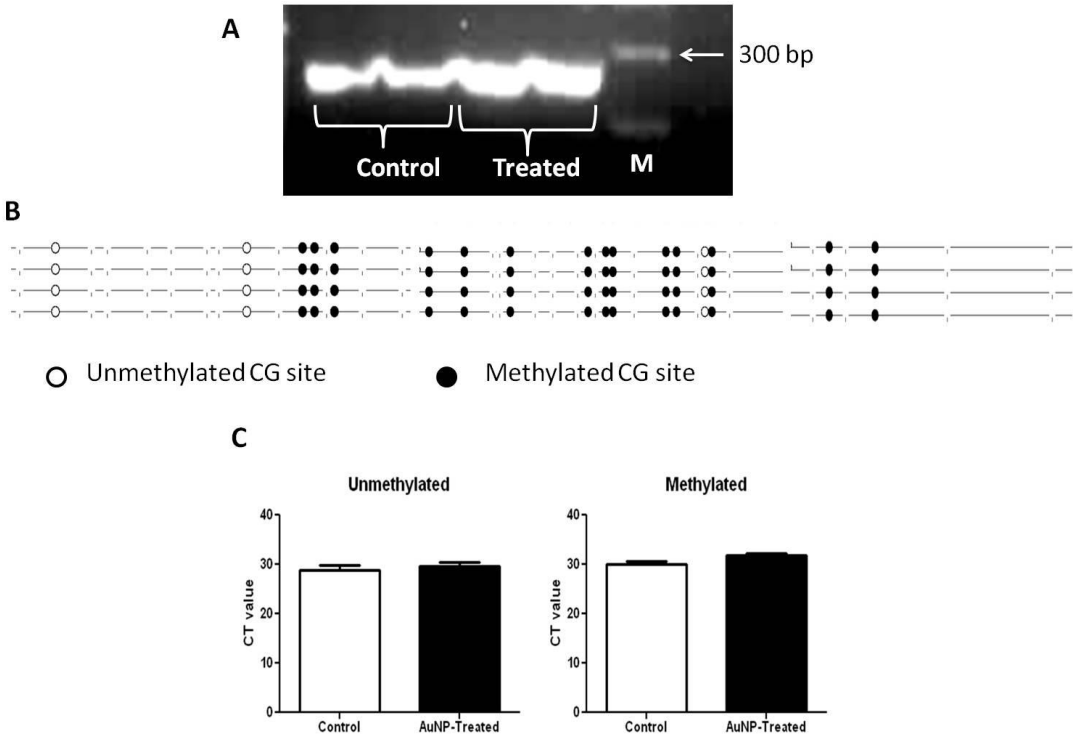

Figure 3.43: DNA methylation status analysis of *PROS1*. (A) Electrophoretic image depicting the specificity of PCR which shows 280 bp amplicon of *PROS1* CpG island. (B) "Lollipop" schematic diagram of methylation patterns of the *PROS1* promoter CpG island region using ClustalW (1.83) multiple sequence alignments. Results are derived from 2 AuNP-untreated samples and 2 AuNP-treated samples are shown. A black lollipop corresponds to a methylated C; white lollipops represent unmethylated C; and a stick corresponds to a non-CpG position. (C) MSP PCR analysis using primers specific for unmethylated (U) and methylated (M) sequences. qRT-PCR values were normalized to input DNA.

(C) Chromatin reorganization in AuNP-treated MRC5 cells

Transmission electron microscopy (TEM) revealed the presence of chromatin condensation in AuNP-treated fibroblasts as compared with untreated fibroblasts (Fig 3.44A). An apparent reorganization of nuclear content and chromatin condensation in AuNP-treated MRC5 lung fibroblasts was observed under confocal microscopy (Fig 3.44B), thereby, complementing the TEM results.

TSA inhibition was also performed and the inhibitory effect on *PROS1* gene was reversed, indicating that *PROS1* gene expression was partly regulated through HDAC activity (Fig 3.44C).

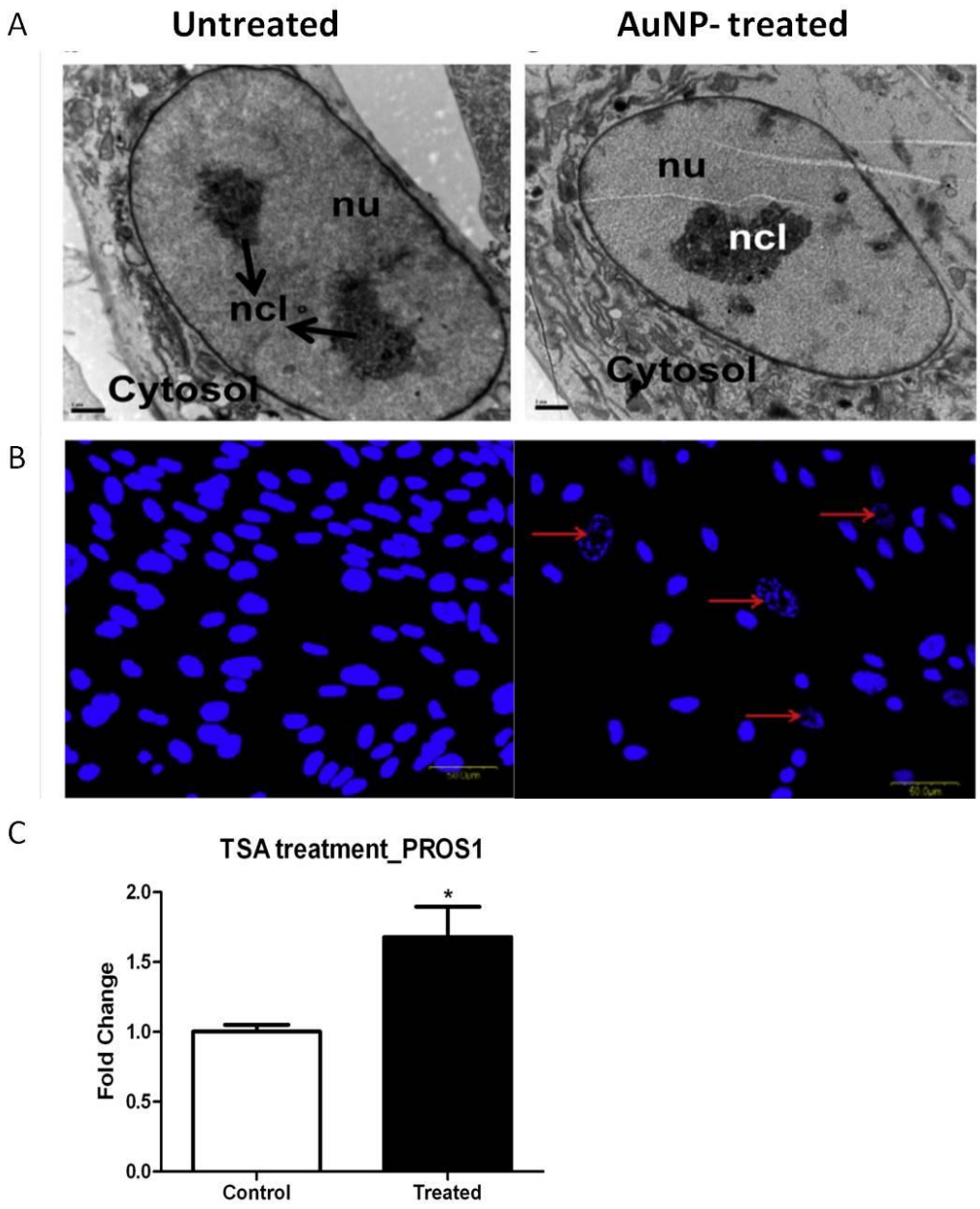

Figure 3.44: Histone modification and its effects on gene expression. (A) EM micrograph on chromatin condensation pattern in AuNP-treated MRC5 cells and large dark bodies are denoted as nucleoli (ncl). Chromatin reorganization was seen as electron-dense heterochromatin areas in the nucleus of AuNP-treated cells that are not present in untreated cells. Scale bar: 2 µm. (B) The morphological appearance of the confocal microscopic image following DAPI staining to stain the nucleus. (Left) Micrograph shows the normal morphology of nucleus. (Right)There was visible nuclear condensation in the nuclei. (C) TSA treatment reversed the inhibition on *PROS1* gene expression. Error bar=SEM; *p< 0.05.

3.4 Biological effects of AuNPs in a co-culture system

3.4.1 Differential protein expression induced by AuNP-exposed SAECs in neighboring lung fibroblasts

SAECs were co-cultured in the upper chamber of a Transwell polycarbonate membrane with SILAC-labelled MRC5 lung fibroblasts in the lower chamber. AuNP pre-exposed to SAECs were subsequently co-cultured with lung fibroblasts to mimic the physiological environment present in the lung.

To ensure that the downstream effects observed later in MRC5 fibroblasts were triggered by cellular crosstalk and not due to AuNPs which could have leaked through the membrane pore, TEM on MRC5 fibroblasts after co-culturing was performed. There were no AuNPs found in both the cytoplasm and nucleus of the MRC5 fibroblasts (Fig 3.45).

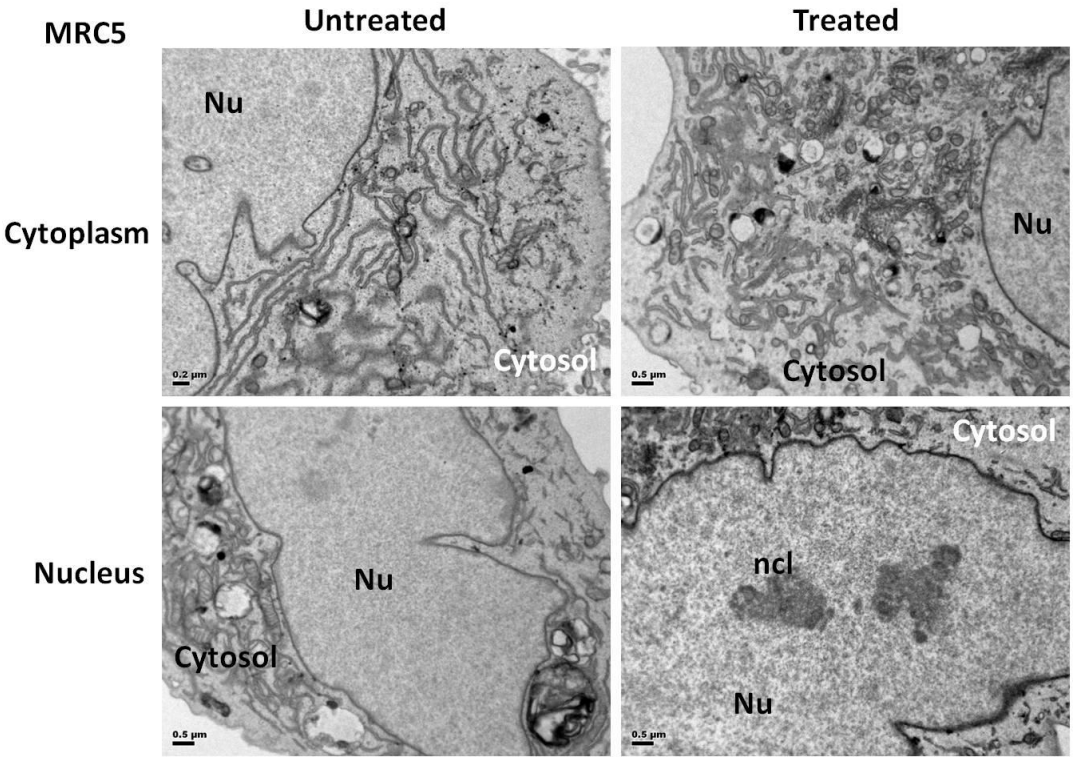

Figure 3.45: EM micrographs of MRC5 cells after co-cultured with AuNP pre-exposed SAECs. Micrographs show that there were no AuNPs found at both cytoplasm and nucleus of the cells, similar with control untreated co-cultured MRC5 cells.

(A) SILAC proteomic analysis

Proteins from the SILAC-labeled MRC5 lung fibroblasts were isolated after 72 h of co-culturing with SAECs for quantitative proteomics analysis. Prior to this, incorporation check was performed and a good incorporation efficiency of 97% was achieved, indicating a successful metabolic incorporation of stable isotope labeled amino acid Arginine and Lysine into MRC5 fibroblasts (Fig 3.46). Based on replicates of the forward and reverse experimental sets, over 3000 proteins were quantified and applied statistical processing to derive high confidence datasets. Protein ratios with significant values of p(forward)<0.05 and p(reverse)<0.05 were considered as differentially expressed proteins. Using these criteria, there were 47 up-regulated proteins and 62 down-regulated proteins being identified in the lung fibroblasts (Table 3.7, 3.8).

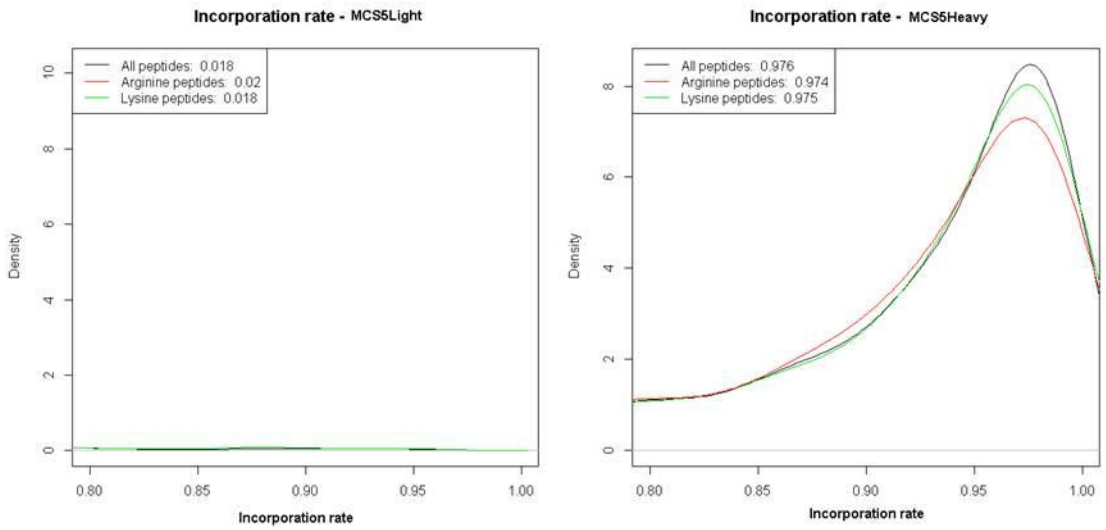

Figure 3.46: Labeling efficiencies for light- and heavy-labeled peptides were determined and clearly distinguishable by using MS analysis. MRC5 cell protein lysates were removed earlier on to check incorporation of the light and heavy amino acids after 4-5 doubling times and revealed a successful and high incorporation rate. (A) Incorporation rate of light peptides and (B) heavy peptides which yields a 97.6% incorporation rate.

Table 3.7: 47 up-regulated proteins in MRC5 fibroblasts based on quantitative mass spectrometry.

Gene Name	Normalized H/L		p(Fwd)xp(Rev)	Counts
	Forward	Reverse		
PDIA5	5.4591	0.60086	6.13E-135	1
PLIN2	4.3003	0.18267	2.83E-114	9
SLC2A14;SLC2A3	3.6165	0.37036	8.98E-100	10
NDRG1	3.341	0.21767	2.09E-67	22
NMES1	3.3287	0.46204	1.04E-28	1
SLC2A1	3.1503	0.39533	2.39E-85	25
FTL	3.0698	0.50011	1.92E-51	35
RHOB	2.2926	0.44888	1.11E-15	3
FTH1	2.1853	0.3553	7.11E-21	66
IRS2	2.111	0.529	1.09E-09	1
DEK	2.0135	0.69679	2.45E-13	10
AHNAK2	1.9154	0.68351	1.43E-08	5
HK2	1.8372	0.58478	1.89E-16	20
ERO1L	1.8056	0.48635	3.19E-11	22
BCAR1	1.8025	0.47369	1.46E-14	8
UAP1	1.7718	0.63016	1.19E-09	18
FAM107B	1.7716	0.6019	4.68E-07	2
PLOD2	1.7673	0.53173	3.46E-10	65
TPBG	1.7617	0.51584	1.08E-10	11
CDK6	1.7383	0.60224	2.17E-07	3
ENO2	1.6915	0.37861	3.98E-15	15
SLC7A5	1.6912	0.62297	5.79E-08	6
S100A10	1.6743	0.53803	3.55E-09	13
AKAP2	1.6273	0.71723	9.71E-07	15
INF2	1.5444	0.71692	9.67E-06	22
PGM2L1	1.5031	0.69229	1.56E-04	3
LOX	1.4909	0.35849	2.56E-09	5
RRAGC;RRAGD	1.4891	0.66958	1.27E-04	3
PTTG1IP	1.4888	0.6217	9.57E-07	6
GBE1	1.4869	0.62165	1.63E-05	56
CAV1	1.4847	0.62148	6.56E-08	24
C4orf3	1.4687	0.62623	8.61E-05	4
PXN	1.4679	0.62124	1.06E-05	10
FAM129A	1.4277	0.5735	8.21E-05	4
ASNS	1.4219	0.49107	4.95E-07	25
PRKCDBP	1.4184	0.64449	5.05E-05	7
CRIP2	1.4127	0.7025	1.19E-04	6
KIAA1609	1.3935	0.68247	3.83E-05	3
BNIP3L;BNIP3	1.3932	0.49714	4.70E-05	2

SLC25A4	1.3719	0.65692	7.59E-04	3
DEGS1	1.354	0.66756	9.14E-05	4
KIAA1715;LNP	1.3459	0.62208	6.97E-04	1
EFTUD1	1.3438	0.68398	1.52E-03	5
FAM210A	1.3191	0.68605	1.88E-03	2
MAP2K1	1.2962	0.69139	1.46E-04	12
PGRMC1	1.2882	0.71251	2.63E-04	14
VKORC1	1.2472	0.62735	6.69E-04	8

Table 3.8: 62 down-regulated proteins in MRC5 fibroblasts based on quantitative mass spectrometry.

Gene Name	Normalized H/L		p(Fwd)xp(Rev)	Counts
	Forward	Reverse		
NACA	0.79062	1.2567	1.87E-03	14
DDX5	0.76527	1.5726	1.72E-07	33
HIST1H1B	0.7462	1.3763	1.82E-04	10
PCNA	0.7396	1.2926	2.62E-04	23
SERPINB2	0.73444	1.3664	4.25E-05	30
G3BP1	0.73344	1.3609	4.74E-05	28
PSME3	0.73332	1.5614	3.98E-06	18
ITGA1	0.72895	1.3761	3.18E-04	41
PRMT1	0.72859	1.3563	4.64E-05	32
AASDHPPT	0.72169	1.3848	6.90E-04	7
FASN	0.71522	1.6752	7.94E-10	193
RANGAP1	0.7126	1.34	1.32E-04	29
G3BP2	0.71001	1.3228	1.53E-03	10
KIAA0664	0.70684	1.5065	4.78E-05	21
HIST1H1C	0.69903	1.3046	6.44E-05	16
GPX4	0.69785	1.5034	1.80E-04	5
KPNA2	0.69768	2.1906	2.76E-18	14
ATXN10	0.6938	1.4889	5.43E-05	7
MAT2A	0.69175	1.4271	8.63E-06	14
VWA5A	0.68396	1.8526	4.52E-11	30
TFRC	0.6814	1.6278	2.00E-09	57
HIST1H1E	0.66914	1.3088	8.38E-04	2
HNRNPL	0.66636	1.5016	1.02E-05	12
CAPRIN1	0.66313	1.5067	3.33E-06	19
CHD4	0.66269	1.4346	2.73E-04	27
STAT1	0.66004	1.2437	6.23E-05	39
SOD2	0.65974	1.4192	1.11E-06	43
RBBP4	0.64746	1.4318	6.53E-05	6
TGM2	0.62083	2.1027	2.35E-21	37
NUP160	0.61909	1.7419	1.74E-04	5
RBM4;RBM4B	0.61524	1.5384	1.24E-04	3
PELP1	0.6078	2.1472	1.79E-07	4
RRM1	0.60579	1.9317	1.58E-11	13
DDX18	0.60532	1.5384	7.67E-04	5
RNF181	0.60477	1.6514	1.03E-03	2
CSDA	0.60371	1.3085	4.37E-05	6
LARP4	0.60174	1.5805	4.15E-04	1
DNMT1	0.57596	1.9552	1.29E-09	12
PABPN1	0.5711	1.3895	7.00E-04	2
C1orf198	0.55695	2.0824	2.30E-06	2
GALNT5	0.54578	1.6776	3.27E-05	9

RANBP2	0.54531	1.9551	1.75E-07	7
CTGF	0.51782	2.0994	3.59E-09	5
IGFBP4	0.50764	2.0219	1.82E-07	7
HNRNPC	0.49956	2.5119	3.17E-25	11
TYMS;TS	0.49653	1.8434	8.27E-09	6
SPARC	0.48948	1.3466	7.67E-05	6
CYP51A1	0.4882	1.6908	1.04E-04	1
WNT5A	0.47709	1.9729	4.27E-08	2
BRIX1	0.47247	1.6834	5.94E-05	2
ACSL4	0.46869	1.9827	1.31E-16	18
FADS2	0.46501	2.2737	1.15E-11	5
PLAU	0.44408	3.0376	3.57E-18	1
COL3A1	0.43769	1.3665	5.94E-08	24
SORT1	0.419	2.033	2.40E-09	3
DHFR	0.38923	2.5522	5.54E-12	2
COL7A1	0.36909	1.3365	3.47E-09	64
TXNL1	0.33098	5.2248	1.17E-163	11
NDUFA4	0.32199	2.311	7.13E-21	13
SAA1	0.30659	4.894	4.02E-49	3
C3	0.27835	2.0353	8.01E-09	3
CXCL1	0.13417	4.2581	1.32E-59	4

(B) Pathway analysis of differentially expressed proteins

For further evaluation of the significance of the altered proteins in the MRC5 lung fibroblasts and elucidation of potential mechanistic pathways, up- and down-regulated proteins clusters were subjected to pathway analyses using the Gene Ontology (GO) program (Fig 3.47A). The results revealed that the dysregulated proteins were mainly involved in cell adhesion and extracellular matrix (ECM)/cytoskeleton remodeling (Fig 3.47B). Proteins associated with promoting cell migration such as Plasminogen activator, urokinase (PLAU, UPA) and chemokine growth-regulated oncogene 1 (GRO-1) were significantly down-regulated in MRC5 lung fibroblasts. These proteins are major hubs in the cell adhesion and migration pathway networks (Fig 3.47C).

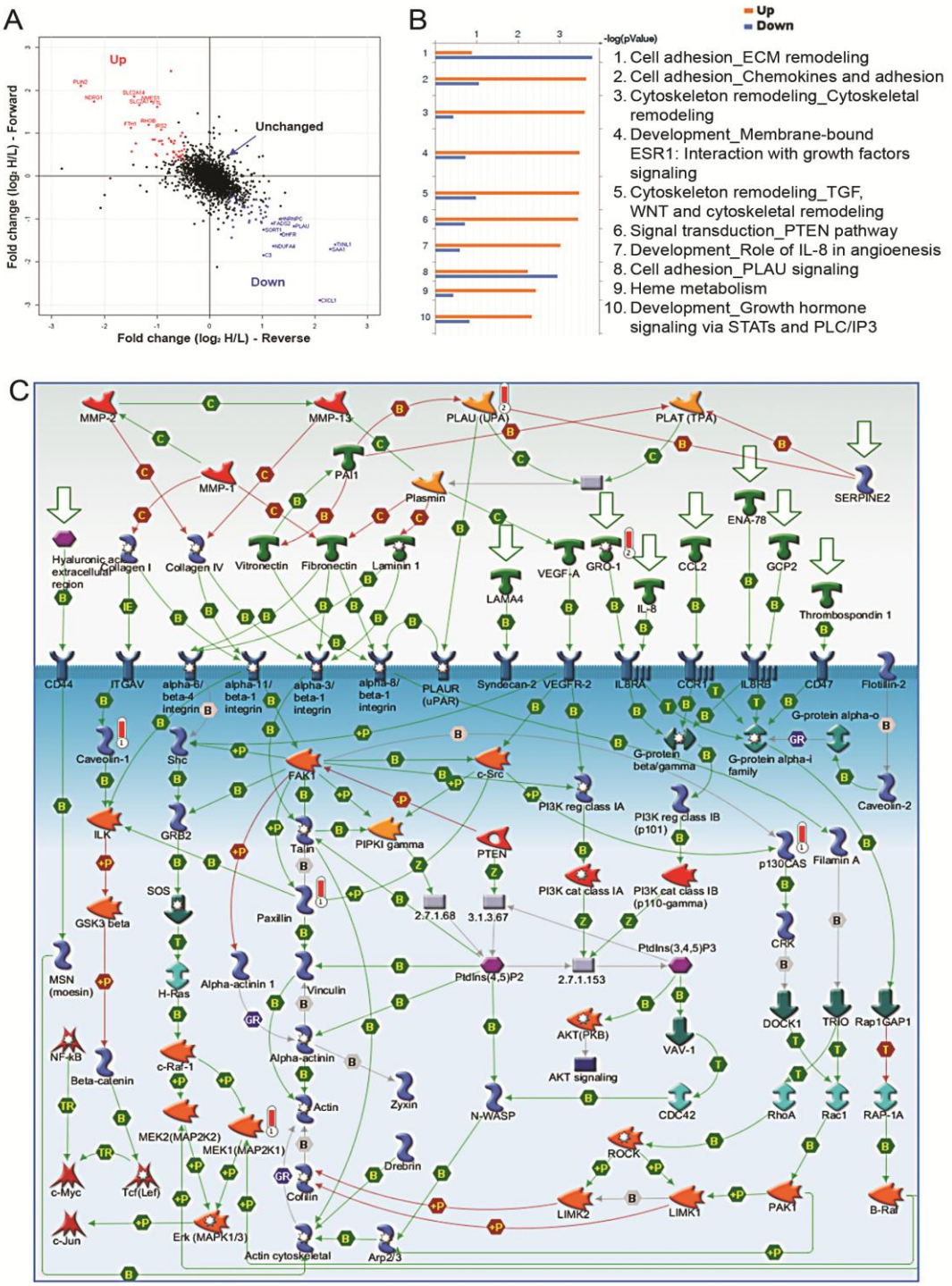

Figure 3.47: AuNP-treated SAECs induced differential protein expression in MRC5 lung fibroblasts. (A) The number of proteins with each ratio value was plotted on the y axis against log2 SILAC ratio values on the x axis. The abundance of each protein which is indicated by the position of the dot on the y axis was determined by summing all individual light and heavy peptide intensities. (B) GO (C) Protein interaction networks for the MRC5 proteins involved in cell adhesion. Four out of five proteins with high enrichment score were involved in regulating cell adhesion.

3.4.2 Cell adhesion and cytoskeleton staining in MRC5 lung fibroblasts

To address the importance of the three up-regulated adhesion proteins Paxillin (PXN), breast cancer anti-estrogen resistance 1 (BCAR1) and Caveolin-1 (Cav-1) with regard to cell adhesion, the differences in adhesive ability using different substrate coating were evaluated. MRC5 lung fibroblasts co-cultured with AuNP-exposed SAECs exhibited a significant increase in cell adhesion towards fibronectin (Fig 3.48A), as well as Collagen I (Fig 3.48B), compared to the control. As up-regulation of PXN, BCAR1 and Cav-1 are known to be involved in FA formation and regulate local FA dynamics, possible disruption of the cytoskeleton in the MRC5 lung fibroblasts was further examined. Indeed, there was altered F-actin arrangement in the cytoskeleton of the MRC5 lung fibroblasts, coupled with an increase in stress fiber or FA formation (Fig 3.48C) and an increase in vinculin binding sites, which are involved in anchoring F-actin to the cell membranes of the fibroblasts (Fig 3.48D).

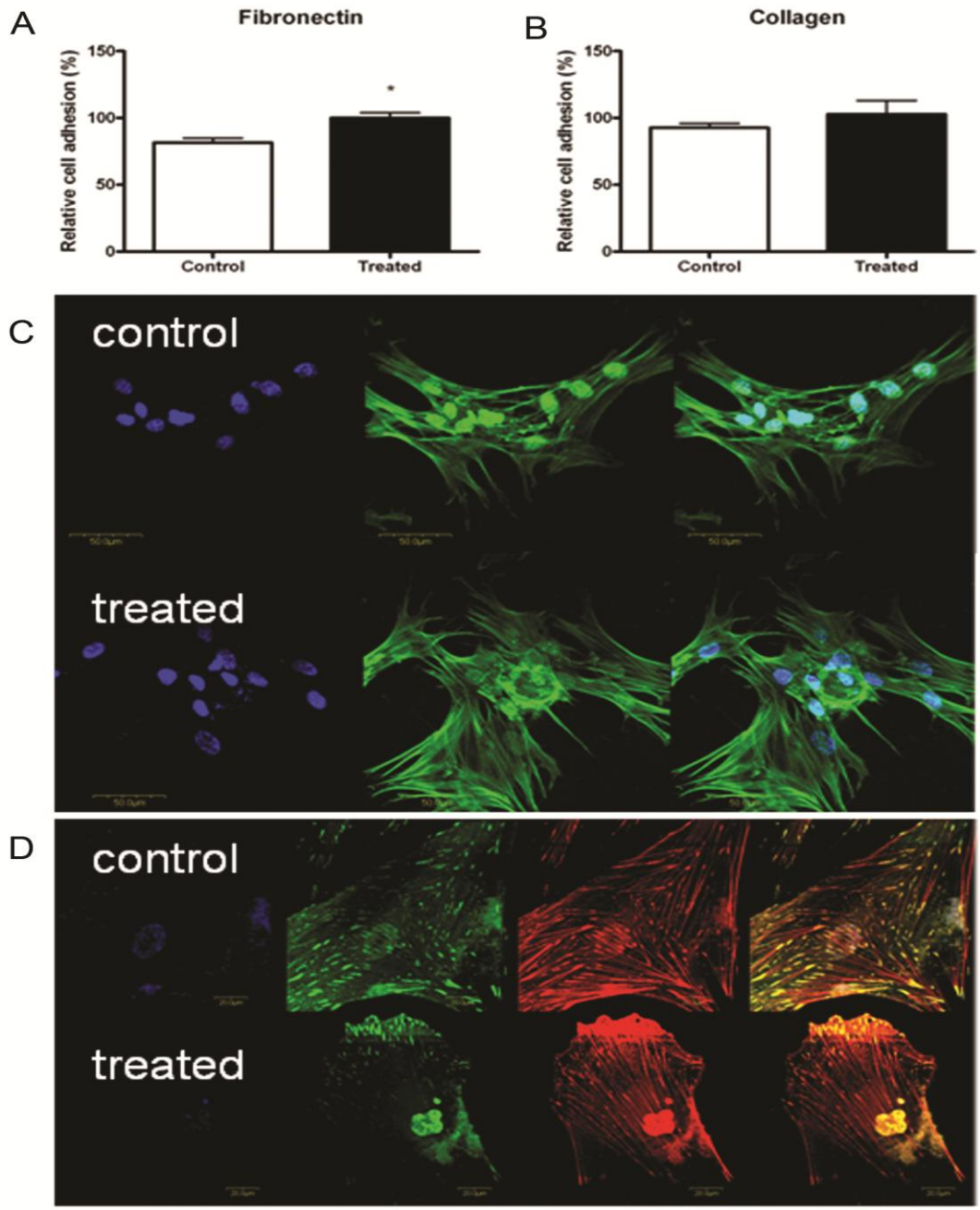

Figure 3.48: Cell adhesion and cell cytoskeleton remodeling. (A) Cell adhesion on fibronectin substrate was approximately 19% higher compared to control MRC5 lung fibroblasts, Error bar=SEM; *$p<0.05$. (B) Cell adhesion on collagen I substrate showed an increase percentage of adhered cells compared to control lung fibroblasts. (C) MRC5 lung fibroblasts co-cultured with SAECs treated with or without AuNPs were stained for F-actin (green) and DAPI (blue). Lung fibroblasts co-cultured with AuNP-treated SAECs exhibited an increase in stress fibers with enrichment at the cell membrane and adhesion sites. Scale bar =20 µm. (D) Alteration of adhesion dynamics in lung fibroblasts co-cultured with AuNP-treated SAECs, showing an increase in vinculin (in green) adhesion sites in anchoring F-actin (in red) to cell membrane. Scale bar =20 µm.

3.5 Biological effects of AuNPs in an *in vivo* model

3.5.1 Dosimetry of AuNPs

ICP-MS analysis of the AuNP stock formulation gave a concentration of 256 µg/ml; thus, single dose at 0.1 mg/kg of the formulation would correspond to ≈ 20 µg of Au, on the basis that a single IV injection was performed into a 200 g rat (assuming even AuNP distribution inside rat body). The dose used for animal study is equivalent to the dose used in a Phase I clinical trial (Libutti et al., 2010), so as to achieve a physiologically relevant dose. The highest dose of AuNPs used in this study (0.2 µg/g) is on the lower side of doses that have been reported in available published literature, which ranges from 0.01 µg/g to 2700 µg/g (Khlebtsov and Dykman, 2011).

3.5.2 Biodistribution of AuNPs

The results of the biodistribution studies after 1 week, 1 month and 2 months post single IV injection are given in Table 3.9 and visualized in Figure 3.49. Au was detected at levels exceeding those of the control rats, and consistently found in the lungs for all treatment groups. Au uptake was the highest in 0.025 mg/kg/p.e 1week rat and lowest in 0.1 mg/kg/p.e 1 month rat, where the average concentrations were 100.8 ng/g and 28.02 ng/g, respectively (Table 3.9). However, it was observed that the level of Au in the lung showed a decrease with time post 1-week, 1 month and 2 months injection (from 64.61 ng/g to 28.02 ng/g) with the same single exposure dose of 0.1 mg/kg, suggesting clearance from the respiratory organ. No traces of Au were detected in the blood of all AuNP-injected rats following injection. As expected, the animals administered with UP water showed negligible Au accumulation. Accumulation of AuNPs in organs such as kidneys and liver decreased over time, indicating that the AuNPs were slowly being cleared (data not shown).

Table 3.9: Biodistribution of Au in rats at 5 doses and 3 time points.

Dose/ Time	*Control; 2 months*	*0.025mg/kg ; 1 week*	*0.05mg/kg; 1 week*	*0.1mg/kg ; 1 week*	*0.2mg/kg ; 1 week*	*0.1mg/kg ;1 month*	*0.1mg/kg; 2 months*
Lung	$0.2x10^{-7}$±18.28	100.8±117.8	96.51±43.5[a**]	64.61±30.1[a**]	51.53±19.02[a*]	58.96±42	28.02±51.94
Kidney	$1.8x10^{-2}$±6.465	13.42±9.508	1.964±14.77	3.692±29.77	12.6±32.97	5.695±12.61	38.06±30.47
Liver	536.7±583.4	NA	NA	NA	2172±2408	4.074±15.16	95.42±189.9

Values indicate mean concentration and standard deviation (ng/g of tissue).
[a] Indicates significant increase compared to non-injected controls based on independent-t test.
There wasn't a significant difference for all comparison using one-way ANOVA with Tukey's post-hoc test. P>0.05.

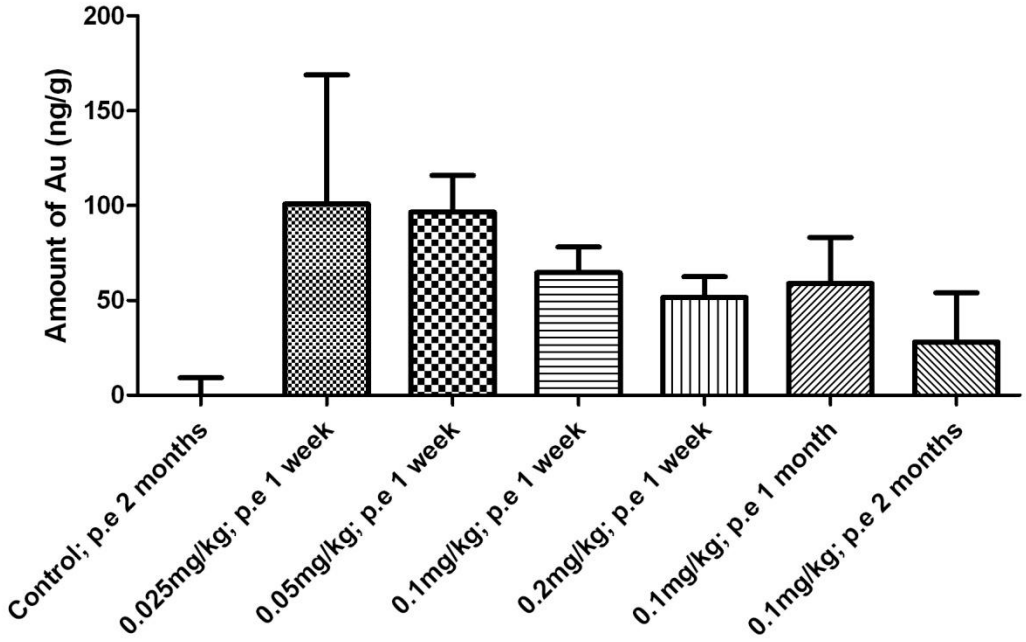

Figure 3.49: Amount of deposited Au measured with ICPMS in the seven experimental groups. In comparison with rats untreated only with AuNPs (below the detection limit), the amount of deposited Au was not significantly different in rats among all the treated groups injected IV once with AuNPs. P.e= post exposure; Error bars=SEM.

3.5.3 Gross observation and body weight changes

The body weight of the rats was monitored and weighed before necropsy. The injections were well tolerated and no adverse effects were observed during the entire experiment (Fig 3.50). There was no lethal effect observed on rat injected with AuNPs. No severe sickness, loss of appetite, weight loss, change in fur color, and shorter average lifespan were observed.

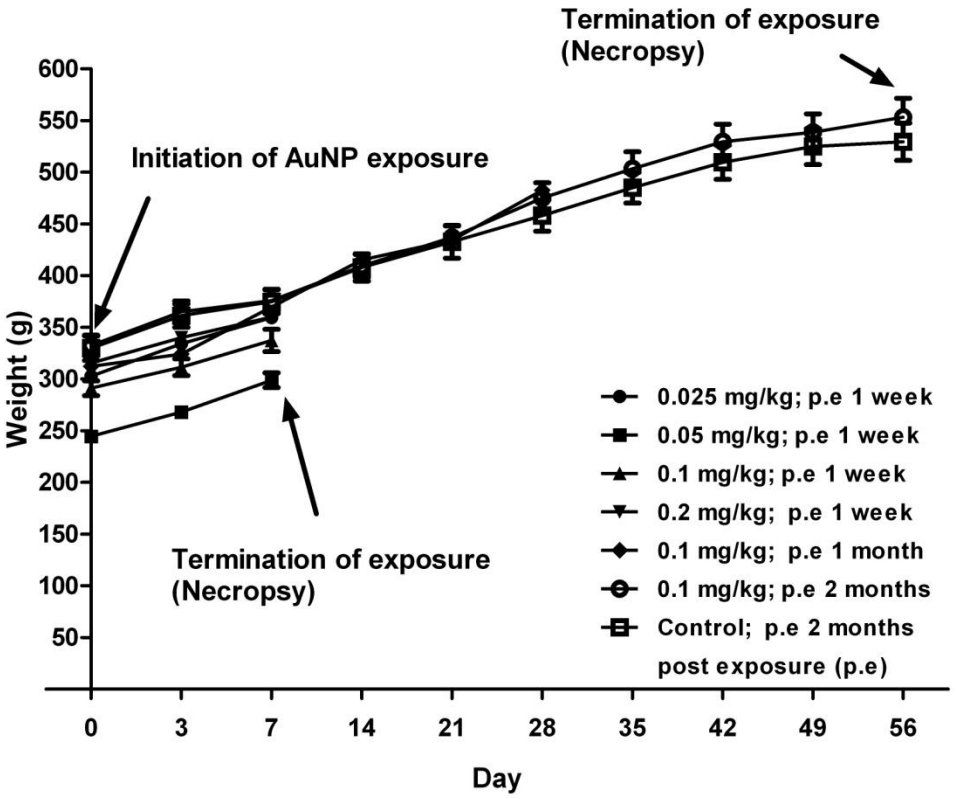

Figure 3.50: Body weight of 7 male *Wistar* rat groups. The body weight was weighted every alternate day from period of 1 week to 2 month experiment period for every experimental groups and control groups. There was no mortality observed in this study. Animals of AuNP-treated groups showed normal and consistent gain in body weight when compared to the control group of animals. The IV injection of AuNPs of six different doses for different duration did not cause significant death and weight loss in *Wistar* rats.

3.5.4 Effects of AuNP exposure on inflammatory cytokine expression

Changes in serum cytokine expression following single dose of AuNP treatment were also noted in this study. There was a significant increase of cytokines in the serum of treatment groups, suggesting the presence of inflammation. 1 week, 1 month and 2 months after single injection of 0.1 and 0.2 mg/kg of AuNPs showed mild systemic inflammation as assessed by blood serum cytokine level using ELISA. Significant expression was observed in serum Transforming growth factor beta (TGF-β) expression in single dose of 0.1 mg/kg AuNP-treated rats post-exposed for 1 week, 1 month and 2 months, as compared to controls (Fig 3.51A). However, at low dose of AuNPs (0.05 mg/kg; p.e 1 week), there was no significant inflammation observed. Proinflammatory cytokine Interleukin 6 (IL-6) expression was significantly higher in 0.1 mg/kg AuNP treated rats and persisted up to 2 months post exposure (Fig 3.51B). Another proinflammatory cytokine, IL-1α, was found to be expressed highly in 0.1 mg/kg and 0.2 mg/kg; p.e 1 week AuNP treated rats (Fig 3.51C).

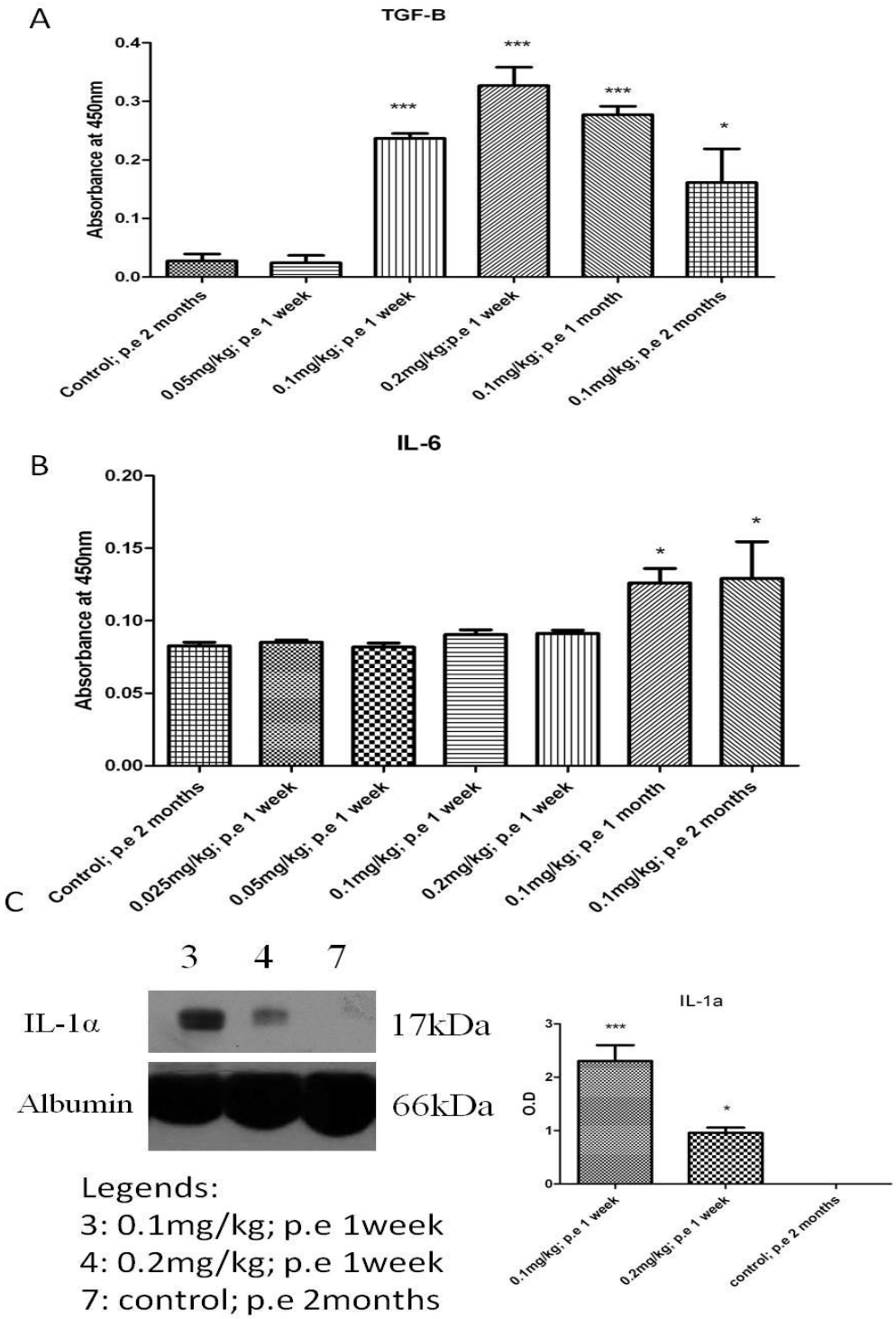

Figure 3.51: Anti- and pro-inflammatory cytokine expression in rat plasma. (A) TGF-β and (B) IL-6 in rat plasma. There was a significant change in inflammatory cytokines, especially for rats exposed to AuNP for 1 month & 2 months. (C) IL-1α in rat plasma was significantly higher in 1 week AuNP exposed rats. P.e= post exposure; Error bar=SEM; *p <0.05; ***p <0.001.

3.5.5 Prothrombin time (PT) test

The Prothrombin time (PT) test was performed using *ex vivo* whole plasma from *Wistar* rats. The plasma was clotted using thromboplastin and $CaCl_2$. In this test, blood clot formation occurred after the addition of $CaCl_2$. The clotting process proceeded normally for control group, 0.025 mg/kg; p.e 1 week and 0.05 mg/kg; p.e 1 week AuNP-exposed group. However, when compared with AuNP unexposed rats, PT was significantly higher in rats injected with single dose of 0.2 mg/kg; p.e 1 week and 0.1 mg/kg; p.e 1 month (Fig 3.52A), indicating the influence of AuNPs on the coagulation pathway. PT was prolonged in both 0.2 mg/kg; p.e 1 week and 0.1 mg/kg; p.e 1 month AuNP-exposed rats as compared to rats exposed to 0.1 mg/kg; p.e 2 months and unexposed rats (Fig 3.52B). Notably, rats exposed to single dose of 0.1 mg/kg for 2 months rats had reversal of prolonged PT, indicating a recovery from AuNP-induced inhibitory effects on blood coagulation, although there was partial coagulation observed in one of the samples.

A

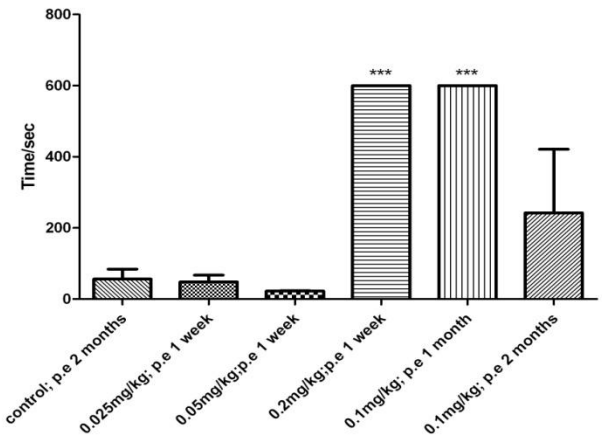

B

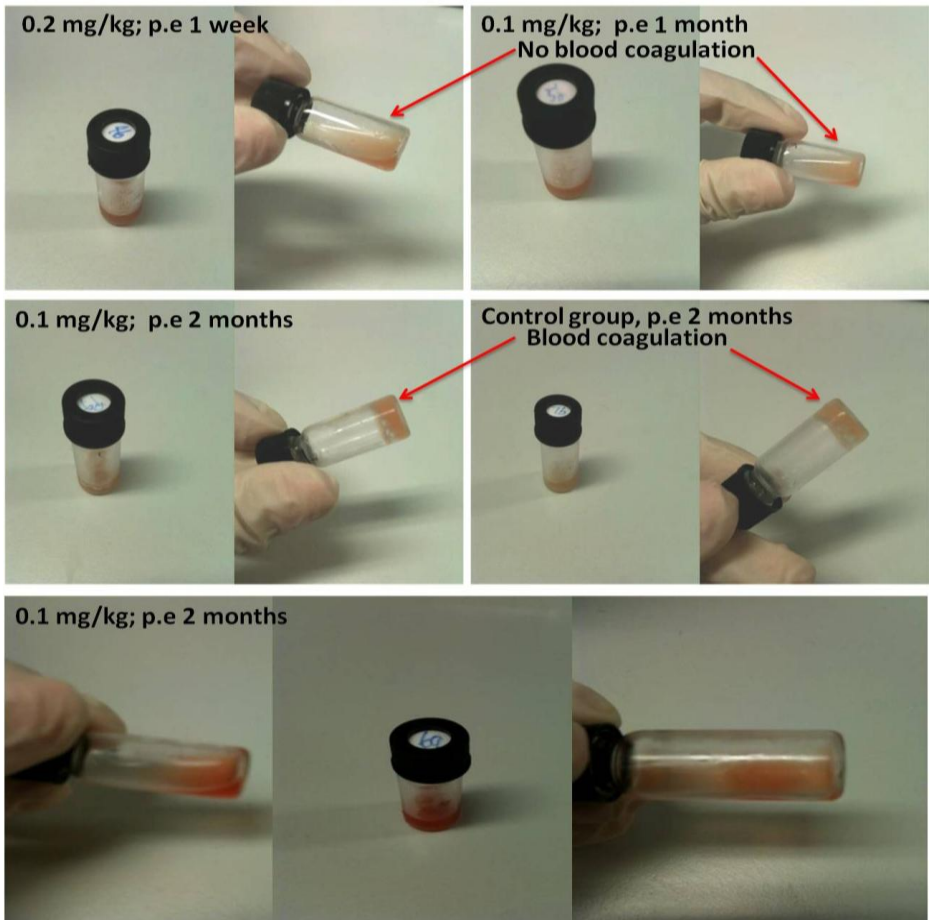

Figure 3.52: Prothrombin time (PT) was prolonged in 0.2 mg/kg; 1 week and 0.1 mg/kg; 1 month AuNP-exposed rats. (A) PT test for rats treated with AuNPs. AuNPs increased prothrombin time/ coagulopathy in rats. (B) The 0.2 mg/kg; 1 week and 0.1 mg/kg; 1 month rat blood plasma did not form a blood clot after 600 seconds. There was formation of blood clot observed in rats exposed to 0.1mg/kg for 2 months and control rats. In 0.1 mg/kg; 2 months AuNP-exposed rat, there was partial/incomplete blood coagulation observed. P.e= post exposure

3.5.6 *PROS1* gene expression in rat lung tissues

As *PROS1* gene expression was found to be altered in MRC5 cells, RT-PCR on *PROS1*, together with *SERPINE1* and *TF* was performed. It was observed that there was a significant increased in *PROS1* gene expression, an upstream target for *SERPINE1*, in 0.2 mg/kg; p.e 1 week AuNP-exposed rats (Fig 3.53). This is also accompanied by a decrease in the expression of *TF* (the primary initiator of coagulation). TF, a key mediator of the activation of coagulation in the lung, which was decreased in 0.2 mg/kg; p.e 1 week and 0.1 mg/kg; p.e 1 month AuNP-exposed rats.

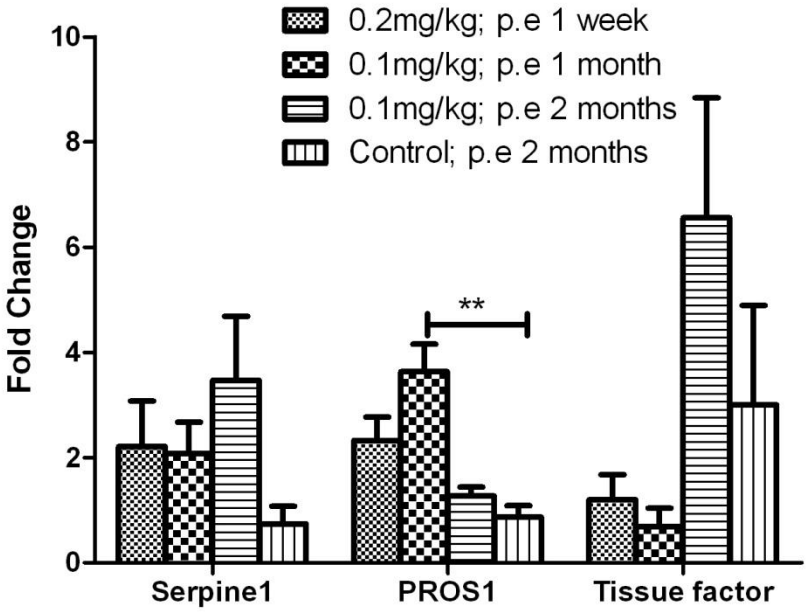

Fig 3.53: *PROS1* gene expression levels in rat lung tissues. There was a significant increase in the pulmonary expression of *PROS1* in single dose 0.1 mg/kg; 1 month rats post AuNP exposure in rats. On the other hand, TF expression was decreased in the 0.1 mg/kg; 1 month post exposure rats. P.e= post exposure; Error bar=SEM; *p <0.05; **p <0.01.

3.5.7 Histopathology of lung tissues

Histpathological analysis was performed on sections of the lungs, for pathological changes. The histopathological examination of the lung revealed signs of focal inflammation with influx of lymphocytes in AuNP-treated rats (Fig 3.54), which were absent in control rats.

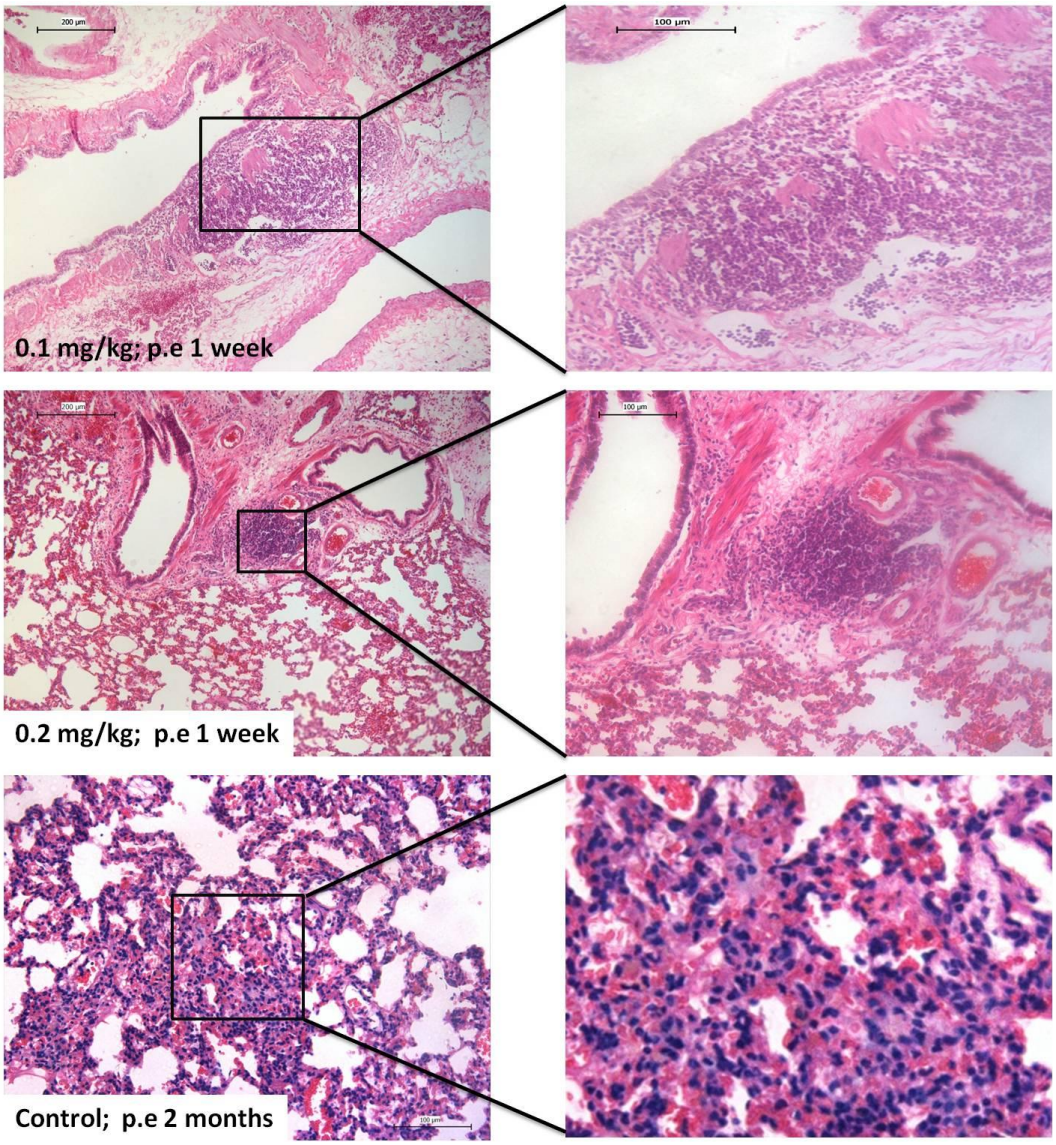

Figure 3.54: Photomicrographs of sections representative of the histological changes observed. In 0.1 mg/kg and 0.2 mg/kg; 1 week post exposure AuNP-treated rats, there were areas with lymphocytic infiltration. High-power magnification (on the right) shows the enlarged boxed area with lymphocytes. The results indicate the presence of inflammation in the rat lung after IV injection of AuNPs in comparison with unexposed control. P.e= post exposure; Scale bar: 200 µm and 100 µm.

Other than induction of plasma IL-1α, expression of IL-1α in rat lung tissues was also studied using IHC. Concomitant with influx of lymphocytes as observed in Figure 3.54, there was a dose-dependent increase in IL-1α staining in 0.2 mg/kg; p.e 1 week AuNP-exposed rats as compared with 0.1 mg.kg; p.e 1 week AuNP-exposed rats. This results indicate that higher amount of AuNPs was capable of triggering more inflammatory response. Control unexposed rat lung tissue showed a faint staining for IL-1α (Fig 3.55).

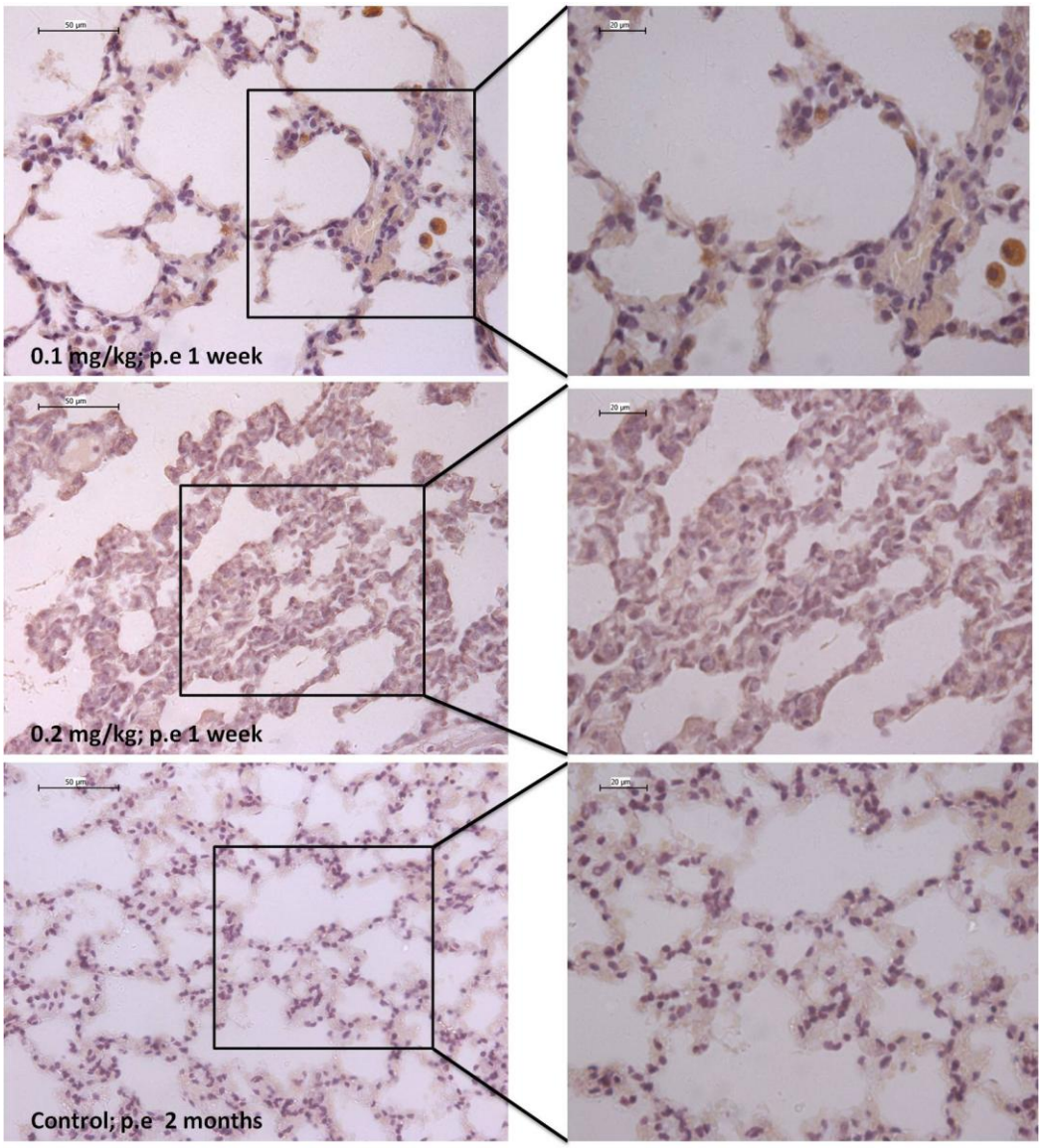

Figure 3.55: IHC staining for IL-1α (in brown) in rat lung tissues. Micrographs on the right (Scale bar: 50 µm) show higher magnification of micrographs on the left (Scale bar: 100 µm). P.e= post exposure

Other than lymphocytes, macrophages in the lung form the first line of defence in response to internal and external insults to the lung. An increased number of macrophages (Fig 3.56, Fig 3.57) and influx of lymphocytes suggested inflammation to the lung tissues.

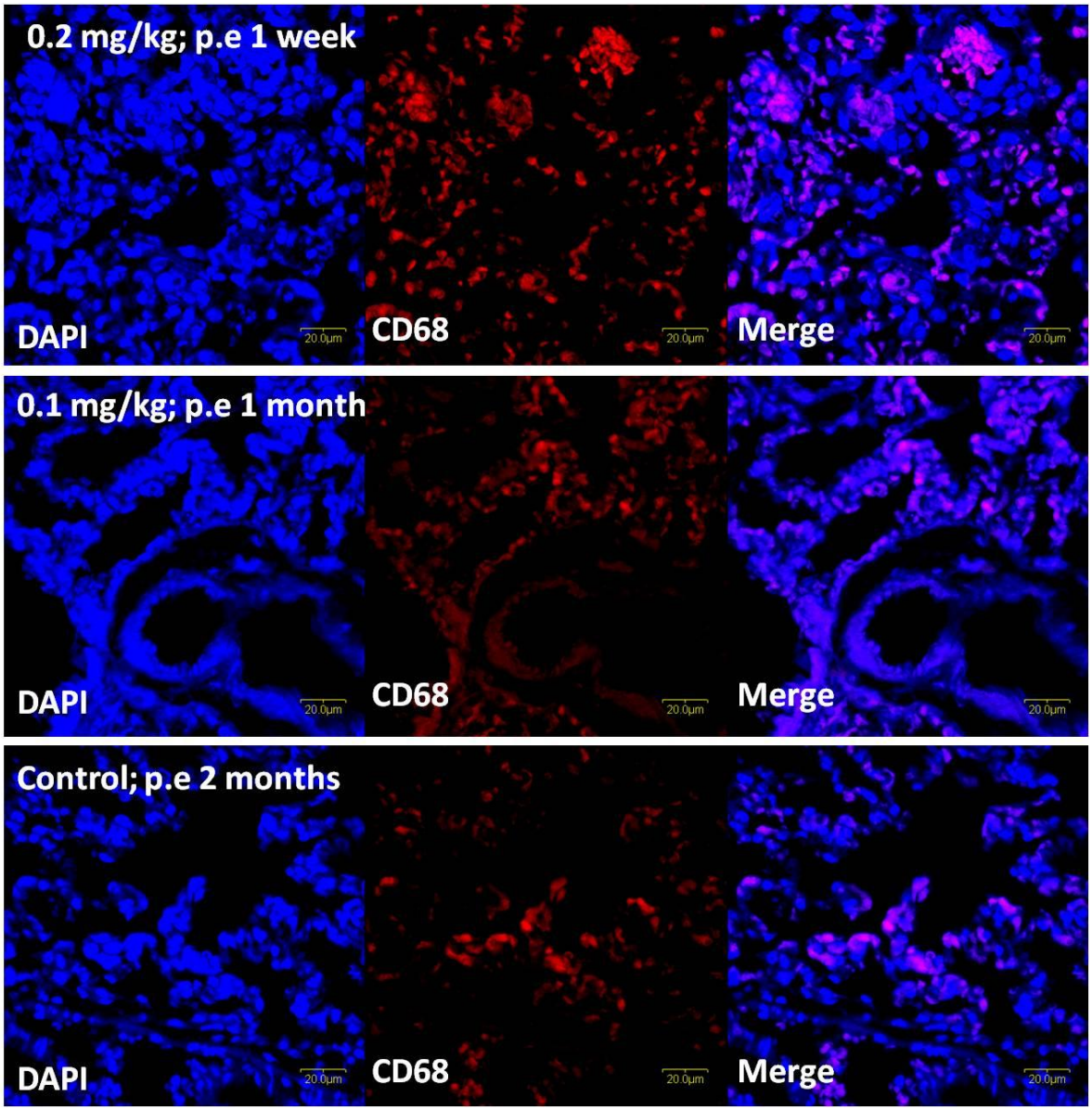

Figure 3.56 Immunofluorescent detection of macrophage in rat lung tissues. The distribution of fluorescence (in red) for CD68, a marker for macrophage in rat lung tissues was examined. The regions of greatest intensity of fluorescence was found in 0.2 mg/kg; 1 week AuNP-exposed rat; lesser intensity in 0.1 mg/kg; 1 month rats. Control rats exhibited CD68 staining too, indicated the presence of resident macrophages in lung. Scale bar: 20 µm. P.e= post exposure

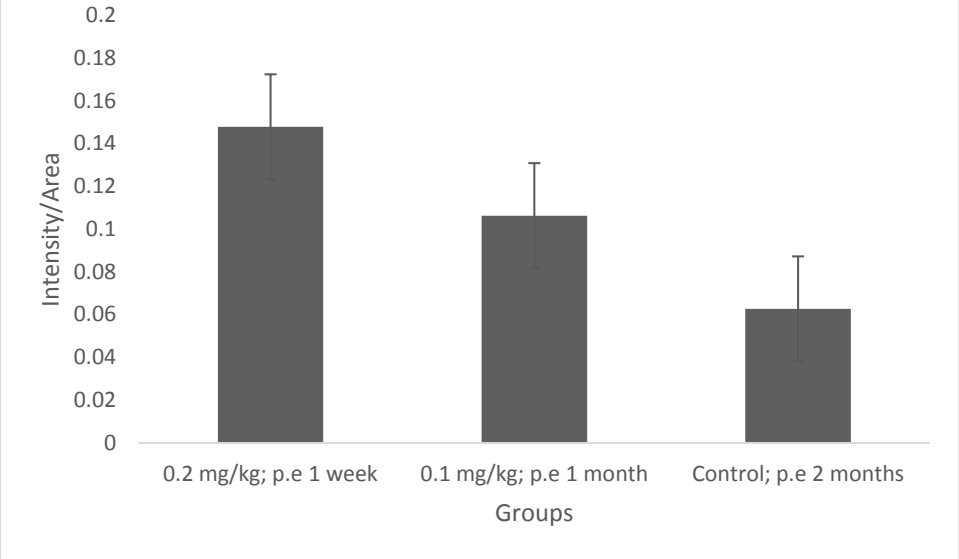

Figure 3.57 Quantitation of the fluorescence intensity of macrophage in rat lung tissues. The distribution of fluorescence intensity for CD68 is the greatest in 0.2 mg/kg; 1 week AuNP-exposed rat; lesser intensity in 0.1 mg/kg; 1 month rats. Control rats exhibited the least CD68 staining. Error bar=SEM; P.e= post exposure

3.5.8 Inflammatory and autoimmune response related miRNA superarray

To identify miRNAs which might play important roles in AuNP toxicity, restricted analyses focusing on inflammatory and autoimmune response was performed. The miRNA expression profile was found to be significantly altered in rats injected once with 0.1 mg/kg and 0.2 mg/kg of AuNPs and exposed for 1 week as compared with control rats. Out of 84 screened miRNAs, three significantly down-regulated miRNAs in rat lung tissues were miR-29b-3p and miR-327. Compared with control group, qRT-PCR results identified significant dysregulation of miR-140-5p and miR-327 in 0.1 mg/kg; p.e 1 week rats; and miR-29b-3p and miR-327 down-regulation in 0.2 mg/kg; p.e 1 week rats (Tables 3.10).

Table 3.10: Dysregulated miRNAs in rat lung tissues.

miRNAs	*Fold Regulation in 0.1 mg/kg; p.e 1 week*	*p-value*	*Fold Regulation in 0.2 mg/kg; p.e 1 week*	*p-value*
rno-let-7a-5p	-1.5987	0.377392	-1.518	0.28784
rno-let-7b-5p	1.1375	0.748189	-1.4408	0.303721
rno-let-7c-5p	-1.0537	0.746078	-1.1065	0.409145
rno-let-7d-5p	1.321	0.409699	1.2435	0.532552
rno-let-7e-5p	-1.0912	0.669534	-1.4926	0.283137
rno-let-7f-5p	-1.0766	0.84545	-1.0693	0.92495
rno-let-7i-5p	-1.7808	0.423329	-1.3422	0.320175
rno-miR-101a-3p	1.8065	0.725296	-1.1982	0.356135
rno-miR-101b-3p	2.148	0.656941	1.0318	0.439434
rno-miR-106b-5p	1.0698	0.74723	-1.2157	0.277403
rno-miR-125a-5p	1.1507	0.879843	-1.1681	0.170959
rno-miR-125b-5p	-1.286	0.389319	-1.2464	0.194409
rno-miR-128-3p	1.8421	0.928627	2.0044	0.355946
rno-miR-136-5p	-10.6111	0.138094	-4.7738	0.090587
rno-miR-140-5p	**2.3299**	**0.040413**	1.4865	0.217244
rno-miR-141-3p	2.5632	0.152477	-1.0025	0.851235
rno-miR-142-3p	1.6901	0.260848	2.1199	0.118308
rno-miR-144-3p	1.7774	0.26639	-3.3497	0.081302
rno-miR-145-5p	1.0514	0.435742	-1.2831	0.30982
rno-miR-148b-3p	1.0083	0.525642	-1.6989	0.14627
rno-miR-152-3p	1.1783	0.419153	-1.1074	0.940519
rno-miR-15b-5p	1.2942	0.703103	1.426	0.698452
rno-miR-16-5p	-1.2472	0.527782	-1.7009	0.118086
rno-miR-17-5p	1.0733	0.885538	-1.2616	0.239769
rno-miR-181a-5p	5.4806	0.315947	2.9008	0.888551
rno-miR-181b-5p	2.8706	0.183425	1.9726	0.514787
rno-miR-181c-5p	2.4091	0.353894	1.4664	0.936107
rno-miR-181d-5p	3.2303	0.272705	1.3028	0.830934
rno-miR-182	1.2914	0.808115	-1.1651	0.40767
rno-miR-183-5p	3.9643	0.240197	2.2358	0.530359
rno-miR-186-5p	2.2634	0.172856	-1.3532	0.577474
rno-miR-195-5p	-1.2782	0.436874	-1.8332	0.144182
rno-miR-19a-3p	-1.1392	0.347601	-1.2906	0.241939
rno-miR-19b-3p	1.9278	0.922583	1.596	0.849849

rno-miR-200a-3p	-1.0134	0.385322	-1.887	0.211852
rno-miR-200c-3p	1.5166	0.82188	1.1599	0.414088
rno-miR-203a-3p	-1.2557	0.557842	-1.3006	0.365274
rno-miR-205	1.2821	0.745461	-1.5056	0.169321
rno-miR-20a-5p	1.4012	0.594993	1.5676	0.352609
rno-miR-20b-5p	1.4612	0.304098	-1.0181	0.782896
rno-miR-21-5p	1.0393	0.859986	-1.0002	0.997611
rno-miR-221-3p	1.2042	0.800468	-1.5474	0.074098
rno-miR-222-3p	1.4622	0.822264	1.401	0.853995
rno-miR-23a-3p	1.0371	0.938106	-1.5491	0.162065
rno-miR-23b-3p	-1.1086	0.987966	-1.2251	0.572609
rno-miR-26a-5p	1.197	0.487675	-1.0976	0.731339
rno-miR-26b-5p	-5.5197	0.856543	-1.024	0.935448
rno-miR-27a-3p	1.8343	0.159152	1.0787	0.908668
rno-miR-27b-3p	-1.0017	0.932404	-1.1636	0.441435
rno-miR-291a-3p	-12.3147	0.084167	-7.5864	0.068704
rno-miR-29a-3p	-1.7434	0.11738	-1.8018	0.750108
rno-miR-29b-3p	-2.3051	0.191506	**-4.5094**	**0.022434**
rno-miR-29c-3p	-1.9427	0.180824	-2.6236	0.068012
rno-miR-30a-5p	-1.0166	0.702256	-1.7904	0.139807
rno-miR-30b-5p	1.1494	0.567398	-1.7255	0.090116
rno-miR-30c-5p	1.135	0.592135	-1.9289	0.097851
rno-miR-30d-5p	-1.1318	0.547435	-1.8733	0.217862
rno-miR-30e-5p	-1.3488	0.258921	-2.1174	0.082282
rno-miR-320-3p	1.2408	0.531505	-1.6922	0.343749
rno-miR-322-5p	-1.4606	0.441302	-1.4653	0.487905
rno-miR-323-3p	-11.2582	0.289463	-6.8182	0.202823
rno-miR-325-3p	-9.9159	0.1702	-6.9777	0.110941
rno-miR-327	**-5.881**	**0.02188**	**-8.4062**	**0.013541**
rno-miR-34a-5p	3.0584	0.272134	1.8963	0.937354
rno-miR-34c-5p	1.3411	0.370652	1.8404	0.646683
rno-miR-351-5p	-1.5468	0.301245	-1.0805	0.325644
rno-miR-369-3p	-11.9486	0.174489	-8.9264	0.115413
rno-miR-374-5p	-1.3261	0.82026	-1.6879	0.43963
rno-miR-381-3p	-5.7765	0.15977	-11.5601	0.073183
rno-miR-384-5p	-6.0376	0.178463	-3.323	0.123838
rno-miR-410-3p	-7.5761	0.10439	-8.7947	0.083526
rno-miR-429	-1.6002	0.240994	-1.9909	0.067821
rno-miR-448-3p	-11.9854	0.174491	-11.7942	0.095204
rno-miR-449a-5p	3.3143	0.144003	1.6855	0.276309

rno-miR-495	-8.7793	0.179737	-5.6918	0.115526
rno-miR-497-5p	-1.1652	0.618521	-1.9703	0.193731
rno-miR-539-5p	-11.7053	0.174876	-9.4508	0.113622
rno-miR-664-3p	-1.4581	0.281782	-1.5736	0.338469
rno-miR-673-5p	-8.4445	0.223204	-6.9911	0.165498
rno-miR-743b-3p	-13.3007	0.233447	-7.5757	0.115296
rno-miR-878	-11.5563	0.166953	-9.6476	0.103136
rno-miR-9a-5p	-2.0776	0.632612	-1.3245	0.509295
rno-miR-93-5p	1.5653	0.744229	1.308	0.908042
rno-miR-98-5p	3.8687	0.142509	1.7355	0.23848
cel-miR-39-3p	-18.4395	0.184699	-28.3843	0.112443
cel-miR-39-3p	-20.9224	0.173605	-13.4429	0.207856

Chapter 4

Discussion

4 DISCUSSION

4.1 Internalization of AuNPs by lung cells

4.1.1 Functionalization of AuNPs with FBS

In this present study, AuNPs were used as a model NP system for toxicity study due to its emergence in biomedical applications and the ease of controlling the size and shape of these NPs during synthesis (Chithrani and Chan, 2007). Moreover, spherical shape AuNPs with diameters between 20 to 30 nm have been reported to exhibit an easier uptake (Chen et al., 2013b). As citrate-capped AuNPs have been reported to be toxic (Tedesco et al., 2010), functionalization of the AuNPs is necessary prior to the toxicity studies. Hence, AuNPs was functionalized with FBS (refer to section 2.1) before use for experimentation. AuNPs pre-coated with FBS as a corona protein possesses lesser non-specific affinity to the cell surface than naked NPs, thereby reducing AuNP toxicity. In addition, opsonization of FBS on AuNPs would aid in the interaction of AuNPs with cell surface receptors and their uptake into the cells (Lynch et al., 2009; Tenzer et al., 2013).

4.1.2 Cellular uptake of AuNPs

To investigate the effects of AuNPs in the lung model, primary airway epithelial cells (SAECs) isolated from distal portion of human lung in the bronchiole area were used. SAECs are reported to be well suited for NP and other air-borne diseases studies (Russell et al., 2008), in addition to MRC5 lung fibroblasts which were used in the previous studies by Li *et al* (2008, 2010a, 2011a) as fibroblasts are present in the stroma of the lung.

Internalization of AuNPs was observed under light and transmission electron microscopy. Under EM, AuNPs were found to be enclosed by cytoplasmic vesicles in cytoplasm of both SAECs and MRC5 cells. Moreover, the AuNPs frequently appeared as clusters since agglomeration was also likely to occur in the majority of engineered NPs, due to inherent properties such as high surface activity (Kim et al., 2009b) and high diffusivity (Gosens et al., 2010). The observation that AuNPs were present in endosome-

like vesicles, lead to the postulation that uptake of AuNPs was mediated by surface adsorption of serum proteins onto the AuNP surface via RME (Chithrani et al., 2006). RME comprises of clathrin- and caveolae-mediated pathways (Hao et al., 2012); and hence the pathway for AuNP uptake was determined by using chemical inhibitors that selectively inhibit specific endocytic pathways (Vercauteren et al., 2010). Quantitative analysis by ICPMS confirmed that internalization of AuNPs by the MRC5 fibroblasts was via clathrin-mediated endocytosis pathway, as inhibition of this pathway by concanavalin A significantly decreased the uptake of AuNPs. Caveolae-mediated endocytosis inhibitor, nystatin, did not markedly inhibit AuNP uptake. This is also consistent with other studies showing that uptake of 20 nm AuNPs in syncytiotrophoblasts of mouse placental tissues (Rattanapinyopituk et al., 2013a) and 20 nm carboxylate-modified polystyrene fluorescent beads in HeLa cells are facilitated by clathrin-mediated endocytosis (Smith et al., 2012). By understanding the mechanism by which AuNPs are taken up by the cells, the design of AuNPs can be tailored for effective intracellular delivery of NPs for diagnostic and therapeutic uses (Wang et al., 2010).

Scavenger receptors are a sub-group of structurally unrelated receptors which function to recognize and mediate the uptake of polyanionic ligands and modified low-density lipoprotein (LDL) (Patel et al., 2010; Wang et al., 2012), as well as nanoscale objects, including engineered NPs (Patel et al., 2010; Kanno et al., 2007). Other than CME, scavenger receptor A mediated endocytosis was reported to mediate the internalization of negatively charged carboxydextran coated iron oxide NPs (diameters of 20 and 60 nm) in human monocyte-derived macrophages (Lunov et al., 2011). Due to the anionic nature of AuNPs used in this study, CME is, however, not the only responsible mechanism responsible for the uptake and intracellular trafficking of AuNPs. Instead, multiple mechanism such as scavenger receptor mediated endocytosis mechanism may coexist to mediate the uptake of AuNPs, which requires further investigation. This is highly relevant as CME of AuNPs occurs when there is a clustering of AuNPs at the cellular plasma membrane; while scavenger receptor mediated endocytosis is required to incorporate

these clustered AuNPs into the double membrane vesicles at the plasma membrane to facilitate their subsequent endosomal trafficking within the cells (Wang et al., 2012).

With regard to the intracellular fate of AuNPs after being internalized into the cells, it has been proposed that the endosomal-lysosomal pathway (comprising early endosomes, late endosomes and lysosomes) is responsible for the processing of the internalized NPs (Gilleron et al., 2013; Yang et al., 2013), or AuNPs could also possibly be sequestered in autophagosomes and then acted upon by lysosomes to form autolysosomes as shown by a previous study (Li et al., 2010a).

4.2 Biological effects of AuNPs in SAECs

4.2.1 Effects of AuNPs on oxidative stress

When SAECs were treated with AuNPs, there was an increase in lipid hydroperoxide content. Studies have shown that AuNPs can cause toxicity due to their ability to bind strongly to the -SH groups and trigger oxidative stress (Sperling and Parak, 2010; Tedesco et al., 2010b; Gerber et al., 2013). Oxidative stress due to an increase in ROS production would affect macromolecules such as proteins, lipids and carbohydrates, which could lead to the disruption of cell functions, oxidative damage (such as peroxidation of lipids) and eventual cell death (Khansari et al., 2009). This finding is also in concert with other studies on different types of NPs used, such as TiO_2NPs and nickel oxide NPs (NiONPs), which showed induction of oxidative stress (Schins and Knaapen, 2007; Jin et al., 2008; Reeves et al., 2008; Lu et al., 2009a; Shukla et al., 2011).

MT is a multi-functional protein that confers cytoprotective effect in the event of cellular insults (Tanaka, 2001). MT detoxifies heavy metals and acts as scavengers of oxidative free radicals (Cherian et al., 2003). Human *MT* genes are localized on chromosome 16 (16q13) (Karin et al., 1984). There are 10 functional isoforms namely *MT-1A, 1B, 1E, 1F, 1G, 1H, 1X, 2A, 3* and *4* which encode the 4 MT proteins. MT-1 and -2 proteins are ubiquitous in all tissues while MT-3 is site-specific (West et al., 1990; Stennard et al., 1994; Mididoddi et al., 1996; Vasak and Hasler, 2000). Only the expression of functional *MT-1* and *MT-2* gene isoforms were assessed initially in SAECs lung epithelial cells. In this study, there was a down-regulation of the *MT-1A, -1X* and *-2A* gene in SAECs. Down-regulation of MTs has also been reported to cause growth arrest and apoptosis in cancer cells (Li et al., 2005). Moreover, there was a general upward trend in the expression of other anti-oxidant genes such as *GPX1, GPX2, SOD1, SOD2, SOD3, Prx1* and *Prx3* in SAECs.

4.2.2 Effects of AuNPs on cytotoxicity

There was no apparent change in morphology after AuNP treatment in both SAECs. However, oxidation of phospholipids due to oxidative stress, may lead to the disruption of the plasma membrane integrity,

which may eventually stimulate intracellular signaling pathways for apoptosis (Ryter et al., 2007). Indeed, plasma membrane destruction was evident in SAECs in a dose dependent manner, when examined using the LDH assay. Moreover, AuNP-treated SAECs were found to have reduced total cell count and cell viability, implying that AuNPs could affect cell proliferation and survival; and these effects became more apparent at higher dose of 2 nM AuNPs. This observation could partially be explained by the difference in anti-oxidant MT expression as mentioned earlier. Additionally, AO/ EtBr staining showed increased incorporation of EtBr staining into the DNA of AuNP-treated SAECs, appearing orange-red color under a fluorescence microscope. On top of the observed color changes, blebbing of the plasma membrane in SAECs was also evident, indicating the occurrence of cell death after 72 h of AuNP treatment.

Moreover, AuNP treatment significantly inhibited cell proliferation in SAECs as shown by a decrease in DNA content in both S and G2/M phases of the cell cycle. This decrease in cell proliferation was accompanied by down-regulation of *CDKN2a* gene expression. CDKN2a is an important regulator of the cell cycle checkpoint and cell cycle arrest (Koike et al., 2014).

4.2.3 AuNPs and genotoxicity

In this current study, there was significant DNA damage in SAECs exposed to 1 nM of AuNPs for 72 h, as revealed by the comet assay. The detection of DNA damage and up-regulation of the *XPA* gene (DNA excision repair gene), suggest the ability of AuNPs to disrupt genomic integrity. XPA is important for nucleotide excision repair (NER); translocation of XPA from cytoplasm to nucleus helps to recruit other NER factors in the presence of genotoxic insults. DNA damage-induced translocation of XPA into the nucleus is regulated by cell cycle phase dependent ataxia telangiectasia and Rad3-related proteins (occurring during S phase) (Li et al., 2013). As *XPA* was found to be up-regulated in this study, it is likely that inhibition of cell proliferation occurred during the S phase of replicative SAECs (for DNA damage repair).

4.2.4 Genomic and proteomic studies of AuNP-treated SAECs

The effects of AuNPs in modulating the genome of SAECs were analyzed using global human DNA microarray study. The Affymetrix Human Gene 1.0 ST Array comprising 764,885 probes which target 28,869 genes, comprehensively covers the human genome, and are retrieved from databases like RefSeq, Ensembl and putative complete CDS GenBank transcripts. The probes cover only well-annotated content and out of 28,869 genes screened, GeneSpring analysis revealed 42 transcripts that were differentially expressed. Of these, there were 40 up-regulated genes and 2 down-regulated genes in 48 h AuNP-treated SAECs. From the gene ontology (GO) analysis, these differentially expressed genes can be categorized into different cellular functions including biosynthesis of steroids, stress-responsive genes, homeostasis, immune system and blood coagulation regulatory genes. Notably, AuNP exposure resulted in increased levels of mRNA for acute phase markers serum amyloid A-1 (SAA1) and immune response gene Toll-like receptor 2 (TLR2) and interferon gamma receptor 1. In addition, microarray analysis revealed aberrant expression of genes which are involved in blood coagulation such as serpin peptidase inhibitor, clade E (SERPINE1) and also FYN binding protein, a gene which is involved in platelet activation. Expression of stress and stimulus responsive genes such as NAD(P)H dehydrogenase, quinone 1 (NQO1), ferritin, heavy polypeptide 1 (FTH1) and FYN binding protein (FYB) were also observed to be elevated

Profiling of proteins using the MS-based dimethyl labeling method between AuNP-treated and untreated SAECs has identified 7 proteins, which were similar to those picked up from microarray data. These proteins were mainly stress-response and immune-response proteins; particularly, TLR2 was detected with a high ratio of 12 although SAA1 was not detected using MS.

The Toll-like receptors (TLRs) family consisting of 10 members, is important in regulating innate immunity. Each member displays high specificity in recognizing different molecular patterns from pathogens, thus enabling detection of invasion by different pathogens (Takeda and Akira, 2004). TLR comprises an ectodomain (which is rich in leucine repeats (LRR) for mediating the recognition of microbe-specific molecular signatures), a transmembrane domain and a cytoplasmic Toll/IL-1 receptor (TIR) domain (which is responsible for initiation of down-stream signaling) (Botos et al., 2011; Kawasaki

and Kawai, 2014). Upon activation by a stimulus, TLRs recruit specific adaptor proteins which subsequently lead to downstream cascade activation, thereby contributing to host defense. Examples of TLRs adaptor proteins include MyD88 and TRIF (contain a cytoplasmic TIR domain) (Kawasaki and Kawai, 2014).

Serum amyloid A (SAA1) is a member of apolipoprotein, as well as an acute phase responder, which is produced in the liver during inflammation and acute injury (Smallridge et al., 1990; He et al., 2003; Paret et al., 2010). SAA plays a pivotal role in restoring homeostasis, thereby protecting biological systems from any insults which could be detrimental. Elevated SAA is associated with inflammation, suggesting its role in immune defense (Marzi et al., 2010). However, persistent inflammation may lead to amyloidosis, atherosclerosis and other clinical complications. Therefore, dysregulation of SAA protein level may serve as a potential biomarker in pulmonary diseases and cancers (Sung et al., 2011b). A previous study has demonstrated the induction of acute phase response genes including SAA after exposure to TiO_2NPs (Halappanavar et al., 2011). Exposure to NPs by inhalation has been implicated in triggering a complex pulmonary response which alters the gene signaling pathway and causing thrombosis (Borm et al., 2006; Halappanavar et al., 2011). Combining the results from both microarray and MS studies, SAA1 and TLR2 were selected for subsequent studies.

4.2.4.1 TLR2-SAA1 interaction triggers NFkB activation

Studies have demonstrated TLR as a novel receptor for SAA1; in which SAA1 can bind to TLR2 and mediate inflammatory response, followed by activation of NFkB signaling pathway after their protein engagement (Filep and El Kebir, 2008; Baranova et al., 2010). Using saturation binding experiment, a previous study has identified TLR2 as a functional receptor to acute phase reactant, SAA1 and could mediate SAA1 regulatory function on pro-inflammatory activity (Baranova et al., 2010). To confirm the biological significance of the three genes/proteins from microarray and MS studies, the identified proteins (TLR2 and SAA1) were further evaluated to verify the presence of protein-protein interaction by co-IP

assays. The two proteins were found to co-immunoprecipitate with each other in SAECs, although the majority of the TLR2 protein pool remained as un-interacted form. This result which indicates that SAA1 specifically interacted with TLR2 and vice versa, was further verified with protein modeling analysis using the Swiss PDB viewer.

The crystallized protein structure of SAA1 indicates that the native SAA1 structure is in hexameric form; comprising helix bundles which are involved in oligomerization of SAA1. Various oligomeric forms of SAA indicate differences in their function and pathogenicity; and it appears that the presence of C-terminal loop at the helix bundle is critical for protein binding and stability maintenance (Lu et al., 2014). Combined structural and functional studies have provided mechanistic insights into the pathogenic contribution of SAA1. Further investigation is needed to confirm if TLR2 interacts with SAA1 at the C-terminal loop.

Following the verification of TLR2-SAA1 protein-protein interaction, a study was performed to investigate if there is an activation of intracellular NFkB transcriptional activity. Using the NFkB luciferase reporter plasmid, the effect of AuNPs on NFkB activity in SAECs pre-treated with 1 nM of AuNPs for 48 h was analyzed. There was a significant induction of NFkB activation, which is in concordance with a recent study by Monita Sharma *et al* (2013), who evaluated the effect of AuNPs on NFkB activation in a B-lymphocyte cell line using 10 nm AuNPs. Engagement of TLRs transmits trans-membrane signals which activate the NFkB pathway, thereby, regulating the downstream signaling cascade. Recently, a study has demonstrated the involvement of MyD-dependent TLR pathways in the expression of ZnONP-induced proinflammatory cytokines. TLR4 has also been reported to play a role ZnONP-induced inflammation (Chen et al., 2014).

The NFkB is a complex transcription factor that comprises five subunits namely p50, p52, RelA, RelB, c-Rel, a family of inhibitors (IkBs), and upstream activating kinase complex (IKKs) (Ling and Kumar, 2012). Upon TGF-beta activated kinase 1 (TAK1) activation, TAK1 binds to the IKK complex (IKKα, IKKβ and NEMO), thereby inducing phosphorylation of IkBα to undergo proteasome degradation, resulting in nuclear translocation of NFkB and activation of the downstream signaling cascade (Perkins,

2007; Ling and Kumar, 2012; Kawasaki and Kawai, 2014). Activation of NFkB could occur via the canonical, alternative or NFkB1/p105 pathways in response to different types of stimuli (Beinke and Ley, 2004; Hoffmann et al., 2006). NFkB activation via the canonical pathway involves nuclear translocation of NFkB following IκBs degradation. On the other hand, activation of the non-canonical NFkB pathway does not involve IκBs degradation, but depends on the inducible processing of p100 (Sun, 2011). Whether the induction of inflammation is through canonical or non-canonical pathway warrants further investigation, although previous reports have demonstrated the involvement of canonical pathway for AuNPs (He et al., 2011; Sharma et al., 2013).

Other than TLR-mediated NFkB activation, another possible mechanism responsible for NFkB activation is postulated to occur via direct Au-thiol group binding at the cysteine residue of NFkB protein (Sharma et al., 2013), a key residue for NFkB signal transduction proteins (IKKa and IKKb) (Perkins, 2012). Since NFkB signaling pathway regulates inflammatory responses, activation of this pathway may be universal to other NM-induced biological effects (Fig 4.1).

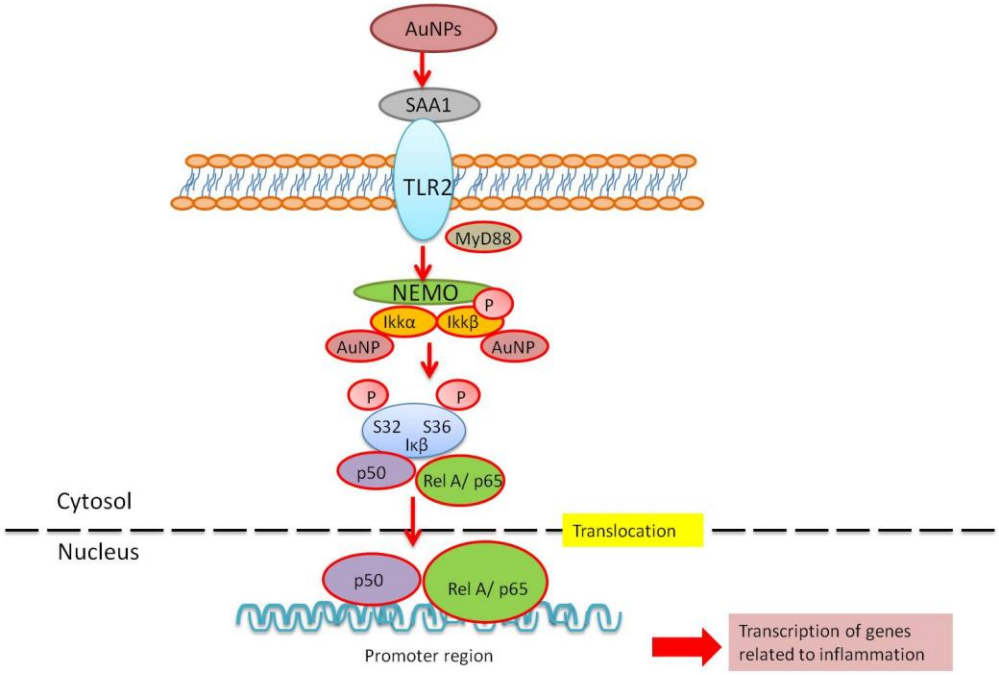

Figure 4.1: Schematic drawing on the proposed mechanism of AuNP-induced NFkB activation mediated through SAA1-TLR2 ligand-receptor interaction. Upon activation of TLR receptor by a stimulus (AuNPs), activation of NFkB trigger increased cytokine expression through the 'canonical' NFkB signaling pathway. A physical interaction between AuNPs and IKKa and IKKb as well as Au-thiol group, which was demonstrated in the study by Sharma *et al* (2013), may participate and contribute to AuNP-induced NFkB activation.

4.3 Biological effects of AuNPs in MRC5 lung fibroblasts

4.3.1 Effects of AuNPs on oxidative stress

MRC5 cells treated with AuNPs also showed an increase in lipid hydroperoxide content which is similar to that reported in previous studies, demonstrating an increased oxidative stress accompanied by cytoprotective effects by anti-oxidants in AuNP-exposed MRC5 lung fibroblasts (Li et al., 2008; Li et al., 2010a). Other than *MT-1* and *MT-2* genes, *MT-3* and *MT-4* were also screened in MRC5 cells, although their expression was low. In this study, there was an up-regulation of the *MT-2A* and *-1X* genes in the MRC5 fibroblasts. This was accompanied by a general upward trend in the expression of other anti-oxidant genes such as *GPX2* and *SOD2*. The difference in *MT* expression between SAECs and MRC5 cells suggests that MT responses to AuNP treatment may be cell-type specific (Khlebtsov and Dykman, 2011; Shukla et al., 2011).

4.3.2 Effects of AuNPs on cytotoxicity

There was no apparent change in the morphology of MRC5 fibroblasts after AuNP treatment, which is similar with the observation in SAECs. AuNP treatment caused an increase in LDH leakage; albeit, less pronounced as compared with SAECs. Moreover, trypan blue assay showed that 1 nM AuNP treatment was not detrimental to cell survival and proliferation, except at the highest dose of 2 nM. As MT expression has been reported to prevent death in cardiac cells by attenuating ER stress (Xu et al., 2009) and up-regulation of *MT* genes could partly account for the less sensitivity of MRC5 towards AuNPs, as mentioned earlier. Additionally, AO/ EtBr staining showed a less extensive and less obvious cell death in AuNP-treated MRC5 cells, suggesting a varying degree of sensitivity towards AuNPs in different cell types. It would appear that AuNP treatment inhibited cell proliferation in MRC5 cells, although this was not significant, which is in concordance with the trypan blue results.

4.3.3 Effects of AuNPs on genotoxicity

A DNA damage study has been previously performed using MRC5 cells (Li et al., 2011a). Other investigators have also observed the presence of genotoxicity induced by other types of NPs such as AgNPs, iron oxide NPs, TiO_2NPs and MWCNT (Johnston et al., 2010b; Naqvi et al., 2010; Petkovic et al., 2010; Guo et al., 2011; Lee et al., 2011; Li et al., 2011a; Shukla et al., 2011). Using 2D gel electrophoresis, a previous study has demonstrated that AuNPs induced oxidative damage-induced genomic instability, concomitant with dysregulation in protein expression (Li et al., 2011a). Down-regulation of hnRNP C1/C2 in MRC5 cells implies involvement of the non-homologous end-joining pathway in repairing DNA damage caused by AuNPs. However, how AuNPs induced DNA damage as they were not found in the nuclei of cells in both cell lines in this study is still unknown. The findings lend support to studies which have established oxidative stress as the possible mechanism responsible for metal based NP-induced genotoxicity through heightened ROS production (Yang et al., 2009).

4.3.4 Genomic and epigenetic studies of AuNP-treated MRC5 cells

4.3.4.1 Transcriptomic study

Global gene microarray analysis was carried out to compare the gene expression patterns of the MRC5 lung fibroblasts treated with or without AuNPs. 19 genes have been found to be differentially expressed. These genes were classified into stress-response genes and genes that regulate blood coagulation, cellular morphogenesis, sterol metabolism, metal ion binding, hemostasis, and hydrolase activity. The genes related to sterol biosynthesis, which include isopentenyl-diphosphate delta isomerase 1 and sterol-C4-methyl oxidase-like, were observed to be down-regulated. Other differentially regulated genes identified in AuNP-treated MRC5 fibroblasts, are known to participate in important cellular pathways, such as cellular morphogenesis, blood coagulation, hemostasis, hydrolase activity, metal ion binding and sterol metabolism (Dennis et al., 2003; Huang da et al., 2009). Similar to the microarray study in SAECs, genes associated with blood coagulation and possibly prothrombotic changes, were also identified.

4.3.4.2 Modulation of miR-155 induced by AuNP exposure

Transcriptomic analysis revealed up-regulation of a non-protein coding RNA, miR-155 concomitant with decreased expression of 10 other genes (including the *PROS1* gene) in AuNP-treated MRC5 cells. miR-155 expression after AuNP treatment was subsequently validated using qRT-PCR analysis and reporter assay. This is the first study which demonstrates that AuNPs can modulate the expression of miR-155.

Alteration in the expression of miRNAs has been implicated in the pathogenesis of diseases (Calin et al., 2005; Du and Zamore, 2007; Pillai et al., 2007; Standart and Jackson, 2007; Inomata et al., 2009). miR-155 is one of the most well-studied miRNAs. Recently, studies have established the role of miR-155 in modulating inflammation and regulating both innate and adaptive immune responses (Tili et al., 2011; Li et al., 2014; Thounaojam et al., 2014). In line with a key role for miR-155 in modulating inflammation, a previous study has shown that miR-155 promotes inflammation and cytokine release by regulating the NFkB signaling pathway, and acts through the SHIP1 protein (Thounaojam et al., 2014). Other than inflammation, activation of TLR and stimulation of NFkB were also found to up-regulate miR-155 expression (Elton et al., 2013). Hence, miR-155 up-regulation in response to the pro-inflammatory environment after AuNP exposure in MRC5 cells suggests that miR-155 is involved in modulating inflammatory response.

Besides the prominent role of miR-155 in innate immunity and inflammation, miR-155 has been identified to participate in a number of cellular pathways, including the LPS signaling pathway (Boesch-Saadatmandi et al., 2010), miR155-mediated pathway of AID regulation (Teng et al., 2008), regulation of type 1 Angiotensin II receptor (AT1R) (Faraoni et al., 2009), angiotensin II-induced extracellular signal-related kinase 1/2 (ERK1/2) activation (Martin et al., 2006), TGF-β/Smad pathway (Kong et al., 2008), MAPK signaling pathway (Bhattacharyya et al., 2011), PI3K/Akt pathway (which subsequently affects the TNFα-dependent growth of B cell lymphomas) (Cremer et al., 2009; Pedersen et al., 2009; Bhattacharyya et al., 2011). These pathways are known to cause autoimmune disorders, carcinogenesis and cardiovascular diseases (Faraoni et al., 2009; Elton et al., 2013).

4.3.4.3 *PROS1* gene as a possible target gene of miR-155

In the present study, inhibition of miR-155 expression led to an increased expression of PROS1 at both the transcript and protein levels. These results indicate that although endogenous miR-155 was expressed at low levels in the lung fibroblasts, inhibition of its expression enhanced the expression of PROS1, thereby suggesting that miR-155 could modulate expression of PROS1. It would appear that the *PROS1* gene is a putative target of miR-155.

A study has shown that mice exposed to TiO_2NPs through the inhalation route suffered from inflammation in the lung tissues, together with up-regulation of miR-449a, miR-1, and miR-135b (Halappanavar et al., 2011). PROS1 deficiency is known to contribute to thrombosis in the pulmonary vasculature, causing lung infarction culminating in death (Zander et al., 2001) and pulmonary hypertension (Piazza and Goldhaber, 2011). The *PROS1* gene encodes for Protein S, a vitamin K–dependent plasma glycoprotein. Protein S participates in the inactivation of Factors Va and VIIIa, resulting in dire consequences such as bleeding diathesis (Simioni et al., 2006). Protein S is mainly synthesized mainly in hepatocytes, endothelial cells, megakaryocytes and interstitial Leydig cells (ten Kate and van der Meer, 2008). Modulation of PROS1 by miR-155 suggests a tight link between inflammation and PROS1 deficiency associated diseases.

Moreover, the *PROS1* gene was also expressed in lung tissues, as quantified by normal tissue array comprising 48 different human tissues. *PROS1* expression was detected in 45/48 normal tissues, excluding lymphocytes, mammary gland and muscle. The highest expression the *PROS1* gene (as denoted by a lower Ct value) was found in lung tissue, followed by small intestine, adrenal gland, uterus, pituitary, heart, stomach, penis, ovary and liver.

4.3.4.4 PROS1 DNA methylation profiling analysis

To study the DNA methylation status at the promoter region of *PROS1* gene, both sequencing-based DNA methylation (BSP) and gene-specific methylation (MSP) analysis were adopted. Both methods

require bisulfite modification of DNA. Total DNA was subjected to sodium bisulfate modification for the conversion of unmethylated cytosines to uracil; so as to differentiate the unmethylated form from methylated form of cytosines. For the BSP sequencing method, BSP primers are used for PCR amplification before sequencing is performed. The percentage of unconverted cytosines (methylated form) and unmethylated cytosines (which has been converted to thymine nucleotides) at the CpG island can then be determined. MSP PCR analysis is achieved using two sets of primers namely the methylated and unmethylated primer sets (Shen and Waterland, 2007).

It has been reported that alteration of miRNA expression contributes to other epigenetic changes such as aberrant DNA methylation (Calin, 2006; Kuhn et al., 2008; Gao et al., 2010). It has also been proposed that DNA methylation is the first step among other epigenetic platforms to modulate gene expression. This is evident as site-specific DNA methylation at the promoter region of a gene often leads to gene silencing (Gong et al., 2012). Both AuNP-treated and untreated MRC5 cells showed virtually no methylation by either bisulfite sequencing or MSP PCR analysis, indicating that AuNP treatment did not alter the DNA methylation status of the *PROS1* gene.

4.3.4.5 AuNP-induced chromatin reorganization/ heterochromatin formation in MRC5 cells

As miRNAs are also known to be negative gene regulators through chromatin remodeling (Finnegan and Matzke, 2003; Gonzalez et al., 2008), changes in nuclear architecture were also evaluated in AuNP-treated MRC5 fibroblasts. There is very limited literature on the effects of NP exposure on chromatin organization. Cellular responses towards NP exposure may show drastic differences in the event of perturbation to either hetero- or euchromatin (Mazumder and Shivashankar, 2007). There was an apparent reorganization of nuclear content and chromatin condensation in AuNP-exposed MRC5 cells. This finding indicates that AuNPs modulate chromatin architecture. Chromatin reorganization coupled to the nuclear architecture organization is important in regulating function of the genome. This process involved histone tail interactions in maintaining nuclear proteins into an organized and dynamic structures

(Mazumder and Shivashankar, 2007). Proper proteinaceous scaffolding is essential in maintaining nuclear architecture, and this is regulated through histone tail modification. TSA, an inhibitor for HDAC, was used to probe if histone modification was instrumental in nuclear organization and hence, *PROS1* gene suppression. HDAC inhibition results in increase acetylation at the histone tails, forming a looser chromatin structure (euchromatin) and allowing for higher gene transcription. Remarkably, the inhibitory effect on *PROS1* gene expression was abrogated in the presence of TSA treatment. This study provided evidence of AuNP-induced perturbation of chromatin assembly. *PROS1* was found to be negatively regulated by HDAC and histone tail modification was partly involved in regulating *PROS1* transcriptional activity, other than miR-155.

4.4 Bystander effects of AuNP exposure in a SAEC-MRC5 co-culture system

4.4.1 Co-culture system and SILAC analysis

Despite the wide availability of toxicity studies, there is a scarcity of knowledge with regard to the AuNP-lung interaction effects on neighboring cells, not exposed to the NPs. Hence, an *in vitro* SAEC-MRC5 lung fibroblasts co-culture system (to mimic the respiratory tract) was adopted for this purpose. SAECs, a lung epithelial cell line, are the first line of contact with inhaled NPs surrounded by stromal lung fibroblasts in the lung (Yu et al., 2013). Primary exposure of SAECs to AuNPs was performed before seeding in the upper cell culture insert of a Transwell polycarbonate membrane and the MRC5 lung fibroblasts were seeded in the lower inserts. AuNPs pre-exposed SAECs were subsequently co-cultured with MRC5 cells to simulate the physiological environment present in the lung. Cellular crosstalk among different cell types present in tissues was studied using the co-culture system, which allows an in depth-understanding of cell-cell communication in response to an external stimulus. Moreover, a co-culture system can serve as a sophisticated *in vitro* model, reflecting a realistic physiological condition in the lung, for NP-related studies in order to minimize the animal usage (Herzog et al., 2014).

The co-culture system has been utilized for modeling biological interactions in immunology, cancer biology, stem cells differentiation as well as in nanotoxicology (Stephens et al., 2001; Gebhardt, 2002; Diabate et al., 2008; Brandenberger et al., 2010; Bogdanowicz and Lu, 2013; Chuang et al., 2013). For example, Brandenberger *et al* has employed a triple cell type (alveolar epithelial cells, macrophages and dendritic cells, simulating the alveolar lung epithelium) co-culture system to study the modulation of inflammation after aerosolized exposure to AuNPs at the air-liquid interface (Brandenberger et al., 2010). Small airway epithelial cells (SAECs) and microvascular endothelial cells (HMVEC) have also been co-cultured to study alveolar-capillary interaction post-exposure to MWCNT for the detection of changes occurred in the vascular endothelium (Snyder-Talkington et al., 2013).

In this present study, a SILAC-MS based proteomics approach was also employed for the study of AuNP toxicity in the co-culture system. SILAC-MS has been identified as a robust tool to quantify and

compare the proteome expression changes (Swa et al., 2012). Metabolic incorporation of stable isotope-labeled Arginine and Lysine into the cellular proteome was achieved by constitutively culturing of cells using SILAC medium for four passages. Next, two populations of cells, namely the light and the heavy cells were mixed in equal proportion after co-culturing before being subjected to MS analysis. Quantification of the relative protein abundance in MRC5 cells after co-culture with SAECs which were pre-exposed and not exposed to AuNPs was determined based on relative MS intensities. Derivatization of protein abundance between the two sets of samples enabled the identification of proteins that were dysregulated in neighboring AuNP-unexposed MRC5 cells. These dysregulated proteins may shed light in identifying the cellular response/ bystander effect on neighboring cells induced by AuNP-exposed cells. A combination of both technologies (co-culture system and SILAC-MS approach) has provided further biological insights into NP-related toxicity.

4.4.2 Pathway analysis of differential protein expression induced by AuNP-exposed SAECS in neighboring MRC5 fibroblasts

Quantitative proteomics analysis has identified 47 up-regulated and 62 down-regulated proteins in the MRC5 fibroblasts, based on replicates of Forward and Reverse experiments. From the GO and pathway analysis, these dysregulated proteins were involved in cell adhesion, extracellular matrix (ECM)/cytoskeleton remodeling and cell migration, accompanied by phenotypic alterations.

One of the key proteins involved in migration and invasion, PLAU was down-regulated, implying a decrease in cell migration (Jung et al., 2010; Lampidonis et al., 2011). Expression of cell adhesion-related proteins such as Paxillin (PXN), breast cancer anti-estrogen resistance 1 (BCAR1) and Caveolin-1 (Cav-1) were increased significantly. Taken together, AuNPs was found to alter key proteins which regulate the cell-cell and cell-matrix adhesive properties in the underlying unexposed MRC5 cell. A survey of the literature also revealed that alterations of these proteins have been implicated in cancer progression, as well as in pulmonary pathologies (Yang et al., 2006; Le Saux et al., 2008; Chanvorachote and Chunhacha, 2013; Kawada et al., 2013). Increased adhesion-related proteins are crucial in regulating

airway inflammation through activation of p38 MAPK and NFkB signaling (Garrean et al., 2006; Liu et al., 2013). Other than NFkB, sustained activation of PI3K/Akt pathway facilitates the ROS formation regulated by Cav-1 after cell detachment (Chanvorachote and Chunhacha, 2013).

The results obtained here revealed that primary exposure of SAECs to AuNPs induced bystander effects, possibly through soluble factors secreted by SAECs into the culture medium, resulting in dysregulation of proteins involved in processes such as increased cell-substrate adhesion in the underlying unexposed MRC5 fibroblasts.

4.4.3 Dysregulated proteins regulates cell adhesion and cytoskeleton in the MRC5 fibroblasts

FA is a site where there is a close contact between cell and the underlying extracellular matrix. Studies have demonstrated PXN, BCAR1 and Cav-1 to be FA-associated (Schaller, 2001) and involved in formation and regulating local FA dynamics (Chao et al., 2010), leading to disruption of the cytoskeleton structure. These findings provide the biological basis for the coordinated signaling between PXN, BCAR1 and Cav-1 in regulating cell spreading. In agreement with previous findings, F-actin arrangement in the cytoskeleton was altered, together with an increased in stress fiber or FA formation. In addition, there was an increased in FA-associated protein, vinculin in MRC5 lung fibroblasts. These altered proteins modulated phenotypic changes in the MRC5 fibroblasts, causing an increase in cell adhesion and changes to cytoskeleton that may affect lung function in the physiological condition. This observation is in line with a previous study in which direct exposure of MWCNT in endothelial cells resulted in manifestation of increased vascular permeability (Pacurari et al., 2012; Snyder-Talkington et al., 2013). Another similar finding is a study by Setyawati *et al* (2013) which showed perturbation of the cytoskeletal network involving formation of stress fibers and actin remodeling by VE–cadherin pathway triggered by TiO_2NPs, leading to endothelial cell leakiness.

4.5 Functional effects of AuNPs in an *in vivo* model

4.5.1 Intravenous route of administration

AuNPs have been identified as agents for drug delivery (Kim et al., 2009a; Jeong et al., 2013). Hence, there is an increase in propensity for human exposure to AuNPs via IV injection in the clinical setting. Entrapment of NPs in the lungs is common if administration of the NPs is mediated via the IV route (Fabian et al., 2008; Kendall and Holgate, 2012), thereby posing a high risk of possible toxicity to the lungs. Thus, assessing potential adverse pulmonary effects of AuNPs *in vivo* is of great importance.

4.5.2 Dosimetry and relevance

As AuNPs are directly administered into the blood stream as drug carriers, the dose applied should be carefully monitored. Administration of a physiologically relevant dose for both *in vitro* and *in vivo* studies has been challenging. There has been a lack of consensus on the dose metrics especially for *in vitro* studies (Joris et al., 2013). Relatively high doses applied in *in vitro* studies have raised questions on the relevance of the findings in the *in vivo* environment (Oberdorster et al., 2005). It has been advocated that the dose administered should be comparable in the different experimental settings (Johnston et al., 2010a), especially in preclinical studies that assess the toxicity of NPs using animal models (Madl and Pinkerton, 2009). Hence, the dose for AuNPs used in this study was rationalized based on published data from a Phase I clinical trial (Libutti et al., 2010) and following US Food and Drug Administration's guidelines.

4.5.3 Biodistribution of AuNPs in rat lungs

Concurrent with other reports (De Jong et al., 2008; Semmler-Behnke et al., 2008), AuNPs has been observed to reach secondary target organs via the systemic blood circulation in healthy rats. The levels of Au detected in the lungs are consistent with an earlier study by Balasubramanian *et al* (2010a), although the dose used in the present study was ten times higher. However, the amount of Au present in the residual amount of blood in the lungs is not known (De Jong et al., 2008) and hence, no correction factor

could be adopted (Hirn et al., 2011). Therefore, it is assumed that amount of Au present in blood is negligible and insufficient to affect the amount of Au measured.

The single dose IV administered AuNPs were translocated to the rat lungs and were retained after 1 week, 1 month and 2 month post-exposure; with higher dose administered showing a faster clearance, decreasing at 2 month post-exposure. Several possible clearance pathways have been proposed for inhaled AuNPs, including mucociliary clearance and pulmonary surfactant protein D modulated clearance (Yu et al., 2007; Semmler-Behnke et al., 2008; Schleh et al., 2013), alveolar elimination by macrophages in the alveolar region (which does not apply to large agglomerates) (Takenaka et al., 2012) and hepato-biliary clearance from the liver (Hirn et al., 2011).

4.5.4 Systemic effects of AuNPs in rats

IV injection of AuNPs induced significant expression of both anti- and pro-inflammatory cytokine expressions. This observation indicates the presence of systemic inflammation in rats following AuNP exposure. In particular, more intense inflammatory response was observed after a higher single dose and a shorter duration post-exposure. The results concerning transient inflammatory response induced by AuNPs are similar to the results as observed by Khan *et al* (2013). In their study, 10 and 50 nm AuNPs induced transcriptional expression of cytokine genes on day 1, which declined on day 5. Exposure to other types of NMs has been reported to cause inflammation *in vivo*, for example, exposure of TiO_2 has been reported to induce pulmonary airway irritation and inflammation in mice (Leppanen et al., 2014) and single-wall carbon nanotube, inflammatory gene expression changes after post intratracheal instillation in rats (Fujita et al., 2014).

The effect of AuNPs on coagulation events was assessed by performing PT test. It has been established that exposure to AgNPs and silica NPs enhanced venous thrombus formation and platelet aggregation (Jun et al., 2011; Corbalan et al., 2012). In this study, administration of AuNPs caused a significant increase in PT, demonstrating that there is an increased risk of bleeding. In line with the

findings in this study, *PROS1* gene was strongly induced in the lungs of rats exposed to AuNPs. PROS1 is an anticoagulant plasma protein which controls thrombin generation; as well as a cofactor to activate protein C which degrades coagulation factors Va and VIIa (ten Kate and van der Meer, 2008). *PROS1* encodes for protein S, which is an anticoagulant and a cofactor for activated protein C to inhibit the blood coagulation cascade. Protein C plays a role in PT prolongation by inactivating FV and FVIII in this PT assay *ex vivo* (Youngwon et al., 2013). Hence, increased *PROS1* expression may be associated with a stronger anticoagulant response.

4.5.5 Pulmonary inflammation induced by AuNPs

Histological and immunohistochemical examination revealed inflammatory features post AuNP exposure in rat lung. Inflammatory infiltrate of lymphocytes and macrophages was evident in the rat lung. Immunohistochemistry revealed a strong positivity of IL-1α staining, confirming pulmonary inflammation. Accumulation of AuNPs in animal models following their biodistribution via inhalation and intravenous route pose immune-modulatory effects and recruitment of macrophages (Hussain et al., 2013). Particulate air pollution has been associated with inflammation, blood coagulation, and autonomic dysfunction (Zuurbier et al., 2011; Bind et al., 2012). Inhalation exposure to TiO_2NPs was found to cause pulmonary inflammation in mice and rats, as characterized by infiltration of neutrophils (Hougaard et al., 2008; Ma-Hock et al., 2009; Halappanavar et al., 2011). Similar inflammogenic response of TiO_2NPs was also observed in *in vitro* studies.

As evidenced by the immunohistochemical staining, there was an enhanced expression of IL-1α, a pro-inflammatory cytokine which is known to play a role in resolving infections through the stimulation of immune responses via recruitment of inflammatory cells and production of enzymes (Kim et al., 2014). In addition to inflammatory responses, there was also an increase in the number of macrophages in rat lung. Together, these results are strong indication to support the induction of pulmonary immunity, inflammatory and blood coagulopathy responses in AuNP-exposed rats.

Rattanapinyopituk *et al* (2013b) reported that translocation of AuNPs to lung tissues caused acute inflammation, accompanied by multifocal infiltration of neutrophils, destruction of alveolar wall, increased cytokine (IL-6 and TNF-α) and oxidative stress. Exposure to other types of NMs has also been reported to cause inflammation *in vivo*. For example, exposure of TiO_2NPs has been reported to induce pulmonary airway irritation and inflammation in mice (Leppanen et al., 2014), while single-wall carbon nanotubes (SWCNT) cause inflammatory gene expression changes after intratracheal instillation in rats (Fujita et al., 2014). The same observation was also made when NiONPs were intratracheally instilled in rats, causing inflammation and changes in pulmonary cytokine and chemokine expression (Morimoto et al., 2010).

4.5.6 miRNA and inflammation

The results from the miRNA PCR array provided evidence that AuNP exposure caused alteration in miRNA expression in the rat lung. Inflammation-related miRNAs were found to be down-regulated. Interestingly, serum protein quantification using the same animals had shown that AuNP exposure up-regulated serum cytokine expression. These opposite trends are in agreement with the expected role of miRNAs, which are negative regulators for transcriptomic and proteomic expression. This finding may aid in understanding the inflammatory response involved in damage caused by AuNP exposure in rat lung. miR-327, the only miRNA that was observed to be down-regulated in both treatment groups, appears to be linked with an induction of inflammatory response. As miR-155 is known to activate NFkB in the event of inflammation; it is noteworthy to investigate its expression in future (Izzotti et al., 2009).

Alteration of miRNA expression after NP exposure has been implicated in inflammation. For example, pulmonary toxicity study using TiO_2NPs revealed up-regulation of SAA protein, together with induction of miR-135b. Similar to the findings in this study, TiO_2NPs was found to induce both systemic and pulmonary toxicity, accompanied by acute phase and inflammation gene and miRNA expression in mice (Halappanavar et al., 2011). miR-21 expressed by murine macrophage was associated with

inflammation following LPS exposure (Lu et al., 2009b); and observed to be down-regulated after exposure to synthetic particulate matter in the myocardium of rats (Farraj et al., 2011). miR-183 and let-7a were observed to be altered in lungs and livers of mice treated with AuNPs (Balansky et al., 2013). Recently, Chew *et al* (2012) performed a blood miRNA profiling in AuNP exposed rats via IV injection and found miR-298 up-regulation, an important regulator for Alzheimer's disease. Several miRNAs (Let-7, miR-10, miR-26, miR-30, miR-34, miR-99 etc) have been implicated in inflammatory lung diseases in rats exposed to cigarette smoke (Izzotti et al., 2009); while miR-181b expression was reported to be suppressed in the silicosis rat model (Faxuan et al., 2012). Accordingly, the susceptibility of miRNAs towards external agents could be profiled to establish their role as a bio-monitoring tool.

4.6 Limitations of the present study

For the *in vitro* study,

(a) only one main dose of AuNPs was evaluated for many of the experiments performed. The size of AuNPs used was restricted to 20 nm diameter and functionalized only with FBS.

(b) experiments were performed in only one epithelial and one fibroblastic lung cell line.

(c) the AuNPs were added into the medium and no experiments were performed by direct exposure using the air liquid interface.

(d) the time points were limited to 24 h-72 h.

For the *in vivo* study,

(a) only single dose injections were performed.

(b) time points limited to one week, one month and two months.

(c) bronchoalveolar lavage was not performed in the animals after exposure to AuNPs.

(d) only male rats were used for the study.

Although *in vitro* set up such as the co-culture system has been designed to simulate *in vivo* system, discrepancies still exist. Therefore, a major challenge to surmount is whether the *in vitro* studies can serve as a good surrogate tool to predict *in vivo* results. Both *in vitro* and *in vivo* studies presented here have consistently demonstrated the toxicity of AuNPs. Further studies are needed to understand the significance of these findings in the context of human beings, which is still lacking in this field.

4.7 Conclusion

This study has shown that FBS-coated AuNPs induced both cytotoxic and genotoxic effects in the lungs upon their entry via RME *in vitro*. AuNPs exposure suppressed cell proliferation, induced DNA damage and oxidative stress in both SAECs and MRC5 cells. These were accompanied by genomic and proteomic changes, as well as the involvement of epigenetic mechanisms especially in the MRC5 cells (Fig. 4.2).

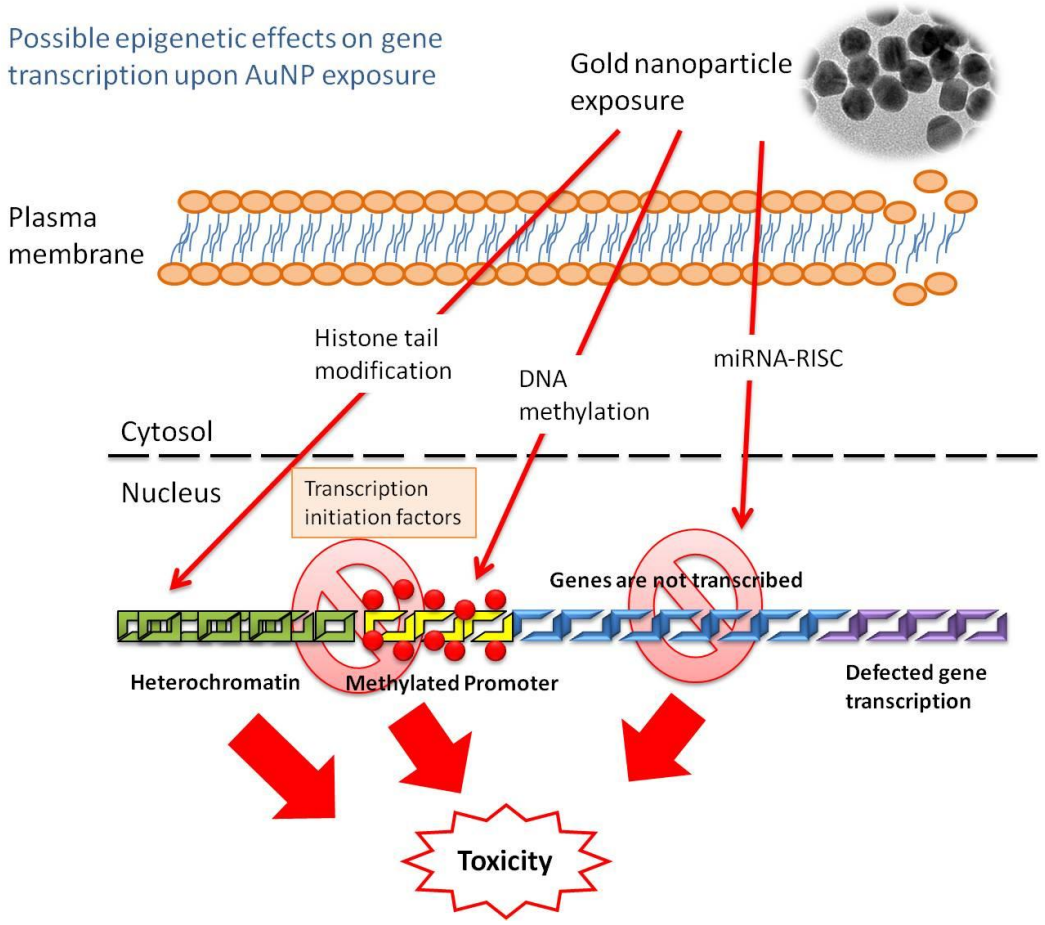

Figure 4.2: Overview of epigenetic mechanisms which may be possibly involved in regulating gene transcription and cellular responses towards AuNP exposure.

The findings also highlight the difference in response and reaction between SAECs and MRC5 cells. Both cell lines are subjected to the same exposure condition; but it appears that the underlying mechanism regulating their responses to AuNPs differ from each other. This present the need to use at least two cell lines for toxicology due to cell-type specific effects. Differential regulation of the antioxidant *MT* could partially explain the difference in cytotoxicity between AuNP-treated SAECs and MRC5 cells by regulation of the levels of oxidative stress in both cell lines.

In addition to the cell type as a factor of AuNP-induced functional effects, cellular crosstalk and microenvironment may play a pivotal role in determining the responses to NPs. Therefore, the co-culture system adopted in this study has shed light on the ability of AuNPs to induce bystander effects to the neighboring unexposed cells, possibly through cell-cell communication via secretion of soluble factors.

While the *in vitro* study has enabled elucidation of the mechanisms involved and signaling pathways triggered in response to AuNP exposure, the *in vivo* study has substantiated some of these findings in the organ system. The animal data has verified that AuNP exposure triggered inflammatory responses and transient bleeding diathesis in rats, concomitant with alteration in inflammation-related miRNA expression in the rat lung. This study has evaluated the cytotoxic and genotoxic effects on AuNPs in lung cells *in vitro*, as well as examined the effects in a co-culture system and *in vivo* model. The results gleaned from this study would contribute to the current understanding of nanotoxicology and also be useful for continued assessment of the safe use of ENMs in biomedical settings.

4.8 Future studies

It would be worthwhile to evaluate the toxicity of different AuNP using multiple sizes with different surface modification, such as Au-S peptide conjugation. Given the strong thiol-binding affinity of AuNPs, Au-S bonding on one terminal has gained popularity. Stable AuNP-peptide systems prepared through Au-S bonds is shown to possess reduced toxicity, thereby leading to the safe and efficacious use of AuNPs for biological applications. Since AuNP-peptide conjugate requires a centrifugation step during its synthesis and preparation, future studies should include the effects of centrifugation on the sedimented amount of AuNP-peptide. In addition, whether the AuNP-peptide could induce protein conformational changes upon adsorption should be examined, as such conformational changes of the adsorbed proteins may cause a reduced functionality of the proteins.

Since NPs are reported to trigger oxidative stress, stability of AuNP-peptide system upon intracellular uptake should be investigated. The effects of $Au^{1+/3+}$ ions release from its peptide conjugate system elicited by the acidic pH condition inside lysosomal cellular compartment should be further evaluated. Previous reports have demonstrated the ability of AuNPs to disturb the oxido-reductase system through the interaction of Au-thiol and Au-S bond, as these bonds are liable to oxidation (Tedesco et al., 2010b). Moreover, intracellular release of Au ions has been shown to inhibit the activity of enzyme thioredoxin reductase through Au-thiol binding (Sabella et al., 2014). Since the stability of AuNP-peptide system may potentially affect the amount of Au ions released and thereby cause cellular redox imbalance, the stability of the Au-S under acidic condition should be determined. A stable Au-S bond which can evade or resist acidic degradation by lysosome would be ideal for subsequent applications.

Other than RME, other pathways such as diffusion, phagocytosis and micro-pinocytosis are also possible mechanisms responsible for the uptake of NPs. Protein corona formation on the surface of NPs affects the mode of interaction between NPs and protein receptors, which in turn alter their uptake into the cells. Analysis of the components present in the medium may provide clues in understanding the cellular uptake of NPs.

Currently, the biological effects of miRNA modulation following AuNP exposure are largely unknown. Induction of miRNAs and modulation of the expression of their putative targets are not well characterized. Proof of concept studies in relation to miRNA-target biological functionality has to be performed. Moreover, the possibility that cellular responses towards AuNPs could be under control of miRNA or other epigenetic mechanisms are yet to be demonstrated after AuNP exposure. Recent publications have seen a surge in the study of epigenetic effects in the field of nanotoxicology. More in-depth studies are required with regard to the involvement of the various epigenetic platforms and their interactions.

In silico analysis and molecular modeling could help to predict effects in real life system. Co-IP results have identified TLR2-SAA1 protein interactions. The next step to validate that such interactions take place, would be to perform a detailed structural modeling so as to confirm their corresponding interaction sites. Once the interaction site is identified, mutation of these sites followed by binding assays could be employed to confirm if these sites are truly functional. Other than an *in silico* model, more advanced cell culture system using 3D model, simulating the 3D *in vivo* environment would be even more relevant than the current 2D model used for the study of NP toxicity.

Finally, a detailed screening of all the blood coagulation factors, and evaluation of the effects of NPs on anti-oxidant gene and *MT* expression should be carried out *in vivo* as they have been observed to be significantly affected in the *in vitro* study. The clearance mechanism of NPs in animal models should also be investigated to determine the bio-persistency of these NPs in the *in vivo* setting.

Chapter 5

References

5 REFERENCES

Annecke K, Schmitt M, Euler U, Zerm M, Paepke D, Paepke S, von Minckwitz G, Thomssen C, Harbeck N. 2008. uPA and PAI-1 in breast cancer: review of their clinical utility and current validation in the prospective NNBC-3 trial. Adv Clin Chem 45:31-45.

Aso Y. 2007. Plasminogen activator inhibitor (PAI)-1 in vascular inflammation and thrombosis. Front Biosci 12:2957-2966.

Aubin-Tam ME, Hamad-Schifferli K. 2008. Structure and function of nanoparticle-protein conjugates. Biomed Mater 3:034001.

Balansky R, Longobardi M, Ganchev G, Iltcheva M, Nedyalkov N, Atanasov P, Toshkova R, De Flora S, Izzotti A. 2013. Transplacental clastogenic and epigenetic effects of gold nanoparticles in mice. Mutat Res 751-752:42-48.

Balasubramanian SK, Jittiwat J, Manikandan J, Ong CN, Yu LE, Ong WY. 2010a. Biodistribution of gold nanoparticles and gene expression changes in the liver and spleen after intravenous administration in rats. Biomaterials 31:2034-2042.

Balasubramanian SK, Yang L, Yung LY, Ong CN, Ong WY, Yu LE. 2010b. Characterization, purification, and stability of gold nanoparticles. Biomaterials 31:9023-9030.

Ball MP, Li JB, Gao Y, Lee JH, LeProust EM, Park IH, Xie B, Daley GQ, Church GM. 2009. Targeted and genome-scale strategies reveal gene-body methylation signatures in human cells. Nat Biotechnol 27:361-368.

Baranova IN, Bocharov AV, Vishnyakova TG, Kurlander R, Chen Z, Fu D, Arias IM, Csako G, Patterson AP, Eggerman TL. 2010. CD36 is a novel serum amyloid A (SAA) receptor mediating SAA binding and SAA-induced signaling in human and rodent cells. J Biol Chem 285:8492-8506.

Bartel DP. 2009. MicroRNAs: target recognition and regulatory functions. Cell 136:215-233.

Beinke S, Ley SC. 2004. Functions of NF-kappaB1 and NF-kappaB2 in immune cell biology. Biochem J 382:393-409.

Bengali Z, Rea JC, Shea LD. 2007. Gene expression and internalization following vector adsorption to immobilized proteins: dependence on protein identity and density. J Gene Med 9:668-678.

Bhattacharyya S, Balakathiresan NS, Dalgard C, Gutti U, Armistead D, Jozwik C, Srivastava M, Pollard HB, Biswas R. 2011. Elevated miR-155 promotes inflammation in cystic fibrosis by driving hyper-expression of interleukin-8. J Biol Chem 286:11604-11615.

Bind MA, Baccarelli A, Zanobetti A, Tarantini L, Suh H, Vokonas P, Schwartz J. 2012. Air pollution and markers of coagulation, inflammation, and endothelial function: associations and epigene-environment interactions in an elderly cohort. Epidemiology 23:332-340.

Boersema PJ, Raijmakers R, Lemeer S, Mohammed S, Heck AJ. 2009. Multiplex peptide stable isotope dimethyl labeling for quantitative proteomics. Nat Protoc 4:484-494.

Boesch-Saadatmandi C, Loboda A, Wagner AE, Stachurska A, Jozkowicz A, Dulak J, Doring F, Wolffram S, Rimbach G. 2010. Effect of quercetin and its metabolites isorhamnetin and quercetin-3-glucuronide on inflammatory gene expression: role of miR-155. J Nutr Biochem.

Bogdanowicz DR, Lu HH. 2013. Studying cell-cell communication in co-culture. Biotechnol J 8:395-396.

Borm PJ, Robbins D, Haubold S, Kuhlbusch T, Fissan H, Donaldson K, Schins R, Stone V, Kreyling W, Lademann J, Krutmann J, Warheit D, Oberdorster E. 2006. The potential risks of nanomaterials: a review carried out for ECETOC. Part Fibre Toxicol 3:11.

Botos I, Segal DM, Davies DR. 2011. The structural biology of Toll-like receptors. Structure 19:447-459.

Brandenberger C, Rothen-Rutishauser B, Muhlfeld C, Schmid O, Ferron GA, Maier KL, Gehr P, Lenz AG. 2010. Effects and uptake of gold nanoparticles deposited at the air-liquid interface of a human epithelial airway model. Toxicol Appl Pharmacol 242:56-65.

Calin GA, Ferracin M, Cimmino A, Di Leva G, Shimizu M, Wojcik SE, Iorio MV, Visone R, Sever NI, Fabbri M, Iuliano R, Palumbo T, Pichiorri F, Roldo C, Garzon R, Sevignani C, Rassenti L, Alder H, Volinia S, Liu CG, Kipps TJ, Negrini M, Croce CM. 2005. A MicroRNA signature associated with prognosis and progression in chronic lymphocytic leukemia. N Engl J Med 353:1793-1801.

Chanvorachote P, Chunhacha P. 2013. Caveolin-1 regulates endothelial adhesion of lung cancer cells via reactive oxygen species-dependent mechanism. PLoS One 8:e57466.

Chao WT, Ashcroft F, Daquinag AC, Vadakkan T, Wei Z, Zhang P, Dickinson ME, Kunz J. 2010. Type I phosphatidylinositol phosphate kinase beta regulates focal adhesion disassembly by promoting beta1 integrin endocytosis. Mol Cell Biol 30:4463-4479.

Chen H, Davids JA, Zheng D, Bryant M, Bot I, van Berckel TJ, Biessen E, Pepine C, Ryman K, Progulski-Fox A, Kesavalu L, Moyer R, McFadden G, Lucas A. 2013a. The serpin solution; targeting thrombotic and thrombolytic serine proteases in inflammation. Cardiovasc Hematol Disord Drug Targets 13:99-110.

Chen H, Dorrigan A, Saad S, Hare DJ, Cortie MB, Valenzuela SM. 2013b. In vivo study of spherical gold nanoparticles: inflammatory effects and distribution in mice. PLoS One 8:e58208.

Chen JK, Ho CC, Chang H, Lin JF, Yang CS, Tsai MH, Tsai HT, Lin P. 2014. Particulate nature of inhaled zinc oxide nanoparticles determines systemic effects and mechanisms of pulmonary inflammation in mice. Nanotoxicology. [Epub ahead of print]

Chen YS, Hung YC, Liau I, Huang GS. 2009. Assessment of the In Vivo Toxicity of Gold Nanoparticles. Nanoscale Res Lett 4:858-864.

Cheresh P, Kim SJ, Tulasiram S, Kamp DW. 2013. Oxidative stress and pulmonary fibrosis. Biochim Biophys Acta 1832:1028-1040.

Cherian MG, Jayasurya A, Bay BH. 2003. Metallothioneins in human tumors and potential roles in carcinogenesis. Mutat Res 533:201-209.

Chew WS, Poh KW, Siddiqi NJ, Alhomida AS, Yu LE, Ong WY. 2012. Short- and long-term changes in blood miRNA levels after nanogold injection in rats--potential biomarkers of nanoparticle exposure. Biomarkers 17:750-757.

Chithrani BD, Chan WC. 2007. Elucidating the mechanism of cellular uptake and removal of protein-coated gold nanoparticles of different sizes and shapes. Nano Lett 7:1542-1550.

Chithrani BD, Ghazani AA, Chan WC. 2006. Determining the size and shape dependence of gold nanoparticle uptake into mammalian cells. Nano Lett 6:662-668.

Chithrani DB. 2010. Intracellular uptake, transport, and processing of gold nanostructures. Mol Membr Biol 27:299-311.

Cho WS, Cho M, Jeong J, Choi M, Cho HY, Han BS, Kim SH, Kim HO, Lim YT, Chung BH. 2009. Acute toxicity and pharmacokinetics of 13 nm-sized PEG-coated gold nanoparticles. Toxicol Appl Pharmacol 236:16-24.

Choi AO, Brown SE, Szyf M, Maysinger D. 2008. Quantum dot-induced epigenetic and genotoxic changes in human breast cancer cells. J Mol Med (Berl) 86:291-302.

Chuang HN, Lohaus R, Hanisch UK, Binder C, Dehghani F, Pukrop T. 2013. Coculture System with an Organotypic Brain Slice and 3D Spheroid of Carcinoma Cells. J Vis Exp : 50881.

Connor EE, Mwamuka J, Gole A, Murphy CJ, Wyatt MD. 2005. Gold nanoparticles are taken up by human cells but do not cause acute cytotoxicity. Small 1:325-327.

Corbalan JJ, Medina C, Jacoby A, Malinski T, Radomski MW. 2012. Amorphous silica nanoparticles aggregate human platelets: potential implications for vascular homeostasis. Int J Nanomedicine 7:631-639.

Cremer TJ, Ravneberg DH, Clay CD, Piper-Hunter MG, Marsh CB, Elton TS, Gunn JS, Amer A, Kanneganti TD, Schlesinger LS, Butchar JP, Tridandapani S. 2009. MiR-155 induction by F. novicida but not the virulent F. tularensis results in SHIP down-regulation and enhanced pro-inflammatory cytokine response. PLoS One 4:e8508.

Das S, Debnath N, Mitra S, Datta A, Goswami A. 2012. Comparative analysis of stability and toxicity profile of three differently capped gold nanoparticles for biomedical usage. Biometals 25:1009-1022.

De Jong WH, Hagens WI, Krystek P, Burger MC, Sips AJ, Geertsma RE. 2008. Particle size-dependent organ distribution of gold nanoparticles after intravenous administration. Biomaterials 29:1912-1919.

Deaton AM, Bird A. 2011. CpG islands and the regulation of transcription. Genes Dev 25:1010-1022.

Dennis G, Jr., Sherman BT, Hosack DA, Yang J, Gao W, Lane HC, Lempicki RA. 2003. DAVID: Database for Annotation, Visualization, and Integrated Discovery. Genome Biol 4:P3.

Desai MP, Labhasetwar V, Amidon GL, Levy RJ. 1996. Gastrointestinal uptake of biodegradable microparticles: effect of particle size. Pharm Res 13:1838-1845.

Diabate S, Mulhopt S, Paur HR, Krug HF. 2008. The response of a co-culture lung model to fine and ultrafine particles of incinerator fly ash at the air-liquid interface. Altern Lab Anim 36:285-298.

Du T, Zamore PD. 2007. Beginning to understand microRNA function. Cell Res 17:661-663.

Dykman LA, Khlebtsov NG. 2011. Gold nanoparticles in biology and medicine: recent advances and prospects. Acta Naturae 3:34-55.

Edwards CA, Ferguson-Smith AC. 2007. Mechanisms regulating imprinted genes in clusters. Curr Opin Cell Biol 19:281-289.

Elton TS, Selemon H, Elton SM, Parinandi NL. 2013. Regulation of the MIR155 host gene in physiological and pathological processes. Gene 532:1-12.

Eom HJ, Chatterjee N, Lee J, Choi J. 2014. Integrated mRNA and micro RNA profiling reveals epigenetic mechanism of differential sensitivity of Jurkat T cells to AgNPs and Ag ions. Toxicol Lett 229:311-318.

Erdely A, Hulderman T, Salmen R, Liston A, Zeidler-Erdely PC, Schwegler-Berry D, Castranova V, Koyama S, Kim YA, Endo M, Simeonova PP. 2009. Cross-talk between lung and systemic circulation during carbon nanotube respiratory exposure. Potential biomarkers. Nano Lett 9:36-43.

Eulalio A, Huntzinger E, Izaurralde E. 2008. Getting to the root of miRNA-mediated gene silencing. Cell 132:9-14.

Fabian E, Landsiedel R, Ma-Hock L, Wiench K, Wohlleben W, van Ravenzwaay B. 2008. Tissue distribution and toxicity of intravenously administered titanium dioxide nanoparticles in rats. Arch Toxicol 82:151-157.

Faraoni I, Antonetti FR, Cardone J, Bonmassar E. 2009. miR-155 gene: a typical multifunctional microRNA. Biochim Biophys Acta 1792:497-505.

Farraj AK, Hazari MS, Haykal-Coates N, Lamb C, Winsett DW, Ge Y, Ledbetter AD, Carll AP, Bruno M, Ghio A, Costa DL. 2011. ST depression, arrhythmia, vagal dominance, and reduced cardiac micro-RNA in particulate-exposed rats. Am J Respir Cell Mol Biol 44:185-196.

Faxuan W, Qin Z, Dinglun Z, Tao Z, Xiaohui R, Liqiang Z, Yajia L. 2012. Altered microRNAs expression profiling in experimental silicosis rats. J Toxicol Sci 37:1207-1215.

Filep JG, El Kebir D. 2008. Serum amyloid A as a marker and mediator of acute coronary syndromes. Future Cardiol 4:495-504.

Finnegan EJ, Matzke MA. 2003. The small RNA world. J Cell Sci 116:4689-4693.

Fraga S, Faria H, Soares ME, Duarte JA, Soares L, Pereira E, Costa-Pereira C, Teixeira JP, de Lourdes Bastos M, Carmo H. 2013. Influence of the surface coating on the cytotoxicity, genotoxicity and uptake of gold nanoparticles in human HepG2 cells. J Appl Toxicol 33:1111-1119.

Freemerman AJ, Johnson AR, Sacks GN, Milner JJ, Kirk EL, Troester MA, Macintyre AN, Goraksha-Hicks P, Rathmell JC, Makowski L. 2014. Metabolic reprogramming of macrophages: glucose transporter (GLUT1)-mediated glucose metabolism drives a pro- inflammatory phenotype. J Biol Chem 289:7884-7896.

Fujita K, Fukuda M, Fukui H, Horie M, Endoh S, Uchida K, Shichiri M, Morimoto Y, Ogami A, Iwahashi H. 2014. Intratracheal instillation of single-wall carbon nanotubes in the rat lung induces time-dependent changes in gene expression. Nanotoxicology:1-12.

G.A. Calin CMC. 2006. MicroRNA signatures in human cancers. Nat Rev Cancer 6:857–866.

Gaiser BK, Biswas A, Rosenkranz P, Jepson MA, Lead JR, Stone V, Tyler CR, Fernandes TF. 2011. Effects of silver and cerium dioxide micro- and nano-sized particles on Daphnia magna. J Environ Monit 13:1227-1235.

Gando S, Sawamura A, Hayakawa M. 2011. Trauma, shock, and disseminated intravascular coagulation: lessons from the classical literature. Ann Surg 254:10-19.

Gao W, Yu Y, Cao H, Shen H, Li X, Pan S, Shu Y. 2010. Deregulated expression of miR-21, miR-143 and miR-181a in non small cell lung cancer is related to clinicopathologic characteristics or patient prognosis. Biomed Pharmacother 64:399-408.

Garrean S, Gao XP, Brovkovych V, Shimizu J, Zhao YY, Vogel SM, Malik AB. 2006. Caveolin-1 regulates NF-kappaB activation and lung inflammatory response to sepsis induced by lipopolysaccharide. J Immunol 177:4853-4860.

Gebhardt R. 2002. Co-cultivation of liver epithelial cells with hepatocytes. Methods Mol Biol 188:337-346.

Gerber A, Bundschuh M, Klingelhofer D, Groneberg DA. 2013. Gold nanoparticles: recent aspects for human toxicology. J Occup Med Toxicol 8:32.

Gilleron J, Querbes W, Zeigerer A, Borodovsky A, Marsico G, Schubert U, Manygoats K, Seifert S, Andree C, Stoter M, Epstein-Barash H, Zhang L, Koteliansky V, Fitzgerald K, Fava E, Bickle M, Kalaidzidis Y, Akinc A, Maier M, Zerial M. 2013. Image-based analysis of lipid nanoparticle-mediated siRNA delivery, intracellular trafficking and endosomal escape. Nat Biotechnol 31:638-646.

Glazer ES, Zhu C, Hamir AN, Borne A, Thompson CS, Curley SA. 2011. Biodistribution and acute toxicity of naked gold nanoparticles in a rabbit hepatic tumor model. Nanotoxicology 5:459-468.

Global-Industry-Analysts. 2012. Nanotechnology (Global Industry Analysts Inc). Available at http://www.directionsmag.com/companies/global-industry-analysts-inc-gia/95184, accessed on 16 October 2014.

Goldberg AD, Allis CD, Bernstein E. 2007. Epigenetics: a landscape takes shape. Cell 128:635-638.

Gong C, Tao G, Yang L, Liu J, Liu Q, Li W, Zhuang Z. 2012. Methylation of PARP-1 promoter involved in the regulation of nano-SiO2-induced decrease of PARP-1 mRNA expression. Toxicol Lett 209:264-269.

Gong C, Tao G, Yang L, Liu J, Liu Q, Zhuang Z. 2010. SiO(2) nanoparticles induce global genomic hypomethylation in HaCaT cells. Biochem Biophys Res Commun 397:397-400.

Gonzalez S, Pisano DG, Serrano M. 2008. Mechanistic principles of chromatin remodeling guided by siRNAs and miRNAs. Cell Cycle 7:2601-2608.

Goodman CM, McCusker CD, Yilmaz T, Rotello VM. 2004. Toxicity of gold nanoparticles functionalized with cationic and anionic side chains. Bioconjug Chem 15:897-900.

Gosens I, Post JA, de la Fonteyne LJ, Jansen EH, Geus JW, Cassee FR, de Jong WH. 2010. Impact of agglomeration state of nano- and submicron sized gold particles on pulmonary inflammation. Part Fibre Toxicol 7:37.

Guo YY, Zhang J, Zheng YF, Yang J, Zhu XQ. 2011. Cytotoxic and genotoxic effects of multi-wall carbon nanotubes on human umbilical vein endothelial cells in vitro. Mutat Res 721:184-191.

Halappanavar S, Jackson P, Williams A, Jensen KA, Hougaard KS, Vogel U, Yauk CL, Wallin H. 2011. Pulmonary response to surface-coated nanotitanium dioxide particles includes induction of acute phase response genes, inflammatory cascades, and changes in microRNAs: a toxicogenomic study. Environ Mol Mutagen 52:425-439.

Hao X, Wu J, Shan Y, Cai M, Shang X, Jiang J, Wang H. 2012. Caveolae-mediated endocytosis of biocompatible gold nanoparticles in living Hela cells. J Phys Condens Matter 24:164207.

He R, Sang H, Ye RD. 2003. Serum amyloid A induces IL-8 secretion through a G protein-coupled receptor, FPRL1/LXA4R. Blood 101:1572-1581.

He X, Young SH, Schwegler-Berry D, Chisholm WP, Fernback JE, Ma Q. 2011. Multiwalled carbon nanotubes induce a fibrogenic response by stimulating reactive oxygen species production, activating NF-kappaB signaling, and promoting fibroblast-to-myofibroblast transformation. Chem Res Toxicol 24:2237-2248.

He Z, Liu J, Du L. 2014. The unexpected effect of PEGylated gold nanoparticles on the primary function of erythrocytes. Nanoscale 6:9017-9024.

Herzog F, Loza K, Balog S, Clift MJ, Epple M, Gehr P, Petri-Fink A, Rothen-Rutishauser B. 2014. Mimicking exposures to acute and lifetime concentrations of inhaled silver nanoparticles by two different in vitro approaches. Beilstein J Nanotechnol 5:1357-1370.

Higby GJ. 1982. Gold in medicine: a review of its use in the West before 1900. Gold Bull 15:130-140.

Hirn S, Semmler-Behnke M, Schleh C, Wenk A, Lipka J, Schaffler M, Takenaka S, Moller W, Schmid G, Simon U, Kreyling WG. 2011. Particle size-dependent and surface charge-dependent biodistribution of gold nanoparticles after intravenous administration. Eur J Pharm Biopharm 77:407-416.

Hoet PH, Bruske-Hohlfeld I, Salata OV. 2004. Nanoparticles - known and unknown health risks. J Nanobiotechnology 2:12.

Hoffmann A, Natoli G, Ghosh G. 2006. Transcriptional regulation via the NF-kappaB signaling module. Oncogene 25:6706-6716.

Hougaard KS, Jensen KA, Nordly P, Taxvig C, Vogel U, Saber AT, Wallin H. 2008. Effects of prenatal exposure to diesel exhaust particles on postnatal development, behavior, genotoxicity and inflammation in mice. Part Fibre Toxicol 5:3.

Huang da W, Sherman BT, Lempicki RA. 2009. Systematic and integrative analysis of large gene lists using DAVID bioinformatics resources. Nat Protoc 4:44-57.

Hussain S, Vanoirbeek JA, Haenen S, Haufroid V, Boland S, Marano F, Nemery B, Hoet PH. 2013. Prior lung inflammation impacts on body distribution of gold nanoparticles. Biomed Res Int 2013:923475.

Hwang JH, Kim SJ, Kim YH, Noh JR, Gang GT, Chung BH, Song NW, Lee CH. 2012. Susceptibility to gold nanoparticle-induced hepatotoxicity is enhanced in a mouse model of nonalcoholic steatohepatitis. Toxicology 294:27-35.

Imperatore R, Carotenuto G, Di Grazia MA, Ferrandino I, Palomba L, Mariotti R, Vitale E, De Nicola S, Longo A, Cristino L. 2014. Imidazole-stabilized gold nanoparticles induce neuronal apoptosis: An in vitro and in vivo study. J Biomed Mater Res A. [Epub ahead of print]

Inomata M, Tagawa H, Guo YM, Kameoka Y, Takahashi N, Sawada K. 2009. MicroRNA-17-92 down-regulates expression of distinct targets in different B-cell lymphoma subtypes. Blood 113:396-402.

Inoue K, Takano H, Shimada A, Satoh M. 2009. Metallothionein as an anti-inflammatory mediator. Mediators Inflamm 2009:101659.

Ivanov AI. 2008. Pharmacological inhibition of endocytic pathways: is it specific enough to be useful? Methods Mol Biol 440:15-33.

Iwaki T, Tanaka A, Miyawaki Y, Suzuki A, Kobayashi T, Takamatsu J, Matsushita T, Umemura K, Urano T, Kojima T, Terao T, Kanayama N. 2011. Life-threatening hemorrhage and prolonged wound healing are remarkable phenotypes manifested by complete plasminogen activator inhibitor-1 deficiency in humans. J Thromb Haemost 9:1200-1206.

Izzotti A, Calin GA, Arrigo P, Steele VE, Croce CM, De Flora S. 2009. Downregulation of microRNA expression in the lungs of rats exposed to cigarette smoke. FASEB J 23:806-812.

Jain PK, Huang X, El-Sayed IH, El-Sayed MA. 2008. Noble metals on the nanoscale: optical and photothermal properties and some applications in imaging, sensing, biology, and medicine. Acc Chem Res 41:1578-1586.

Jain PK, Lee KS, El-Sayed IH, El-Sayed MA. 2006. Calculated absorption and scattering properties of gold nanoparticles of different size, shape, and composition: applications in biological imaging and biomedicine. J Phys Chem B 110:7238-7248.

Jeong EH, Jung G, Hong CA, Lee H. 2013. Gold nanoparticle (AuNP)-based drug delivery and molecular imaging for biomedical applications. Arch Pharm Res 37:53-59.

Jia HY, Liu Y, Zhang XJ, Han L, Du LB, Tian Q, Xu YC. 2009. Potential oxidative stress of gold nanoparticles by induced-NO releasing in serum. J Am Chem Soc 131:40-41.

Jiang W, Mashayekhi H, Xing B. 2009. Bacterial toxicity comparison between nano and micro-scaled oxide particles. Environ Pollut 157:1619-1625.

Jin CY, Zhu BS, Wang XF, Lu QH. 2008. Cytotoxicity of titanium dioxide nanoparticles in mouse fibroblast cells. Chem Res Toxicol 21:1871-1877.

Jin H, Heller DA, Sharma R, Strano MS. 2009. Size-dependent cellular uptake and expulsion of single-walled carbon nanotubes: single particle tracking and a generic uptake model for nanoparticles. ACS Nano 3:149-158.

Johnston HJ, Hutchison G, Christensen FM, Peters S, Hankin S, Stone V. 2010a. A review of the in vivo and in vitro toxicity of silver and gold particulates: particle attributes and biological mechanisms responsible for the observed toxicity. Crit Rev Toxicol 40:328-346.

Johnston HJ, Hutchison GR, Christensen FM, Aschberger K, Stone V. 2010b. The biological mechanisms and physicochemical characteristics responsible for driving fullerene toxicity. Toxicol Sci 114:162-182.

Joris F, Manshian BB, Peynshaert K, De Smedt SC, Braeckmans K, Soenen SJ. 2013. Assessing nanoparticle toxicity in cell-based assays: influence of cell culture parameters and optimized models for bridging the in vitro-in vivo gap. Chem Soc Rev 42:8339-8359.

Juhan-Vague I, Alessi MC. 1997. PAI-1, obesity, insulin resistance and risk of cardiovascular events. Thromb Haemost 78:656-660.

Jun EA, Lim KM, Kim K, Bae ON, Noh JY, Chung KH, Chung JH. 2011. Silver nanoparticles enhance thrombus formation through increased platelet aggregation and procoagulant activity. Nanotoxicology 5:157-167.

Jung JJ, Noh S, Jeung HC, Jung M, Kim TS, Noh SH, Roh JK, Chung HC, Rha SY. 2010. Chemokine growth-regulated oncogene 1 as a putative biomarker for gastric cancer progression. Cancer Sci 101:2200-2206.

Kanno S, Furuyama A, Hirano S. 2007. A murine scavenger receptor MARCO recognizes polystyrene nanoparticles. Toxicol Sci 97:398-406.

Karin M, Eddy RL, Henry WM, Haley LL, Byers MG, Shows TB. 1984. Human metallothionein genes are clustered on chromosome 16. Proc Natl Acad Sci U S A 81:5494-5498.

Kawada I, Hasina R, Lennon FE, Bindokas VP, Usatyuk P, Tan YH, Krishnaswamy S, Arif Q, Carey G, Hseu RD, Robinson M, Tretiakova M, Brand TM, Iida M, Ferguson MK, Wheeler DL, Husain AN, Natarajan V, Vokes EE, Singleton PA, Salgia R. 2013. Paxillin mutations affect focal adhesions and lead to altered mitochondrial dynamics: relevance to lung cancer. Cancer Biol Ther 14:679-691.

Kawasaki T, Kawai T. 2014. Toll-like receptor signaling pathways. Front Immunol 5:461.

Kean WF, Forestier F, Kassam Y, Buchanan WW, Rooney PJ. 1985. The history of gold therapy in rheumatoid disease. Semin Arthritis Rheum 14:180-186.

Keel T HR, Harper T. 2010. Gold for good. Gold and nanotechnology in the age of innovation. World Gold Council.1-20.

Kendall M, Holgate S. 2012. Health impact and toxicological effects of nanomaterials in the lung. Respirology 17:743-758.

Khan HA, Abdelhalim MA, Al-Ayed MS, Alhomida AS. 2012. Effect of gold nanoparticles on glutathione and malondialdehyde levels in liver, lung and heart of rats. Saudi J Biol Sci 19:461-464.

Khan HA, Abdelhalim MA, Alhomida AS, Al Ayed MS. 2013. Transient increase in IL-1beta, IL-6 and TNF-alpha gene expression in rat liver exposed to gold nanoparticles. Genet Mol Res 12:5851-5857.

Khlebtsov N, Dykman L. 2011. Biodistribution and toxicity of engineered gold nanoparticles: a review of in vitro and in vivo studies. Chem Soc Rev 40:1647-1671.

Kim CK, Ghosh P, Rotello VM. 2009a. Multimodal drug delivery using gold nanoparticles. Nanoscale 1:61-67.

Kim HK, Lee DS, Kang SH, Kim JQ, Park S, Cho HI. 2007. Utility of the fibrinogen/C-reactive protein ratio for the diagnosis of disseminated intravascular coagulation. Acta Haematol 117:34-39.

Kim KT, Zaikova T, Hutchison JE, Tanguay RL. 2013. Gold nanoparticles disrupt zebrafish eye development and pigmentation. Toxicol Sci 133:275-288.

Kim S, Choi JE, Choi J, Chung KH, Park K, Yi J, Ryu DY. 2009b. Oxidative stress-dependent toxicity of silver nanoparticles in human hepatoma cells. Toxicol In Vitro 23:1076-1084.

Kim YJ, Lee JH, Lee Y, Jia J, Paek SH, Kim HB, Jin S, Ha UH. 2014. Nucleoside diphosphate kinase and flagellin from Pseudomonas aeruginosa induce interleukin 1 expression via the Akt/NF-kappaB signaling pathways. Infect Immun 82:3252-3260.

Koike H, Ueno Y, Naito T, Shiina T, Nakata S, Ouchi R, Obana Y, Sekine K, Zheng YW, Takebe T, Isono K, Koseki H, Taniguchi H. 2014. Ring1B promotes hepatic stem/progenitor cell expansion through simultaneous suppression of Cdkn1a and Cdkn2a in mice. Hepatology 60:323-333.

Kong W, Yang H, He L, Zhao JJ, Coppola D, Dalton WS, Cheng JQ. 2008. MicroRNA-155 is regulated by the transforming growth factor beta/Smad pathway and contributes to epithelial cell plasticity by targeting RhoA. Mol Cell Biol 28:6773-6784.

Kouzarides T. 2007. Chromatin modifications and their function. Cell 128:693-705.

Krpetic Z, Anguissola S, Garry D, Kelly PM, Dawson KA. 2014. Nanomaterials: impact on cells and cell organelles. Adv Exp Med Biol 811:135-156.

Kuhn DE, Nuovo GJ, Martin MM, Malana GE, Pleister AP, Jiang J, Schmittgen TD, Terry AV, Jr., Gardiner K, Head E, Feldman DS, Elton TS. 2008. Human chromosome 21-derived miRNAs are overexpressed in down syndrome brains and hearts. Biochem Biophys Res Commun 370:473-477.

Lampidonis AD, Theodorou G, Pecorini C, Rebucci R, Baldi A, Politis I. 2011. Cloning of the 5' regulatory regions and functional characterization of the core promoters of ovine PLAU (u-PA) and SERPIN1 (PAI-1). Gene 489:11-20.

Lasagna-Reeves C, Gonzalez-Romero D, Barria MA, Olmedo I, Clos A, Sadagopa Ramanujam VM, Urayama A, Vergara L, Kogan MJ, Soto C. 2010. Bioaccumulation and toxicity of gold nanoparticles after repeated administration in mice. Biochem Biophys Res Commun 393:649-655.

Le Saux O, Teeters K, Miyasato S, Choi J, Nakamatsu G, Richardson JA, Starcher B, Davis EC, Tam EK, Jourdan-Le Saux C. 2008. The role of caveolin-1 in pulmonary matrix remodeling and mechanical properties. Am J Physiol Lung Cell Mol Physiol 295:L1007-1017.

Lee J, Lilly GD, Doty RC, Podsiadlo P, Kotov NA. 2009. In vitro toxicity testing of nanoparticles in 3D cell culture. Small 5:1213-1221.

Lee K, Lee H, Lee KW, Park TG. 2011. Optical imaging of intracellular reactive oxygen species for the assessment of the cytotoxicity of nanoparticles. Biomaterials 32:2556-2565.

Leppanen M, Korpi A, Mikkonen S, Yli-Pirila P, Lehto M, Pylkkanen L, Wolff H, Kosma VM, Alenius H, Joutsensaari J, Pasanen P. 2014. Inhaled silica-coated TiO nanoparticles induced airway irritation, airflow limitation and inflammation in mice. Nanotoxicology. [Epub ahead of print]

Levi M, van der Poll T, Buller HR. 2004. Bidirectional relation between inflammation and coagulation. Circulation 109:2698-2704.

Li J, Liu Y, Ru B. 2005. Effect of metallothionein on cell viability and its interactions with cadmium and zinc in HEK293 cells. Cell Biol Int 29:843-848.

Li JJ, Hartono D, Ong CN, Bay BH, Yung LY. 2010a. Autophagy and oxidative stress associated with gold nanoparticles. Biomaterials 31:5996-6003.

Li JJ, Muralikrishnan S, Ng CT, Yung LY, Bay BH. 2010b. Nanoparticle-induced pulmonary toxicity. Exp Biol Med (Maywood) 235:1025-1033.

Li JJ, Lo SL, Ng CT, Gurung RL, Hartono D, Hande MP, Ong CN, Bay BH, Yung LY. 2011. Genomic instability of gold nanoparticle treated human lung fibroblast cells. Biomaterials 32:5515-5523.

Li JJ, Zou L, Hartono D, Ong CN, Bay BH, Yung LY. 2008. Gold nanoparticles induce oxidative damage in lung fibroblasts in vitro. Adv Mater 20:138–142.

Li K, Du Y, Jiang BL, He JF. 2014. Increased microRNA-155 and decreased microRNA-146a may promote ocular inflammation and proliferation in Graves' ophthalmopathy. Med Sci Monit 20:639-643.

Li LC, Dahiya R. 2002. MethPrimer: designing primers for methylation PCRs. Bioinformatics 18:1427-1431.

Li S, Wang H, Qi Y, Tu J, Bai Y, Tian T, Huang N, Wang Y, Xiong F, Lu Z, Xiao Z. 2011b. Assessment of nanomaterial cytotoxicity with SOLiD sequencing-based microRNA expression profiling. Biomaterials 32:9021-9030.

Li S, Wang Y, Wang H, Bai Y, Liang G, Huang N, Xiao Z. 2011c. MicroRNAs as participants in cytotoxicity of CdTe quantum dots in NIH/3T3 cells. Biomaterials 32:3807-3814.

Li Z, Musich PR, Cartwright BM, Wang H, Zou Y. 2013. UV-induced nuclear import of XPA is mediated by importin-alpha4 in an ATR-dependent manner. PLoS One 8:e68297.

Libutti SK, Paciotti GF, Byrnes AA, Alexander HR, Jr., Gannon WE, Walker M, Seidel GD, Yuldasheva N, Tamarkin L. 2010. Phase I and pharmacokinetic studies of CYT-6091, a novel PEGylated colloidal gold-rhTNF nanomedicine. Clin Cancer Res 16:6139-6149.

Lin W, Xu Y, Huang CC, Ma Y, Shannon KB, Chen DR, Huang YW. 2009. Toxicity of nano-and micro-sized ZnO particles in human lung epithelial cells. J Nanopart Res 11:25-39.

Ling J, Kumar R. 2012. Crosstalk between NFkB and glucocorticoid signaling: a potential target of breast cancer therapy. Cancer Lett 322:119-126.

Liu Y, Shao LL, Pang W, Lan XM, Lu JX, Cong YL, Wang CB. 2013. Induction of adhesion molecule expression in co-culture of human bronchial epithelial cells and neutrophils suppressed by puerarin via down-regulating p38 mitogen-activated protein kinase and nuclear factor kappa B pathways. Chin J Integr Med 20:360-368.

Lopez-Otin C, Blasco MA, Partridge L, Serrano M, Kroemer G. 2013. The hallmarks of aging. Cell 153:1194-1217.

Lu J, Yu Y, Zhu I, Cheng Y, Sun PD. 2014. Structural mechanism of serum amyloid A-mediated inflammatory amyloidosis. Proc Natl Acad Sci U S A 111:5189-5194.

Lunov O, Zablotskii V, Syrovets T, Röcker C, Tron K, Nienhaus GU, Simmet T. 2011. Modeling receptor-mediated endocytosis of polymer-functionalized iron oxide nanoparticles by human macrophages. Biomaterials 32:547-555.

Lu S, Duffin R, Poland C, Daly P, Murphy F, Drost E, Macnee W, Stone V, Donaldson K. 2009a. Efficacy of simple short-term in vitro assays for predicting the potential of metal oxide nanoparticles to cause pulmonary inflammation. Environ Health Perspect 117:241-247.

Lu TX, Munitz A, Rothenberg ME. 2009b. MicroRNA-21 is up-regulated in allergic airway inflammation and regulates IL-12p35 expression. J Immunol 182:4994-5002.

Lynch I, Salvati A, Dawson KA. 2009. Protein-nanoparticle interactions: What does the cell see? Nat Nanotechnol 4:546-547.

Ma-Hock L, Burkhardt S, Strauss V, Gamer AO, Wiench K, van Ravenzwaay B, Landsiedel R. 2009. Development of a short-term inhalation test in the rat using nano-titanium dioxide as a model substance. Inhal Toxicol 21:102-118.

Madl AK, Pinkerton KE. 2009. Health effects of inhaled engineered and incidental nanoparticles. Crit Rev Toxicol 39:629-658.

Markelc B, Skvarca E, Dolinsek T, Kloboves VP, Coer A, Sersa G, Cemazar M. 2014. Inhibitor of endocytosis impairs gene electrotransfer to mouse muscle in vivo. Bioelectrochemistry. [Epub ahead of print]

Martin MM, Lee EJ, Buckenberger JA, Schmittgen TD, Elton TS. 2006. MicroRNA-155 regulates human angiotensin II type 1 receptor expression in fibroblasts. J Biol Chem 281:18277-18284.

Marzi C, Albrecht E, Hysi PG, Lagou V, Waldenberger M, Tonjes A, Prokopenko I, Heim K, Blackburn H, Ried JS, Kleber ME, Mangino M, Thorand B, Peters A, Hammond CJ, Grallert H, Boehm BO, Kovacs P, Geistlinger L, Prokisch H, Winkelmann BR, Spector TD, Wichmann HE, Stumvoll M, Soranzo N, Marz W, Koenig W, Illig T, Gieger C. 2010. Genome-wide association study identifies two novel regions at 11p15.5-p13 and 1p31 with major impact on acute-phase serum amyloid A. PLoS Genet 6:e1001213.

Mateo D, Morales P, Avalos A, Haza AI. 2014. Oxidative stress contributes to gold nanoparticle-induced cytotoxicity in human tumor cells. Toxicol Mech Methods 24:161-172.

Mazumder A, Shivashankar GV. 2007. Gold-nanoparticle-assisted laser perturbation of chromatin assembly reveals unusual aspects of nuclear architecture within living cells. Biophys J 93:2209-2216.

Mididoddi S, McGuirt JP, Sens MA, Todd JH, Sens DA. 1996. Isoform-specific expression of metallothionein mRNA in the developing and adult human kidney. Toxicology Letters 85:17-27.

Miranda KC, Huynh T, Tay Y, Ang YS, Tam WL, Thomson AM, Lim B, Rigoutsos I. 2006. A pattern-based method for the identification of MicroRNA binding sites and their corresponding heteroduplexes. Cell 126:1203-1217.

Mironava T, Hadjiargyrou M, Simon M, Jurukovski V, Rafailovich MH. 2010. Gold nanoparticles cellular toxicity and recovery: effect of size, concentration and exposure time. Nanotoxicology 4:120-137.

Moos PJ, Chung K, Woessner D, Honeggar M, Cutler NS, Veranth JM. 2010. ZnO particulate matter requires cell contact for toxicity in human colon cancer cells. Chem Res Toxicol 23:733–739.

Morales-Avila E, Ferro-Flores G, Ocampo-Garcia BE, Gomez-Olivan LM. 2012. Engineered multifunctional RGD-gold nanoparticles for the detection of tumour-specific alpha(v)beta(3) expression: chemical characterisation and ecotoxicological risk assessment. J Biomed Nanotechnol 8:991-999.

Morimoto Y, Ogami A, Todoroki M, Yamamoto M, Murakami M, Hirohashi M, Oyabu T, Myojo T, Nishi K, Kadoya C, Yamasaki S, Nagatomo H, Fujita K, Endoh S, Uchida K, Yamamoto K, Kobayashi N, Nakanishi J, Tanaka I. 2010. Expression of inflammation-related cytokines following intratracheal instillation of nickel oxide nanoparticles. Nanotoxicology 4:161-176.

Morisco C, Marrone C, Galeotti J, Shao D, Vatner DE, Vatner SF, Sadoshima J. 2008. Endocytosis machinery is required for beta1-adrenergic receptor-induced hypertrophy in neonatal rat cardiac myocytes. Cardiovasc Res 78:36-44.

Munoz A, Costa M. 2012. Elucidating the mechanisms of nickel compound uptake: a review of particulate and nano-nickel endocytosis and toxicity. Toxicol Appl Pharmacol 260:1-16.

Myllynen P. 2009. Nanotoxicology: damaging DNA from a distance. Nat Nanotechnol 4:795-796.

Nair S, Sasidharan A, Rani VVD, Menon D, Nair S, Manzoor K, Raina S. 2009. Role of size scale of ZnO nanoparticles and microparticles on toxicity toward bacteria and osteoblast cancer cells. J Mater Sci Mater Med 20:235–241.

Naqvi S, Samim M, Abdin M, Ahmed FJ, Maitra A, Prashant C, Dinda AK. 2010. Concentration-dependent toxicity of iron oxide nanoparticles mediated by increased oxidative stress. Int J Nanomedicine 5:983-989.

Nativo P, Prior IA, Brust M. 2008. Uptake and intracellular fate of surface-modified gold nanoparticles. ACS Nano 2:1639-1644.

Nemmar A, Albarwani S, Beegam S, Yuvaraju P, Yasin J, Attoub S, Ali BH. 2014. Amorphous silica nanoparticles impair vascular homeostasis and induce systemic inflammation. Int J Nanomedicine 9:2779-2789.

Ng CT, Dheen ST, Yip WC, Ong CN, Bay BH, Lanry Yung LY. 2011. The induction of epigenetic regulation of PROS1 gene in lung fibroblasts by gold nanoparticles and implications for potential lung injury. Biomaterials 32:7609-7615.

Oberdorster G, Oberdorster E, Oberdorster J. 2005. Nanotoxicology: an emerging discipline evolving from studies of ultrafine particles. Environ Health Perspect 113:823-839.

Ogiso T, Iwaki M, Mori K. 1981. Fluidity of human erythrocyte membrane and effect of chlorpromazine on fluidity and phase separation of membrane. Biochim Biophys Acta 649:325-335.

Pacurari M, Qian Y, Fu W, Schwegler-Berry D, Ding M, Castranova V, Guo NL. 2012. Cell permeability, migration, and reactive oxygen species induced by multiwalled carbon nanotubes in human microvascular endothelial cells. J Toxicol Environ Health A 75:129-147.

Pan Y, Leifert A, Ruau D, Neuss S, Bornemann J, Schmid G, Brandau W, Simon U, Jahnen-Dechent W. 2009. Gold nanoparticles of diameter 1.4 nm trigger necrosis by oxidative stress and mitochondrial damage. Small 5:2067-2076.

Pan Y, Neuss S, Leifert A, Fischler M, Wen F, Simon U, Schmid G, Brandau W, Jahnen-Dechent W. 2007. Size-dependent cytotoxicity of gold nanoparticles. Small 3:1941-1949.

Paret C, Schon Z, Szponar A, Kovacs G. 2010. Inflammatory protein serum amyloid A1 marks a subset of conventional renal cell carcinomas with fatal outcome. Eur Urol 57:859-866.

Patel PC, Giljohann DA, Daniel WL, Zheng D, Prigodich AE, Mirkin CA. 2010. Scavenger receptors mediate cellular uptake of polyvalent oligonucleotide-functionalized gold nanoparticles. Bioconjug Chem 21:2250-2256.

Pedersen IM, Otero D, Kao E, Miletic AV, Hother C, Ralfkiaer E, Rickert RC, Gronbaek K, David M. 2009. Onco-miR-155 targets SHIP1 to promote TNFalpha-dependent growth of B cell lymphomas. EMBO Mol Med 1:288-295.

Perkins ND. 2007. Integrating cell-signalling pathways with NF-kappaB and IKK function. Nat Rev Mol Cell Biol 8:49-62.

Perkins ND. 2012. Cysteine 38 holds the key to NF-kappaB activation. Mol Cell 45:1-3.

Petkovic J, Zegura B, Stevanovic M, Drnovsek N, Uskokovic D, Novak S, Filipic M. 2010. DNA damage and alterations in expression of DNA damage responsive genes induced by TiO(2) nanoparticles in human hepatoma HepG2 cells. Nanotoxicology 5:341-353.

Piazza G, Goldhaber SZ. 2011. Chronic thromboembolic pulmonary hypertension. N Engl J Med 364:351-360.

Pillai RS, Bhattacharyya SN, Filipowicz W. 2007. Repression of protein synthesis by miRNAs: how many mechanisms? Trends Cell Biol 17:118-126.

Pizarro JG, Folch J, Vazquez De la Torre A, Verdaguer E, Junyent F, Jordan J, Pallas M, Camins A. 2009. Oxidative stress-induced DNA damage and cell cycle regulation in B65 dopaminergic cell line. Free Radic Res 43:985-994.

Rattanapinyopituk K, Shimada A, Morita T, Sakurai M, Asano A, Hasegawa T, Inoue K, Takano H. 2013a. Demonstration of the Clathrin- and Caveolin-Mediated Endocytosis at the Maternal-Fetal Barrier in Mouse Placenta after Intravenous Administration of Gold Nanoparticles. J Vet Med Sci.

Rattanapinyopituk K, Shimada A, Morita T, Togawa M, Hasegawa T, Seko Y, Inoue K, Takano H. 2013b. Ultrastructural changes in the air-blood barrier in mice after intratracheal instillations of Asian sand dust and gold nanoparticles. Exp Toxicol Pathol 65:1043-1051.

Reeves JF, Davies SJ, Dodd NJ, Jha AN. 2008. Hydroxyl radicals (*OH) are associated with titanium dioxide (TiO(2)) nanoparticle-induced cytotoxicity and oxidative DNA damage in fish cells. Mutat Res 640:113-122.

Rejman J, Oberle V, Zuhorn IS, Hoekstra D. 2004. Size-dependent internalization of particles viat the pathways of clathrin- and caveolae-mediated endocytosis. Biochemical Journal 377:159-169.

Richards DG, McMillin DL, Mein EA, Nelson CD. 2002. Gold and its relationship to neurological/glandular conditions. Int J Neurosci 112:31-53.

Ros-Baro A, Lopez-Iglesias C, Peiro S, Bellido D, Palacin M, Zorzano A, Camps M. 2001. Lipid rafts are required for GLUT4 internalization in adipose cells. Proc Natl Acad Sci U S A 98:12050-12055.

Russell BH, Vasan R, Keene DR, Koehler TM, Xu Y. 2008. Potential dissemination of Bacillus anthracis utilizing human lung epithelial cells. Cell Microbiol 10:945-957.

Ryter SW, Kim HP, Hoetzel A, Park JW, Nakahira K, Wang X, Choi AM. 2007. Mechanisms of cell death in oxidative stress. Antioxidants & redox signaling 9:49-89.

Sabella S, Carney RP, Brunetti V, Malvindi MA, Al-Juffali N, Vecchio G, Janes SM, Bakr OM, Cingolani R, Stellacci F, Pompa PP. 2014. A general mechanism for intracellular toxicity of metal-containing nanoparticles. Nanoscale 6:7052-7061.

Schaeublin NM, Braydich-Stolle LK, Schrand AM, Miller JM, Hutchison J, Schlager JJ, Hussain SM. 2011. Surface charge of gold nanoparticles mediates mechanism of toxicity. Nanoscale 3:410-420.

Schaller MD. 2001. Paxillin: a focal adhesion-associated adaptor protein. Oncogene 20:6459-6472.

Schins RP, Knaapen AM. 2007. Genotoxicity of poorly soluble particles. Inhal Toxicol 19 Suppl 1:189-198.

Schleh C, Holzwarth U, Hirn S, Wenk A, Simonelli F, Schaffler M, Moller W, Gibson N, Kreyling WG. 2013. Biodistribution of inhaled gold nanoparticles in mice and the influence of surfactant protein D. J Aerosol Med Pulm Drug Deliv 26:24-30.

Semmler-Behnke M, Kreyling WG, Lipka J, Fertsch S, Wenk A, Takenaka S, Schmid G, Brandau W. 2008. Biodistribution of 1.4- and 18-nm gold particles in rats. Small 4:2108-2111.

Setyawati MI, Tay CY, Chia SL, Goh SL, Fang W, Neo MJ, Chong HC, Tan SM, Loo SC, Ng KW, Xie JP, Ong CN, Tan NS, Leong DT. 2013. Titanium dioxide nanomaterials cause endothelial cell leakiness by disrupting the homophilic interaction of VE-cadherin. Nat Commun 4:1673.

Sharma M, Salisbury RL, Maurer EI, Hussain SM, Sulentic CE. 2013. Gold nanoparticles induce transcriptional activity of NF-kappaB in a B-lymphocyte cell line. Nanoscale 5:3747-3756.

Shen L, Waterland RA. 2007. Methods of DNA methylation analysis. Curr Opin Clin Nutr Metab Care 10:576-581.

Shukla RK, Sharma V, Pandey AK, Singh S, Sultana S, Dhawan A. 2011. ROS-mediated genotoxicity induced by titanium dioxide nanoparticles in human epidermal cells. Toxicol In Vitro 25:231-241.

Simioni P, Tormene D, Spiezia L, Tognin G, Rossetto V, Radu C, Prandoni P. 2006. Inherited thrombophilia and venous thromboembolism. Semin Thromb Hemost 32:700-708.

Simone TM, Higgins CE, Czekay RP, Law BK, Higgins SP, Archambeault J, Kutz SM, Higgins PJ. 2014. SERPINE1: A Molecular Switch in the Proliferation-Migration Dichotomy in Wound-"Activated" Keratinocytes. Adv Wound Care (New Rochelle) 3:281-290.

Singh RD, Puri V, Valiyaveettil JT, Marks DL, Bittman R, Pagano RE. 2003. Selective caveolin-1-dependent endocytosis of glycosphingolipids. Mol Biol Cell 14:3254-3265.

Smallridge RC, Burman KD, Wartofsky L. 1990. Malabsorption of thyroxine, calcium, and vitamin D in a thyroparathyroidectomized woman: efficacy of therapy with medium-chain triglyceride oil. Mil Med 155:156-158.

Smith PJ, Giroud M, Wiggins HL, Gower F, Thorley JA, Stolpe B, Mazzolini J, Dyson RJ, Rappoport JZ. 2012. Cellular entry of nanoparticles via serum sensitive clathrin-mediated endocytosis, and plasma membrane permeabilization. Int J Nanomedicine 7:2045-2055.

Snyder-Talkington BN, Schwegler-Berry D, Castranova V, Qian Y, Guo NL. 2013. Multi-walled carbon nanotubes induce human microvascular endothelial cellular effects in an alveolar-capillary co-culture with small airway epithelial cells. Part Fibre Toxicol 10:35.

Sonavane G, Tomoda K, Makino K. 2008. Biodistribution of colloidal gold nanoparticles after intravenous administration: effect of particle size. Colloids Surf B Biointerfaces 66:274-280.

Sperling RA, Parak WJ. 2010. Surface modification, functionalization and bioconjugation of colloidal inorganic nanoparticles. Philos Trans A Math Phys Eng Sci 368:1333-1383.

Standart N, Jackson RJ. 2007. MicroRNAs repress translation of m7Gppp-capped target mRNAs in vitro by inhibiting initiation and promoting deadenylation. Genes Dev 21:1975-1982.

Stennard FA, Holloway AF, Hamilton J, West AK. 1994. Characterisation of six additional human metallothionein genes. Biochimica et Biophysica Acta (BBA) - Gene Structure and Expression 1218:357-365.

Stephens LA, Mottet C, Mason D, Powrie F. 2001. Human CD4(+)CD25(+) thymocytes and peripheral T cells have immune suppressive activity in vitro. Eur J Immunol 31:1247-1254.

Stoccoro A, Karlsson HL, Coppede F, Migliore L. 2013. Epigenetic effects of nano-sized materials. Toxicology 313:3-14.

Sule N, Singh R, Srivastava DK. 2008. Alternative Modes of Binding of Recombinant Human Histone Deacetylase 8 to Colloidal Gold Nanoparticles. J Biomed Nanotechnol 4:463-468.

Sung JH, Ji JH, Park JD, Song MY, Song KS, Ryu HR, Yoon JU, Jeon KS, Jeong J, Han BS, Chung YH, Chang HK, Lee JH, Kim DW, Kelman BJ, Yu IJ. 2011a. Subchronic inhalation toxicity of gold nanoparticles. Part Fibre Toxicol 8:16.

Sung HJ, Ahn JM, Yoon YH, Rhim TY, Park CS, Park JY, Lee SY, Kim JW, Cho JY. 2011b. Identification and validation of SAA as a potential lung cancer biomarker and its involvement in metastatic pathogenesis of lung cancer. J Proteome Res 10:1383-1395.

Swa HL, Blackstock WP, Lim LH, Gunaratne J. 2012. Quantitative proteomics profiling of murine mammary gland cells unravels impact of annexin-1 on DNA damage response, cell adhesion, and migration. Mol Cell Proteomics 11:381-393.

Takeda K, Akira S. 2004. TLR signaling pathways. Semin Immunol 16:3-9.

Takenaka S, Moller W, Semmler-Behnke M, Karg E, Wenk A, Schmid O, Stoeger T, Jennen L, Aichler M, Walch A, Pokhrel S, Madler L, Eickelberg O, Kreyling WG. 2012. Efficient internalization and intracellular translocation of inhaled gold nanoparticles in rat alveolar macrophages. Nanomedicine (Lond) 7:855-865.

Tanaka S, Niioka, T 2001. Cytoprotective effects of metallothionein induced by metals against oxidative stress induced by hydrogen peroxide. Biomed Res Trace Elem 12:353- 354.

Tatur S, Maccarini M, Barker R, Nelson A, Fragneto G. 2013. Effect of functionalized gold nanoparticles on floating lipid bilayers. Langmuir 29:6606-6614.

Tedesco S, Doyle H, Blasco J, Redmond G, Sheehan D. 2010a. Exposure of the blue mussel, Mytilus edulis, to gold nanoparticles and the pro-oxidant menadione. Comp Biochem Physiol C Toxicol Pharmacol 151:167-174.

Tedesco S, Doyle H, Blasco J, Redmond G, Sheehan D. 2010b. Oxidative stress and toxicity of gold nanoparticles in Mytilus edulis. Aquat Toxicol 100:178-186.

ten Kate MK, van der Meer J. 2008. Protein S deficiency: a clinical perspective. Haemophilia 14:1222-1228.

Teng G, Hakimpour P, Landgraf P, Rice A, Tuschl T, Casellas R, Papavasiliou FN. 2008. MicroRNA-155 is a negative regulator of activation-induced cytidine deaminase. Immunity 28:621-629.

Tenzer S, Docter D, Kuharev J, Musyanovych A, Fetz V, Hecht R, Schlenk F, Fischer D, Kiouptsi K, Reinhardt C, Landfester K, Schild H, Maskos M, Knauer SK, Stauber RH. 2013. Rapid formation of plasma protein corona critically affects nanoparticle pathophysiology. Nat Nanotechnol 8:772-781.

Thounaojam MC, Kundu K, Kaushik DK, Swaroop S, Mahadevan A, Shankar SK, Basu A. 2014. MicroRNA 155 regulates Japanese encephalitis virus-induced inflammatory response by targeting Src homology 2-containing inositol phosphatase 1. J Virol 88:4798-4810.

Tili E, Michaille JJ, Wernicke D, Alder H, Costinean S, Volinia S, Croce CM. 2011. Mutator activity induced by microRNA-155 (miR-155) links inflammation and cancer. Proc Natl Acad Sci U S A 108:4908-4913.

Truong L, Saili KS, Miller JM, Hutchison JE, Tanguay RL. 2012. Persistent adult zebrafish behavioral deficits results from acute embryonic exposure to gold nanoparticles. Comp Biochem Physiol C Toxicol Pharmacol 155:269-274.

Tsai CY, Shiau AL, Chen SY, Chen YH, Cheng PC, Chang MY, Chen DH, Chou CH, Wang CR, Wu CL. 2007. Amelioration of collagen-induced arthritis in rats by nanogold. Arthritis Rheum 56:544-554.

Tsyusko OV, Unrine JM, Spurgeon D, Blalock E, Starnes D, Tseng M, Joice G, Bertsch PM. 2012. Toxicogenomic responses of the model organism Caenorhabditis elegans to gold nanoparticles. Environ Sci Technol 46:4115-4124.

Uboldi C, Bonacchi D, Lorenzi G, Hermanns MI, Pohl C, Baldi G, Unger RE, Kirkpatrick CJ. 2009. Gold nanoparticles induce cytotoxicity in the alveolar type-II cell lines A549 and NCIH441. Part Fibre Toxicol 6:18.

USEPA (United States Environmental Protection Agency). 2007. Nanotechnology White Paper. EPA/100/B-07/001. Prepared for the U.S. Environmental Protection Agency by members of the nanotechnology workgroup, a group of EPA's science policy council. Available at

http://www.epa.gov/osa/pdfs/nanotech/epa-nanotechnology-whitepaper-0207.pdf, accessed 24 September 2014.

Vasak M, Hasler DW. 2000. Metallothioneins: new functional and structural insights. Curr Opin Chem Biol 4:177-183.

Vecchio G, Galeone A, Brunetti V, Maiorano G, Rizzello L, Sabella S, Cingolani R, Pompa PP. 2012. Mutagenic effects of gold nanoparticles induce aberrant phenotypes in Drosophila melanogaster. Nanomedicine 8:1-7.

Vercauteren D, Vandenbroucke RE, Jones AT, Rejman J, Demeester J, De Smedt SC, Sanders NN, Braeckmans K. 2010. The use of inhibitors to study endocytic pathways of gene carriers: optimization and pitfalls. Mol Ther 18:561-569.

Wang H, Wu L, Reinhard BM. 2012. Scavenger receptor mediated endocytosis of silver nanoparticles into J774A.1 macrophages is heterogeneous. ACS Nano 6:7122-7132.

Wang S, Lawson R, Ray PC, Yu H. 2011. Toxic effects of gold nanoparticles on Salmonella typhimurium bacteria. Toxicol Ind Health 27:547-554.

Wang SH, Lee CW, Chiou A, Wei PK. 2010. Size-dependent endocytosis of gold nanoparticles studied by three-dimensional mapping of plasmonic scattering images. J Nanobiotechnology 8:33.

Warheit DB, Sayes CM, Reed KL, Swain KA. 2008. Health effects related to nanoparticle exposures: environmental, health and safety considerations for assessing hazards and risks. Pharmacol Ther 120:35-42.

West AK, Stallings R, Hildebrand CE, Chiu R, Karin M, Richards RI. 1990. Human metallothionein genes: Structure of the functional locus at 16q13. Genomics 8:513-518.

Wojnicki M, Luty-Blocho M, Bednarski M, Dudek M, Knutelska J, Sapa J, Zygmunt M, Nowak G, Fitzner K. 2013. Tissue distribution of gold nanoparticles after single intravenous administration in mice. Pharmacol Rep 65:1033-1038.

Wolfgang L. 2004. Industrial application of nanomaterials–chances and risks. Technology analysis, VDI Technologiezentrum. Available at http://www.innovationsbegleitung.de/11.pdf, accessed 25 September 2014.

Xiang S, Tong H, Shi Q, Fernandes JC, Jin T, Dai K, Zhang X. 2012. Uptake mechanisms of non-viral gene delivery. J Control Release 158:371-378.

Xu J, Wang G, Wang Y, Liu Q, Xu W, Tan Y, Cai L. 2009. Diabetes- and angiotensin II-induced cardiac endoplasmic reticulum stress and cell death: metallothionein protection. J Cell Mol Med 13:1499-1512.

Yamamoto K, Takeshita K, Kojima T, Takamatsu J, Saito H. 2005. Aging and plasminogen activator inhibitor-1 (PAI-1) regulation: implication in the pathogenesis of thrombotic disorders in the elderly. Cardiovasc Res 66:276-285.

Yang G, Rosen DG, Zhang Z, Bast RC, Jr., Mills GB, Colacino JA, Mercado-Uribe I, Liu J. 2006. The chemokine growth-regulated oncogene 1 (Gro-1) links RAS signaling to the senescence of stromal fibroblasts and ovarian tumorigenesis. Proc Natl Acad Sci U S A 103:16472-16477.

Yang H, Liu C, Yang D, Zhang H, Xi Z. 2009. Comparative study of cytotoxicity, oxidative stress and genotoxicity induced by four typical nanomaterials: the role of particle size, shape and composition. J Appl Toxicol 29:69-78.

Yang L, Shang L, Nienhaus GU. 2013. Mechanistic aspects of fluorescent gold nanocluster internalization by live HeLa cells. Nanoscale 5:1537-1543.

Yao Y, Costa M. 2013. Genetic and Epigenetic Effects of Nanoparticles. J Mol Genet Med 7:86.

Youngwon N, Kim JE, Lim HS, Han KS, Kim HK. 2013. Coagulation proteins influencing global coagulation assays in cirrhosis: hypercoagulability in cirrhosis assessed by thrombomodulin-induced thrombin generation assay. Biomed Res Int 2013:856754.

Yu B, Chen X, Li J, Qu Y, Su L, Peng Y, Huang J, Yan J, Yu Y, Gu Q, Zhu Z, Liu B. 2013. Stromal fibroblasts in the microenvironment of gastric carcinomas promote tumor metastasis via upregulating TAGLN expression. BMC Cell Biol 14:17.

Yu LE, Yung L-YL, Ong C-N, Tan Y-L, Balasubramanian SK, Hartono D, et al. 2007. Translocation and effects of gold nanoparticles after inhalation exposure in rats Nanotoxicology 1(3): 235-242.

References

Zander DS, Baz MA, Visner GA, Staples ED, Donnelly WH, Faro A, Scornik JC. 2001. Analysis of early deaths after isolated lung transplantation. Chest 120:225-232.

Zhang XD, Wu HY, Wu D, Wang YY, Chang JH, Zhai ZB, Meng AM, Liu PX, Zhang LA, Fan FY. 2010. Toxicologic effects of gold nanoparticles in vivo by different administration routes. Int J Nanomedicine 5:771-781.

Zuurbier M, Hoek G, Oldenwening M, Meliefste K, Krop E, van den Hazel P, Brunekreef B. 2011. In-traffic air pollution exposure and CC16, blood coagulation, and inflammation markers in healthy adults. Environ Health Perspect 119:1384-1389.